NATIONAL AERONAUTICS AND SPACE ADMINISTRATION

Space Programs Summary 37-48, Vol. II

The Deep Space Network

For the Period September 1 to October 31, 1967

JET PROPULSION LABORATORY
CALIFORNIA INSTITUTE OF TECHNOLOGY
PASADENA, CALIFORNIA

November 30, 1967

NATIONAL AERONAUTICS AND SPACE ADMINISTRATION

Space Programs Summary 37-48, Vol. II

The Deep Space Network

For the Period September 1 to October 31, 1967

JET PROPULSION LABORATORY
CALIFORNIA INSTITUTE OF TECHNOLOGY
PASADENA, CALIFORNIA

November 30, 1967

SPACE PROGRAMS SUMMARY 37-48, VOL. II

Prepared Under Contract No. NAS 7-100
National Aeronautics & Space Administration

Preface

The Space Programs Summary is a bimonthly publication that presents a review of engineering and scientific work performed, or managed, by the Jet Propulsion Laboratory for the National Aeronautics and Space Administration during a two-month period. Beginning with the 37-47 series, the Space Programs Summary is composed of four volumes:

Vol. I. *Flight Projects* (Unclassified)

Vol. II. *The Deep Space Network* (Unclassified)

Vol. III. *Supporting Research and Advanced Development* (Unclassified)

Vol. IV. *Flight Projects and Supporting Research and Advanced Development* (Confidential)

Approved by:

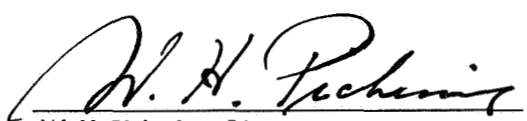

W. H. Pickering, *Director*
Jet Propulsion Laboratory

Contents

Contents (contd)

Contents (contd)

I. Introduction

The Deep Space Network (DSN) is a facility established by the NASA Office of Tracking and Data Acquisition under the system management and technical direction of JPL, and is responsible for two-way communications with unmanned spacecraft traveling approximately 10,000 miles from Earth to interplanetary distances. The DSN is distinct from other NASA networks such as the Space Tracking and Data Acquisition Network (STADAN), which tracks Earth-orbiting scientific and communication satellites, and the Manned Space Flight Network (MSFN), which tracks the manned spacecraft of the *Gemini* and *Apollo* programs.

The DSN performs four basic functions in support of each space flight project: tracking, data acquisition, command, and control. Tracking is the function of locating the spacecraft, calculating its distance, velocity, and position, and following its course. Data acquisition consists of the recovery of information from the spacecraft in the form of telemetry—the recorded measurements of the condition of, and the scientific data obtained by, the spacecraft. The command function involves the sending of signals to the spacecraft to guide it in its flight and to operate scientific and engineering equipment on board the spacecraft. Control refers to the making of command decisions from a central facility and to the overall direction of flight operations, including the network of ground stations, during a mission. Present facilities permit simultaneous control of a newly launched spacecraft and a second one already in flight. In preparation for the increased number of U.S. activities in space, a capability is being developed for simultaneous control of either two newly launched spacecraft plus two in flight, or four spacecraft in flight. With the advanced communications techniques now being implemented, it may soon be possible to obtain data from, and track spacecraft to, planets as far out in space as Jupiter.

The DSN supports, or has supported, the following NASA space exploration projects: *Ranger, Surveyor,* and *Mariner* (JPL); *Lunar Orbiter* (Langley Research Center); *Pioneer* (Ames Research Center); *Voyager;* and *Apollo* (Manned Spacecraft Center), as backup to the MSFN.

The main elements of the network are: the Deep Space Instrumentation Facility (DSIF), with space communications and tracking stations located around the world; the Ground Communications System (GCS), which provides communications between all elements of the DSN; and the JPL Space Flight Operations Facility (SFOF), the command and control center.

The DSIF is a worldwide chain of deep space stations that provide radio contact with the spacecraft (Table 1). JPL operates the U.S. and the Ascension Island stations. The overseas stations are normally staffed and operated

Table 1. Deep Space Instrumentation Facility

Deep Space Communication Complex (DSCC)	Deep Space Station (DSS)	DSS serial designation	Geodetic longitude, deg
Goldstone	Pioneer	11	243.1 E
	Echo	12	243.2 E
	Venus	13	243.2 E
	Mars	14	243.1 E
	Pasadena[a] (Flight Project/ Tracking Data System Interface)	21	241.8 E
Canberra	Woomera	41	136.9 E
	Tidbinbilla	42	149.0 E
	Booroomba[b]	43	—
	Johannesburg	51	27.7 E
Madrid	Robledo	61	355.7 E
	Cebreros	62	355.6 E
	Rio Cofio[b]	63	—
	Cape Kennedy (Spacecraft Monitoring)	71	279.4 E
	Ascension Island (Spacecraft Guidance and Command)	72	345.7 E

[a]Presently being implemented.
[b]Not yet authorized.

by government agencies of the respective countries, with the assistance of U.S. support personnel. To maintain continuous mission coverage, the stations are placed approximately 120 deg apart in longitude around the Earth, so that the spacecraft is always within the field of view of at least one of the ground stations.

Radio contact with the spacecraft begins when it is poised on the launch pad at Cape Kennedy, and is maintained throughout the mission as the spacecraft passes from the field of view of one station to that of another. The Cape Kennedy tracking facility monitors the spacecraft during and immediately after launch. Later in the launch trajectory, while the spacecraft is relatively low in altitude, the signal is picked up by the 30-ft antenna at Ascension Island. Once the spacecraft is in orbit, the deep space stations with the large antennas, low-noise phase-lock receiving systems, and high-power transmitters take over radio communications and follow the vehicle to its destination. These stations obtain angular position, velocity (doppler), and distance (range) data for the spacecraft, and provide command control (up-link) and data reception (down-link) for the spacecraft. The standard 85-ft-diameter antennas in use at the deep space stations have gains of 53 db at 2295 MHz, permitting the receipt of significant data at distances as far as Mars. To improve the data-rate and distance capability, a 210-ft-diameter antenna having a gain of 61.81 $\pm$0.32 db at 2295 MHz has been built at DSS 14; two additional antennas of this size are planned for installation at overseas stations. In the present configuration, with the exception of DSS 51 which has an S-band receiver–exciter subsystem, all stations are full S-band.

The DSN continuously conducts research and development of new components and systems to maintain a state-of-the-art capability. Therefore, the Goldstone DSCC is also used for extensive investigation of space tracking and telecommunications techniques, establishment of DSIF–spacecraft compatibility, and development of new DSIF hardware and software. New DSIF system equipment is installed and tested at the Goldstone DSCC before being accepted for systemwide integration into the DSIF. After acceptance for general use, it is classed as Goldstone Duplicate Standard (GSDS) equipment, thus standardizing the design and operation of identical items throughout the system.

The GCS, using facilities of the worldwide NASA Communications System (NASCOM), provides voice and teletype communications among the overseas DSIF stations, Goldstone, Cape Kennedy, and the SFOF. A special microwave link, which includes a video channel, is used between the SFOF and Goldstone to transmit critical data during a mission. Overseas communications are transmitted by land lines, submarine cables, microwave relays, high-frequency radio circuits, and even communication satellites.

Teletype is the primary means of transmitting tracking and telemetry data from the DSIF stations to the SFOF and sending predictions and other data to the stations. Voice circuits are used for transmission of high-priority communications other than data.

The SFOF at JPL is equipped with operations control consoles, status and operations displays, computers, and data-processing systems, and is the focal point of the DSN. From launch through mission completion, it is the control center for DSIF tracking and data-acquisition activities, as well as for spacecraft trajectory determinations, generation of the commands transmitted to the spacecraft, and analysis and interpretation of the data received.

Internal communications at the SFOF are maintained by means of telephones, voice intercom units, a public address system, closed-circuit TV, and other types of visual displays. Incoming spacecraft telemetry and tracking data from the deep space stations are automatically routed to the SFOF data-processing system, where special telemetry-processing equipment and high-speed digital computers convert the data into information for use by scientific experimenters and spacecraft engineers.

II. Tracking and Navigational Accuracy Analysis

A. DSN Inherent Accuracy Project, *T. W. Hamilton and D. W. Trask*

The DSN Inherent Accuracy Project was formally established by the DSN Executive Committee in July 1965. The objectives of the Project are:

(1) Determination (and verification) of the inherent accuracy of the DSN as a radio navigation instrument for lunar and planetary missions.

(2) Formulation of designs and plans for refining this accuracy to its practical limits.

Achievement of these goals is the joint responsibility of the Telecommunications Division (33) and the Systems Division (31) of JPL. To this end, regular monthly meetings are held to coordinate and initiate relevant activities. The Project leader and his assistant (from Divisions 31 and 33, respectively) report to the DSN Executive Committee, and are authorized to task Project members to (1) conduct analyses of proposed experiments, (2) prepare reports on current work, and (3) write descriptions of proposed experiments. The Project is further authorized to deal directly with those flight projects using the DSN regarding data-gathering procedures that bear on inherent accuracy.

The various data types and tracking modes provided by the DSIF in support of lunar and planetary missions are discussed in SPS 37-39, Vol. III, pp. 6–8. Technical work directly related to the Inherent Accuracy Project is presented in SPS 37-38, Vol. III, and in subsequent issues, and is continued in the following sections of this volume.

A lunar ephemeris (LE 5) has been constructed by fitting an integrated lunar trajectory to the positions available from the Brown lunar theory as represented by the current JPL lunar ephemeris (LE 4). This work is part of a continuing effort by the JPL Ephemeris Development Project to improve the accuracy of the tabulated

positions of the major planets and the moon; previous reports have appeared in SPS 37-47, Vol. II, by Mulholland (pp. 6–7) and by Devine and Lawson (pp. 8–20).

When ranging and doppler observations of space probes either near or on the moon are reduced using LE 4, residuals as large as 500 m in position and 2 mm/s in velocity are observed. The residuals are greatly reduced when the calculations are repeated using LE 5 (see Section B). Through the double-precision trajectory program, which provides a convenient means for generating an integrated lunar ephemeris, an independent check of LE 5 is available. This check is reported in Section C and is in excellent agreement with the results obtained in Section B.

The status of the various DSS location solutions obtained by postflight analysis of doppler and ranging tracking data from deep space probes is discussed in Section D. Uncertainties in DSS locations can become a limiting factor to the navigational accuracy obtained with earth-based radio tracking data. To meet the navigational accuracy goals currently being considered for some planetary projects, the DSS longitude and distance off the earth's spin axis must be known to within 1 m. The intent of this article is to define available solutions and to indicate the relative level of sophistication of each. At present, the variation from solution to solution is large when compared with the 1-m goal. The quality of the lunar ephemeris as discussed in Sections B and C is an important consideration in meeting these goals; i.e., lunar positional errors of 60 m in the longitude direction will cause a 1-m error in the DSS absolute longitude solution.

The Navigation Technology Project, a companion to the Inherent Accuracy and the Ephemeris Development Projects, is described in Section E, and articles relating to the work (discussed in Sections F, G, and H) are summarized.

In Section I (the last of the tracking and navigational accuracy analysis articles), results from the second phase of the doppler–ranging calibration experiment are described. This experiment is concerned with the discrepancies in range increments when measured by (1) integrating doppler over a time interval, and (2) differencing the ranging point at the end of the interval from that at the start. From this experiment, it is concluded that the observed discrepancies cannot be explained solely in terms of the differential effect due to the ionosphere or the change in the electrical path length due to temperature variations in the spacecraft or DSS equipment.

B. Lunar Ephemeris Errors Confirmed by Radio Observations of Lunar Probes, *W. L. Sjogren and C. N. Cary*

The tabulated positions of the moon which appear on ephemeris tapes prepared at JPL and used throughout the U.S. space program are calculated from modern versions of the Brown lunar theory (Refs. 1 and 2). Lunar velocities are obtained by numerically differentiating the positions. Recent reports (SPS 37-47, Vol. III, pp. 6–7; SPS 37-47, Vol. III, pp. 8–20; SPS 37-48, Vol. II, pp. 7–12; and Ref. 3) describe integrations of the moon's equations of motion and compare the resulting coordinates with those tabulated in JPL lunar ephemeris 4 (LE 4), with position differences as large as 500 m and velocity differences as large as 2 mm/s reported. Range data from four *Lunar Orbiters*, as well as doppler (range-rate) data from a *Surveyor* resting on the lunar surface, confirm the presence of systematic errors of this size in LE 4 and demonstrate the greater accuracy of the integrated ephemeris (LE 5) described in SPS 37-47, Vol. III, pp. 8–20.

A previous report (Ref. 3) described the use of *Lunar Orbiter* range data to detect ephemeris errors. It was shown that the incorporation of a set of known corrections to an earlier ephemeris (LE 2) caused range residuals as large as 1700 m to be reduced by an order of magnitude—most of them becoming less than 100 m. These results, although correct, were somewhat misleading, since data obtained later showed residuals as large as 440 m. By coincidence, the errors due to gravitational inconsistencies were unusually small during the period covered by Ref. 3.

The way in which observations of a *Lunar Orbiter* are used to detect ephemeris errors may be understood with the aid of Fig. 1. The spacecraft, at S, moves in an elliptical orbit about the moon. Range and doppler measurements, which are independent of one another, are recorded at the tracking station *T*. The doppler data alone are used to establish the spacecraft's orbit; from this, the selenocentric position vector **r** can be calculated to an accuracy of ± 100 m. This computation is insensitive to even very large errors in the lunar ephemeris.

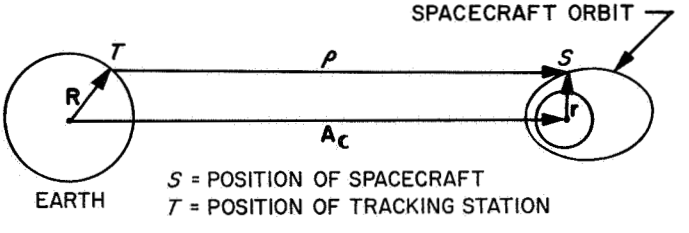

Fig. 1. Geometry of the *Lunar Orbiter* problem

From *a priori* information, **R**, the position vector of the tracking station, is known to ±30 m; $\mathbf{A}_{\mathbb{C}}$, the geocentric position vector of the moon, is obtained from the ephemeris. The range of the spacecraft is calculated as

$$\rho = |\boldsymbol{\rho}| = |\mathbf{A}_{\mathbb{C}} + \mathbf{r} - \mathbf{R}|$$

with an additional error of ±4 m being introduced at this point by the finite computer word size. A direct comparison is made between the calculated range values and the high-precision range measurements, which have not been used in the computation. Since **r** and **R** are well-known, any large differences must be attributed to errors in $\mathbf{A}_{\mathbb{C}}$. Because the earth–moon distance is much larger than the magnitudes of **r** and **R**, **ρ** is nearly parallel to $\mathbf{A}_{\mathbb{C}}$. For this preliminary analysis, it is assumed that these two vectors are parallel and, therefore, that range data directly measure errors in the radial distance to the moon and are insensitive to errors in the other coordinates. This assumption introduces an error of about 0.1 m, which is negligible for the present purpose.

The solid curve in Fig. 2 is a plot of the difference in radial distance to the moon between the integrated ephemeris (LE 5) and LE 4, the latest ephemeris based on Brown's theory (see SPS 37-47, Vol. III, pp. 8–20). The dots are *Lunar Orbiter* range residuals (observed minus computed), which were calculated using LE 4 as the source of $\mathbf{A}_{\mathbb{C}}$.[1] The residuals are in excellent agreement with the curve—generally better than 50 m—thus confirming the improved accuracy of the integrated ephemeris.

An additional test is provided by data obtained from *Surveyor I*, which landed in the Ocean of Storms on June 2, 1966. *Surveyor I* was tracked continuously for two weeks after it landed and then intermittently for the next six months, at which time it apparently ceased functioning. Because *Surveyor I* did not include ranging equipment, only doppler range-rate data were recorded.

For this case, the geometry is the same as that shown in Fig. 1, except that the vectors **ρ** and **r** meet at the lunar surface. The vector **r** and its time derivative depend only upon the selenographic coordinates of the spacecraft, and are calculated from the theory of lunar rotation (Ref. 4). The spacecraft range rate as observed at the tracking station is calculated as

$$\dot{\rho} = \dot{\boldsymbol{\rho}} \cdot \mathbf{u} = (\dot{\mathbf{A}}_{\mathbb{C}} + \dot{\mathbf{r}} - \dot{\mathbf{R}}) \cdot \mathbf{u}$$

where **u** is a unit vector in the direction of **ρ**. This data type is sensitive to those errors in the lunar velocity that project on **u**; because this is very nearly the direction of

[1]Nominally, each point represents the average of 100 ranging measurements recorded over a 12-hour period. There are many additional points which have not yet been reduced.

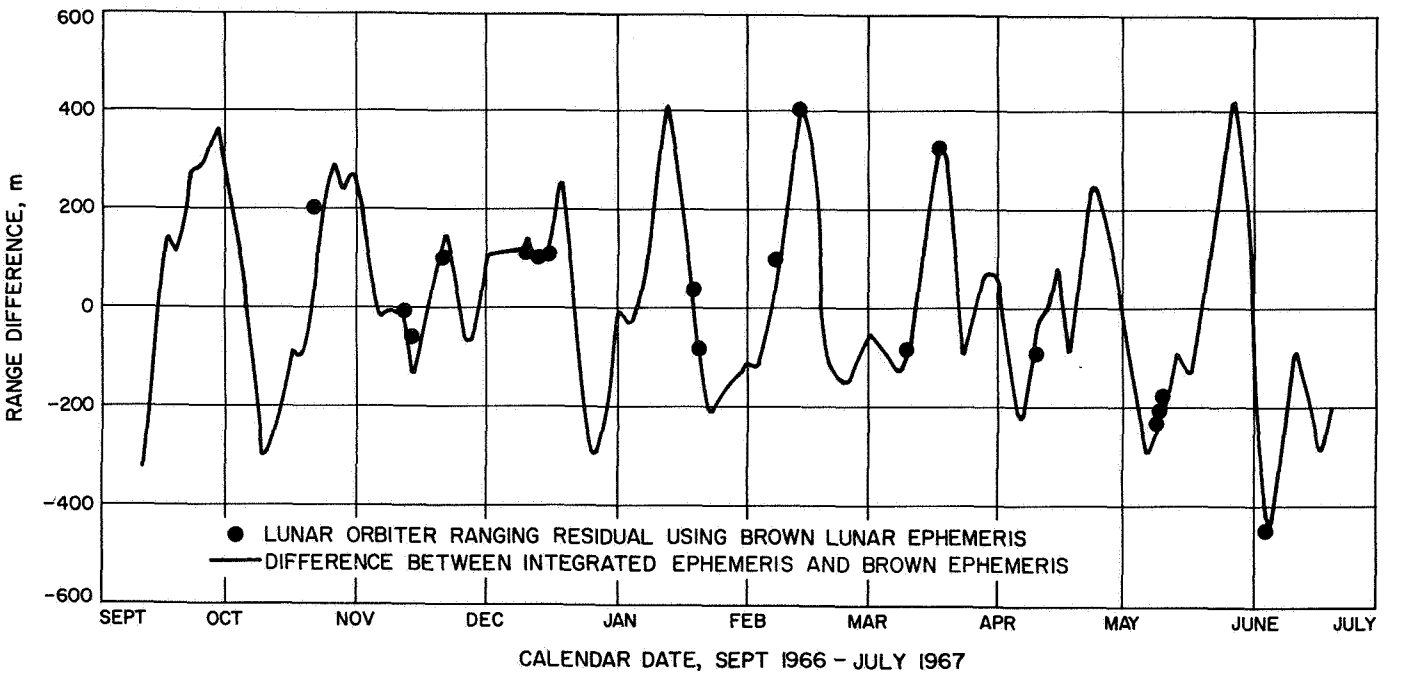

Fig. 2. Range residuals on the geocentric radial coordinate of the moon

A_α, doppler observations are most sensitive to errors in the moon's radial velocity.

Because of uncertainties in the flight path, the precise location of the spacecraft on the lunar surface was not known *a priori*. An orbit determination program was used to adjust the spacecraft coordinates (and those of the tracking station) so as to minimize the weighted sum of squares of doppler residuals. When this was done using LE 4 as the source of lunar positions and velocities, the residuals shown as dots in Fig. 3a were obtained.[2] Each group of dots represents several hundred doppler observations made during a twelve-hour tracking period. For comparison, differences in the moon's geocentric radial velocity between LE 5 and LE 4 are shown as a solid

[2]The residuals shown are for data recorded at DSS 42; residuals from other stations had a similar appearance.

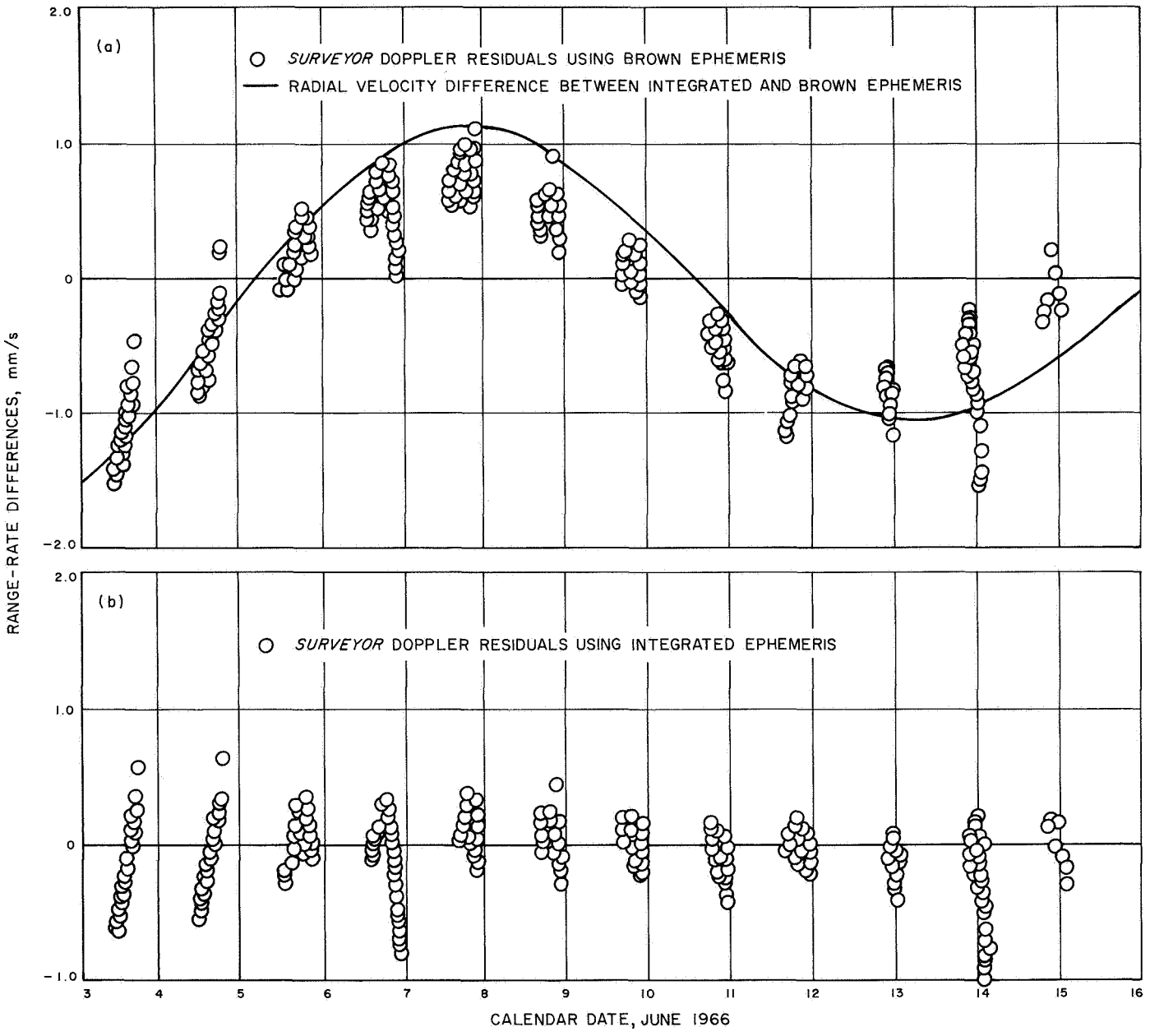

Fig. 3. Doppler residuals from *Surveyor I* on the lunar surface

curve. The estimated spacecraft location was nearly 6 km below the accepted lunar radius,[3] which is further evidence of the presence of systematic errors. When the computations were repeated using LE 5 in place of LE 4, the residuals shown in Fig. 3b were obtained, and the estimated spacecraft location moved to within 120 m of the accepted lunar radius.[4]

The lack of long-term variations in the final set of residuals and the more reasonable estimate of the lunar radius clearly demonstrate the improved quality of the integrated ephemeris. However, as shown in Fig. 3b, the use of LE 5 has not removed all the systematic trends—variations with a period of about one day are still evident. While these errors may be due in part to deficiencies in other aspects of the physical model used in the JPL orbit determination program, preliminary analysis indicates that use of an obsolete value of the oblateness of the earth in the computation of the integrated lunar ephemeris is probably a major contributor to the errors[5] (SPS 37-47, Vol. III, pp. 8–20); this discrepancy evidently produces errors of about 0.″2 (400 m) in the moon's latitude and longitude. An ephemeris incorporating a modern value of the oblateness constant is now in preparation at JPL.

At JPL, where unmanned missions to other planets are being planned and executed, these gratifying results are of extreme importance. These missions require precise knowledge of the locations of the tracking stations, since small errors in these coordinates will directly affect trajectory estimates made from tracking data, and hence will degrade mission experiments at planetary encounter. Therefore, a 1-m accuracy goal has been established for station coordinates. The primary method of achieving this goal will be the reduction of *Lunar Orbiter* tracking data, which provide the inertial reference necessary for good determinations. However, to achieve 1-m accuracy at the stations, the ephemeris of the moon must be accurate to 60 m; the present errors of nearly 500 m would severely degrade the data reductions. When the integrated ephemeris has been subjected to some further refinements, the goal should be attainable.

[3] "Accepted radius" refers to a value 2.5 km smaller than that shown on the lunar charts prepared by the Aeronautical Chart and Information Center. This adjustment is based on observed impact times of *Ranger* spacecrafts.

[4] In these calculations, the corrections to all lunar position and velocity coordinates were taken into account.

[5] Mulholland, J. D., private communication to the authors, Oct. 20, 1967.

C. An Integrated Lunar Ephemeris, *F. M. Sturms, Jr.*

1. Introduction

The ephemeris of the moon tabulated on the standard JPL ephemeris tapes (Ref. 5) is obtained from the Brown improved lunar theory. From the basic theory, rectangular position coordinates are obtained with respect to the mean equator and equinox of 1950.0. The lunar velocity components are then calculated by numerical differentiation. The format of the tabulated data is described in Ref. 6.

Recent improvements in the lunar theory by Eckert have been incorporated into the latest and most accurate JPL ephemeris: development ephemeris 19 (DE 19), which contains lunar ephemeris 4 (LE 4).

In the past, it has been suspected that errors in the lunar ephemeris, particularly in the lunar velocity components, might seriously affect tracking data from spacecraft landed on or orbiting the moon. Devine and Lawson (SPS 37-47, Vol. III, pp. 8–20) derived bounds of about 500 m on the position error and about 38 mm/s on the velocity error. Two sources for the velocity errors exist. One of these is the truncation error in the numerical differential formulas. This error is insignificant in comparison with the error resulting from the second source—errors in the position data derived from the lunar theory. It is also shown that error from interpolation between data points is very small.

A study was conducted to evaluate the errors in the lunar ephemeris by comparison with a numerical integration of the moon's motion. This study was prompted by the appearance of unexplained residuals in the tracking data of the landed *Surveyor I* during June 1966. The recent completion of the double-precision trajectory program (DPTRAJ) provided a convenient means for generating an integrated lunar ephemeris. The physical constants used in the DPTRAJ to generate a lunar ephemeris are generally consistent with those recommended for that purpose by Mulholland (SPS 37-47, Vol. III, pp. 6–7).

This study provides an independent check on the results obtained by Devine and Lawson, and the two methods show excellent agreement. The results of the study using DPTRAJ were instrumental in leading to the studies by Sjogren and Cary reported in the previous article (pp. 4–7). Together, as part of a concerted ephemeris improvement effort at JPL, they demonstrate the superiority of and need for an integrated lunar ephemeris.

2. Adjusting the Program To Integrate the Moon

In the DPTRAJ, by properly setting an input flag to zero, the moon may be turned off as a perturbing body.

This permits a probe to be located arbitrarily close to the center of the moon. At the initial epoch, a probe is placed at a geocentric position and velocity equal to that obtained for the moon from the ephemeris tapes.

The standard equations of motion in the DPTRAJ assume that the probe has negligible mass, which of course the moon does not. This situation is corrected by substituting for $GM_\oplus$, the gravitational constant of the earth, the sum

$$GM_\oplus = GM_{\oplus 0} + GM_{\leftmoon 0} \tag{1}$$

This substitution will result in a correct computation of the acceleration due to the point-mass earth–moon attraction.

The substitution in Eq. (1), however, will disturb the location of the earth–moon barycenter—and consequently, the solar and planetary perturbations. The heliocentric position of the earth is obtained from

$$\mathbf{E} = \mathbf{B} - \left(\frac{GM_\leftmoon}{GM_\oplus + GM_\leftmoon}\right)\mathbf{L} \tag{2}$$

where

$\mathbf{E}$ = sun–earth vector

$\mathbf{B}$ = sun–barycenter vector

$\mathbf{L}$ = earth–moon vector

$\mathbf{B}$ and $\mathbf{L}$ are obtained from the ephemeris tapes. The correct coefficient of $\mathbf{L}$ can be reestablished as follows. Rewrite Eq. (1) as

$$\begin{aligned} GM_\oplus &= GM_{\oplus 0} + GM_{\leftmoon 0} \\ &= GM_{\oplus 0}\left(1 + \frac{GM_{\leftmoon 0}}{GM_{\oplus 0}}\right) = GM_{\oplus 0}(1+\mu) \end{aligned} \tag{3}$$

Now input

$$GM_\leftmoon = GM_{\leftmoon 0}(1+\mu) \tag{4}$$

Then, in Eq. (2), we have

$$\begin{aligned} \frac{GM_\leftmoon}{GM_\oplus + GM_\leftmoon} &= \frac{GM_{\leftmoon 0}(1+\mu)}{(GM_{\oplus 0} + GM_{\leftmoon 0})(1+\mu)} \\ &= \frac{GM_{\leftmoon 0}}{GM_{\oplus 0} + GM_{\leftmoon 0}} \end{aligned} \tag{5}$$

Note that, since the moon is turned off as a perturbing body, the new input value of $GM_\leftmoon$ serves only to provide the correct value of the coefficient of $\mathbf{L}$ in Eq. (2).

Actually, the *integrated* value of $\mathbf{L}$ should be used, rather than the tabulated value from the ephemeris tapes. However, if it is assumed that the errors in the lunar ephemeris are small, and since the differential correction makes the integrated $\mathbf{L}$ very nearly the same as the ephemeris values, the errors in the solar and planetary perturbations should be negligible.

Since $GM_\oplus$ and $GM_\leftmoon$ are artificially increased by the factor $(1+\mu)$, the spherical harmonic terms of the earth–moon potential will yield acceleration terms that are too high. Only second-order oblateness terms were included in this study; therefore, corrective action was taken by replacing the mean radii in the potential by

$$R = \frac{R_0}{(1+\mu)^{1/2}} \tag{6}$$

The substitution indicated in Eq. (6) will yield correct computation of the direct earth oblateness and the indirect earth–moon oblateness[6] (SPS 37-29, Vol. IV, pp. 1–6) accelerations. [If higher-order harmonic terms are desired, the correction can be made by multiplying all harmonic coefficients by the terms $1/(1+\mu)$.]

The integration is performed in the 1950.0 system, and output is obtained at 0:00 and 12:00 ephemeris time (ET) in order to compare directly with the tabulated values on the ephemeris tape.

3. Constants and Initial Conditions

The reference values are obtained from the ephemeris tape by scaling with the recommended value for DE 19:

$$REM = 6378.1495 \text{ km}$$

(where REM is the earth–moon ephemeris scale factor.) The physical constants, corresponding to this value of REM, used in the DPTRAJ integration are:

$$\text{AU} = 149{,}597{,}900 \text{ km}$$

$$GM_{\oplus 0} = 398{,}601.3 \text{ km}^3/\text{s}^2$$

$$GM_{\leftmoon 0} = 4{,}902.7244 \text{ km}^3/\text{s}^2$$

$$\mu^{-1} = 81.302$$

[6]The indirect oblateness, which has not been sufficiently checked out, was not turned on in this study. The effect is certainly small and will be evaluated in the near future.

The remaining planetary and solar masses are generally those recommended by the International Astronomical Union, except for improved JPL values for Mars and Venus. Oblateness constants for the earth are:

$$R_0 = 6378.160 \text{ km}$$

$$J_2 = 1082.7 \times 10^{-6}$$

$$C_{22} = 1.57 \times 10^{-6}$$

$$S_{22} = -0.897 \times 10^{-6}$$

and, for the moon:

$$R_0 = 1738.09 \text{ km}$$

$$J_2 = 2.048 \times 10^{-6}$$

$$C_{22} = 0.23 \times 10^{-6}$$

$$S_{22} = 0$$

The initial epoch for the numerical integration is June 1, 1966, 0:00 ET (Julian ephemeris date 243,9277.5). At that epoch, the components of lunar position and velocity from the ephemeris tape (DE 19 containing LE 4) are:

$$x = -284712.8420283288 \text{ km}$$

$$y = -227629.4324744221 \text{ km}$$

$$z = -89291.81481464000 \text{ km}$$

$$\dot{x} = 0.6557927461197528 \text{ km/s}$$

$$\dot{y} = -0.7107018225251831 \text{ km/s}$$

$$\dot{z} = -0.4090104972607203 \text{ km/s}$$

These values are used to start the numerical integration. They are then differentially corrected to perform a least-squares fit. The seventh solve-for parameter in the fit is

$$GM_\oplus = GM_{\oplus 0} + GM_{\leftmoon 0} = 403504.0244 \text{ km}^3/\text{s}^2$$

4. Differential Correction of Integrated Ephemeris

A least-squares fit of the integration to the ephemeris was performed on the IBM 1620 computer. The fit was made to position data only, on the assumption that the positions from lunar theory are a good representation of actual observations.

The differential correction performed on the IBM 1620 is expressed in terms of the "normal equation" in matrix form:

$$\delta Q = (A^T W A)^{-1} A^T W \delta X \tag{7}$$

This is the form resulting from no *a priori* or "consider" terms, where

δQ = matrix of corrections to $GM_\oplus$ and the initial state vector

δX = matrix data residuals. (This matrix is made up of position component residuals δx, δy, and δz for time points every twelve hours from June 1 to July 1, 1966, taken in the sense ephemeris minus integrated.)

A = matrix of partial derivatives of the position components with respect to the solve-for parameters Q

W = weighting matrix

The data points are considered uncorrelated and each is assigned a unit weight. Therefore, W, being simply a unit matrix, drops out of Eq. (7). The covariance matrix on the solution is then simply

$$\Lambda_Q = \sigma_x^2 (A^T A)^{-1} \tag{8}$$

where σ_x is the one-sigma "noise" on the ephemeris positions; $(A^T A)^{-1}$ is obtained in the process of solving Eq. (7).

The matrix of partial derivatives, A, was generated by finite differences of perturbed trajectories. The perturbations were 1 km in initial position, 1 mm/s in initial velocity, and 1 km^3/s^2 in $GM_\oplus$.

Figure 4 lists the standard deviation (for unit data weights) for each of the solution parameters and the correlation matrix extracted from the values in $(A^T A)^{-1}$. The solution parameters are quite separable, since the maximum correlation is only -0.824.

A meaningful estimate of the solution statistics is obtained by multiplying each of the sigmas of Fig. 4 by the data noise σ_x, as represented in Eq. (8). From the results noted above, an upper bound is probably $\sigma_x = 0.5$ km, in which case each of the sigmas in Fig. 4 is reduced approximately half.

	$GM_\oplus$	x	y	z	$\dot{x}$	$\dot{y}$	$\dot{z}$	
	1.0	−0.665	0.104	0.129	0.095	−0.606	−0.435	$GM_\oplus$
		1.0	−0.625	−0.461	0.628	0.773	0.498	x
			1.0	0.507	−0.824	−0.771	−0.480	y
				1.0	−0.614	−0.588	−0.374	z
					1.0	0.547	0.381	$\dot{x}$
		SYMMETRIC				1.0	0.404	$\dot{y}$
							1.0	$\dot{z}$

$\sigma(GM_\oplus) = 0.440\ \text{km}^3/\text{s}^2$

$\sigma(x) = 0.224$ km $\quad \sigma(\dot{x}) = 0.542$ mm/s
$\sigma(y) = 0.292$ km $\quad \sigma(\dot{y}) = 0.856$ mm/s
$\sigma(z) = 0.214$ km $\quad \sigma(\dot{z}) = 0.604$ mm/s

Fig. 4. Standard deviations and correlation matrix for solution vector

These statistics are in good agreement with the actual residuals observed in the converged solution.

5. Comparison of Integrated and Tabulated Ephemerides

The differential correction converged in one iteration. The sum-of-the-squares (SOS) of the 183 data residuals was 259.0 km² on the initial integration. This gives an rms position *component* error of 1.19 km, or an rms position *vector* error of 2.06 km.

The δQs resulting from the initial integration were as follows:

$$\delta GM_\oplus = 0.038180405\ \text{km}^3/\text{s}^2$$

$$\delta x_0 = -0.0521179008\ \text{km}$$

$$\delta y_0 = -0.0678788219\ \text{km}$$

$$\delta z_0 = -0.09148988609\ \text{km}$$

$$\delta \dot{x}_0 = 1.4248451434\ \text{mm/s}$$

$$\delta \dot{y}_0 = 1.4793605566\ \text{mm/s}$$

$$\delta \dot{z}_0 = 0.4497819903\ \text{mm/s}$$

Applying these corrections yielded an SOS of 4.223 km² on the first iteration:

$$\text{rms component error} = \left(\frac{\text{SOS}}{183}\right)^{1/2} = 0.152\ \text{km}$$

$$\text{rms vector error} = \left(\frac{\text{SOS}}{61}\right)^{1/2} = 0.263\ \text{km}$$

A second iteration (with the same partials) produced a negligible improvement in SOS.

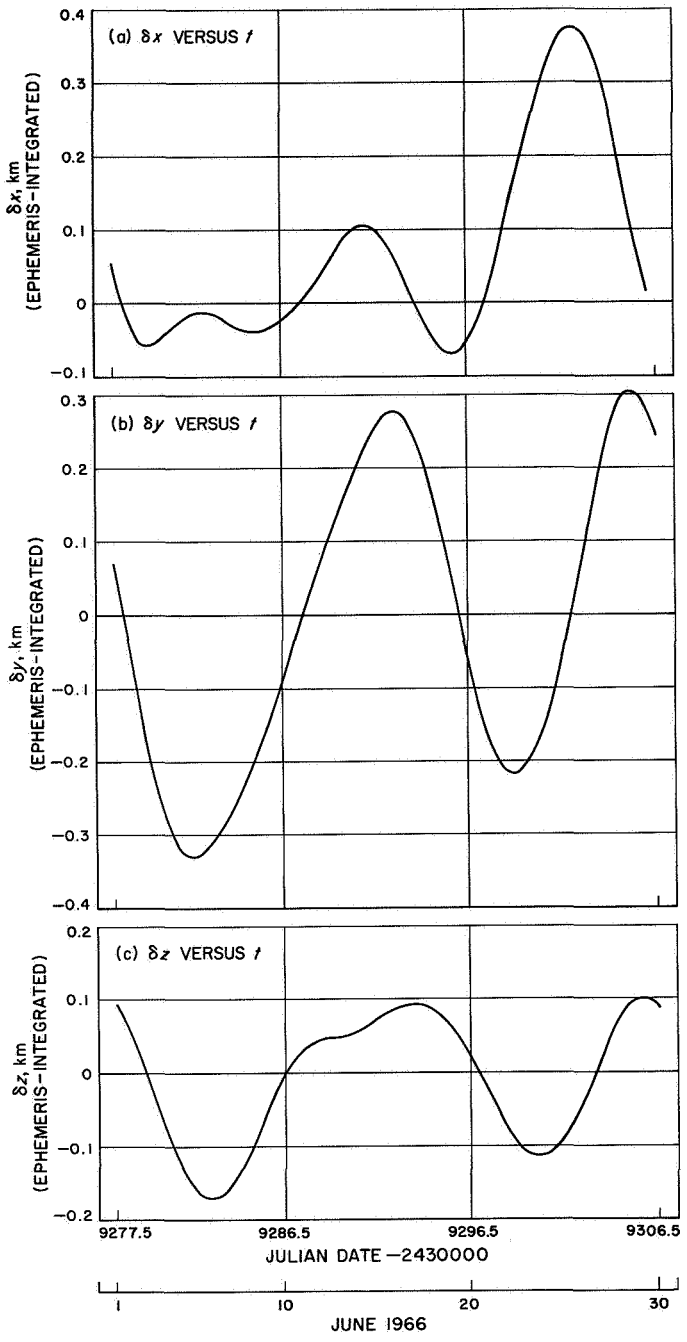

Fig. 5. Position component residuals versus time for the converged integration on DPTRAJ

Figures 5a–c show the position component errors as a function of time on the converged integration. Figures 6a–c show the corresponding velocity component errors, and Fig. 7 shows the geocentric range-rate component of the velocity error

$$\delta\rho = \frac{x\delta\dot{x} + y\delta\dot{y} + z\delta\dot{z}}{(x^2 + y^2 + z^2)^{1/2}} \tag{9}$$

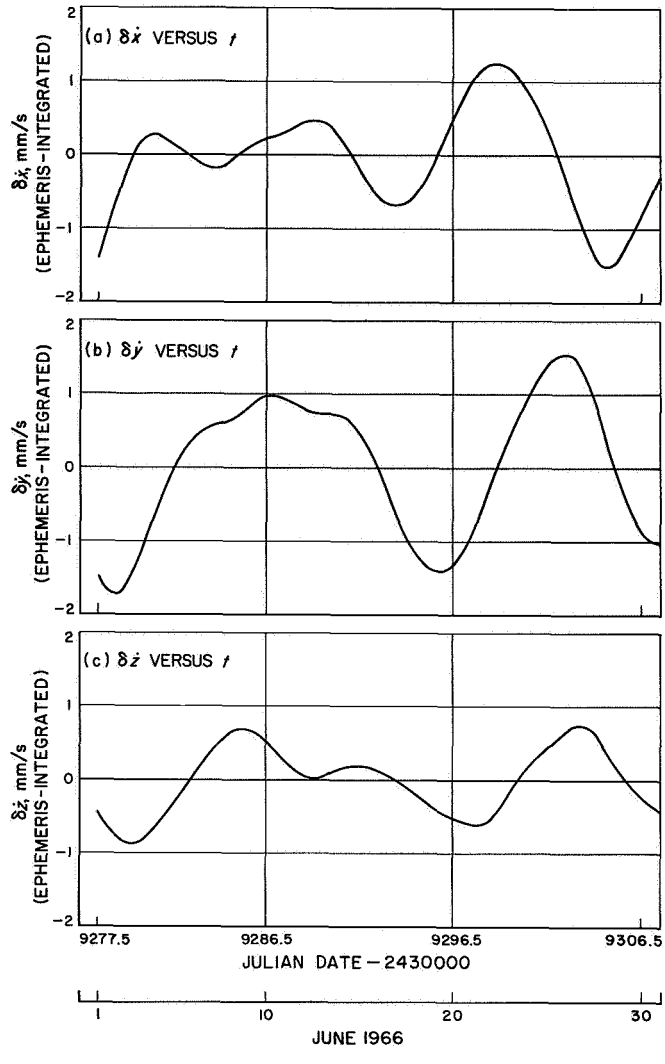

Fig. 6. Velocity component residuals versus time for the converged integration on DPTRAJ

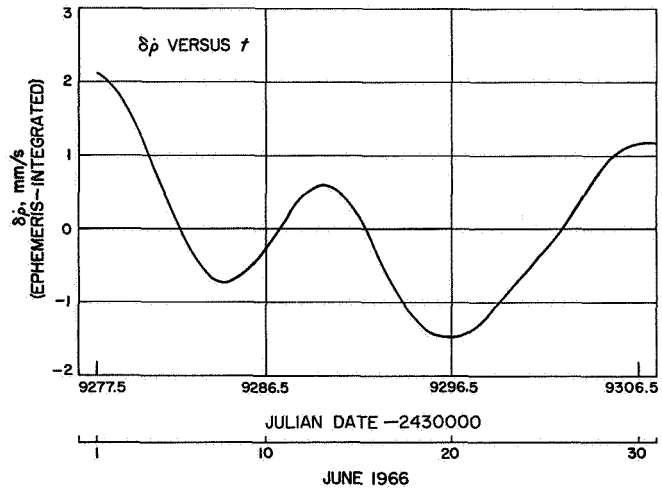

Fig. 7. Geocentric range-rate residuals versus time for the converged integration on DPTRAJ

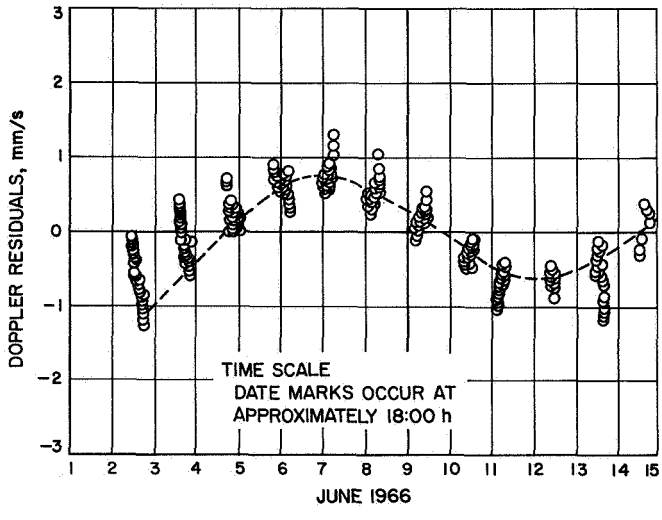

Fig. 8. Comparison of ephemeris residuals with *Surveyor I* post-touchdown tracking

Figures 5 and 6 show very good agreement in both shape and amplitude with residuals obtained by Devine and Lawson (SPS 37-47, Vol. III, pp. 8–20), which were obtained by an independent fit with PLOD II over a year interval. This agreement confirms the DPTRAJ fit over a shorter interval, and also attests to the accuracy of the somewhat untried integrator in DPTRAJ.

The converged range-rate residual, shown in Fig. 7, agrees remarkably well with the residuals observed in the postlanding tracking data for *Surveyor I*. The *Surveyor* residuals are shown in Fig. 8.[7] Superimposed on the *Surveyor* data are the results of Fig. 7, which have been reversed in sense to agree with that in Fig. 8. The agreement is such as to remove almost all doubt that a large part of the *Surveyor* residuals is, indeed, the result of errors in the lunar velocities on the ephemeris tapes.

6. Conclusions

The results of the above comparison with *Surveyor* data prompted additional comparisons of range residuals with those obtained by Sjogren from *Lunar Orbiter* tracking data (Ref. 7). The results (see Section B, pp. 4–7) demonstrate the superiority and basic accuracy of the integrated lunar ephemeris.

[7] Figure provided by C. N. Cary, whose results will soon be published in a collection of papers presented recently at a JPL-sponsored symposium on the lunar ephemeris.

Clearly, the present lunar ephemeris is of questionable accuracy for obtaining good solutions of physical constants from landed *Surveyor* and *Lunar Orbiter* data. The extent of improvement in the solutions for landing location, station locations, lunar harmonics, etc., is difficult to predict at present without more experience using an integrated ephemeris. It is important, therefore, that an interim ephemeris be constructed by numerical integration and used until a more sophisticated integrated lunar ephemeris can be provided. The results obtained with the interim lunar ephemeris may provide useful guides in determining the nature and extent of development of a new JPL lunar ephemeris.

D. Status of DSS Location Solutions for Deep Space Probe Missions: I. Initial Comparisons,

N. A. Mottinger and D. W. Trask

1. Introduction

Uncertainties in DSS locations can become a limiting factor to the navigational accuracy obtainable with earth-based radio tracking data. To meet the navigational goals under consideration for some planetary projects, the uncertainties in the DSS longitude σ_λ and distance off the earth's spin axis σ_{r_s} must be known on the order of 1 m. In an earlier article by Hamilton, Grimes, and Trask (SPS 37-44, Vol. III, pp. 4–11), an approximate method for determining the navigational accuracy obtainable during the encounter phase of a mission was presented, and the parameters that limit this accuracy were discussed.

This paper is the first in a series on the status of the various DSS location solutions obtained by postflight analysis of DSS tracking data (doppler and ranging) of deep space probes. The purpose of this series is to define available solutions and to indicate the relative level of sophistication of each.

To date, all work has been performed with the single precision orbit determination program (SPODP), described in Ref. 8, which lacks the precision required for computing DSS locations to the 1-m level. This 1-m goal will be realized with the availability of the double precision orbit determination program (DPODP), which, in addition to the extended precision of arithmetic operations, has models for antenna motion, polar motion, ionospheric effects, and ephemerides, as reported by Warner[8] and Moyer (SPS 37-38, Vol. III, pp. 24–27, and subsequent issues of Vol. III).

[8]Warner, M. R., *Double Precision Orbit Determination Program, Vol. I*, EPD 426, Nov. 1, 1966.

2. Discussion

The current status of station location solutions draws upon the following missions for its contents: *Ranger* Block III, (*Rangers VI, VII, VIII,* and *IX*); *Surveyors I* and *III; Lunar Orbiters II* and *III; Mariner II* (Venus, 1962); *Mariner IV* (Mars, 1964); and a span of *Pioneer VI.* Flight information and analysis for each are summarized in Table 1. Included in the individual analyses is such pertinent information as data type received, flight time, planetary and lunar ephemeris used, and the number identifying the magnetic tape on which this information is stored at JPL.

Two columns are devoted to timing relationships: (1) Ephemeris Time (ET), which is used to determine positions of celestial bodies, minus Universal Time Coordinated (UTC), time broadcast by the National Bureau of Standards; and (2) Universal Time 1 (UT1), used to determine the location of a tracking station in space (i.e., to define the orientation of the earth with respect to a celestial reference system), minus UTC. The DSS clocks are synchronized with UTC, which is used as a time tag associated with the actual tracking data. A detailed discussion of this subject appears in SPS 37-39, Vol. III, pp. 7–16, by Trask and Muller.

Complementing the analysis is a final reduction of the station location solutions to account for movements of the earth's axis of figure with respect to its axis of rotation. This movement, called polar motion, is essentially a displacement of the earth's crust with respect to the spin axis, and results in a continual change in the DSS latitude and longitude. However, no change occurs in the distance between the DSS and the earth's center of gravity. The International Polar Motion Service (IPMS) collects and disseminates (Ref. 9) the polar motion information in terms of the coordinates (x, y) of the instantaneous pole with respect to a standard pole (normally the mean pole of 1903.0).[9] The x, y values used to convert the individual mission DSS location solutions to the mean pole of 1903.0 are given in Table 1 along with the range of these values that occurred over the extended flights.

The effective data-weighting sigmas σ_{eff} based on range or continuous count doppler sampled once a minute are also shown in Table 1. These effective data weights take

[9]Use of the nomenclature mean pole of 1903.0 in place of the new mean pole of 1900–1905 was recommended at the Stress Symposium on Polar Motion, March 1967, as noted by W. Markowitz in a personal communication to D. Trask.

Table 1. Flight analysis summary

Flight	Tracking type	Span	Ephemeris		SDODP Mod	ET—UTC, s	UT1—UTC, ms	Effective data weights (based on 1 point/min),		Instantaneous polar position,[b] m				Polar motion during mission	Available documentation
			DE, LE[a]	JPL tape number				Doppler, mm/s	Ranging, m	x	Range in x	y	Range in y		
Ranger VI	Doppler[d]	67-70 h	DE 15, LE 3[f]	9302	2	35.201	−112	13	—	6.2	—	6.5	—	No changes	Ref. 10
Ranger VII	Doppler[d]	67-70 h	DE 15, LE 3[f]	9302	2	35.538	−119	13	—	7.5	—	9.4	—	No changes	Ref. 11
Ranger VIII	Doppler[d]	67-70 h	DE 15, LE 3[f]	9302	2	35.940	−49	13	—	4.4	—	4.1	—	No changes	—
Ranger IX	Doppler[d]	67-70 h	DE 15, LE 3[f]	9302	2	36.015	19	13	—	6.0	—	7.8	—	No changes	—
Surveyor I	Doppler[d]	2 wk	DE 15, LE 3	9302	4	—	—	13	—	3.7	—	7.8	—	No changes[g]	—
Surveyor III	Doppler[d]	3 days	DE 15, LE 3	9302	4	—	—	13	—	−0.2	—	4.8	—	No changes	—
Lunar Orbiter II	Doppler[e] and ranging	90 h	DE 15, LE 3	9302	4	—	—	6.5	15	3.9	—	9.0	—	No changes	SPS 37-46, Vol. III, p. 18
Lunar Orbiter III[c]	Doppler[d] and ranging	90 h	DE 15, LE 3	9302	4	—	—	6.5	15	1.7	—	5.9	—	No changes	—
Mariner II	Doppler[d]	3.5 mo	DE 3, LE2	9530	2	—	—	3	—	−1.0	2.2 to −3.4	3.9	1.9 to 6.7	[h]	Ref. 12
Mariner IV															
Cruise	Doppler[e]	7.5 mo	DE 3, LE 2	9530	4	—	—	3	—	−3.1	−6.1 to 2.2	7.5	1.4 to 14.0		Ref. 13
Post-encounter	Doppler[e]	2.5 mo	DE 3, LE 2	9530	4	—	—	3	—	4.9	1.8 to 6.8	10.8	13.2 to 8.0		Ref. 13
Pioneer VI (12/65–6/66)	Doppler[e]	6 mo	DE 3, LE 2	9530	4	—	—	32.5	—	−1.3	3.8 to −3.7	4.3	7.3 to 2.9		—

[a]Nomenclature defined in JPL Section 314 Internal Memorandum 314-145 (Footnote 11) and Ref. 15.

[b]The terms *x* and *y* define the location of the instantaneous pole with respect to the earth-fixed system pole (1903.0); *x* is positive toward Greenwich along the 0° meridian; *y* is positive along the meridian of 90°W, or, as used in this article, 270°E.

[c]Solar pressure computation not included in the data.

[d]L-band = 29.981×10^6 Hz up leg, 29.910×10^6 Hz down leg.

[e]S-band = 22.13×10^6 Hz up leg, 23.20×10^6 Hz down leg.

[f]Initial results only; earlier analysis performed with LE 2.

[g]Data from first two weeks after touchdown.

[h]Effect of variation during flight is difficult to analyze. Solution will be highly compromised because of SPODP limitations.

into account the nature of the various error sources,[10] as explained in Refs. 10 and 11.

Since statistics associated with the DSS locations are directly proportional to σ_{eff}, meaningful comparisons of flights depend on a correct relative weighting of the tracking data from flight to flight as well as on the relative weight assigned to doppler versus ranging. Past experience with the *Ranger* missions has shown that realistic statistics on the solve-for parameters (physical constants and probe orbital elements) result when σ_{eff} doppler = 13 mm/s is used. The σ_{eff} used during the translunar phase of the *Lunar Orbiter* missions is currently being reexamined. In particular, computing noise is a major contributor to σ_{eff} when the SPODP is used. This error source is a strong function of the probe trajectory. Therefore, it is expected that the contribution is larger for the *Lunar Orbiter* 90-h trajectory than for the *Ranger* 67- to 70-h translunar trajectories. Also, because the SPODP essentially cannot solve for biases on ranging data, for future analysis of the *Lunar Orbiter* translunar phase, the σ_{eff} (ranging) will be increased from the 15 m shown in Table 1 to $\approx$ 250 m. That is, although an individual range point is accurate to better than 15 m, because of the high correlation of the data errors it is necessary to use this large effective weighting sigma when processing the data in the SPODP, which assumes (except by the use of this "equivalent or worse" weighting scheme) that the noise on the data is uncorrelated.

Additional columns in Table 1 will be set aside for other effects that will be accounted for in advanced SPODP work and uniquely with DPODP. Such items presently include corrections for ionospheric effects and antenna motion.

Of all the flights mentioned, the *Ranger* Block III missions have undergone the most detailed analysis—originally with LE 2, and again with LE 3.[11] The cruise phase of *Lunar Orbiter II* is being analyzed to determine the consistency of doppler and ranging data. Early results by Mottinger and Sjogren are reported in SPS 37-46, Vol. III, pp. 19–23. The initial postflight analyses of *Mariners II* and *IV* are reported in Refs. 12 and 13, respectively. Results from the initial orbit of *Lunar Orbiter II* about the moon, as well as from *Surveyors I* and *III* and *Pioneer VI*, are provisional. The initial postflight analysis of this phase of *Lunar Orbiter II* and *Surveyor I* is still in progress, and *Surveyor III* and *Pioneer VI* results are those obtained during the real-time data analysis.

With the aid of an adaptation of the IPMS information by Muller,[12] the DSS location solutions are corrected for polar motion. The SPODP does not account directly for polar motion, and the correction applied to the ODP estimate is obtained by averaging the polar motion that occurs during the span of tracking data analyzed. In such cases as the *Rangers* or the translunar phase of the *Lunar Orbiters*, polar changes are insignificant. However, in an extended mission covering several months (as was the case for *Mariners II* and *IV*), the station locations may vary as much as 12 m during the flight. This motion, which has been neglected during processing of tracking data, compromises the DSS location solutions. The corrections apply to the latitude and longitude (the distance of the DSS from the earth's center of gravity is not affected by polar motion), from which r_s, the correct distance off the earth's spin axis,[13] is computed and plotted, along with the corrected geocentric longitudes. These parameters (r_s and λ) are the natural coordinates determined from earth-based radio tracking data. In addition to the absolute values for r_s and λ, the relative values (λ differences and r_s differences) for various station combinations are plotted to aid in checking consistency between various flight analyses.

3. Results

Figures 9, 10, and 11 are representative of the final plotted outputs that have been prepared for DSS 11, 12,

[10]The general form for the effective data-weighting sigma is

$$\sigma_{f_2(eff)} = \left[\sum_{i=1}^{n} \sigma_i^2 \max\left(1, \frac{T_{1_i}}{T_s}\right)\right]^{1/2}$$

where

σ_i is the standard deviation of the ith error source

T_{1_i} is the correlation width of the ith error source

T_s is the sample spacing of data points (60 sec for this article)

$$\max\left(1, \frac{T_{1_i}}{T_s}\right) = \begin{cases} 1, & \frac{T_{1_i}}{T_s} \leq 1 \\ \frac{T_{1_i}}{T_s}, & \frac{T_{1_i}}{T_s} > 1 \end{cases}$$

[11]The improved lunar ephemeris, LE 2, is contained in the initial JPL ephemeris system (Ref. 14), also known as development ephemeris 3 (DE 3). LE 3 represents the modified lunar ephemeris described in JPL Section 314 Internal Memorandum 314-145 (C. L. Lawson, *Announcement of Development Ephemeris 15*, Nov. 2, 1966), which includes the Eckert corrections in addition to other changes from LE 2. LE 3 is a pilot version and was used at JPL on an experimental basis. Minor discrepancies were found and corrected, resulting in the generation of LE 4 (Ref. 15) for general release.

[12]Muller, P., *Polar Motion and DSN Station Locations*, JPL Section 312 Internal Memorandum 312-799, Apr. 20, 1967.

[13]$r_s = R \cos \phi$, where R = geocentric radius and ϕ = geocentric latitude.

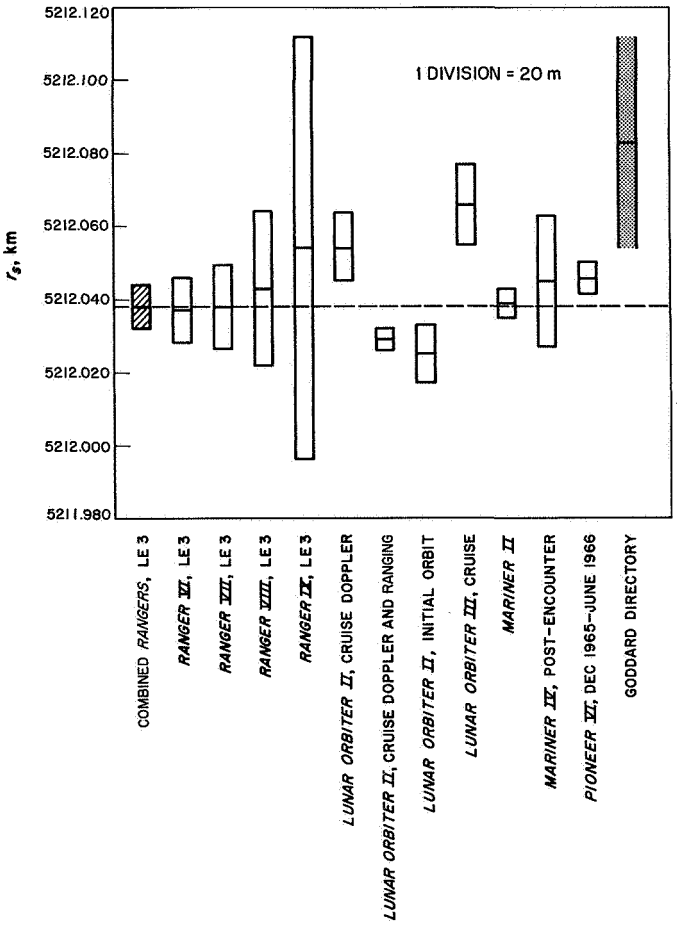

Fig. 9. Distance off spin axis, DSS 12 (1903.0 pole)

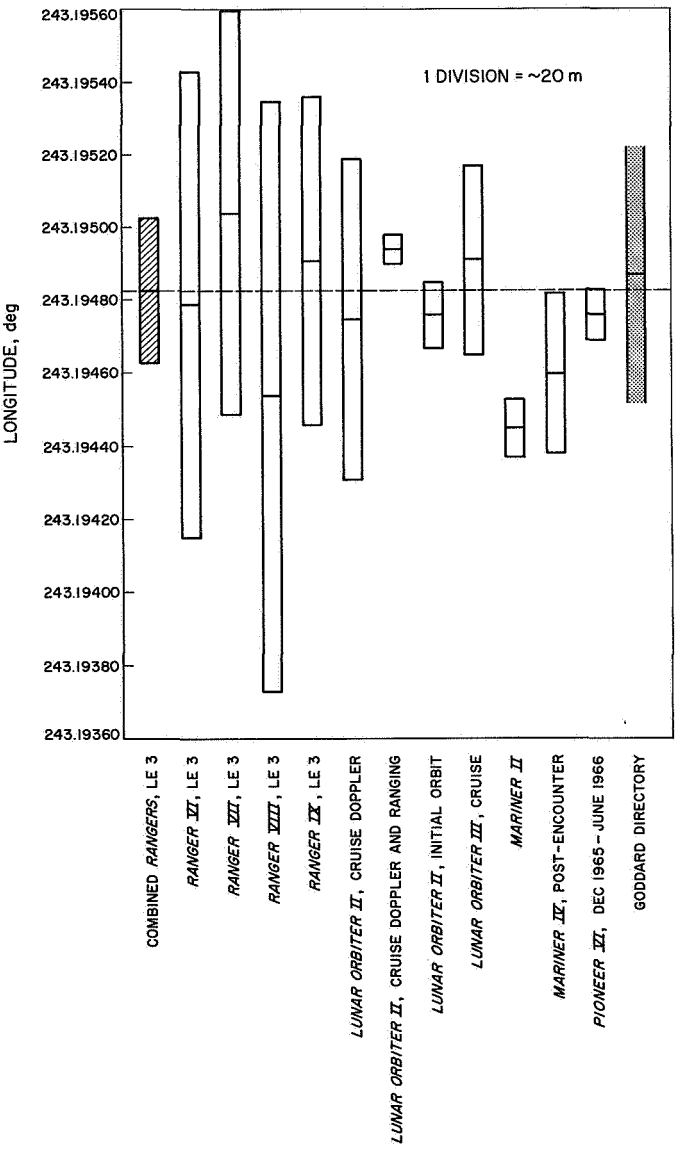

Fig. 10. Geocentric longitude, DSS 12 (1903.0 pole)

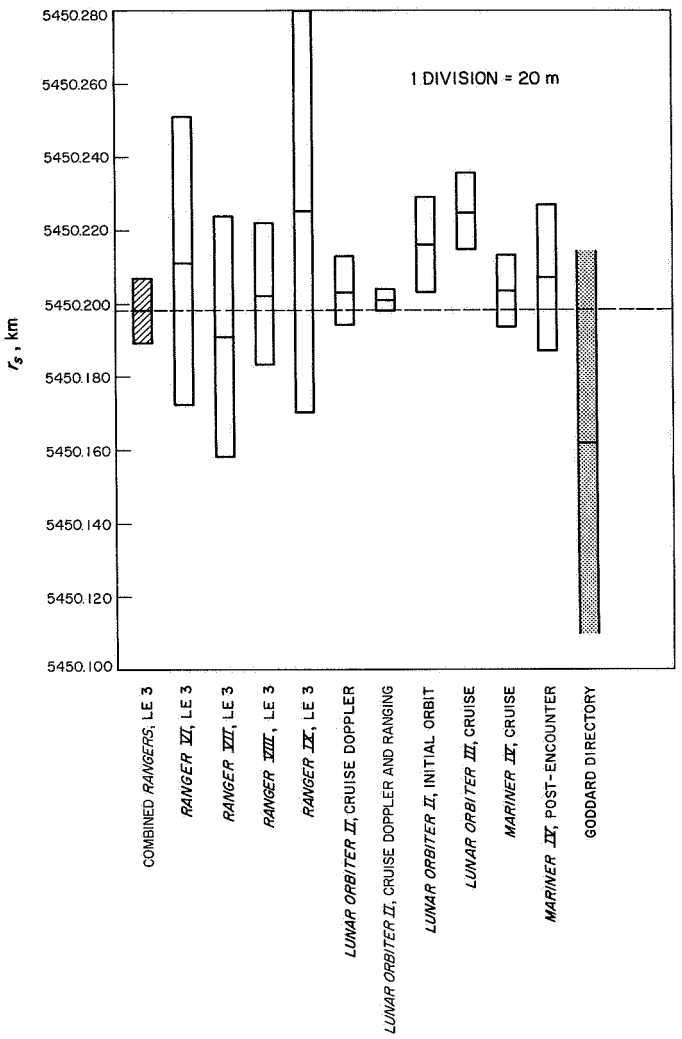

Fig. 11. Distance off spin axis, DSS 41 (1903.0 pole)

and 14 (Goldstone, California); DSS 41 and 42 (Woomera and Canberra, Australia, respectively); DSS 51 (Johannesburg, South Africa); and DSS 61 (Madrid, Spain). Likewise, Figs. 12 and 13 indicate results for relative locations.

The first set of figures was chosen as representative of the agreement for r_s and λ for the various missions. In Fig. 9, which shows r_s for DSS 12, the *Lunar Orbiter* results reported by Mottinger and Sjogren (SPS 37-46, Vol. III, pp. 19–23) should be noted. The *Lunar Orbiter* cruise doppler result for r_s of DSS 12 is 15 m greater than that of the combined *Rangers;* the same analysis with doppler and ranging data yields a value only 7 m less than the combined *Rangers.* The initial orbit result for this same probe, which was based on doppler data only, is definitely in keeping with the doppler and ranging results. The *Lunar Orbiter III* analysis is incomplete but has been included, and is even 20 m farther from the combined *Ranger* solution than the *Lunar Orbiter II* doppler results. The *Mariner II* value is within 1 m of the combined *Ranger* value. Both the *Mariner IV* post-encounter and *Pioneer VI* data are consistent with one another. Also, it should be noted that the probe results agree moderately well with the Goddard land survey results (Ref. 16).

Extreme caution must be taken[14] in determining the uncertainties associated with land surveys, particularly for absolute longitude.[15] Land surveys basically establish locations on a survey datum, within which the relative positions are more accurately known than the position of the datum with respect to the UT1 origin meridian. These latter uncertainties are not well defined, and the values quoted here are approximations presented for purposes of comparison with mission results. To obtain uncertainties for the geocentric radius (latitude and longitude), it is suggested that the error to the center of the earth (errors are assumed spherical), as listed in Ref. 16, be multiplied by $3^{-1/2}$.

Except for the *Mariner II* and the *Ranger* series which were tracked in the earlier L-band configuration, the DSIF tracked all missions in the S-band. This distinction is noted since the difference in ionospheric effects could cause a discrepancy between the L- and S-band results. Because the effects are inversely proportional to the square of the frequency, the ionosphere should have one-sixth the effect on the higher frequency S-band tracking data than that at L-band. (The frequencies are footnoted in Table 1.)

The ionospheric effect on the L-band data, which was ignored during this analysis, may result in a 5- to 10-m error in r_s and a 10- to 20-m error in λ, depending on the elevation angle, time history for the particular DSS, and the sun–earth probe geometry (see SPS 37-43, Vol. III, p. 16, by Trask and Vegos). Because the *Ranger* Block III flights are the most thoroughly analyzed to date, the combined *Ranger* solution is used as a baseline for this article. However, the four flights had a similar sun–earth-probe geometry (all launched during the lunar third quarter), which probably resulted in a biased statistical combination caused by similarities in the ionospheric effects. Therefore, part of this comparison is intended to determine if any ionospheric trend is apparent. That is, in the absence of other errors, a bias due to ionospheric effects should be detectable by comparing the

[14]According to T. Gunther of Geonautics, Inc., the agency responsible for the data appearing in the directory.

[15]Absolute longitude is the angular position with respect to the reference meridian (nominally Greenwich), used as the origin for UT1.

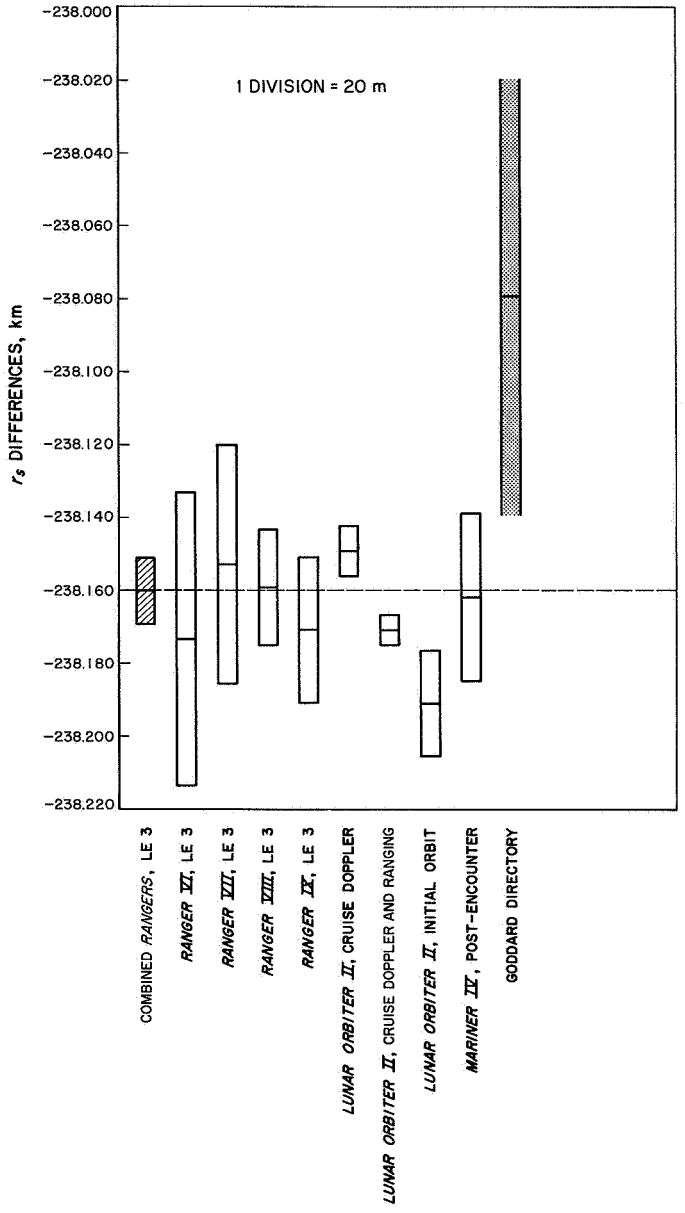

Fig. 12. Spin axis differences, DSS 12 values minus DSS 41 values (1903.0 pole)

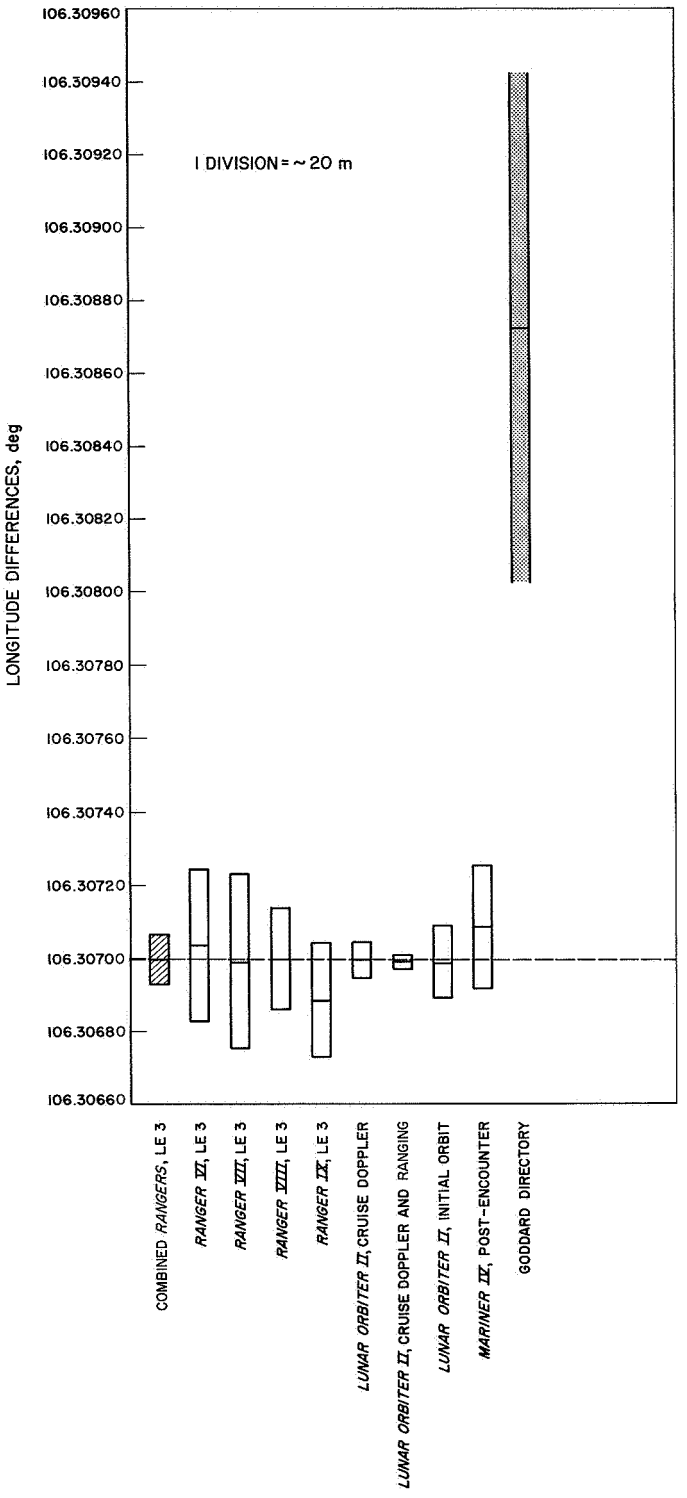

Fig. 13. Geocentric longitude differences, DSS 12 values minus DSS 41 values (1903.0 pole)

combined *Ranger* results with the results from the S-band missions, which are only one-sixth as sensitive to the ionosphere. For *Mariner II* (L-band), the sun–earth probe geometry varied slowly throughout the mission. However, a large portion of the tracking took place during the daylight hours (as opposed to the predominantly nighttime tracking for the *Rangers*). Although some averaging may take place, the DSS locations determined from *Mariner II* data may be more in error than those from the *Ranger* missions because of the ionospheric effects.

Figure 9 shows no clear distinction between the L- and S-band flights. However, the solutions for DSS 12 are influenced by more than just ionospheric effects. Because of operational considerations, a Goldstone station tracks during such critical events as encounter (impact), and at these times the doppler tracking data are most sensitive to any errors that exist between the model of the universe contained in the SPODP and the real universe. These model discrepancies will be reflected as errors in the solution vector (which includes DSS locations). Although all station locations will be shifted, the Goldstone stations, because of their more sensitive data, will experience the largest effect. On the other hand, in Fig. 11, which shows the solution of DSS 41 for r_s, a difference between the L- and S-band results is evident.

The longitude of DSS 12 is shown in Fig. 10 for the same flights used in Fig. 9. Again, in this figure, the S-band results are scattered about the combined *Ranger* solution; however, this time the *Mariner II* probe results differ from the combined *Ranger* value by 40 m. As previously discussed, 10- to 20-m errors in longitude may be due to ionospheric effects on the L-band data; however, longitude errors can also be caused by inaccurate ephemerides. The absolute DSS longitude is not determined until the spacecraft is under the influence of a body other than the earth; i.e., the λ is inferred from the known right ascension of the attracting body with respect to the earth. As discussed in SPS 37-43, Vol. III, pp. 3–18, a 1-km ephemeris error in lunar longitude with respect to the earth, which is not unreasonable, will cause a 16-m error in DSS longitudes. In the case of *Mariner II*, ephemeris errors may cause DSS longitude errors on the order of 35 m.

Figures 12 and 13 show the relative locations of DSS 12 and 41. Relative locations—in particular, longitude differences—are the coordinates best determined from the radio tracking data; therefore, variations in these solutions are helpful in spotting inconsistencies in the data or in showing the effects of charged particles (ionosphere). Since timing errors (which are common to all stations) and ephemeris errors affect the absolute longitude solutions of each DSS equally, the effect of these error sources cancels when considering the longitude difference between two stations. On the other hand, only part of the ionospheric effect is common to all stations. Also, while tracking-data anomalies peculiar to a particular DSS disturb the whole solution, they have the greatest effect on the offending station.

The disagreement between the Goddard land survey and the probe results should be noted. The methods of determining land survey errors between points (stations) lack a rigorous mathematical foundation; instead, they involve empirical estimations derived after studying vast quantities of Coast and Geodetic Survey data. The validity of these methods in determining uncertainties has been questioned. Authorities disagree as to whether they are lower or upper bounds on the error estimate.

To reduce these empirically obtained spherical errors between stations (Table IV of Ref. 16) to errors in radius and longitude, it is suggested that these percentage errors be multiplied by $2^{-1/2}$ for stations on the same datum and by $3^{-1/2}$ for stations not within the same datum.[14]

Figures 14 and 15, showing r_s and λ for DSS 11, respectively, are composites of probe results. One set contains the DSS locations directly obtained from probe analyses. The other set was obtained by determining the relative location of DSS 11 and DSS 12 from the *Goddard Directory* and then applying these relative results to the individual DSS 12 mission solutions.[16] As expected, the referenced values are in general agreement with the direct solutions for DSS 11 (Fig. 15), since the distance between DSS 11 and DSS 12 is 10 km. Therefore, the survey differentials should be good to 1 m, though the absolute errors may be larger.

Other results of importance occur for the *Mariner II*, *Mariner IV* post-encounter, and *Pioneer VI*. Values for r_s and λ appear twice for these three missions in plots for DSS 11: first, as they were directly solved for, and second, as they were obtained with the referencing process. For r_s of DSS 11, the *Mariner II* results agree within 10 m and the *Mariner IV* within 4 m, while the *Pioneer* results disagree by approximately 20 m.

[16]The differences used to reference DSS 11 from DSS 12 are -5.7117 km for r_s, -0.04393 deg for λ. These values were obtained from the *Goddard Directory*.

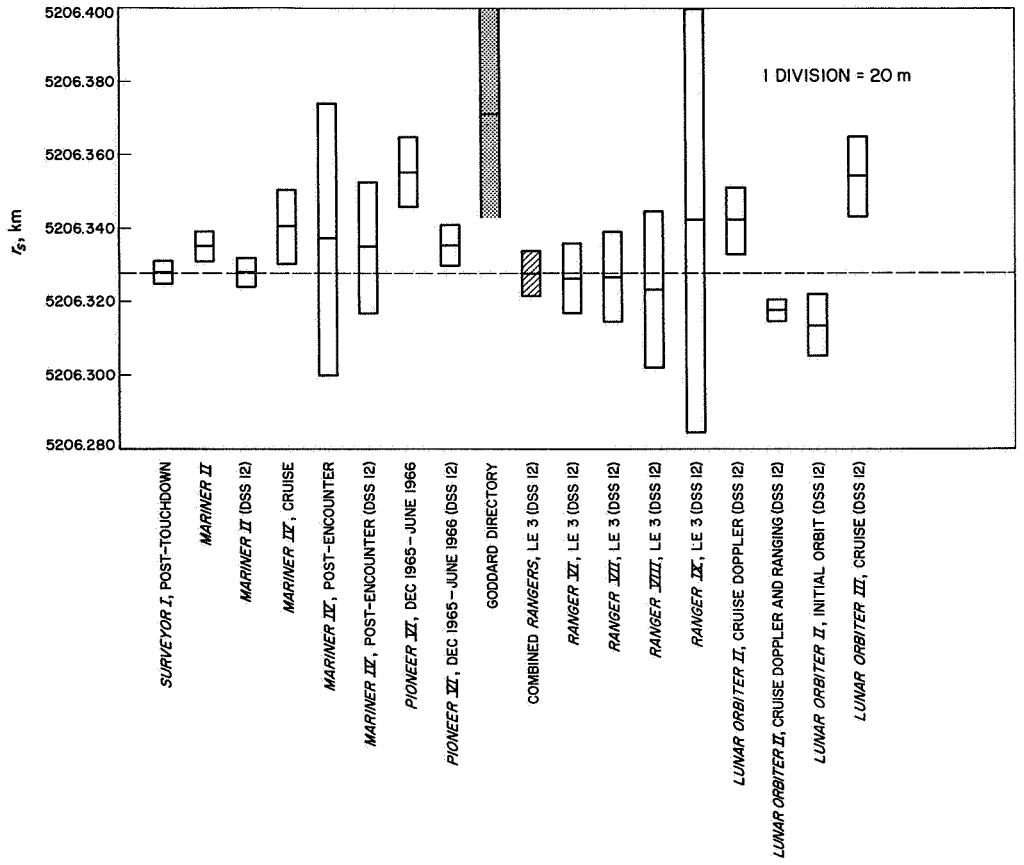

Fig. 14. Distance off spin axis, DSS 11 (1903.0 pole)

Most doppler tracking data obtained during the *Mariner II* mission were coherent three-way doppler. In this configuration, DSS 12 transmitted while DSS 11 received both the return signal from the spacecraft and the oscillator reference frequency over a microwave link from DSS 12, thus allowing the doppler to be taken in a coherent mode. Unlike other missions, which obtained two-way doppler independently from DSS 11 and 12 (although never at the same time), the *Mariner II* data type is physically dependent on the locations of DSS 11 and DSS 12. In addition, as described in Ref. 12, while an uncertainty of 1 km was assigned to the *a priori* value of absolute station locations, a 10-m uncertainty was assigned to the relative locations. Further, the current survey values were not available during the *Mariner II* reduction which used

$$\lambda_{11} - \lambda_{12} = -0.04387 \text{ deg}$$

and

$$r_{s_{11}} - r_{s_{12}} = -5.7041 \text{ km}$$

The disagreement by 0.00006 deg (~6 m) and 7.6 m in the differential λ and r_s, respectively, from the values used in Figs. 14 and 15 contributes to the *Mariner II* discrepancies. This disagreement in r_s may be explained partially by determining the specific times each of the stations tracked the probe and comparing these times with the polar motion effects. Since all three flights cover times of significant polar motion, averaging this motion will distort DSS location solutions if, for example, a station tracked only at the beginning or end of the period. As shown by Muller,[12] this could cause the 4-m discrepancy for *Mariner IV*, but could cause only approximately 2 of the 10-m disagreement for *Mariner II* and 2 of the 20 m for *Pioneer*.

Figure 15, which shows λ for DSS 11, was prepared in the same manner as Fig. 14. Here again, similar results are shown, although the land survey values are much more in line with probe results. Polar motion could account for approximately 4 m of the discrepancy in the longitude during the *Mariner IV* and *Pioneer VI* spans.

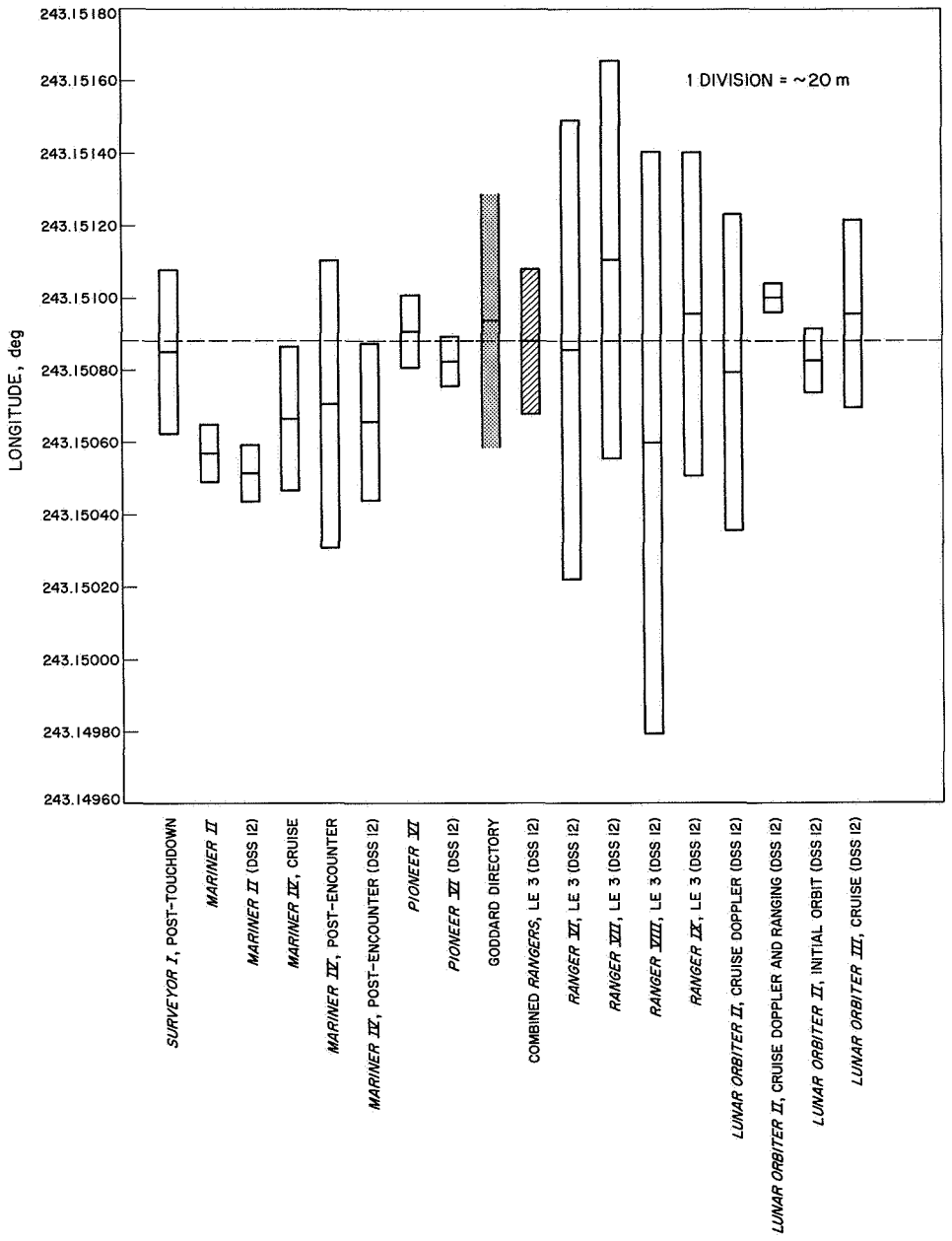

Fig. 15. Geocentric longitude, DSS 11 (1903.0 pole)

Table 2 presents a collection of existing DSS location solutions. The scatter of the solutions (partially illustrated in Figs. 9–15 for DSS 11, 12, and 41) is large when compared with the goal of obtaining σ_{r_s} and σ_λ on the order of 1 m. To facilitate identification with the source computer runs, R and ϕ, the coordinates used as input to the SPODP, are included in this table. However, direct comparisons of R and ϕ with survey data are not valid because $r_s = R \cos \phi$ is the parameter actually determined by the tracking data, which are relatively insensitive to the distance of the DSS from the earth's equatorial plane (z). This means that the resultant R and ϕ from the data reduction are artificial because they are strong functions of the equivalent assumed *a priori* value of z and are also quite sensitive to the noise on the tracking data.

4. Conclusion

The objective of further efforts is to reduce the spread of the data in Table 2 and to meet the project accuracy

Table 2. Absolute station locations and statistics

DSS	Data source	Distance off spin axis, km	1-σ standard duration, m	Geocentric longitude, deg[a]	1-σ standard deviation, m[a]	Geocentric radius, deg	Geocentric latitude, deg
11		5206.xxxx		243.15xxx		6372.xxxx	35.2xxxxx
	Surveyor I, post-touchdown	3271	2.9	085	23.8	6446	16317
	Mariner II	3357	3.9	058	8.8	0044	08035
	Mariner IV, cruise	3404	10.0	067	20.0	0188	08144
	Mariner IV, post-encounter	3378	37.0	072	40.0	0161	08151
	Pioneer VI, Dec 1965–June 1966	3359	9.6	092	10.3	0286	08030
	Goddard land survey,[b] Aug 1966	3718	29.0	094	~35.0	0640	08230
12		5212.xxxx		243.19xxx		637x.xxxx	35.11xxxx
	Combined *Rangers*, LE 3	0392	5.8	483	20.8	1.8770	7357
	Ranger VI, LE 3	0380	9.5	479	64.2	1.8744	7340
	Ranger VII, LE 3	0383	12.3	504	56.1	1.8786	7390
	Ranger VIII, LE 3	0427	21.5	454	81.8	1.8745	7332
	Ranger IX, LE 3	0541	58.2	489	45.0	1.8879	7263
	Lunar Orbiter II, doppler	0540	9.21	473	44.0	1.9016	7439
	Lunar Orbiter II, doppler and ranging	0295	3.1	494	4.3	1.8717	7439
	Lunar Orbiter II, initial orbit	0256	8.4	476	9.3	2.0149	9331
	Lunar Orbiter III, cruise	0660	10.8	489	26.4	1.8086	7341
	Mariner II	0398	4.2	445	8.7	1.8770	7347
	Mariner IV, post-encounter	0469	18.0	460	22.0	1.8832	7316
	Pioneer VI, Dec 1965–June 1966	0466	4.8	476	7.7	1.8851	7342
	Goddard land survey,[b] Aug 1966	0835	29.0	487	~35.0	2.0480	8850
14		5204.xxxx		243.11xxx		6372.xxxx	35.24xxxx
	JPL land survey[c]	0536	~29.0	042	~29.0	6790	4419
41		5450.xxxx		136.88xxx		6372.xxxx	−31.21xxxx
	Combined *Rangers*, LE 3	1987	8.6	783	21.2	5986	2076
	Ranger VI, LE 3	2113	39.6	775	67.1	6006	1859
	Ranger VII, LE 3	1913	33.3	805	60.6	5983	2172
	Ranger VIII, LE 3	2020	19.8	754	80.8	6076	2312
	Ranger IX, LE 3	2252	55.0	800	49.7	6392	2191
	Lunar Orbiter II, doppler	2032	9.5	773	43.2	6014	2010
	Lunar Orbiter II, doppler and ranging	2008	2.7	797	3.9	5986	2010
	Lunar Orbiter II, initial orbit	2161	13.1	781	9.6	8563	5569
	Lunar Orbiter III, cruise	2243	10.5	794	24.9	6415	2240
	Mariner IV, cruise	2031	10.0	758	20.0	6181	2261
	Mariner IV, post-encounter	2071	20.0	751	24.0	6179	2189
	Goddard land survey,[b] Aug 1966	1628	90.0	615	~30.0	5770	2350
42		5205.xxxx		148.98xxx		6371.xxxx	−35.2xxxxx
	Surveyor I, post-touchdown	3474	3.5	130	22.1	6651	19123
	Surveyor III, cruise and touchdown	3556	2.5	125	9.2	6881	19287
	Mariner IV, cruise	3478	10.0	136	20.0	6882	19410
	Mariner IV, post-encounter	3480	28.0	134	29.0	6824	19333
	Pioneer VI, Dec 1965–June 1966	3384	5.0	151	8.1	6932	19620
	Goddard land survey,[b] Aug 1966	2740	52.0	006	~61.0	7030	20750
51		5742.xxxx		27.68xxx		6375.xxxx	−25.73xxxx
	Combined *Rangers*, LE 3	9315	8.5	572	22.2	5066	9169
	Ranger VI, LE 3	9203	19.7	572	69.3	4972	9215
	Ranger VII, LE 3	9211	25.5	583	61.3	4950	9157
	Ranger VIII, LE 3	9372	22.3	548	85.0	5090	9159
	Ranger IX, LE 3	9626	56.6	580	49.5	5322	8993
	Surveyor III, cruise to landing	9431	5.7	535	10.8	5193	9154
	Mariner IV, cruise	9363	10.0	540	20.0	5120	9148
	Mariner IV, post-encounter	9365	40.0	556	38.0	5143	9198
	Pioneer VI, Dec 1965–June 1966	9332	11.6	567	12.0	5094	9176
	Goddard land survey,[b] Aug 1966	9706	39.0	586	~43.0	5410	8990
61		4862.xxxx		355.75xxx		63xx.xxxx	40.2xxxxx
	Surveyor III, cruise to landing	5947	2.7	100	8.5	69.9982	38787
	Lunar Orbiter II, doppler	6067	9.6	115	44.4	69.9932	38566
	Lunar Orbiter II, doppler and ranging	6118	3.4	138	4.0	69.9999	38566
	Lunar Orbiter II, initial orbit	6030	15.4	146	10.1	70.2311	41146
	Mariner IV, post-encounter	6063	14.0	099	24.0	70.0009	38655
	Pioneer VI, Dec 1965–June 1966	6059	8.8	103	10.4	70.0060	38715

[a] 1m $\simeq 10^{-5}$ deg; for purposes of comparison, xxx may be read as meters.
[b] See text discussion concerning standard deviation of land survey data.
[c] No uncertainty given; values listed are those of Goddard land survey for DSS 12.

goals. Much additional analysis is needed, even for the *Ranger* Block III missions. As reported in SPS 37-43, Vol. III, pp. 3–18, the analysis of these flights can be extended to obtain better DSS location solutions. As this work proceeds, revisions of Tables 1 and 2 will be included in subsequent issues of this volume.

E. Navigation Technology Project, *D. W. Curkendall*

The Navigation Technology Project was formally established within the Systems Analysis and Systems Analysis Research Sections in June 1966 to organize and coordinate the technological development of estimation and maneuver-strategy techniques necessary to realize flight-project guidance-accuracy goals. It forms a companion to the Inherent Accuracy and the Ephemeris Development Projects. The Navigation Technology Project has six principal objectives:

(1) To understand and develop adequate statistical models describing the nongravitational forces affecting the spacecraft trajectory.

(2) To develop computationally tractable techniques for trajectory estimation in the presence of these nongravitational forces and to describe the navigation accuracy achieved, with the use of these techniques, from the navigational data available.

(3) To perform approach-navigation studies and explore the potentialities of the combination of earth-based tracking data and spacecraft onboard observables.

(4) To construct simple geometrical approaches to compute navigation accuracies and develop data-compression techniques to facilitate the tasks of orbit selection and of processing long spans of tracking data.

(5) To develop the navigation technology required for orbital-capsule operations, including trajectory integration and observable computational techniques, bus-capsule relay-link navigation data, and landed-capsule observation.

(6) To develop appropriate guidance-maneuver strategies for such advanced interplanetary missions as *Voyager*.

Work relating to the Navigation Technology Project is supported by the various flight projects and by the Supporting Research and Advanced Development Office, as well as by the Deep Space Network. However, to simplify presentation, it is planned that all such work progress be reported in Vol. II of the SPS series.

In this issue, an investigation of a nonlinearity effect arising in the regression equation for the determination of probe declination with doppler is presented. It is shown that, while linear analysis indicates a singular situation for zero declination, the second-order term is significant and prohibits the occurrence of this phenomenon. Also included is the first of a series of articles describing progress with a continuous, nondiscrete formulation of the estimation problem. A computer program, the continuous estimation program, is described, and preliminary results, both analytic and numerical, are given. Finally, a plan is presented for the reorganization of the spacecraft's attitude control system to reduce its effective contribution to random nongravitational forces.

F. Navigation Technology: Errors in the Declination of a Distant Spacecraft for Near-Zero Declinations, *J. D. Anderson*

In SPS 37-39, Vol. III, pp. 18–23, Hamilton and Melbourne show that it is possible to obtain a direct measurement of the quantity $R_s \cos \delta$ from a single pass of doppler data of a distant spacecraft. Here, R_s is the perpendicular distance of the tracking station from the earth's axis of rotation, and δ is the geocentric declination of the spacecraft. If δ, itself, is to be obtained for a given value of R_s, the declination would be uncertain because of an uncertainty in the distance. Indeed, by taking the first variation of $R_s \cos \delta$, a relationship for an error $\Delta\delta$ in δ as a function of an error ΔR_s in R_s can be derived, which is

$$\Delta\delta = \cot \delta \frac{\Delta R_s}{R_s} \tag{1}$$

The purpose of this note is, first, to show that this formula leads to an erroneous result for small values of δ, and second, to illustrate the point that first-order variations do not always yield reliable expressions for purposes of error analyses. In the particular example considered here, the error in δ grows without bound as δ approaches zero. To show that this is not so, it is necessary to consider terms beyond the first-order in the increment $\Delta\delta$ that is exactly related to ΔR_s by the relation

$$(R_s + \Delta R_s) \cos (\delta + \Delta\delta) = R_s \cos \delta \tag{2}$$

Then, to the second order in $\Delta\delta$, Eq. (2) can be approximated by

$$\frac{1}{2}\Delta\delta^2 + \tan\delta\Delta\delta - \frac{\Delta R_s}{R_s} = 0 \qquad (3)$$

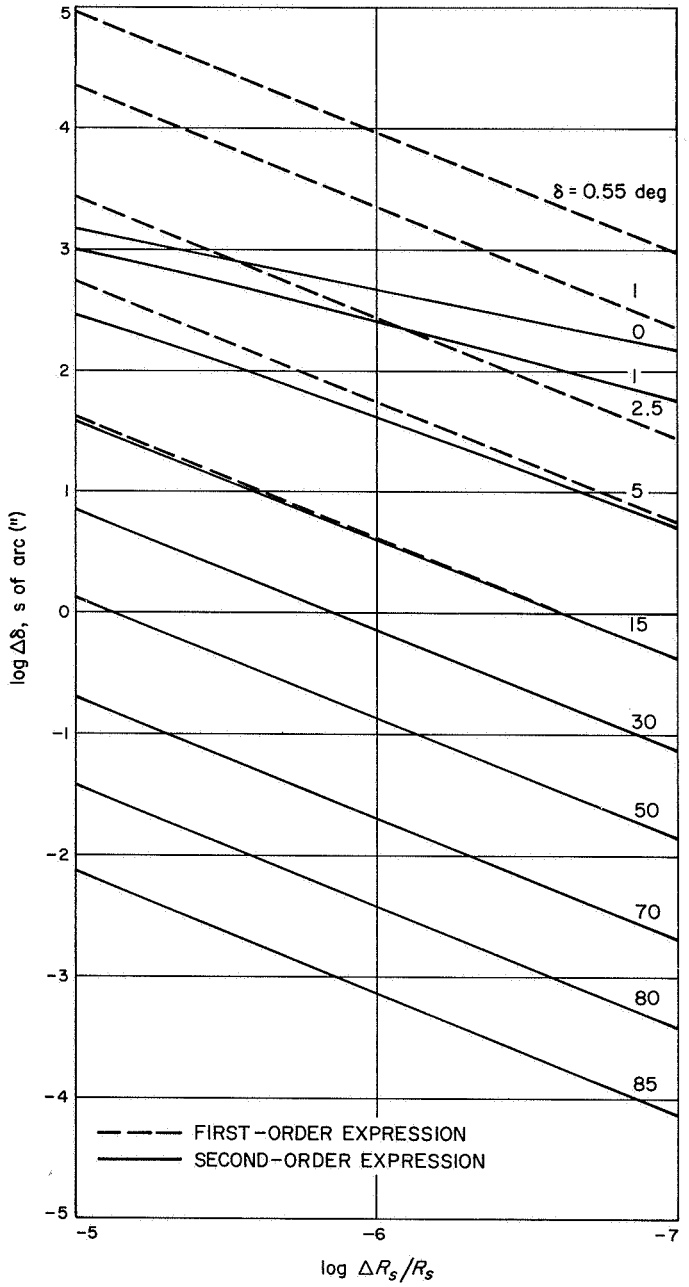

Fig. 16. Sensitivity of spacecraft declination to errors in distance of tracking station from the earth's axis of rotation

and a second-order expression for $\Delta\delta$ is obtained by solving the quadratic equation. The result is

$$\Delta\delta = -\tan\delta + \left(\tan^2\delta + 2\frac{\Delta R_s}{R_s}\right)^{1/2} \qquad (4)$$

Now it can be seen that, as δ approaches zero, the value for $\Delta\delta$ approaches

$$\left(2\frac{\Delta R_s}{R_s}\right)^{1/2}$$

To show how the more accurate expression for $\Delta\delta$ differs from the first-order expression of Eq. (1), log $\Delta\delta$ is plotted as a function of log $\Delta R_s/R_s$ for various values of δ over a realistic range of $\Delta R_s/R_s$ (see Fig. 16).[17] The dotted lines on the plot correspond to the linear relation of Eq. (1), while the solid lines correspond to the second-order expression of Eq. (4). Note that, below a declination of 5 deg, the validity of the linear relation as an accurate error formula deteriorates rapidly.

G. Navigation Technology: Preliminary Results From the Continuous Estimation Program,

J. F. Jordan

1. Introduction

The continuous estimation program (CEP) is currently being used for applied research in the field of orbit determination. The main purpose of the program is to explore the feasibility of the use of continuous estimation techniques for future orbit-determination tasks in which the nongravitational disturbing forces are expected to have large effects on space vehicle trajectories. To achieve this purpose, the program has been designed to study the performance of continuous minimum-variance estimators of the instantaneous values of both time-varying and constant parameters associated with a space vehicle traveling on a near-conic trajectory. Some of the features that make the CEP unique among the various applied research computer programs at JPL are listed as follows:

(1) Observational data are supplied to the observer continuously.

(2) The data type is range difference (counted doppler), contaminated by continuous exponentially correlated noise.

[17]The numerical calculations and the plot were furnished by S. Chesne.

(3) The spacecraft can be allowed to be perturbed by continuously acting random nongravitational low-thrust forces (process noise), which are assumed exponentially correlated in time.

The program is based on the theory of Pfeiffer for obtaining the minimum variance estimate of the time-varying state of a stochastic process from continuous observations that are contaminated by correlated noise (Ref. 17). Pfeiffer's work is essentially a revisal of the work of Kalman (Ref. 18), which treated only the case of white data noise.

The most complete documentation of the CEP was written by Nishimura,[18] who also originated the programming request.[19] The CEP is a FORTRAN IV, double-precision IBM 7094 program.

2. Program Description

The CEP studies the performance of a continuous estimator by means of the time history of the covariance matrix of the errors in the estimate. The parameters that can be estimated in the program are the space vehicle six-dimensional state (cartesian coordinates), constant and time-varying components of the three-dimensional nongravitational force, the mass constant and the principal oblateness term of the central body, constant and time-varying portions of the difference between universal and ephemeris time, the initial station location (geocentric spherical coordinates), and constant and time-varying portions of the data noise. In all, there are 21 estimated parameters.

If the deviations in the 21 parameters from the *a priori* values are listed as a single vector $\delta\mathbf{q}$, the differential equation that describes the motion of $\delta\mathbf{q}$ can be written as

$$\delta\dot{\mathbf{q}} = E\,\delta\mathbf{q} + \Gamma\mathbf{w} \tag{1}$$

where $\mathbf{w}$ is a white noise vector forcing function. Furthermore, the observational data vector $\boldsymbol{\phi}$ can be related to the 21 dimensional state deviation $\delta\mathbf{q}$ by a linear relation

$$\boldsymbol{\phi} = A\,\delta\mathbf{q} \tag{2}$$

If the minimum variance estimate of $\delta\mathbf{q}(t)$, given the continuous observation $\boldsymbol{\phi}(\tau)$, $0 \leq \tau \leq t$, is designated by $\delta\hat{\mathbf{q}}(t)$, and if the covariance matrix of the error in the estimate is defined as

$$\Lambda = \mathcal{E}\left[(\delta\mathbf{q} - \delta\hat{\mathbf{q}})\,(\delta\mathbf{q} - \delta\hat{\mathbf{q}})^{\mathrm{T}}\right] \tag{3}$$

where $\mathcal{E}$ denotes the expected value operator, then the differential equation that describes the time history of the covariance matrix is a Riccati equation of the form

$$\dot{\Lambda} = F\Lambda + \Lambda F^{\mathrm{T}} - \Lambda G\Lambda + H \tag{4}$$

A more detailed elaboration of Eqs. (1) through (4) and the definitions of the matrices E, Γ, A, F, G, and H appear in Nishimura's internal publications.[18,19]

The input of the program consists of initial conditions of the space vehicle and tracking station, the *a priori* values of the estimated constants, the initial standard deviations and the correlation times of the components of the process noise and data noise, and a (21×21) *a priori* covariance matrix $\Lambda(0)$.

The main function of the program is the numerical integration of the matrix Riccati differential equation for the covariance matrix at any time t. This is accomplished by an Adams–Moulton numerical integration scheme, using a Runge–Kutta starter.

The output of the program consists of the instantaneous standard deviation of each of the 21 estimated parameters; i.e., the square roots of the respective diagonal elements of Λ, as well as the instantaneous *a priori* state history of the space vehicle.

3. Preliminary Results of the Program

During the checkout phases of the program development, attention has been directed to solving simple problems, and the emphasis has been on noting the effects of the standard deviation and correlation time of the exponentially correlated data noise on the estimation procedure.

In this article, results from the program will be given for the simple one-dimensional problem of a stationary observer at the origin, tracking a spacecraft traveling radially away from the origin with uniform velocity. The

[18]Nishimura, T., *Continuous Estimation of Time-Varying Parameters of a Low-Thrusted Spacecraft*, JPL Section 312 Internal Memorandum 312-667, Mar. 4, 1966.

[19]Nishimura, T., *Continuous Estimation Program Used for Orbit Determination of a Low-Thrusted Space Probe, Part II: Estimation of Time-Varying Parameters*, JPL Section 312 Internal Memorandum 312-481, Feb. 3, 1966.

equations of motion of the space vehicle can be written as follows:

$$\begin{aligned} \dot{v} &= 0 \\ \dot{x} &= v \end{aligned} \tag{5}$$

where v designates the space vehicle velocity and x designates its displacement.

The observer records the continuous time history of the noise-contaminated range difference, i.e.,

$$\phi(t) = x(t) + \epsilon(t) - [x(t_0) - \epsilon(t_0)] \tag{6}$$

where $\epsilon(t)$ is stationary, exponentially correlated noise, possessing the following first- and second-order *a priori* statistics:

$$\begin{aligned} \mathcal{E}[\epsilon(\tau)] &= 0 \\ \mathcal{E}[\epsilon(\tau)\,\epsilon(\rho)] &= \sigma_{\varepsilon 0}^2\, e^{-\beta_\varepsilon |\,\tau - \rho\,|} \end{aligned} \tag{7}$$

where $\sigma_{\varepsilon 0}$ is the standard deviation of $\epsilon(\tau)$, and β_ε is the reciprocal of the noise correlation time τ_ε.

If v, x, and ϵ are designated by a three-dimensional vector $\mathbf{q}$, i.e.,

$$\mathbf{q} = \begin{bmatrix} v \\ x \\ \epsilon \end{bmatrix} \tag{8}$$

and the covariance matrix associated with the errors in the minimum variance estimate of $\mathbf{q}$, given $\phi(\tau)$, $0 < \tau < t$, is

$$\Lambda = \mathcal{E}[(\mathbf{q} - \hat{\mathbf{q}})\,(\mathbf{q} - \hat{\mathbf{q}})^{\mathrm{T}}] = \begin{bmatrix} \lambda_{11} & \lambda_{12} & \lambda_{13} \\ \lambda_{21} & \lambda_{22} & \lambda_{23} \\ \lambda_{31} & \lambda_{32} & \lambda_{33} \end{bmatrix} \tag{9}$$

then the following set of differential equations describes the time histories of the six independent covariance matrix elements:

$$\begin{aligned}
\dot{\lambda}_{11} &= -\frac{1}{2\sigma_{\varepsilon 0}^2}\,[\tau_\varepsilon \lambda_{11}^2 - 2\lambda_{11}\lambda_{13} + \beta_\varepsilon \lambda_{13}^2] \\
\dot{\lambda}_{12} &= \lambda_{11} - \frac{1}{2\sigma_{\varepsilon 0}^2}\,[\tau_\varepsilon \lambda_{11}\lambda_{12} - \lambda_{11}\lambda_{23} - \lambda_{12}\lambda_{13} + \beta_\varepsilon \lambda_{13}\lambda_{23}] \\
\dot{\lambda}_{13} &= -\lambda_{11} - \frac{1}{2\sigma_{\varepsilon 0}^2}\,[\tau_\varepsilon \lambda_{11}\lambda_{13} - \lambda_{11}\lambda_{33} - \lambda_{13}^2 + \beta_\varepsilon \lambda_{13}\lambda_{33}] \\
\dot{\lambda}_{22} &= 2\lambda_{12} - \frac{1}{2\sigma_{\varepsilon 0}^2}\,[\tau_\varepsilon \lambda_{11}\lambda_{12} - \lambda_{11}\lambda_{23} - \lambda_{12}\lambda_{13} + \beta_\varepsilon \lambda_{13}\lambda_{23}] \\
\dot{\lambda}_{23} &= -\lambda_{12} + \lambda_{13} - \frac{1}{2\sigma_{\varepsilon 0}^2}\,[\tau_\varepsilon \lambda_{12}\lambda_{13} - \lambda_{12}\lambda_{33} - \lambda_{13}\lambda_{23} + \beta_\varepsilon \lambda_{23}\lambda_{33}] \\
\dot{\lambda}_{33} &= -2\lambda_{13} - \frac{1}{2\sigma_{\varepsilon 0}^2}\,[\tau_\varepsilon \lambda_{13}^2 - 2\lambda_{13}\lambda_{33} + \beta_\varepsilon \lambda_{33}^2]
\end{aligned} \tag{10}$$

Analytic solutions to Eqs. (10) are presented here in order to give the reader some insight into the nature of the solutions of the Riccati equation. After establishing the following definitions:

$$\left.\begin{aligned} \lambda_{11} &= \sigma_v^2 & \qquad \lambda_{22} &= \sigma_x^2 \\ \lambda_{12} &= \sigma_{xv} & \qquad \lambda_{23} &= \sigma_{x\varepsilon} \\ \lambda_{13} &= \sigma_{v\varepsilon} & \qquad \lambda_{33} &= \sigma_\varepsilon^2 \end{aligned}\right\} \tag{11}$$

and assuming the following initial conditions:

$$\left.\begin{aligned} \sigma_v(t_0) &= \sigma_{v0} & \qquad \sigma_\varepsilon(t_0) &= \sigma_{\varepsilon 0} \\ \sigma_x(t_0) &= \sigma_{x0} & \qquad \sigma_{xv}(t_0) &= \sigma_{v\varepsilon}(t_0) = \sigma_{x\varepsilon}(t_0) = 0 \end{aligned}\right\} \tag{12}$$

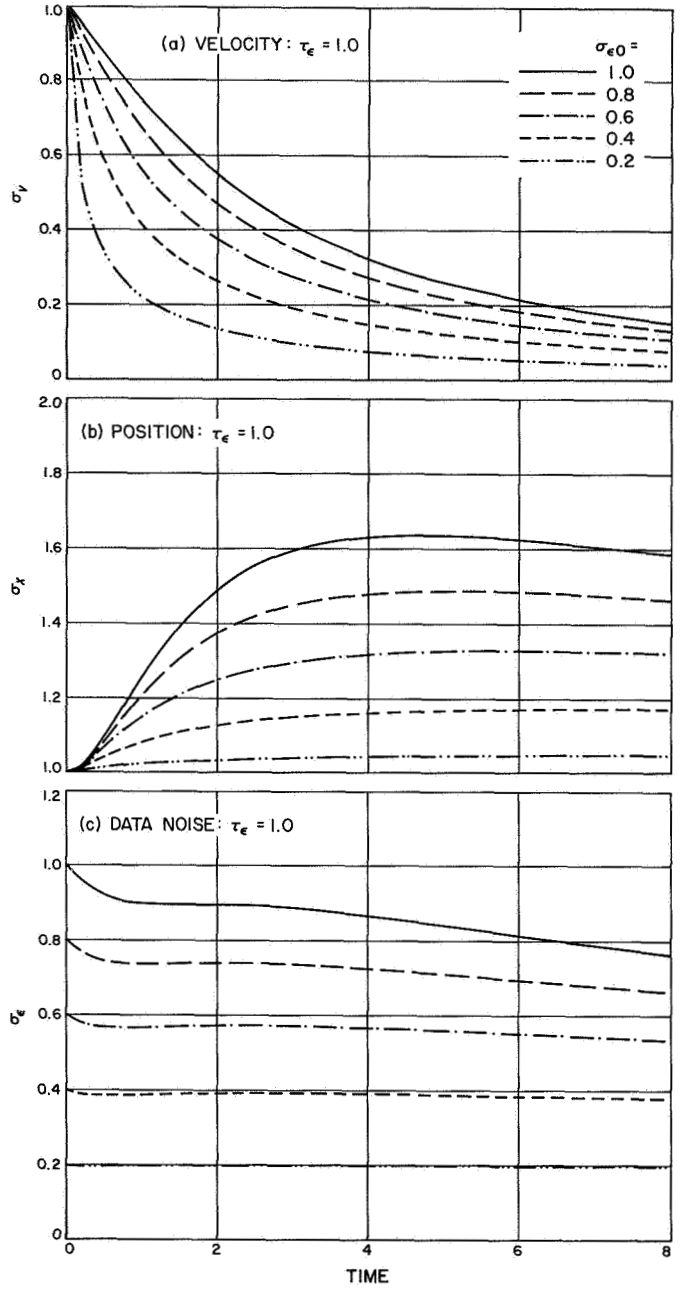

Fig. 17. Standard deviation time histories for various values of $\sigma_{\varepsilon 0}$

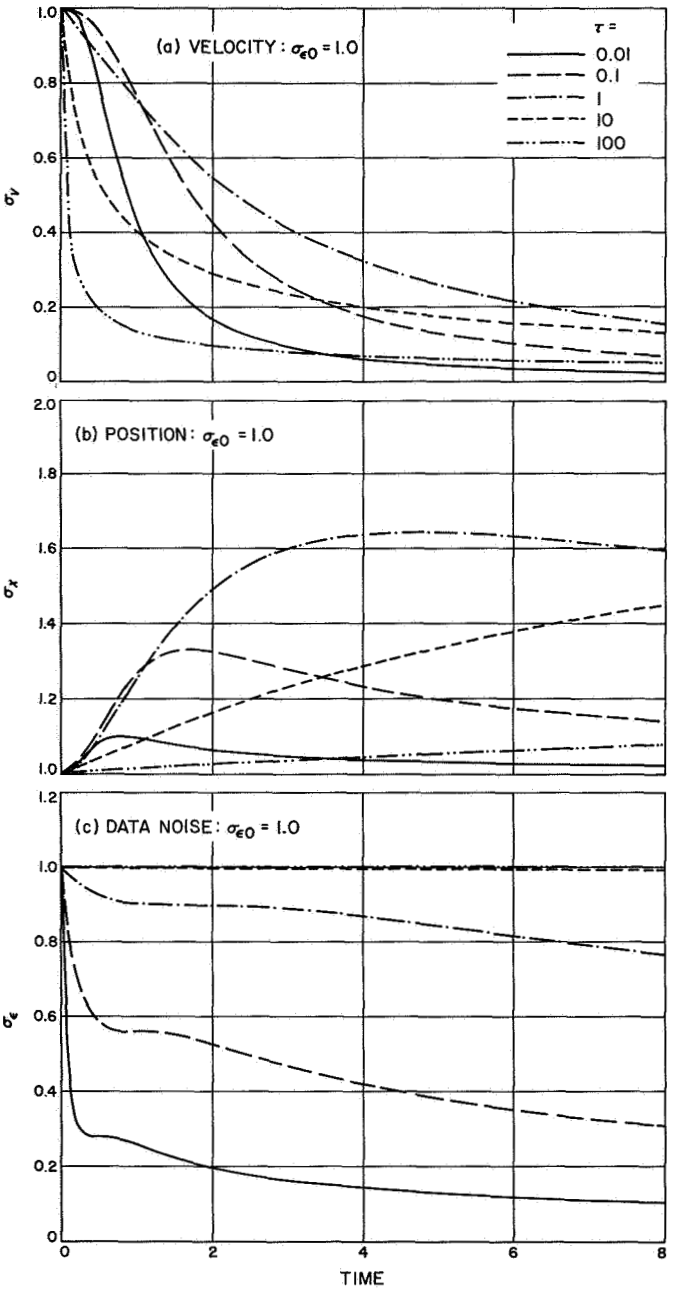

Fig. 18. Standard deviation time histories for various values of τ_ε

the analytic solutions to Eqs. (10) can be stated as

$$\sigma_v^2 = \frac{1}{D}\left(\frac{\hat{1}}{\sigma_{\varepsilon 0}^2} + \frac{t}{2\sigma_{\varepsilon 0}^2 \tau_\epsilon}\right)$$

$$\sigma_{vx} = \sigma_v^2 t$$

$$\sigma_{v\varepsilon} = \frac{1}{D}\left\{\left[\frac{\tau_\varepsilon}{2\sigma_{\varepsilon 0}^2}\left(t - \frac{t^2}{\tau_\varepsilon} + \frac{t^3}{3\tau_\varepsilon^2}\right) + \frac{1}{\sigma_{v0}^2}\right] - t\left(\frac{t}{2\sigma_{\varepsilon 0}^2} + \frac{t^2}{4\tau_\varepsilon \sigma_{\varepsilon 0}^2}\right)\right\} \tag{13}$$

$$\sigma_x^2 = \sigma_{x0}^2 + \sigma_v^2 t^2$$

$$\sigma_{x\varepsilon} = \frac{1}{D}\left(\frac{t}{2\sigma_{\varepsilon 0}^2} + \frac{t^2}{4\tau_\varepsilon \sigma_{\varepsilon 0}^2}\right) t - \sigma_v^2 t^2$$

$$\sigma_\varepsilon^2 = \sigma_{v\varepsilon} - \sigma_{x\varepsilon}$$

where

$$D = \frac{1}{\sigma_{v0}^2 \sigma_{\varepsilon 0}^2} + \frac{\tau_\varepsilon t}{2\sigma_{\varepsilon 0}^2}\left(\frac{1}{\sigma_{\varepsilon 0}^2} + \frac{1}{\tau_\varepsilon^2 \sigma_{v0}^2}\right) + \frac{t}{2\sigma_{\varepsilon 0}^4}\left(t + \frac{t^2}{3\tau_\varepsilon}\right) + \frac{t^4}{48\sigma_{\varepsilon 0}^4 \tau_\varepsilon^2} \tag{14}$$

The time histories of σ_v, σ_x, and σ_ε are illustrated in Figs. 17 and 18, for *a priori* state standard deviations $\sigma_{v0} = 1$ and $\sigma_{x0} = 1$. Figure 17 shows the time histories of σ_v, σ_x, and σ_ε for various values of $\sigma_{\varepsilon 0}$. The figures are designed to illustrate the sensitivity of the observing procedure to the standard deviation of the noise in the data. Figure 18 shows the time histories of σ_v, σ_x, and σ_ε for various values of the correlation time of the data noise τ_ϵ. From the behavior of the σ time histories in the figures, the following conclusion can be drawn.

The continuous counted-doppler observation technique, when the data are contaminated by exponentially correlated noise, obtains velocity estimates with steadily decreasing standard deviations. The position estimate standard deviations are inhibited from growing large, but never fall below the *a priori* value. This is a consequence of the linearity of the dynamic system. For small correlation times, the standard deviation of the data noise decreases in time, indicating the ability of the technique to estimate the data noise. The standard deviations of the velocity, position, and data noise all vary directly with the *a priori* data noise standard deviation. The standard deviations of the probe state are larger when the data noise correlation time is comparable to the tracking interval. The standard deviation of data noise estimate error is smaller for shorter data noise correlation time.

It is expected that some of the characteristics of the continuous estimation technique (discussed in the above conclusions) when applied to the linear one-dimensional problem will also appear in future results as the CEP is applied to practical deep-space orbit determination problems. Two specific problems that are being explored by means of the CEP are:

(1) The application of the CEP to the problem of determining the information content of a single pass of data, with comparisons of the results to those reported by Hamilton and Melbourne (SPS 37-39, Vol. III).

(2) The application of the CEP to the problem of estimating the state of a space vehicle being perturbed by large nongravitational random forces. Investigation of the feasibility of data compression schemes in the presence of such forces.

Results of these studies will be reported in subsequent issues of this volume.

H. Navigation Technology: A Technique for the Reduction of Random Attitude-Control-System-Generated Nongravitational Forces,

R. Bourke, D. Curkendall, and S. McReynolds

Analysis of the flight path of *Mariner IV* indicates that the attitude control system imparted significant translational momentum to the spacecraft. Conclusive arguments have been advanced by Null, et al., (Ref. 13) to show that uneven gas leakage from the attitude control

thrusters is one source of a net translational force; others are the difference in impulse delivered by different jets and variation of impulse from firing to firing in the same jet (see SPS 37-47, Vol. II, pp. 21–27). In this article a different arrangement for the attitude control thrusters is proposed which will substantially reduce the random components of the nongravitational forces. An additional benefit of the new system is that the trajectory is unaffected by a valve failure during flight.

The *Mariner IV* attitude control configuration (described in detail in Ref. 19) is briefly summarized here. The *Mariner IV* was designed so that opposite jets fire in pairs, delivering a net angular momentum impulse but (theoretically) no net translational momentum (Fig. 19). For redundancy, a dual gas system is employed, and jets on a single solar panel are connected to the same gas source. Thus, if one jet sticks open, leading to the eventual depletion of one gas source, the spacecraft will maintain proper attitude as long as the other gas supply is available.

Unfortunately, the system has the drawbacks cited above. Furthermore, if a stick-open failure of one of the valves occurs during the flight, the translational force to be imparted to the spacecraft blowdown can move the aiming point as much as 5000 km for a typical Mars mission. This figure would, at best, be troublesome, and if failure occurs after the last midcourse maneuver has been performed, the mission might be lost.

The proposed arrangement is shown in Fig. 20. Note that it is asymmetric, as all four jets that control the attitude about a given axis are at the end of the same solar

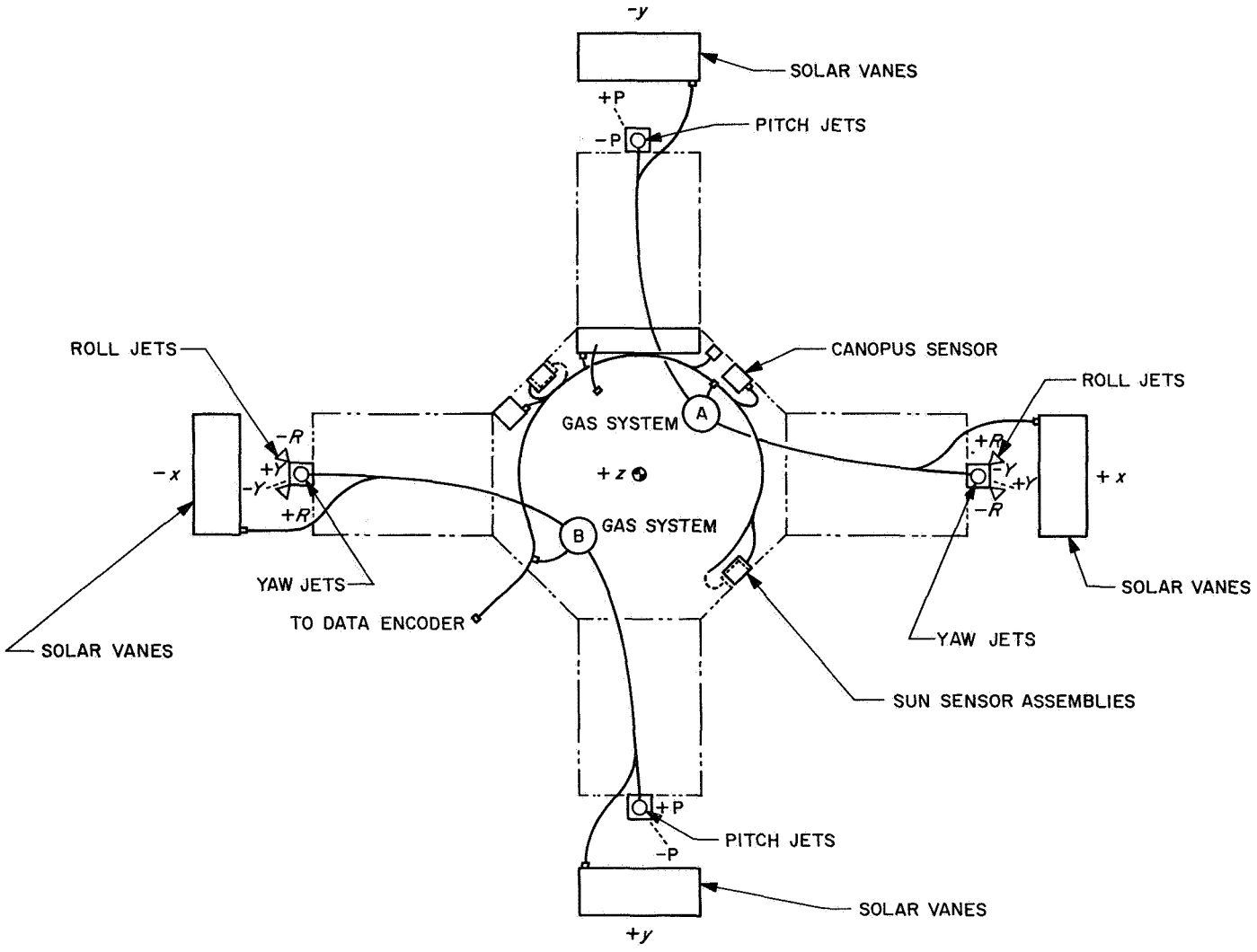

Fig. 19. Attitude control thruster and tankage arrangement

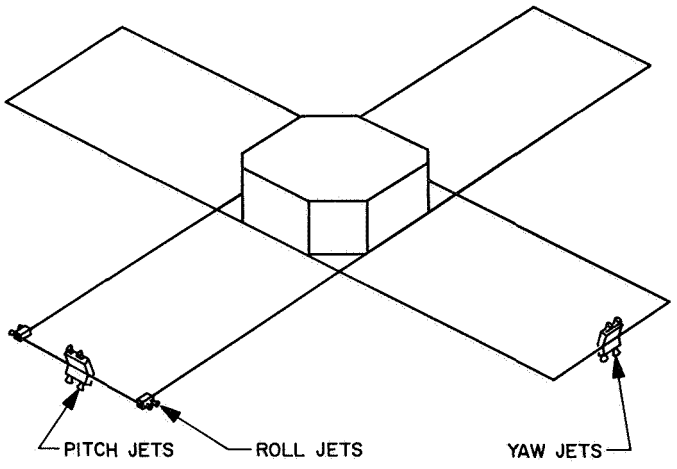

Fig. 20. Proposed attitude jet configuration

panel. As will be shown, this configuration cancels out biases due to gas leakage and impulse variations between jets. Furthermore, the dual gas feature can be retained by using four jets for control of one axis—one in each direction fed by a single gas source. These advantages are accrued at the expense of causing the spacecraft to counteract *externally* generated torques with a response that does produce translational motion. These effects are small, however, and simply add (or subtract) to the external forces that generate these torques. In addition, these forces are relatively constant in character and do less violence to the orbit estimation procedure than do random valve leakage and impulse variation.

To investigate the performance of the proposed system, it is convenient to consider separately the spacecraft-generated torques (due to jet firings and leakage) and external torques (due to solar pressure and other effects). Let the first be denoted by $\mathbf{M}_i(t)$. The change in spacecraft angular velocity over a time interval t_0, t_f due to $\mathbf{M}_i$ will be

$$I[\omega(t_f) - \omega(t_0)] = \int_{t_0}^{t_f} \mathbf{M}_i(t)\, dt \qquad (1)$$

where I is the moment of inertia dyadic. When only a single axis is considered, the torque integral can be expressed in terms of the average force exerted by the control jets over the interval

$$\int_{t_0}^{t_f} \mathbf{M}_i(t)\, dt = \mathbf{F}(t_0, t_f)(t_f - t_0)r \qquad (2)$$

where r is the center of mass–gas jet distance. Thus, the average force F exerted by a set of jets controlling one axis is

$$F(t_0, t_f) = \frac{I[\omega(t_f) - \omega(t_0)]}{(t_f - t_0)r} \qquad (3)$$

Since the attitude system keeps ω bounded, the average force will vanish over a long time. For instance, on *Mariner IV*, where the ω was less than 2×10^{-5} rad/s, the bias force averaged over 1 h for the proposed configuration would be held to less than 6×10^{-6} dynes. This force is inconsequential compared with that of 2×10^{-2} dynes caused by a leakage (Ref. 13) or 10^{-2} dynes resulting from a 10% bias in the impulse delivered by opposite thrusters. Note that this average force result is due to the fact that all the thrusters are on one solar panel; i.e., the *Mariner IV*-type symmetrical system does not have the monotonically decreasing average force characteristic exhibited by Eq. (3).

To ensure full cancelation, the thrusters on the proposed system must be aligned in such a way that they fire along the same inertial line on both sides of the limit cycle, as shown in Fig. 21. In addition, impingement of gas on the solar panels can no longer be precluded by canting the roll jets away from the axis of the panel as they appear in Fig. 19. Rather, an arrangement somewhat like that of Fig. 20 must be used.

The response of the proposed system to external torques, the most important of which is due to solar pressure, is to create an average translational force proportional to those torques. For instance, in *Mariner IV* the 6-dyne solar pressure force caused a net external torque of approximately 9 dyne-cm due to the 1.5-cm offset between the center of pressure and center of mass. The effect of this force on the proposed system would be a counteracting net average force of 0.057 dynes. This additional bias is roughly 1% of the solar pressure and may be either in the direction of, or opposite to, solar force. It should be noted that 0.057 dynes is approximately the same order of magnitude as that quoted for leaks and impulse variations. In essence then, the proposed system trades one type of force for another, but

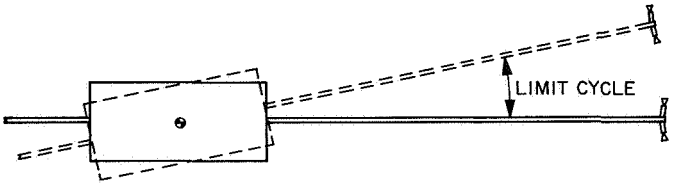

Fig. 21. Jet alignment

does not provide a substantial net reduction in the total nongravitational forces. However, this trade is of significant benefit to the navigation and guidance process for several reasons, as discussed in the following paragraphs.

After a short exposure time to the interplanetary environment (perhaps a few days), the relationship between center of mass and center of pressure should remain relatively constant. At least, it should be possible to calculate shifts in the center of mass due to midcourse propellant usage or any minor spacecraft configuration change. Thus, the ratio of this force to the total solar pressure force will remain constant, and the gas jet force effectively becomes part of the solar pressure. Its effects are then automatically included in the solar pressure solution during the orbit determination procedure. The *a priori* uncertainty in the solar pressure at the beginning of a flight is approximately 5%. When combined statistically, the additional 1% contributions about the pitch and yaw axis cause a negligible increase in this *a priori* uncertainty.

Because of the basic geometrical symmetry of the spacecraft, externally produced roll torques are negligible. In this case, the proposed configuration would eliminate all forces in the plane perpendicular to the spacecraft sun line. All nontrivial forces would therefore be along a known direction so that a directly observed scalar acceleration in the tracking data could be interpreted as a component of the sun line acceleration.

Sources of external torque other than solar pressure (such as micrometeoroid impacts), although small, should be considered. If such a torque-producing force is applied, the attitude control system will produce an additional force given by

$$F_{jets} = \frac{x}{r} F_{external}$$

where x is the distance from the center of mass to the point of application of the external force. Note that the attitude control system magnifies the external force by a factor $(1 + x/r)$, where $-r \leqq x \leqq r$. Therefore, the net force is between zero and twice the applied force. Since nonsolar external forces have not been a significant source of perturbation in the past, they are not expected to create problems with this system in the future.

To the proposed system, stick-open or stick-closed valve failures in flight would simply appear to be large imbalances in the thrust magnitudes. Hence, this configuration will automatically null the force produced by such a failure.

In summary, the attitude control system configuration presented here offers an attractive means for achieving better spacecraft performance both in terms of reducing the random components of the nongravitational forces and in terms of reliability of operation.

I. Results of the Doppler-Ranging Calibration Experiment, Phase II, A. Liu

1. Introduction

Phase I of the doppler–ranging calibration experiment used the Mark IA ranging system at DSS 12 (Goldstone Echo) and was restricted to two-way doppler and ranging measurements of *Lunar Orbiters II* and *III* (see SPS 37-46, Vol. III, pp. 23–28, for Phase I results). For Phase II, doppler and Mark IA ranging measurements of *Lunar Orbiters II* and *IV* were used. During the tracking period, *Lunar Orbiter IV* was at high inclination and at a nearly constant temperature, which offered an opportunity for the study of ranging residuals without concern for temperature variation effects. Measurements of *Lunar Orbiter II* served as a means for comparing the periodic effects observed in Phase I with those of Phase II.

As for Phase I, the tracking data were received from DSS 12. Three sets of measurements of the *Lunar Orbiters* were accomplished. The first set, called Track 1, was taken of *Lunar Orbiter IV* from 11:16 to 23:00 GMT on June 4, 1967; the second, Track 2, of *Lunar Orbiter IV* from 22:30 GMT on June 17 to 09:20 GMT, June 18, 1967; the third, Track 3, of *Lunar Orbiter II* from 06:45 to 14:50 GMT on June 25, 1967. All three sets were horizon-to-horizon measurements of doppler counts (CC 3) and range units (RU) at a data rate of 1 point/s. $\overline{RES}$, the net mean observed differences between CC 3 and RU, were calculated every minute by the DSS computer, where

$$\overline{RES} = \sum_{i=1}^{60} RES(t_i)/60$$

RES at time t is given as

$$RES(t) = R(t) - R_0 - \frac{1}{16}[D(t) - D_0 - B(t - t_0)]$$

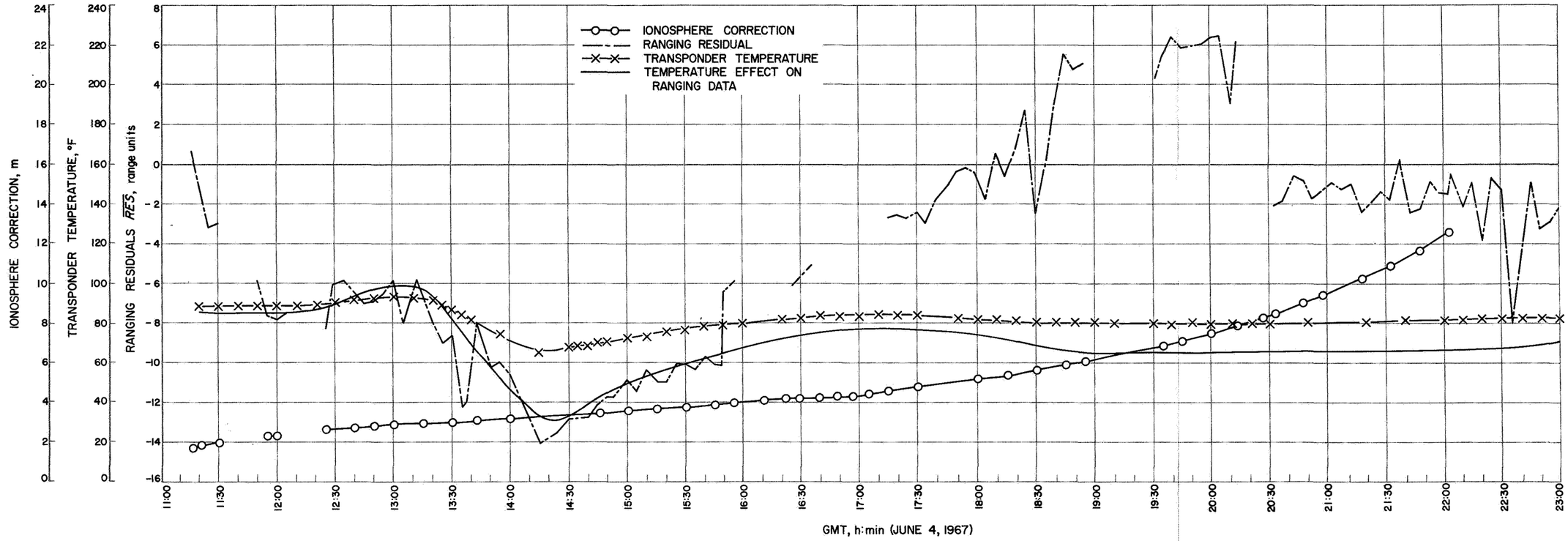

Fig. 22. Mark IA ranging residual, ionosphere correction, and transponder temperature versus time for *Lunar Orbiter IV* (Track 1)

where

$R(t)$ = ranging measurement at time t

$D(t)$ = doppler count at time t

t_0 = GMT at beginning of the pass

R_0 = ranging measurement at time t_0

D_0 = doppler count at time t_0

B = doppler bias frequency = (10^6 Hz)

$\overline{RES}$ is plotted against GMT and compared with telemetered spacecraft transponder temperature (*CT* 02) data and model ionospheric effects.

2. Data Analysis, Track 1

In terms of geometry, on June 4, 1967, the track was most favorable for observing the effects of the ionosphere upon the tracking data. The spacecraft was in continuous view for twelve hours from DSS 12. The pass began at about 3 a.m. and ended at 3 p.m. local time, which meant that DSS 12 was tracking *Lunar Orbiter IV* at low elevations through the thickest part of the ionosphere at the time of station set.

It is interesting to note in Fig. 22, that $\overline{RES}$ showed a dip extending from 13:20 to 15:50 GMT, and a corresponding drop in temperature of 25°F of the transponder over the same time interval. Investigation revealed that, during this time period, a battery discharge experiment was conducted and the spacecraft was pitched 95 deg off the sun line with the heaters turned off. The temperature remained constant after 16:00 GMT, but $\overline{RES}$ began to increase and reached a maximum at about 19:00 GMT. After 16:00 GMT, $\overline{RES}$ displayed effects that might have been due to the expected increase in ionospheric activity. Figure 23 shows electron content measurements of *Applications Technology Satellite-B* received from Stanford.[20] Electron content is in units of electrons/m^2 where 10^{17} electrons/m^2 corresponds to 0.825 m in range. On this basis, the ionospheric effects for June 4, 1967, caused an 8-m increase in the RU measurements, which is twice that shown in Fig. 23 since RU represents twice the distance from the station to the spacecraft. In Fig. 22 it is noted that the slope of $\overline{RES}$ has the correct sign, and that the change of $\overline{RES}$ from −6 to +6 RU—a total increase

[20]Data received from F. L. Smith III of Stanford Radio Science Lab., Stanford University, in a personal communication to the author, 1967.

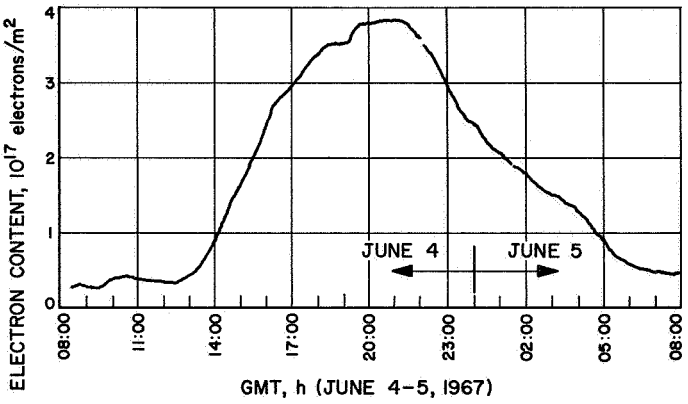

Fig. 23. Electron content measurement plot from Stanford based on *ATS-B* observations

of 12 RU—agrees somewhat with the increase in the assumed RU correction. The 30% discrepancy here between Stanford and Goldstone could be due to local irregularities in the ionosphere. The range correction predicted on the basis of an assumed Chapman model ionosphere, using a solar activity index $\overline{R}$ of 100 and an electron density of 2×10^5 electron/cm^3 (shown as a solid line with circles in Fig. 22) shows an increase from 3 to 13 m, a net change of 10 m from the beginning to the end of the track.

3. Data Analysis, Track 2

The track began at 15:30 local time when the orbiter was low on the horizon, at which time the ionospheric activity is quite heavy. The station tracking configuration and performance were continuously monitored, with no unusual events noted. The spacecraft attitude remained fixed for the entire track.

CT 02 was held to 81°F throughout the track, which began on June 17, 1967, 22:30 GMT and ended on June 18, 1967, 09:20 GMT. DSS 12 measured CC 3 and RU of *Lunar Orbiter IV* continuously. Figure 24 shows a plot of $\overline{RES}$ versus time. The behavior of $\overline{RES}$ does not seem to correspond to the behavior of the ionosphere. It is apparent that there are error sources present other than temperature and ionosphere.

4. Data Analysis, Track 3

Lunar Orbiter II was the object of this track, and the purpose was to see if the $\overline{RES}$ corresponded in some fashion with the $\overline{RES}$ observed during Phase I for the same spacecraft. For Phase I, $\overline{RES}$ (Fig. 25) showed periodic effects that were parabolic. In contrast, this track (Fig. 26) shows $\overline{RES}$ to be linear with respect to time.

The tracking was done at night so that the ionospheric activity was at a minimum. The *CT* 02 readings, however, are much different from those received during Phase I, Track 2, which could account for the differing shapes between this track and Phase I.

From preflight calibration data of the *Lunar Orbiter II* spacecraft transponder it was determined that 1°F change in temperature causes a −0.36 RU change. Since the temperature increases and then drops at the end of each lunar orbit, $\overline{RES}$ appears to have the correct sign. The temperature variation has been translated into the corresponding change in RU and plotted in Fig. 26. This curve does not match very well with the $\overline{RES}$ plot, but it is conceivable that the spacecraft transponder has changed characteristics from the time that the preflight calibrations of the transponder were made.

5. Conclusions

Track 3, Phase II, completes the data acquisition of the ranging–doppler calibration experiment. From this experiment, it is concluded that there is little transponder response time delay due to temperature variations. It is apparent from Track 1 of this phase that the transponder reacts to temperature changes rather quickly (on the order of minutes). The dynamical delay in the transponder was previously conjectured to be on the order of 30 min.

Also, other error sources which have not yet been determined do exist. The anomalous behavior of Track 2 has yet to be explained in terms of other than ionospheric and temperature effects. Until these other error sources are understood and accounted for, the ionospheric effects will be masked.

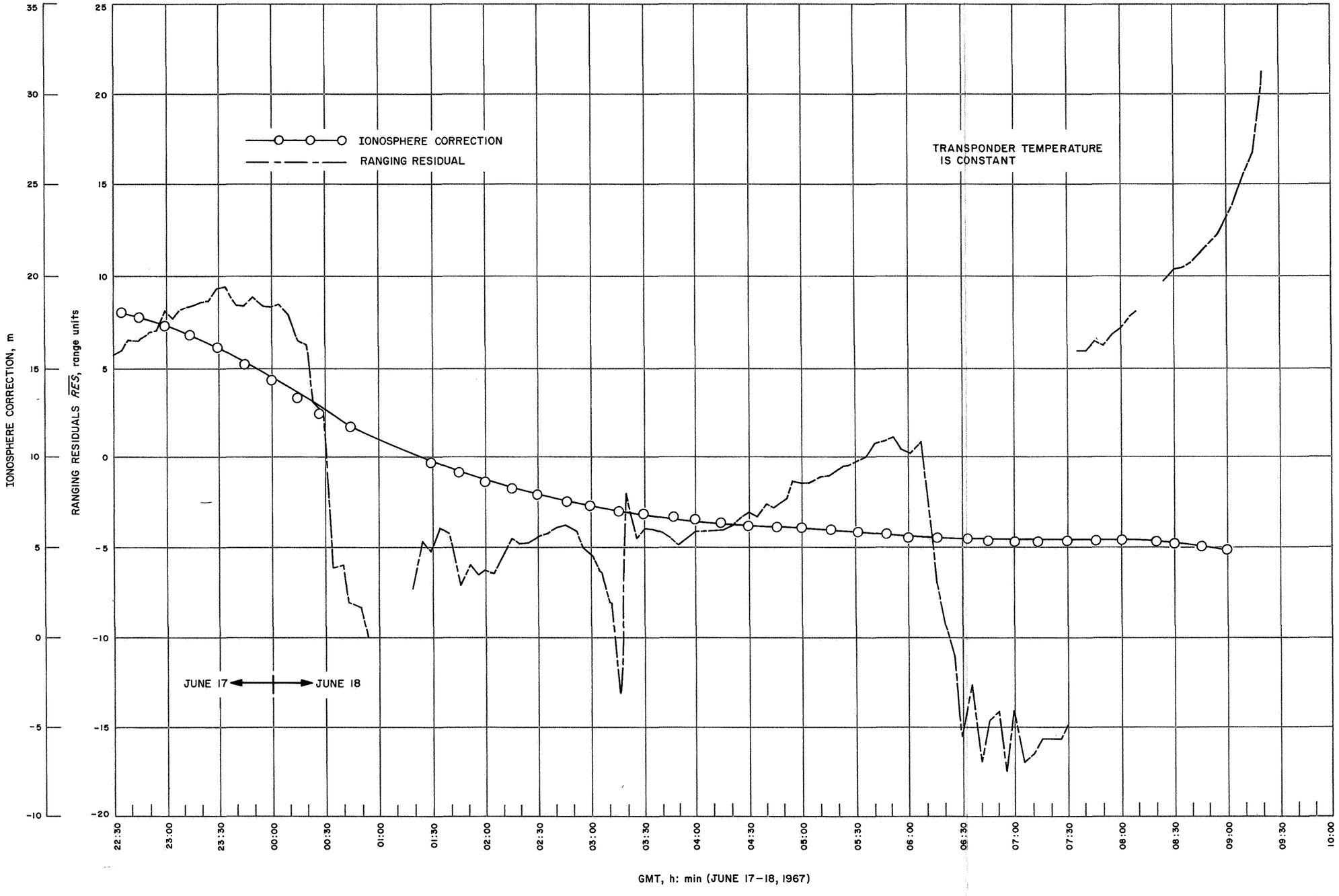

Fig. 24. Mark IA ranging residual and ionosphere correction versus time for *Lunar Orbiter IV* (Track 2)

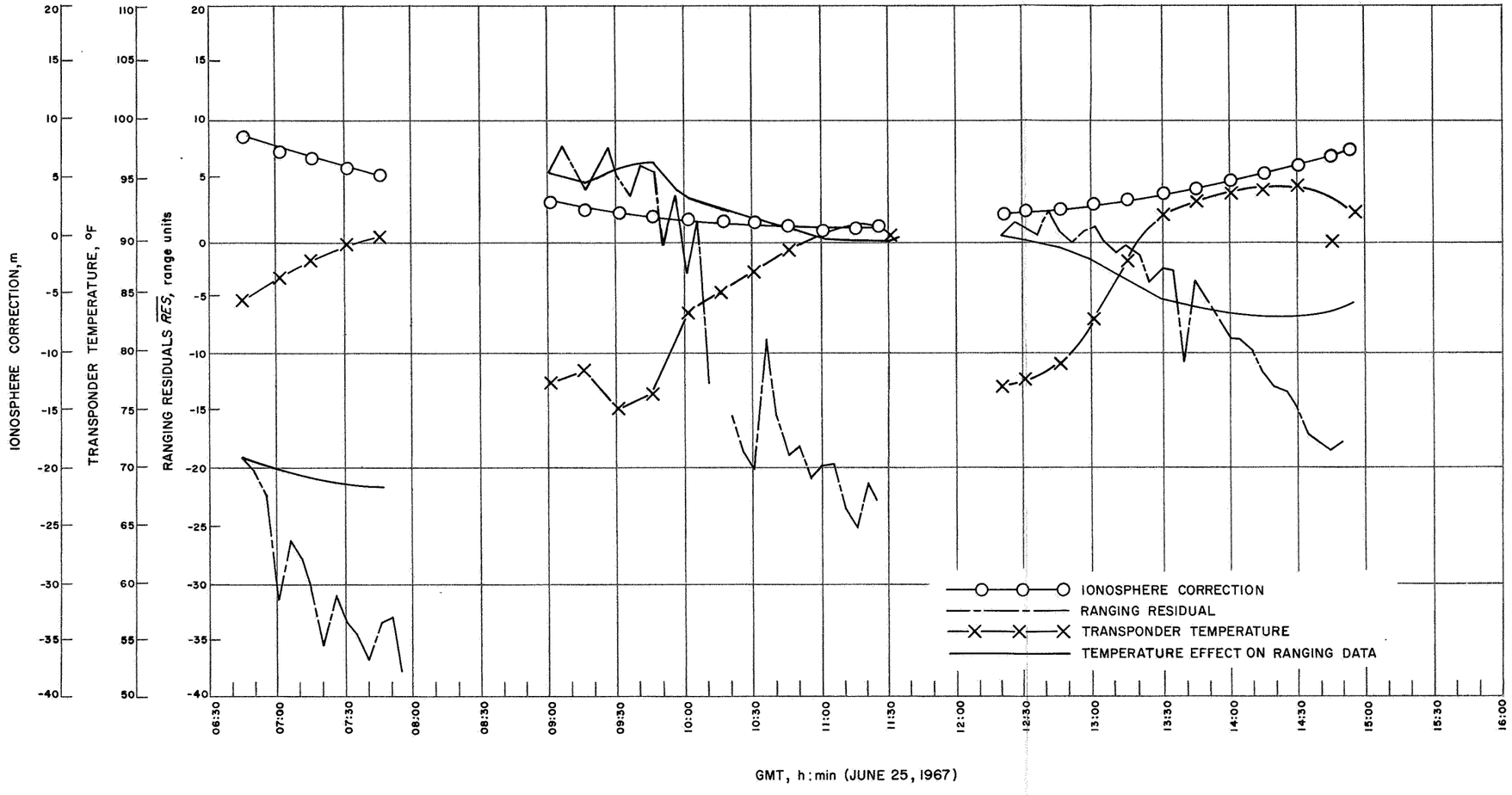

Fig. 25. Mark IA ranging residual, ionosphere correction, and transponder temperature versus time for *Lunar Orbiter II* (Track 3)

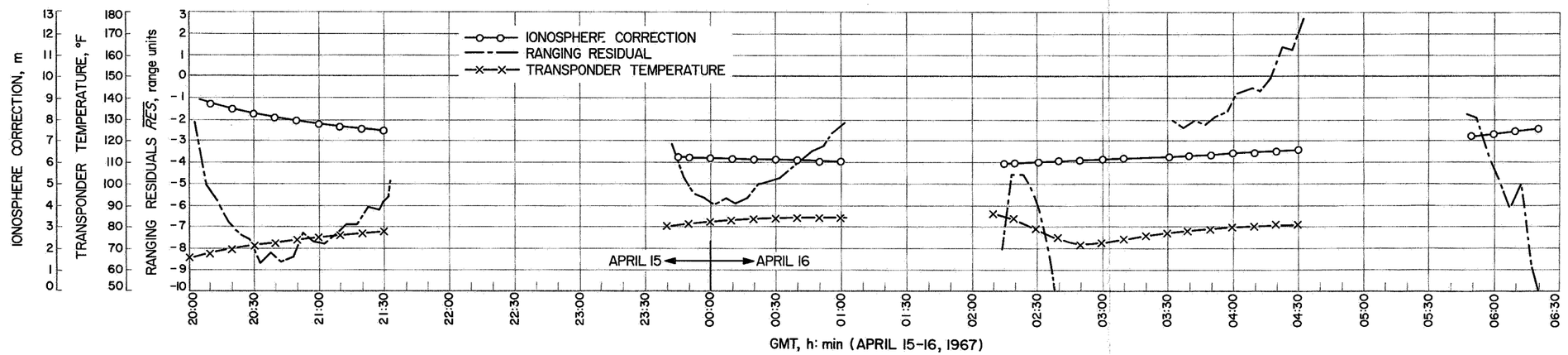

Fig. 26. Mark IA ranging residual, ionosphere correction, and transponder temperature versus time for *Lunar Orbiter II* (Track 2, Phase I)

References

1. Eckert, W. J., Jones, R., and Clark, H. K., *Improved Lunar Ephemeris 1952–1959.* U.S. Government Printing Office, Washington, D.C., 1954.

2. Mulholland, J. D., and Block, N., *JPL Lunar Ephemeris Number 4,* Technical Memorandum 33-346. Jet Propulsion Laboratory, Pasadena, Calif., Apr. 15, 1967.

3. Mulholland, J. D., and Sjogren, W. L., "Lunar Orbiter Ranging Data: Initial Results," *Science,* Vol. 155, pp. 74–76, Jan. 6, 1967.

4. Eckhardt, D. H., "Computer Solutions of the Forced Physical Libration of the Moon," *Astron. J.,* Vol. 70, pp. 466–471, 1965.

5. Peabody, P. R., et al., *JPL Ephemeris Tapes E9510, E9511, and E9512,* Technical Memorandum 33-167. Jet Propulsion Laboratory, Pasadena, Calif., Mar. 2, 1964.

6. Peabody, P. R., Scott, J. F., and Orozco, E. G., *Users' Description of JPL Ephemeris Tapes,* Technical Report 32-580. Jet Propulsion Laboratory, Pasadena, Calif., Mar. 2, 1964.

7. Mulholland, J. D., and Sjogren, W. L., *Lunar Orbiter Ranging Data: Initial Results,* Technical Report 32-1087. Jet Propulsion Laboratory, Pasadena, Calif. (Also appears in *Science,* Vol. 155, No. 3758, pp. 74–76, Jan. 6, 1967.)

8. Warner, M. R., and Nead, M. W., *SPODP—Single Precision Orbit Determination Program,* Technical Memorandum 33-204. Jet Propulsion Laboratory, Pasadena, Calif., Feb. 15, 1965.

9. Yumi, S., *Annual Report of the International Polar Motion Service for 1962.* International Polar Motion Service Observatory, Mizusawa, Japan, 1964.

10. Sjogren, W. L., Curkendall, D. W., Hamilton, T. W., Kirhofer, W. E., Liu, A. S., Trask, D. W., Winneberger, R. A., and Wollenhaupt, W. R., *The Ranger VI Flight Path and Its Determination From Tracking Data,* Technical Report 32-605. Jet Propulsion Laboratory, Pasadena, Calif., Dec. 15, 1964.

11. Wollenhaupt, W. R., Trask, D. W., Sjogren, W. L., Piaggi, E. G., Curkendall, D. W., Winneberger, R. A., Liu, A. S., and Berman, A. L., *The Ranger VII Flight Path and Its Determination From Tracking Data,* Technical Report 32-694. Jet Propulsion Laboratory, Pasadena, Calif., Dec. 15, 1964.

12. Anderson, J. D., *Determination of Masses of the Moon and Venus and the Astronomical Unit From Radio Tracking Data of the Mariner II Spacecraft,* Technical Report 32-816. Jet Propulsion Laboratory, Pasadena, Calif., July 1, 1967.

13. Null, G., Gordon, H., and Tito, D., *The Mariner IV Flight Path and Its Determination From Tracking Data,* Technical Report 32-1108. Jet Propulsion Laboratory, Pasadena, Calif., Aug. 1, 1967.

14. Peabody, P. R., Scott, J. F., Orozco, E. G., *JPL Ephemeris Tapes, E9510, E9511, E9512,* Technical Memorandum 33-167. Jet Propulsion Laboratory, Pasadena, Calif., Mar. 2, 1964.

References (contd)

15. Mulholland, J. D., and Block, N., *JPL Lunar Ephemeris 4*, Technical Memorandum 33-346. Jet Propulsion Laboratory, Pasadena, Calif., Aug. 1, 1967.

16. *Goddard Directory of Tracking Station Locations*, X-554-67-54. Prepared by Geonautics, Inc., Washington, D.C., for Goddard Space Flight Center, Aug. 1966 (DSS 11 is based on Geodetic Data Sheet (GDS) D-1; DSS 12 on GDS D-2; and DSS 41 on GDS D-5.).

17. Pfeiffer, C. G., *Continuous Estimation of Sequentially Correlated Random Variables*, Technical Report 32-524. Jet Propulsion Laboratory, Pasadena, Calif., Oct. 30, 1963.

18. Kalman, R. E., *New Methods and Results in Linear Prediction and Filtering Theory*, RIAS TR 61-1. Martin Marietta Corp., Research Institute for Advanced Studies, Baltimore, Md., 1961.

19. *Mariner Mars 1964 Project Report: Mission and Spacecraft Development; Vol. I, From Project Inception Through Midcourse Maneuver*, Technical Report 32-740. Jet Propulsion Laboratory, Pasadena, Calif., Mar. 1, 1965.

III. Communications Engineering and Development

A. Digital Tracking Subsystem, *P. L. Lindley and P. Askren*

A new digital tracking subsystem is planned for those DSIF stations which are, or will be, equipped with 210-ft antennas. This subsystem ultimately is to include five functions, consolidated to use a single third-generation digital computer in their implementation. The functions involved are:

(1) Tracking data handling (TDH), Phase II.

(2) Ranging (RNG), Phase II.

(3) Programmed local oscillator (PLO).

(4) Programmed exciter (PE).

(5) Antenna pointing subsystem (APS), Phase IA.

The initial version of the digital tracking subsystem will be a TDH Phase II and RNG Phase II configuration. Its first use is planned for the *Mariner* Mars 1969 mission at DSS 14. Compared with the presently operational Phase I versions of TDH and RNG, the Phase II concept will enhance the reliability and versatility of TDH, and enable RNG to be operable to planetary distances at the signal levels that will be available.

Since the previous report on this activity, an automatic data processing equipment (ADPE) acquisition plan has been evolved, which is to form the justification and basis for procurement of the required third-generation computer. The functional requirements and proposed features of the subsystem are being developed in the form of block diagrams and specifications.

Analysis of data rate requirements, appropriately extrapolated for several years to come, has indicated that the previously planned 1000/s maximum sample rate for TDH Phase II is not required; the figure has, therefore, been revised to 100/s maximum, which should comfortably exceed expected needs. The proposed high-speed data line (HSDL) between the TDH at a station and the space flight operations facility (SFOF) at JPL is now conceived as a two-way data link of 2400 bits/s transmission capability.

Since the previous report, the developmental ranging equipment presently installed at DSS 14 has been tested and has performed successfully as part of the *Mariner* Venus 67 mission. Results of experience with this equipment, and recent changes made to it on the basis of this experience, are being incorporated into the RNG Phase II concept.

A design team, composed of members of the systems and telecommunications divisions, has been formed to evaluate and recommend in the areas of system functions and system interfaces. As a link with the needs of the computer equipment in the SFOF and the needs of the ultimate data users, this team promises to be of great value in arriving at the optimum and most practical concepts of the digital tracking subsystem.

B. Interim Monitor Program, Version "G,"

R. M. Thomas

The interim monitor program (IMP), version "G", provides (1) automatic gain control (AGC) mean and standard deviation computations, (2) doppler (one-, two-, and three-way) mean and standard deviation computations, and (3) station configuration verification via monitoring switch positions in the DSIF.

AGC mean and standard deviation are computed by the computer program by utilizing "sliding mean" and "sliding standard deviation" approaches. The mathematics of both approaches will be presented in a later section. AGC (dc voltages) values are converted to dBmW and the sliding mean and sliding standard deviation are computed once each second (assuming receiver is in lock). However, the mean and standard deviation are printed out at either 10-s (breakpoint 6-set) or 60-s intervals (breakpoint 6-reset).

The doppler mean and standard deviation computer calculations are quite similar to the AGC calculations, with only two basic differences. The mean is computed using the difference between the actual and predicted doppler, and the sampling rate for doppler is variable. Otherwise, the computations and printout intervals (10 or 60 s) are identical. The mathematics associated therewith will be presented in a later section.

This program is classified as operational and will be used throughout the Deep Space Network (DSN) with an SDS 920 computer (8192-word memory) of the digital instrumentation subsystem (DIS). The programming language used is SYMBOL. Six of the eight breakpoint switches are used for various control functions. These functions are presented in Table 1.

Table 1. Breakpoint switch functions

Switch No.	Reset	Set
1	Do not access input–output typewriter	Access input–output typewriter
2	Not used	— — —
3	Inhibit AGC and doppler printout	Enable AGC and doppler printout
4	Do not process doppler data	Process doppler data
5	Full printout	Inhibit DCC and last doppler sample printout
6	1-min printout of AGC and doppler	10-s printout of AGC and doppler
7	Input–output on beta (920) typewriter	Input–output on alpha (910) typewriter. Note: typewriter switch on DIS control panel 1 must be in up (beta) position.
8	Not used	— — —

1. Use of Doppler in the Interim Monitor Program (IMP)

One-, two-, and three-way doppler are used by the IMP. Several questions must be resolved with respect to doppler data samples. Specifically:

(1) Is the data usable or nonusable?

(2) How does the computer determine the doppler that is being received? Is the doppler one-, two-, or three-way?

The answers to these questions are derived using the data condition code word (DCC). The DCC word consists of four digits; Table 2 and the following are used to explain the DCC word:

Digit 1 indicates the doppler averaging time of the sample taken. Digit values 0–8 indicate selected averaging times.

Digit 2 indicates receiver and servo data conditions. Digit values 0–7 indicate specific conditions. Some of the values represent automatically sensed data and other values represent data generated by manual switch positioning (refer to Table 3).

Digit 3 specifies ground tracking or doppler mode of the Deep Space Station (DSS). Digit values 0–3 represent doppler modes as provided from Counter 1 of doppler frequency counter. Digit values from 4–7 represent doppler modes as provided from Counter 2 of doppler frequency counter.

Note: The DSS doppler frequency counter consists of two counters: Counter 1 and Counter 2 which can be employed singularly or alternatively, to provide either a cumulative or destructive count.

Digit 4 specifies condition of frequency control for exciter VCO. Digit values 0, 1, and 2 represent each condition.

Table 2. Data condition code identification

Digit 1 Doppler averaging time		Digit 2 Receiver and servo data condition	
Digit	Time, s	Digit	Data condition
0	1	0	Good doppler and angle data
1	5	1	Bad angle data (automatically sensed)
2	10	2	Bad doppler data (automatically sensed)
3	20	3	Bad doppler and angle data (automatically sensed)
4	30		
5	40	4	Bad doppler data (manual switch)
6	50	5	Bad angle data (automatically sensed) and bad doppler data (manual switch)
7	60		
8	Nondestruct	6	Bad doppler data (both manual switch and automatically sensed)
		7	Bad angle and doppler data (automatically sensed) and bad doppler data (manual switch)

Digit 3 Doppler mode				Digit 4 Frequency control of exciter VCO	
Digit		Ground doppler mode	Spacecraft	Digit	Condition
Counter 1	Counter 2				
		1 way	N/C[a]		
1	5	2 way	N/C[a]	0	Rubidium standard and synthesizer VCO loop in-lock
		3 way	N/C[a]		
0	4	2 way	C[b]		
2	6	3 way	C[b]	1	One of above out-of-lock
3	7	3 way	C[b]	2	N/C[a] (used in a non-standard situation to indicate above system is not being used)

[a]N/C: Noncoherent

[b]C: Coherent, via microwave

Table 3. Regulations for use of manual *good–bad* data condition switches

Angle switch	Doppler switch
Servo *good–bad* switch must remain at *good*. When auto tracking on station control and monitor console subsystem (SCM) and angle data are good.	Receiver *good–bad* data switch must be at *good*, except when doppler data are known to be bad.
When doubt exists regarding quality of angle data, servo switch must be positioned at *bad*.	When doubt exists regarding quality of doppler data, receiver switch must be positioned at *bad*.

2. Sliding Mean Computer Computation for Automatic Gain Control

Let A_i = ith sample (first sample of a 10- or 60-s printout interval) of automatic gain control (AGC) voltage which has been converted to dBmW for any 10- or 60-s printout interval. The AGC sample rate is 60-samples/min. The number of samples used for a mean or standard deviation printout computation can be varied between 1 and 300.

For this development, 60 samples and a corresponding 10-s printout interval are chosen. A mean is computed each second. However, the mean values will only be printed out at the selected 10-s print interval. The first mean to be printed using the selected 10-s print interval will be:

$$\left[\sum_{i=1}^{10}(A_i)\right]/10$$

The second mean printout will be:

$$\left[\sum_{i=1}^{20}(A_i)\right]/20$$

and the first printed mean that contains the preselected 60 samples will be:

$$\left[\sum_{i=1}^{60}(A_i)\right]/60$$

As was noted above, only 10 samples had been acquired after 10 s, 20 samples after 20 s, etc. As a second example: The seventh printed mean, and this is the second printed mean which contains the desired 60 samples, is:

$$\left[\sum_{i=11}^{70}(A_i)\right]/60$$

This mean calculation is the first mean that emphasizes the sliding mean concept (containing the selected 60 samples).

SAMPLES USED

(e.g., first mean containing 60 samples) → 1 ——— 60

(e.g., second mean containing 60 samples) → 11 ——— 70

3. Sliding AGC Computer Computation for Standard Deviation (SD)

Simultaneously, the samples obtained for computing the sliding mean are used to compute the SD about the mean. One additional comment required is that for $n = 1$ (1 data point sample/computation) the computer will print 0 for the SD. For sample 1, the SD is 0 as defined above. For this example, the SD printout interval is equal to 10 s.

$$\text{First printed SD} = \left[\frac{\sum_{i=1}^{10}(A_i)^2 - \frac{\left[\sum_{i=1}^{10} A_i\right]^2}{10}}{9}\right]^{1/2}$$

$$\text{Second printed SD (20)} = \left[\frac{\sum_{i=1}^{20}(A_i)^2 - \frac{\left[\sum_{i=1}^{20} A_i\right]^2}{20}}{19}\right]^{1/2}$$

For $n \geqq 60$, the SD for the sliding mean reduces to:

$$\text{The first printed SD containing the required 60 samples} = \left[\frac{\sum_{i=1}^{60}(A_i)^2 - \frac{\left[\sum_{i=1}^{60}(A_i)\right]^2}{60}}{59}\right]^{1/2}$$

$$\text{The second printed SD containing the required 60 samples} = \left[\frac{\sum_{i=11}^{70}(A_i)^2 - \frac{\left[\sum_{i=11}^{70}(A_i)\right]^2}{60}}{59}\right]^{1/2}$$

This is the first printed SD computation that emphasizes the sliding SD concept. For a graphical analogy, refer to the previous section containing the sliding mean presentation.

For $n \geqq 60$ the sliding SD for AGC becomes:

$$\text{SD}\,(n \geqq 60) = \left[\frac{\sum_{i=n-59}^{n}(A_i)^2 - \frac{\left[\sum_{i=n-59}^{n}(A_i)\right]^2}{60}}{59}\right]^{1/2}$$

4. Sliding Mean Doppler (One-, Two-, and Three-Way) Computer Computation

The sample interval is variable (3 through 21 inclusive). For this development, a 7-data point sample interval is chosen:

Assume that:

D_{pi} = predicted ith doppler value

D_{oi} = observed ith doppler value

The first seven samples are chosen for this development and the printout interval is chosen to be 10 s. The tracking data handling subsystem (TDH) sampling rate can vary from 1 to 60 data samples/min. For this example, 60 data samples/min are assumed.

A mean will be *computed* each second. After 10 s (from the start of sampling) the first mean will be printed. This mean will utilize the first 7-data samples (assuming no blunder points in the data). The eighth data sample is used with the previous 6-data samples and a mean is computed.

The development is as follows:

$$\text{First printed mean} = \left[\sum_{i=4}^{10}(D_{oi} - D_{pi})\right]/7$$

10 s after sampling commences—(contains required number of samples)

$$\text{Second printed mean} = \left[\sum_{i=14}^{20}(D_{oi} - D_{pi})\right]/7$$

(20 s after start of sampling)

The second mean computation above also emphasizes the sliding mean concept,

e.g., first mean used samples

second mean used samples

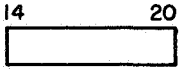

The mean computations and printouts will continue for the duration of the chosen operation and in some instances continue through a post-pass operation.

5. Sliding Doppler (One-, Two-, and Three-Way) Standard Deviation Computer Computation

The same basic assumptions used for the mean are applicable for SD calculations. The 10-s printout interval is chosen and the sample rate is 1 data point/s.

The SD is likewise computed each second and printed every 10 s. The sampling interval chosen is 7 (same as the mean). It follows that:

$D_{01} - D_{p1}$ = first doppler sample. The computer will not print the SD for this $n = 1$ case because the elapsed time is insufficient.

For a sample interval of 7 we have the first printed SD 10 s after sampling commences, and it does contain the required number of samples.

$$\mathrm{SD}(7) = \left[\frac{\sum_{i=14}^{10} (D_{0i} - D_{pi})^2 - \frac{\left[\sum_{i=14}^{10} (D_{0i} - D_{pi}) \right]^2}{7}}{6} \right]^{1/2}$$

The second SD computation also emphasizes the sliding SD concept. The graphical interpretation of the samples used for computation is the same as is shown for the doppler sliding mean.

6. Station Configuration

The capability exists for monitoring 96 switch positions in the DSIF. This is accomplished in the following way:

At the time that the IMP program is loaded, the corresponding mode "tables" and "masks" are loaded from a separate paper tape. Each mode table is a 96-bit word (4 computer words) and has a corresponding "mask," which is also a 96-bit word. Each bit position corresponds to one of the 96 switch positions in the DSIF (these switches are external to the computer).

Each second, the computer reads the 96 DSIF switches as a 96-bit word. A zero (0) in a bit position indicates switch closure and a one (1) indicates switch open.

If a bit in the mask word is a 1, then the corresponding DSIF switch is to be monitored and if the bit is a 0, then the DSIF switch will not be monitored. If a switch is to be monitored, then the contents (0 or 1) of its bit position in the DSIF switch word is compared with its counterpart in the mode table word. All such bits (1 through 96) that do not agree when compared are printed out initially. Subsequently, each time thereafter that there is a change of switch positions, then the corresponding change is printed out by the typewriter. There will be a different switch position configuration (DSIF configuration) for every DSIF operation. The DSIF configuration is clearly defined for each operational mode (e.g., mode 01 is *Surveyor* acquisition and mode 02 is *Surveyor* cruise).

C. Development of a 60-kW Broadwall Multihole Waveguide Directional Coupler, *B. W. Harness*

1. Introduction

The DSN S-band transmitters presently use resistive loop waveguide directional couplers for forward and reflected power monitoring. Although this coupler has the advantage of compactness, it is inferior to the multihole type in bandwidth and directivity, and is susceptible to loss of calibration due to accidental movement of the loops. A multihole directional coupler was developed for use in the 10- and 20-kW DSN transmitter subsystems.

2. Directional Coupler

The coupler is a waveguide multihole dual coupler with two separate arms; one arm for forward power monitoring and one arm for reverse power monitoring. The coupling arrays were designed to have a Chebyshev response because of its superior directivity properties.

The waveguide directional coupler (WGDC) shown in Fig. 1 was fabricated from WR 430 aluminum waveguide material using inert gas heliarc welding techniques. The coupling hole patterns were machined in the primary waveguide, and the secondary waveguides and flanges were welded to the primary waveguide. The secondary arms include waveguide-to-coaxial transitions equipped with type N female connectors. There are no adjustments necessary to achieve the specified directivity. Table 4 presents the critical specifications for the unit.

3. WGDC Test Results

The prototype WGDC has been tested at Goldstone DSCC Microwave Standards Laboratory in accordance with the following measurement techniques:

a. VSWR. The VSWR of the main arm input was measured by the sliding load method described in Ref. 1. The slotted section, sliding load, and sliding short were all

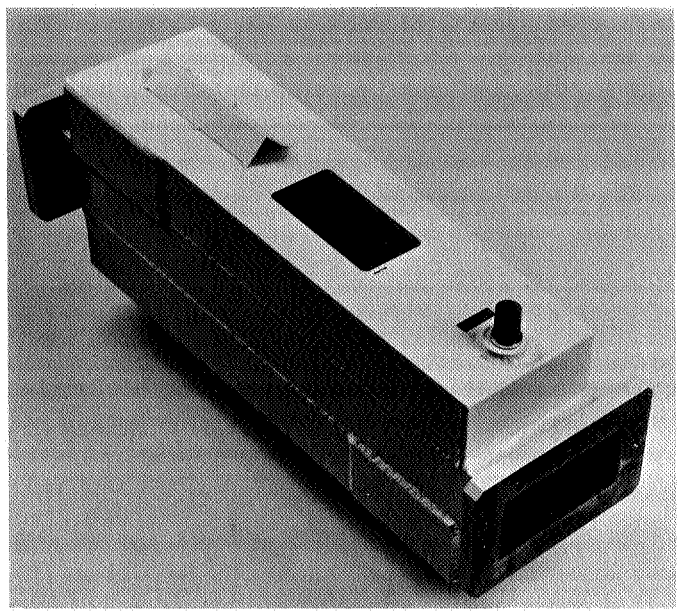

Fig. 1. Waveguide directional coupler

WR 430 waveguide components. The VSWR was measured at five equally spaced frequencies covering the 40-MHz band centered at f_0 (2110 MHz).

b. Directivity. The sliding load method of directivity measurement (described in referenced text) was used. The directivity of the reflected port and the forward port was measured at five equally spaced points covering the 40-MHz band centered at f_0. In addition, the two frequencies (one above and one below f_0) at which the directivity of the reflected port falls below 40 dB were determined.

c. Coupling coefficient. The coupling coefficient of both forward and reflected arms was measured at f_0 and four other points within the 40-MHz band centered at f_0. The measurement error is specified to be less than ± 0.20 dB. The coupling coefficient throughout the 40-MHz band was measured by swept techniques using the precision measurement at f_0 as the data.

Table 4. Design specifications for waveguide directional couplers

Coupling coefficient, dB	Maximum coupling coefficient variation, dB	Power rating, kW	Band center frequency, GHz	Directivity, dB	Maximum VSWR
Forward 50 ±1.0	0.20	60	2.110	30	1.03:1.0
Reverse 40 ±1.0	0.20			40	

The test results of the prototype WGDC are shown in Table 5 and surpass the design specifications outlined in Table 4.

4. Conclusion

Since the primary concern for development of a new WGDC was to improve bandwidth and directivity, the requirement has been fulfilled. Other advantages of the multiholed WGDC over the resistive loop coupler include: better accuracy of reflected power measurements, no tedious adjustments for calibration, and calibration is not impaired by rough handling.

5. Future Plans

The DSN 20-kW transmitter subsystem forward and reflected power is presently being monitored using crystal detectors in conjunction with resistive loop couplers. The 20-kW subsystems will be upgraded by incorporating the new WGDC in the near future. A complete description of the 20-kW transmitter modification will be detailed in a future article.

Table 5. Test results for prototype waveguide directional couplers

Frequency, GHz	Coupling coefficient, dB		Directivity, dB		VSWR	Maximum coupling variation, dB
	Forward	Reverse	Forward	Reverse		
2.090	50.13	40.29	37.89	41.00	<1.03:1.00	
2.100	50.22	40.37	41.77	42.00	<1.03:1.00	
2.110	50.20	40.38	45.92	41.90	<1.03:1.00	0.10
2.120	50.22	40.39	43.82	40.10	<1.03:1.00	
2.130	50.22	49.37	39.70	41.60	<1.03:1.00	

D. Digital Communication and Tracking: Determination of the Bias in the Identification Algorithm, *J. K. Holmes*

1. Introduction

Some new results are presented for an algorithm previously reported in SPS 37-43, Vol. IV, pp 307–309, concerning a new method of system identification for time discrete, time invariant, finite memory systems. These results determine the bias (error) in the linear estimate for the noisy input–output measurement case. The class of linear systems that are time invariant, time discrete, and finite memory is denoted by $\mathcal{S}$, and algorithmic solutions to systems in $\mathcal{S}$ are considered.

Consider the block diagram illustrated in Fig. 2. The basic problem is to determine an optimum estimate of the unknown system (discrete impulse response) given the noisy measurement sequences u'_n and v'_n, where $u'_n = u_n + {}^1N_n$ and $v'_n = v_n + {}^2N_n$.

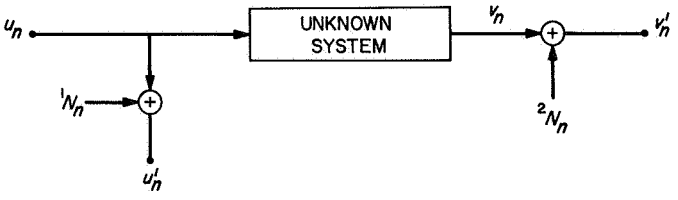

Fig. 2. Unknown system and associated sequences

2. Error of the Estimate

Figure 3 illustrates the additional apparatus needed to obtain the estimate of the unknown system with the algorithm.

Let the input measurement noise ^1N_n and the output measurement noise ^2N_n be statistically independent from sample to sample, and let their respective variances be σ_1^2 and σ_2^2. Let the input sequence u_n have covariance

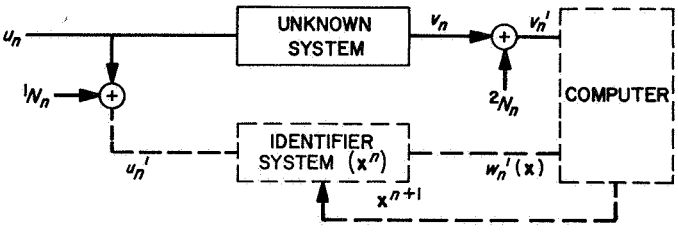

Fig. 3. Apparatus used to identify the unknown system

matrix R, and let the unknown system have the following system representation:

$$v_n = \sum_{j=0}^{m-1} \phi_j u_{n-j} \tag{1}$$

The linear estimator of the identifier system, based on noisy input samples u'_n, has the following form:

$$w'_n(\mathbf{x}^n) = \sum_{j=0}^{\ell-1} x_j^n u'_{n-j} \tag{2}$$

where we have assumed that the memory "$m-1$" is finite and "ℓ" satisfies $\ell \geqq m$. For convenience append $\ell - m$ terms to Eq. (1), satisfying $\phi_j = 0, j = m, \cdots, \ell - 1$, then Eq. (1) can be written in the form

$$v_n = \sum_{j=0}^{\ell-1} \phi_j u_{n-j}, \qquad \phi_j = 0, \qquad j = m, \cdots, \ell - 1 \tag{3}$$

The algorithm derived in the previously mentioned SPS article is of the following form:

$$\mathbf{x}^{n+1} = \mathbf{x}^n - 4a_n \mathbf{u}'_n (\mathbf{u}'_n)^\tau \mathbf{x}^n + 4a_n v'_n \mathbf{u}'_n, \qquad u'_n = \begin{Bmatrix} u'_n \\ u'_{n-1} \\ \vdots \\ u'_{n-\ell} \end{Bmatrix} \tag{4}$$

where $(\mathbf{u}'_n)^\tau$ is the transpose of the vector $\mathbf{u}'_n$. Using the explicit form of $\mathbf{u}'_n$ and v'_n, Eq. (4) becomes

$$\mathbf{x}^{n+1} = \mathbf{x}^n - 4a_n \mathbf{u}'_n (\mathbf{u}'_n)^\tau \mathbf{x}^n + 4a_n [(\boldsymbol{\phi})^\tau \mathbf{u}_n + {}^2N_n] \mathbf{u}'_n \tag{5}$$

Now using the fact that $E[(\cdot)] = EE[(\cdot)|\mathbf{x}^n]$, we have

$$\overline{\mathbf{x}^{n+1}} = \overline{\mathbf{x}^n} - 4a_n (R + \sigma_1^2 I) \overline{\mathbf{x}^n} + 4a_n R\boldsymbol{\phi} \tag{6}$$

It is easy to show that $\overline{\mathbf{x}^{n+1}} = [R + \sigma_1^2 I]^{-1} R\boldsymbol{\phi}$ is a solution to Eq. (6) for all n. The general solution to Eq. (6) has the property that as $n \to \infty$ the solution approaches $[R + \sigma_1^2 I]^{-1} R\boldsymbol{\phi}$. The reason that this satisfies the vector difference equation, while not being a function of n, can easily be seen from the following argument. First write Eq. (6) in the form

$$\mathbf{x}^{n+1} - \mathbf{x}^n = -4a_n (R + \sigma_1^2 I) \mathbf{x}^n + 4a_n R\boldsymbol{\phi} \tag{7}$$

Then, letting the time difference approach zero, we can approximate Eq. (7) as

$$\frac{d\mathbf{x}(t)}{dt} = -4a(t)\,[R + \sigma_1^2 I]\,\mathbf{x}(t) + 4a(t)\,R\boldsymbol{\phi} \tag{8}$$

The steady-state solution satisfies

$$\frac{d\mathbf{x}(t)}{dt} = 0$$

for all t. That is to say, the solution obtained from Eq. (8), call it $\mathbf{x}(t)$, converges to a vector $\mathbf{x}_0$ independent of t. It is easy to show that the steady-state solution to Eq. (8) is $\mathbf{x}_0 = [R + \sigma_1^2 I]^{-1} R\boldsymbol{\phi}$. Further, it is not hard to show (Ref. 2) that $b_n = E[\|\mathbf{x}^n - \mathbf{x}_0\|^2]$ approaches zero as $n \to \infty$. Consequently, $\mathbf{x}^n$ converges to $[R + \sigma_1^2 I]^{-1} R\boldsymbol{\phi}$ in mean square. This leads us to our first result.

Theorem I: For the linear estimate of a system $s \in \mathcal{S}$, identified by the identification algorithm (Eq. 4), the estimate of a non-zero system is consistent iff the input variance is zero.

Proof: Clearly, if the input noise variance is zero, $\ell.\mathrm{i.m.}\,\mathbf{x}^n = \boldsymbol{\phi}$; therefore, the estimate is consistent. If the estimate is consistent, then we must have $[R+\sigma_1^2 I]^{-1} R\boldsymbol{\phi} = \boldsymbol{\phi}$ or $R\boldsymbol{\phi} = R\boldsymbol{\phi} + \sigma_1^2\boldsymbol{\phi}$. Therefore, if $\boldsymbol{\phi} \neq 0$, then σ_1^2 must be zero.

Now let us consider a modified algorithm that converges to the true vector $\mathbf{x}_0$ if the input noise variance is known exactly. This algorithm has the following form:

$$\mathbf{x}^{n+1} = \mathbf{x}^n - 4a_n\,[\mathbf{u}_n'(\mathbf{u}_n')^T - \sigma_1^2 I]\,\mathbf{x}^n + 4a_n\,\mathbf{u}_n'\,v_n' \tag{9}$$

where I is the identity matrix. Again it is assumed that the output of the unknown system can be written as

$$v_n = \sum_{j=0}^{\ell-1} \phi_j\, u_{n-j}$$

and the identifier system output is given by

$$w_n'(\mathbf{x}^n) = \sum_{j=0}^{\ell-1} x_j^n\, u_{n-j}'$$

Using $E[(\cdot)] = E\,E[(\cdot)|\mathbf{x}^n]$ on both sides of Eq. (9), one obtains

$$\overline{\mathbf{x}^{n+1}} = \overline{\mathbf{x}^n} - 4a_n R\,\overline{\mathbf{x}^n} + 4a_n R\boldsymbol{\phi} \tag{10}$$

It is a simple matter to show that $\mathbf{x}_0 = \boldsymbol{\phi}$ is the steady-state solution to Eq. (10). It can be shown, by the methods used in Ref. 2, that $E[\|\mathbf{x}^n - \boldsymbol{\phi}\|^2]$ approaches zero as n approaches infinity. Consequently, $\mathbf{x}^n$ converges in mean square to $\boldsymbol{\phi}$ even if $\sigma_1^2 \neq 0$. We have just proved Theorem II.

Theorem II: An algorithm to identify systems in $\mathcal{S}$ without error, in the limit as $t \to \infty$, is given by

$$\mathbf{x}^{n+1} = \mathbf{x}^n - 4a_n\,[\mathbf{u}_n'(\mathbf{u}_n')^T - \sigma_1^2 I]\,\mathbf{x}^n + 4a_n\,\mathbf{u}_n'\,v_n'$$

E. Low Noise Receivers: Microwave Maser Development, Second Generation Maser,

R. C. Clauss and W. Higa

1. Summary

The second-generation maser and its initial performance were described in SPS 37-47, Vol. II, pp. 71–73. Increased isolation has resulted in improved stability, slightly reduced gain and bandwidth. The effects of variations in pump frequency, magnetic field, and package temperature have been measured.

2. Isolation

The use of single crystal yttrium iron garnet, as an isolator material, has been discussed previously (SPS 37-44, Vol. III, pp. 69–72 and SPS 37-46, Vol. III, pp. 67–72). In order to provide more isolation than was used during initial testing, the isolator disc size was increased from 0.036- to 0.045-in. diam. Thickness of the isolator discs was adjusted to give isolation over a frequency range from 2220 to 2350 MHz.

The isolator performance is affected by magnetic field direction and uniformity. Figure 4 shows the maser gain and bandwidth at two magnetic field orientations. Maximum isolation is accompanied by an increase of forward loss through the maser. The major loss increase occurs on the skirts of the pass band and results in a bandwidth reduction.

Increased isolation has reduced the maser's sensitivity to magnetic field distortion. Changes in the maser pass band, caused by movement of magnetic materials near the maser magnet, can be corrected by adjustment of current through the coils used to determine center frequency and gain.

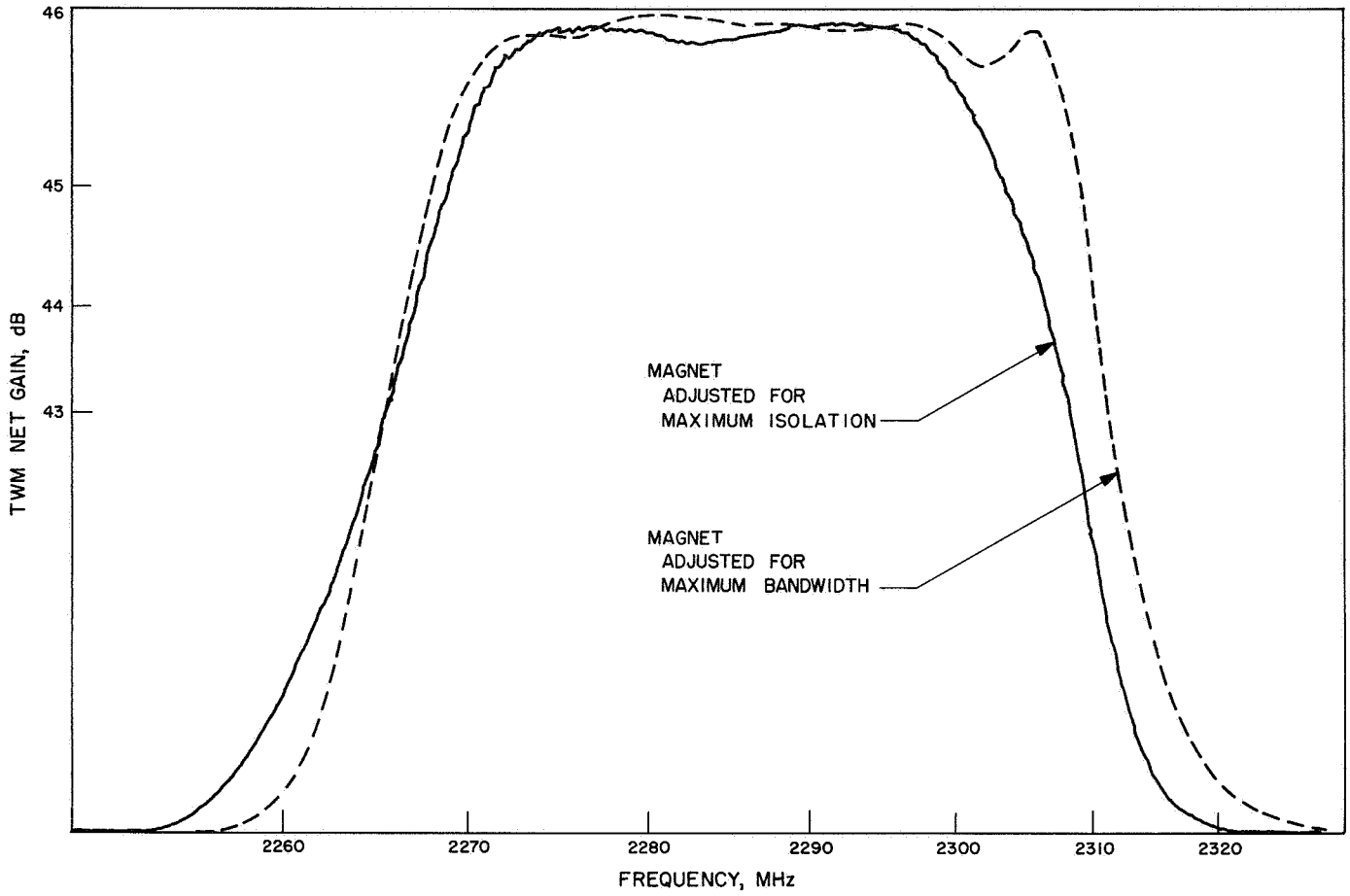

Fig. 4. Second generation maser gain and bandwidth

3. Stability

Maser gain changes, caused by variations in pump frequency, magnetic field, and package temperature have been measured.

The maser is relatively insensitive to changes in pump power. When pumped at the optimum frequency (with 200 mW power) an 0.5-dB change in pump power does not change the gain or the shape of the maser pass band. The maser, however, is sensitive to changes in pump frequency. Table 6 lists stability requirements based on test data available at this time. The requirements are necessary for short- and long-term stability in a situation where the maser is fixed-tuned and does not require daily adjustments. It is expected that the pump source used must be capable of stable operation at any frequency in the range 12.66 to 12.71 GHz.

Changes in package temperature do not directly affect the maser performance. A change in gain observed when changing package temperature is caused by the temperature sensitivity of the maser magnet. Because the magnet is temperature-compensated, the average field strength is constant during temperature changes between 80 and 125°F (SPS 37-43, Vol. III, pp. 51–52). The uniformity of the field does vary with temperature, causing the gain to increase at the rate of 1 dB per 20°F. The change in gain can be corrected by a change in current through the gain adjustment coil. This permits maser operation, with the required bandwidth at any package temperature between 80 and 125°F. Temperature regulation obtained by the controller now in use is adequate to maintain stable operation.

Two power supplies are used to adjust the magnetic field strength and the field shape. These supplies determine the gain, bandwidth, and center frequency of the maser; 0.1% regulation is essential for each power supply.

Values shown in Table 6 represent the maximum deviation allowable on both a short- and long-term basis.

Table 6. Stability requirements for maximum gain variation of ±0.05 dB

Function	Required stability	
	Maximum allowable change	Percentage regulation, %
Pump power	±10 mW	5
Pump frequency	±0.5 MHz	0.004
Package temperature	±1°F	—
Magnet field control power supplies	±0.3 mA	±0.1

These tolerances are based on variations which could individually produce maser gain changes of ±0.05 dB.

F. Improved RF Calibration Techniques,

C. T. Stelzried, T. Y. Otoshi, and D. L. Welling

1. Receiving System Noise Temperature Calibrations With Ambient Termination, C. T. Stelzried

The receiving system noise temperature calibration using the ambient load technique at the Mars and Venus DSSs has been discussed in detail (SPS 37-42, Vol. III, p. 25). Noise temperature calibrations are made by switching the maser input with a waveguide switch between the antenna and a waveguide ambient termination. The principal advantage of this technique is long-term stability and reliability of the ambient waveguide termination. Another advantage is that it is not necessary to evaluate the waveguide losses when the system temperature is defined at the maser input. This technique does depend on a previous calibration of the maser input noise temperature; however, a 10% error in this parameter results in only about a 1% error in the system temperature measurement for a typical Goldstone installation.

A tabulation of the principal results of the daily noise temperature calibrations is presented in Table 7 for July 2 to October 2, 1967, for the Goldstone Mars and Venus Stations.[1] This does not include the data taken at the Mars DSS when used in the standard DSN mode of operation. The probable errors of the measurement dispersions are identified as $(pe_i)_D$ for the individual measurements and $(pe)_D$ for the mean. These errors do not include bias errors such as those due to nonlinearities, etc. The system temperature averages were computed using only data with: antenna at zenith, clear weather, no RF spur in receiver pass band. The follow-up contributions, reflectometer readings on the antenna and ambient termination and the maser gain averages were computed using all data points available. The maser gain was optimized prior to each daily track precalibration.

The first reported system temperature measurement of the S-band cassegrain ultra cone (SCU) operational on the antenna (SPS 37-46, Vol. III, p. 72) is $[16.3 \pm 0.06\ (pe)_D]$°K.

[1]All measurements were taken by Venus Station personnel.

Table 7. Summary of reflectometer, maser gain, total system temperature and follow-up contribution parameters for Venus and Mars Station R & D systems for July 2 to October 2, 1967

Station	Cone	Frequency, MHz	Reflectometer reading, dB		Maser gain, dB	System temperature, °K	Follow-up contribution, °K
			Antenna	Ambient			
DSS 13	SPR,[a] on antenna	2388	34.2 $\pm 1.8\ (pe_i)_D$ $\pm 0.3\ (pe)_D$ 36 data points	39.6 $\pm 2.4\ (pe_i)_D$ $\pm 0.4\ (pe)_D$ 36 data points	37.6 $\pm 1.4\ (pe_i)_D$ $\pm 0.2\ (pe)_D$ 36 data points	22.8 $\pm 0.37\ (pe_i)_D$ $\pm 0.08\ (pe)_D$ 21 data points	0.75 $\pm 0.12\ (pe_i)_D$ $\pm 0.02\ (pe)_D$ 36 data points
	SCU,[b] on antenna	2297	48.1 $\pm 1.2\ (pe_i)_D$ $\pm 0.5\ (pe)_D$ 5 data points	35.5 $\pm 4.6\ (pe_i)_D$ $\pm 2.0\ (pe)_D$ 5 data points	47.9 $\pm 0.08\ (pe_i)_D$ $\pm 0.03\ (pe)_D$ 5 data points	16.3 $\pm 0.11\ (pe_i)_D$ $\pm 0.06\ (pe)_D$ 4 data points	0.24 $\pm 0.11\ (pe_i)_D$ $\pm 0.05\ (pe)_D$ 5 data points
	SCU, on ground	2297	49.7 $\pm 5.0\ (pe_i)_D$ $\pm 1.1\ (pe)_D$ 22 data points	53.4 $\pm 6.7\ (pe_i)_D$ $\pm 1.4\ (pe)_D$ 22 data points	47.1 $\pm 0.30\ (pe_i)_D$ $\pm 0.06\ (pe)_D$ 22 data points	12.6 $\pm 0.21\ (pe_i)_D$ $\pm 0.06\ (pe)_D$ 13 data points	0.08 $\pm 0.01(pe_i)_D$ $\pm 0.002\ (pe)_D$ 21 data points
DSS 14	SMF,[c] on antenna	2388	—	—	38.4 $\pm 0.3\ (pe_i)_D$ $\pm 0.1\ (pe)_D$ 10 data points	23.9 $\pm 0.54\ (pe_i)_D$ $\pm 0.13\ (pe)_D$ 16 data points	0.74 $\pm 0.11\ (pe_i)_D$ $\pm 0.03\ (pe)_D$ 19 data points

[a]S-band planetary radar.
[b]S-band cassegrain ultra cone.
[c]S-band multifrequency.

The increase in zenith system temperature between operating on the ground and the antenna is $[3.6 \pm 0.1 (pe)_D]$°K for these operational periods. (Proper account was taken of the follow-up contributions).

2. Ultra Cone Line Loss Calibrations, *T. Y. Otoshi and D. L. Welling*

a. Introduction. This article presents a summary of critical insertion losses and reflection coefficients which were measured for the S-band cassegrain ultra cone (SCU). These data are essential for the absolute noise temperature calibrations of individual noise sources which contribute to system temperature.

As described in SPS 37-46, Vol. III, p. 63, the ultra cone is an operational cassegrain feed and front end system which was designed to give ultra low-noise performance (target system temperature of less than 18°K). Figure 5 is a block diagram of the ultra cone system. A discussion of the complete system may be found in the referenced SPS. The measured insertion losses and reflection coefficients are tabulated and will be used in a future report describing system and antenna temperature calibrations. The 2297-MHz dissipative loss between reference points 1 to 2a (this includes the 33-dB waveguide coupler, waveguide switch, and the broadband coupler) contributes about 1.4°K to the system temperature (see previous Section 1 of this article).

b. Calibration method and results. Accurate calibration of the individual noise sources which contribute to system temperature requires meticulous calibrations of line losses and reflection coefficients at specific reference points (see Fig. 5). The influence of noise source and transmission line reflection coefficients on the absolute

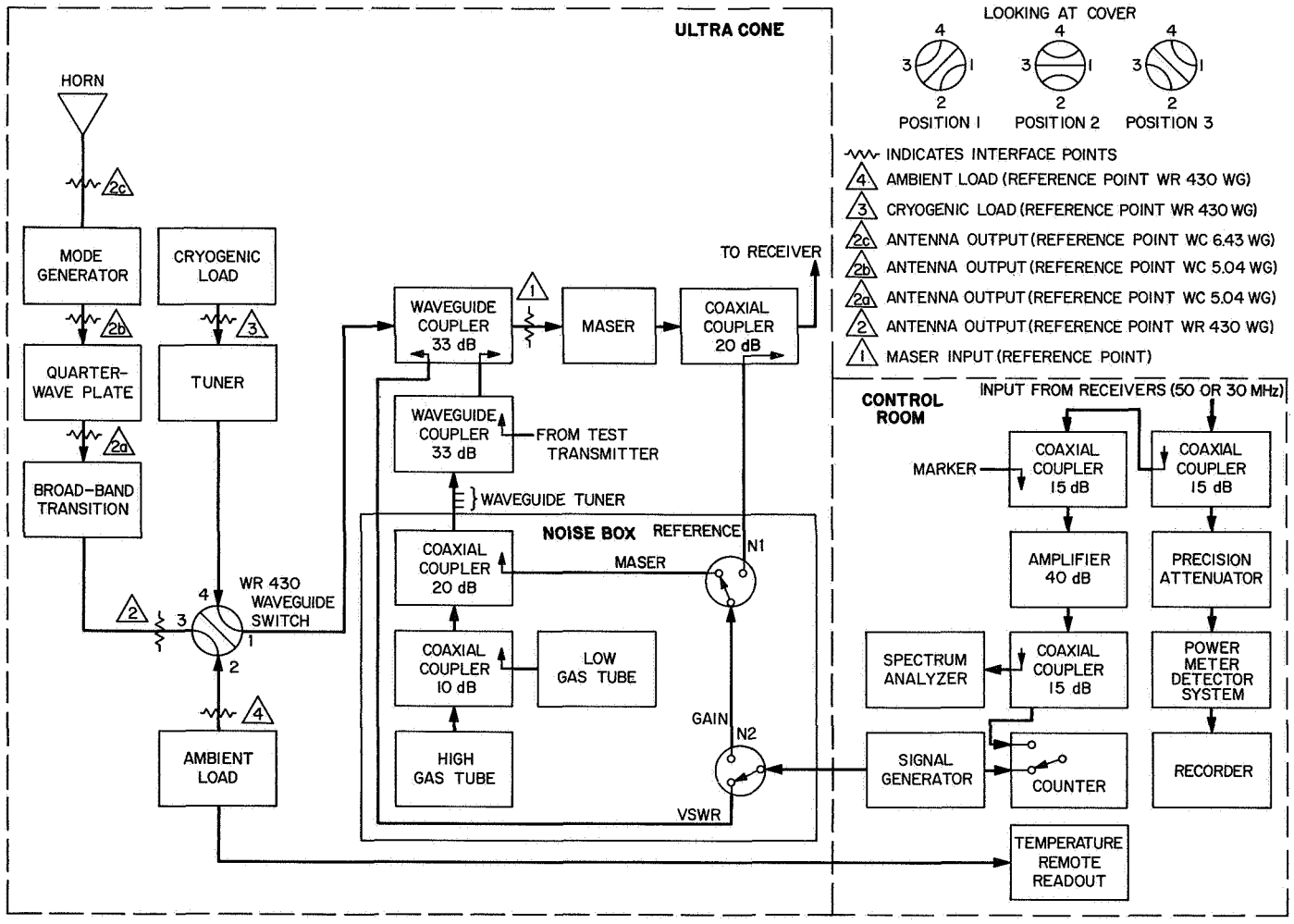

Fig. 5. S-band ultra cone and RF instrumentation rack block diagram

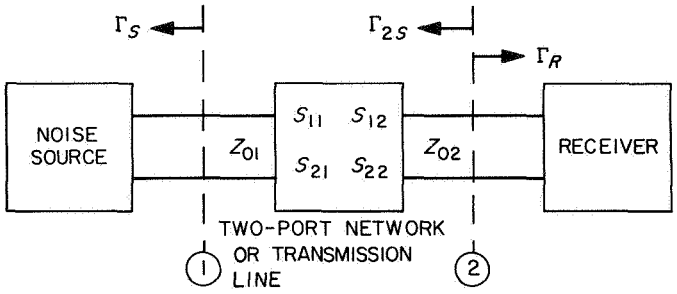

Fig. 6. Critical scattering parameters and voltage reflection coefficients for noise temperature calibrations

accuracy of noise temperature calibrations was discussed in SPS 37-40, Vol. IV, p. 190.

Figure 6 depicts critical parameters of a basic receiving system which must be calibrated or accounted for in absolute noise temperature calibrations. The symbols shown in the figure are defined as follows:

Z_{01} = characteristic impedance of the receiving system at the network input port

Z_{02} = characteristic impedance of the receiving system at the network output port

Γ_S = voltage reflection coefficient of a general case noise source

Γ_R = voltage reflection coefficient of the receiver

Γ_{2S} = input voltage reflection coefficient, as seen looking into the network at port 2 when port 1 is terminated in a Γ_S load

S_{11} = voltage reflection coefficient, as seen looking into the network at port 1 when port 2 is terminated in a matched load

S_{12} = voltage transmission coefficient of the network when the source is connected to port 2 and a matched receiver is connected to port 1

S_{21} = voltage transmission coefficient of the network when the source is connected to port 1 and a matched receiver is connected to port 2

S_{22} = voltage reflection coefficient, as seen looking into the network at port 2 when port 1 is terminated in a matched load

Table 8. Noise source and receiver reflection coefficients

Description of noise source or load	Input reference point		Voltage reflection coefficient	
	Description	System reference point No. (Fig. 5)	2297 MHz	2388 MHz
Feed is in the standard RCP configuration radiating into free space	WR 430 antenna ref.	2	0.0060 $\pm$0.0012 p_{e_T}	0.0123 $\pm$0.0017 p_{e_T}
Feed is in the standard RCP configuration radiating into free space	WR 430 maser ref.	1	0.00631 $\pm$0.00030 p_{e_T}	0.01496 $\pm$0.00054 p_{e_T}
Feed is in the RCP configuration terminated by an aperture ambient load	WR 430 maser ref.	1	0.00794 $\pm$0.00035 p_{e_T}	0.01995 $\pm$0.00068 p_{e_T}
Feed is in a substituted piece-LP configuration radiating into free space	WR 430 maser ref.	1	0.01778 $\pm$0.00062 p_{e_T}	0.02239 $\pm$0.00075 p_{e_T}
Feed is in a substituted piece-LP configuration terminated by an aperture ambient load	WR 430 maser ref.	1	0.05012 $\pm$0.00148 p_{e_T}	0.04842 $\pm$0.00144 p_{e_T}
WR 430 LN_2 load assembly (MMC SR 8135 SN002)	WR 430 cryo. load ref.	3	0.00813 $\pm$0.00035 p_{e_T}	0.02483 $\pm$0.00081 p_{e_T}
WR 430 LN_2 load assembly (MMC SR 8135 SN002)	WR 430 maser ref.	1	0.00631 $\pm$0.00029 p_{e_T}	0.02512 $\pm$0.00082 p_{e_T}
WR 430 LHe load assembly (RFT Part No. 270)	WR 430 cryo. load ref.	3	0.03981 $\pm$0.00121 p_{e_T}	0.09441 $\pm$0.00257 p_{e_T}
WR 430 LHe load assembly (RFT Part No. 270)	WR 430 maser ref.	1	—	—
WR 430 ambient load assembly	WR 430 maser ref.	1	0.00251 $\pm$0.00021 p_{e_T}	0.11220 $\pm$0.00300 p_{e_T}
Maser assembly	WR 430 maser ref.	1	0.100 $\pm$0.011 p_{e_T}	0.112 $\pm$0.012 p_{e_T}

Table 9. Calibration data for ultra cone transmission lines

Input/output (I/O) path description	I/O reference point No. (Fig. 5)	2297 MHz				2388 MHz			
		S_{11}	S_{22}	A_{T_f}[a] dB	A_{D1}, dB	S_{11}	S_{22}	A_{T_f}[a] dB	A_{D1}, dB
Antenna/maser flanges via 3-position switch, plus 33-dB coupler	2/1	0.00055 $\pm 0.00034\ pe_T$	0.00042 $\pm 0.00034\ pe_T$	0.0184 $\pm 0.0004\ pe_T$	0.0184 $\pm 0.0004\ pe_T$	0.02407 $\pm 0.00064\ pe_T$	0.00818 $\pm 0.00039\ pe_T$	0.0148 $\pm 0.0004\ pe_T$	0.0123 $\pm 0.0004\ pe_T$
Cryo load maser flanges via 3-position switch, plus 33-dB coupler	3/1	0.00246 $\pm 0.00035\ pe_T$	0.00028 $\pm 0.00034\ pe_T$	0.0268 $\pm 0.0004\ pe_T$	0.0268 $\pm 0.0004\ pe_T$	0.00663 $\pm 0.00037\ pe_T$	0.00826 $\pm 0.00039\ pe_T$	0.0415 $\pm 0.0004\ pe_T$	0.0413 $\pm 0.0004\ pe_T$
WC 504/WR 430 flanges of copper broadband transition	2a/2	0.00798 $\pm 0.00040\ pe_T$	0.00847 $\pm 0.00023\ pe_T$	0.0019 $\pm 0.0002\ pe_T$	0.0016 $\pm 0.0002\ pe_T$	0.01007 $\pm 0.00042\ pe_T$	0.01066 $\pm 0.00027\ pe_T$	0.0035 $\pm 0.0002\ pe_T$	0.0031 $\pm 0.0002\ pe_T$
WC 504/WC 504 flanges of circular waveguide section (20-in. length substitution piece)		0.00058 $\pm 0.00014\ pe_T$	0.00058 $\pm 0.00014\ pe_T$	0.0048 $\pm 0.0004\ pe_T$	0.0048 $\pm 0.0004\ pe_T$	0.00104 $\pm 0.00016\ pe_T$	0.00104 $\pm 0.00016\ pe_T$	0.0042 $\pm 0.0004\ pe_T$	0.0042 $\pm 0.0004\ pe_T$

[a]The measured insertion loss corresponds to A_T in this table.

The attenuation of the network, which includes both reflective and dissipative losses, is given as

$$(A_T)_{DB} = 10 \log_{10} \left[\frac{Z_{02}}{Z_{01}} \frac{1}{|S_{21}|^2} \right]$$

This attenuation is also the insertion loss which would be measured in a matched system. The dissipative attenuation, when the input port is defined as port 1, is given as

$$(A_{D1})_{DB} = 10 \log_{10} \left[\frac{Z_{02}}{Z_{01}} \frac{(1 - |S_{11}|^2)}{|S_{21}|^2} \right]$$

Reflection coefficients of the ultra cone noise sources, transmission lines, and receiver were measured, in most cases, with high-precision reflectometers. Results of the noise source and receiver reflection coefficient measurements are shown in Table 8. Transmission line attenuation measurements were made with a dc insertion loss test set (Ref. 3) in a laboratory setup. The calibrated reflection coefficients and attenuations associated with the ultra cone transmission lines can be found in Table 9.

The total probable error (pe_T) associated with each calibrated reflection coefficient value includes probable errors due to (1) imperfect reflectometer system tuning, (2) imperfect sliding load housings, and (3) resolution and nonlinearity errors in the reflectometer system. The total probable error (pe_T) associated with each attenuation value includes the probable error due to (1) measurement dispersion, (2) insertion loss measurement system resettability and nonlinearity errors, (3) mismatch errors, and (4) imperfections of the sliding load housings. All data reduction and calculations of probable errors were performed by the IBM 7094 computer through the use of computer program TYØ050[2] and program CTS/3.[3]

It is believed that the results given in this article represent the most accurate attenuation and reflection coefficient data obtained to date on a JPL-built cassegrain cone waveguide system. The high accuracy can be attributed to (1) well-matched and low-loss waveguide components, (2) refinements in the measurement techniques, and (3) the use of a computer for data reduction and error analysis calculations.

[2]This program was written by Lois Busch.

[3]This program is described in Ref. 3.

G. Spacecraft CW Signal Power Calibration with Microwave Noise Standards, *C. T. Stelzried and D. L. Nixon*

1. Introduction

The CW power level received from a spacecraft is an important parameter required for the evaluation of a deep space communication system. A precise measurement method which compares CW signal power with microwave noise power was used to calibrate the *Mariner IV* spacecraft received power level at encounter (Ref. 4). This technique with improved instrumentation is being used to calibrate the received power level of *Mariner V*.

2. CW Power Calibration Instrumentation

The *Mariner IV* spacecraft received power measurements were performed with a minimum of station instrumentation modification. Several small errors are obtained with this installation. One source of error is the difference in the diode detector sensitivity to signal and noise power due to imperfect square law characteristics (SPS 37-36, Vol. III, p. 44). Instrumentation RF leakage results in further measurement errors especially in the narrow-band filter bandwidth calibrations (SPS 37-36, Vol. IV, p. 269).

Authorization was received July 27, 1967, to implement DSS 12 (DSIF File No. 67-268) with improved instrumentation to be used with *Mariner V*. Figure 7 is a block diagram of the ground station receiving system calibration instrumentation. A power meter using a themistor

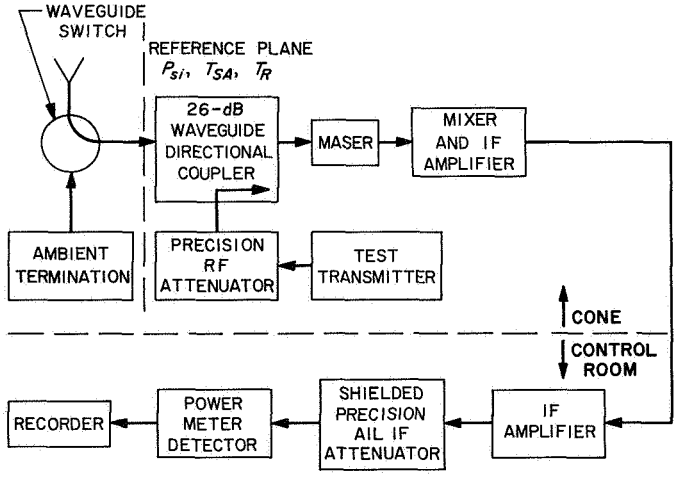

Fig. 7. Ground station receiving system calibration instrumentation

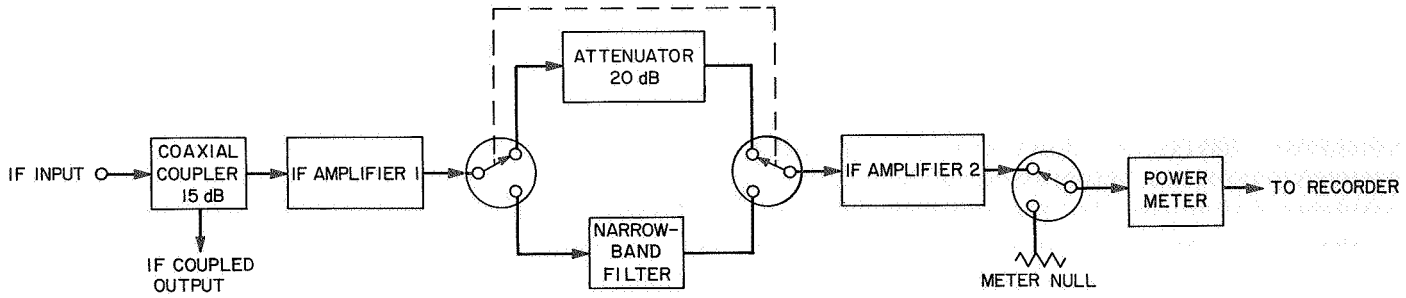

Fig. 8. Block diagram of power meter detector assembly

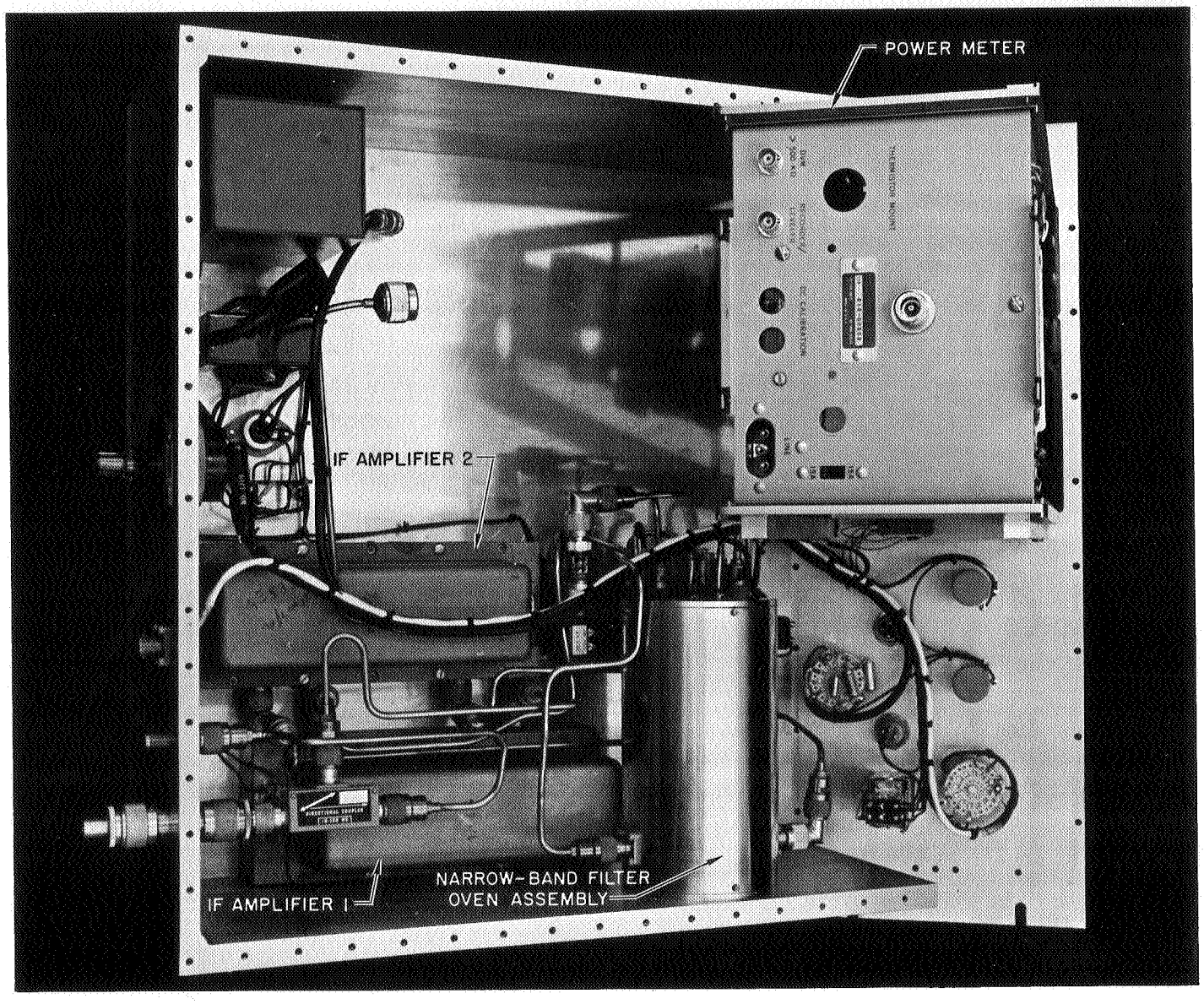

Fig. 9. Power meter detector assembly

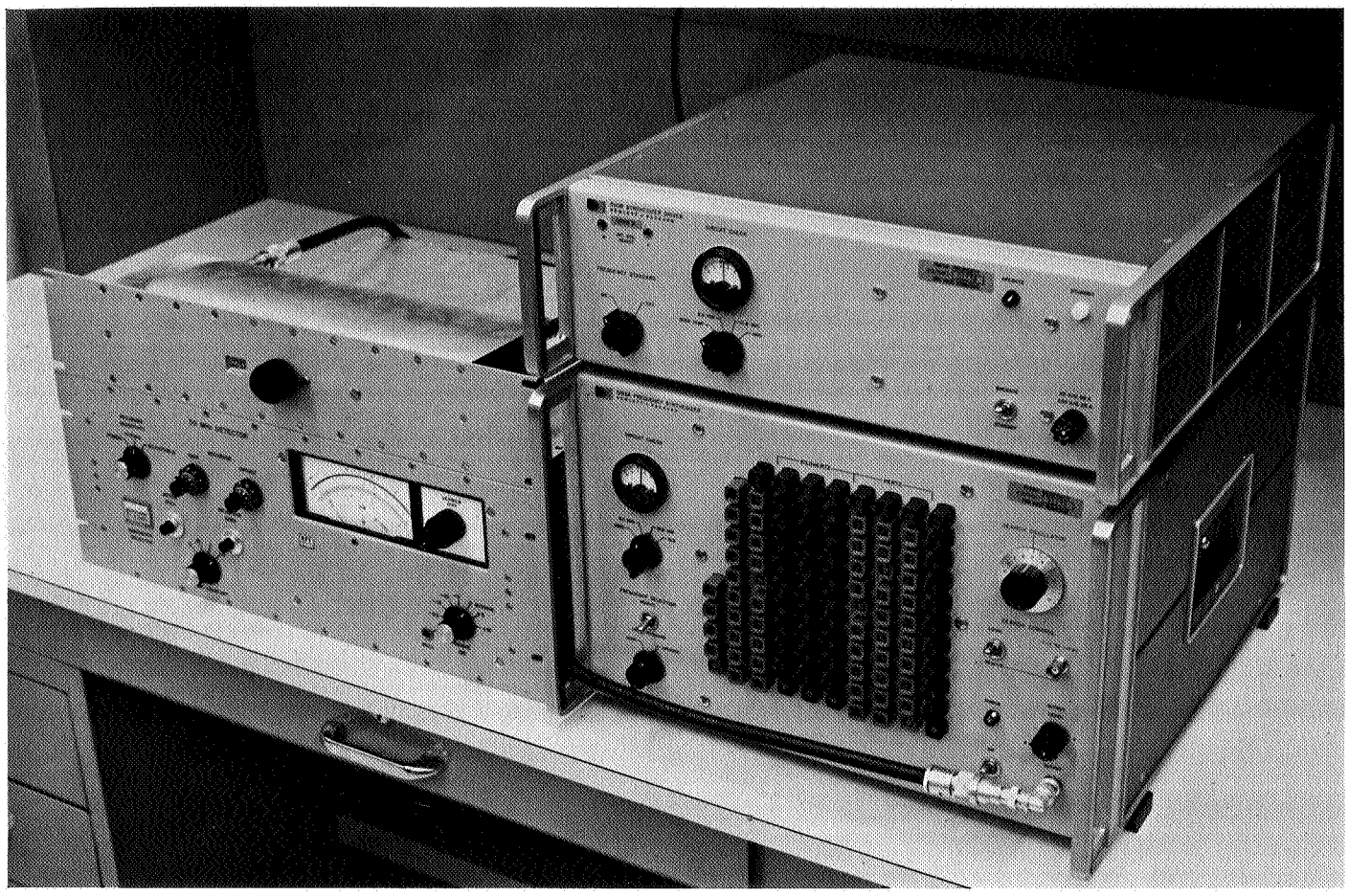

Fig. 10. Power meter detector undergoing laboratory bandwidth calibrations

heat-sensing detector is used to eliminate the diode unequal sensitivity problem. The power meter detector assembly is illustrated by the block diagram and photograph shown in Figs. 8 and 9. The IF amplifiers are required to compensate for the reduced sensitivity of the power meter as compared to the diode detector and the further gain required with the narrow-band filter mode of operation. The power meter detector is shown in Fig. 10 during a bandwidth calibration using a frequency synthesizer and precision waveguide beyond cut-off IF attenuator. The shielding has been greatly improved and is adequate for greater than 55-dB dynamic range in the narrow-band filter bandwidth integration calibration.

Figure 11 shows the maser instrumentation rack at DSS 12 with the shielded IF attenuator and power meter detector installed.

The microwave WR 430 waveguide ambient termination required for the noise temperature calibrations (SPS 37-36, Vol. IV, p. 269) is located in the antenna cassegrain cone assembly. The standard assembly has been replaced with a ⅞-in. coaxial polyiron termination enclosed in a copper heat sink and waveguide transition filled with urethane foam (Fig. 12). The temperature is measured with a Hewlett-Packard model 2850B quartz thermometer probe provided with a remote readout indicator.

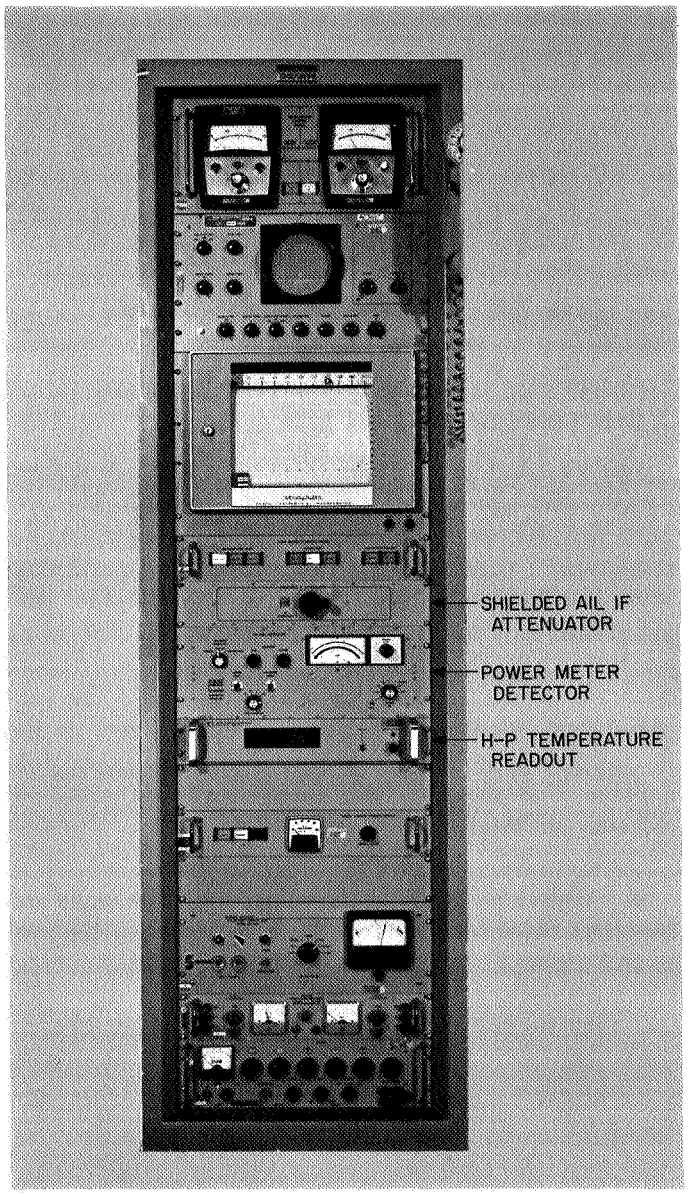

Fig. 11. Echo Station maser instrumentation rack with power meter detector installed

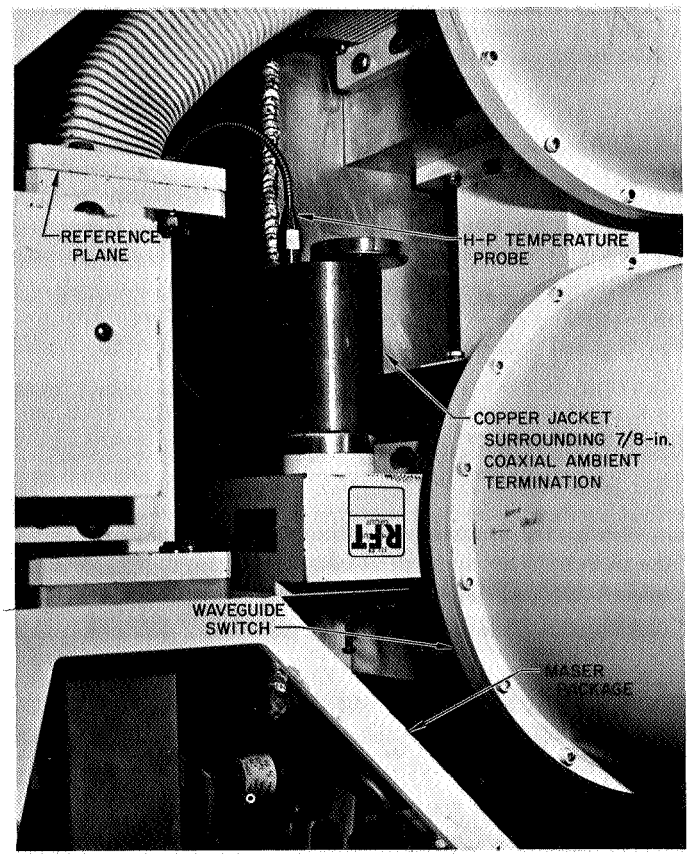

Fig. 12. Ambient termination with temperature probe located in antenna cassegrain cone

H. Efficient Antenna Systems: A Program to Calculate the Optical Blockage by the Quadripod on Large Microwave Antennas,

J. Herndon

1. Introduction

One of the factors which seriously affects the efficiency of cassegrain-fed antennas is the blockage of the aperture by the subreflector and its support structure. A computer program in FORTRAN II has been written to calculate the percent blockage of the 210-ft antenna at DSS 14. The problem is formulated in terms of optical geometry; diffraction effects are not included. The program has two uses: (1) the blockage calculated by the computer can be compared with the blockage calculated by other methods, and thus it provides an independent check on these methods, and (2) the input data which defines certain antenna dimensions can be varied to give an idea of how small changes in the antenna structure will affect the percent blockage.

A similar program for the 85-ft az-el antenna at DSS 13 was written. The results of that program are also discussed.

2. Definition of Blockage

The beam of transmitted or received energy is taken to be all the rays parallel to the axis of the paraboloid which fall within the radius of the paraboloid; in other words, a cylinder. The intensity in the beam is taken to be uniform over its circular cross section. The *blockage area* is the portion of the beam cross section representing the optically obstructed rays. The *percent blockage* is the percentage of the total cross section area which is blocked on an optical basis.

It may be desirable to think of the total blockage as the sum of two kinds of blockage: (1) the blockage which occurs where the wave front is spherical, and (2) the blockage which occurs where the wave front is plane.

Figure 13 shows the distribution of plane wave and spherical wave blockage in the aperture plane of the 210-ft reflector. In Fig. 13 the shaded area inside the dashed circle is caused by the plane wave blockage, while the shaded area outside the dashed circle is caused by the spherical wave blockage. Figure 14 shows the DSS 13 30-ft reflector, a model of the 210, which clearly demonstrates both kinds of blockage.

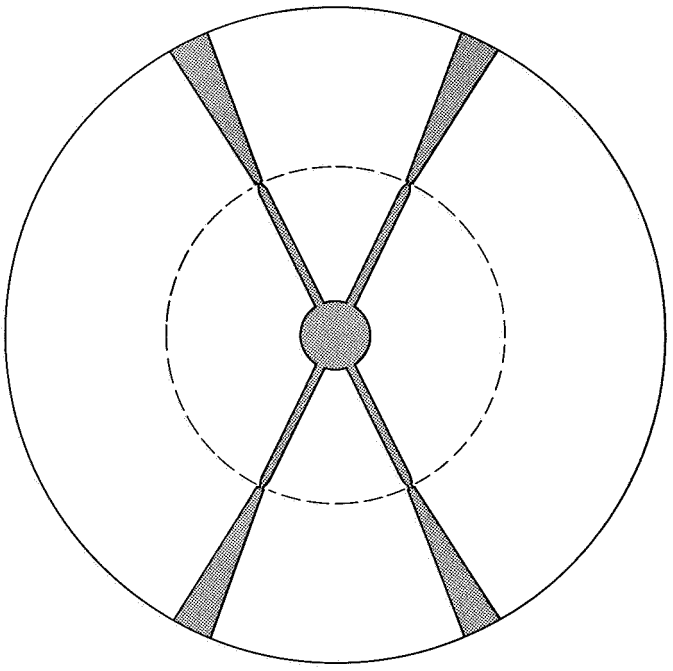

Fig. 13. 210-ft antenna plane wave and spherical wave blockage

3. 210-ft Blockage Program

The size and proportions of the antenna are defined by 10 input values on the data cards (Fig. 15). The program first calculates the spherical wave blockage, i.e., the shadow of a quadripod leg projected on the paraboloid when it is illuminated from the focus. The computer integrates this area inward from the edge of the dish using approximately 300 increments. (The exact number of increments depends on the specific input values.) The program then calculates the plane wave blockage as the simple projection of the subreflector and quadripod onto a plane. The program adds these areas and prints out the sum as "total blockage area" (Fig. 16).

If it is desired, the separate values for plane wave and spherical wave blockage can be obtained from the program output:

$$\text{Spherical wave blockage} = 8\,(\text{area } 1) - 4\,(\text{area } 2)$$

$$\text{Plane wave blockage} = \text{area } 3 + 4\,(\text{area } 4)$$

where the areas are defined in Fig. 17.

If a plot of the blockage area is desired, the computer sense switch 1 is turned on. The computer will punch cards which can then be used with Nixon's general plot

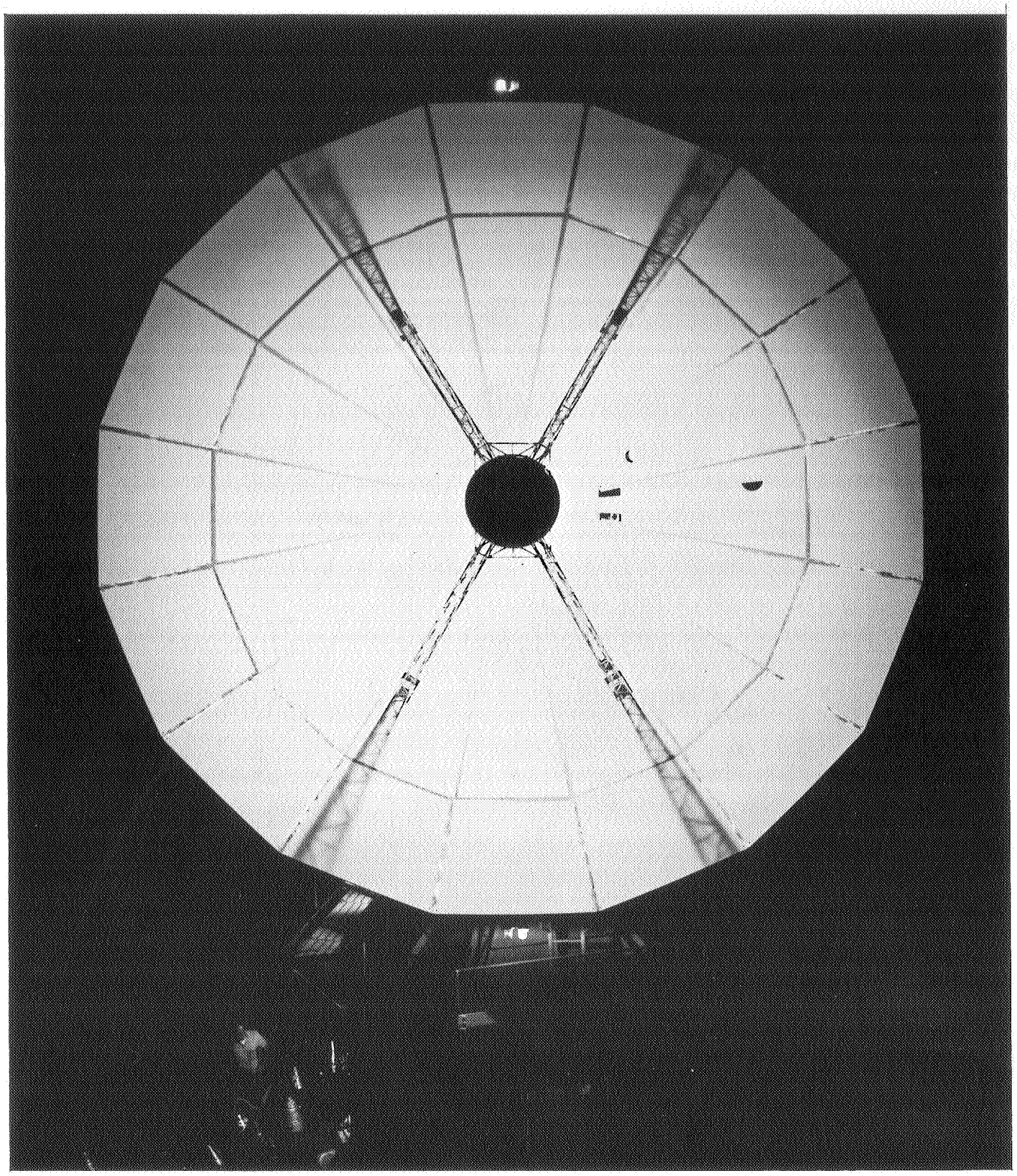

Fig. 14. 210-ft az–el model illuminated from focus

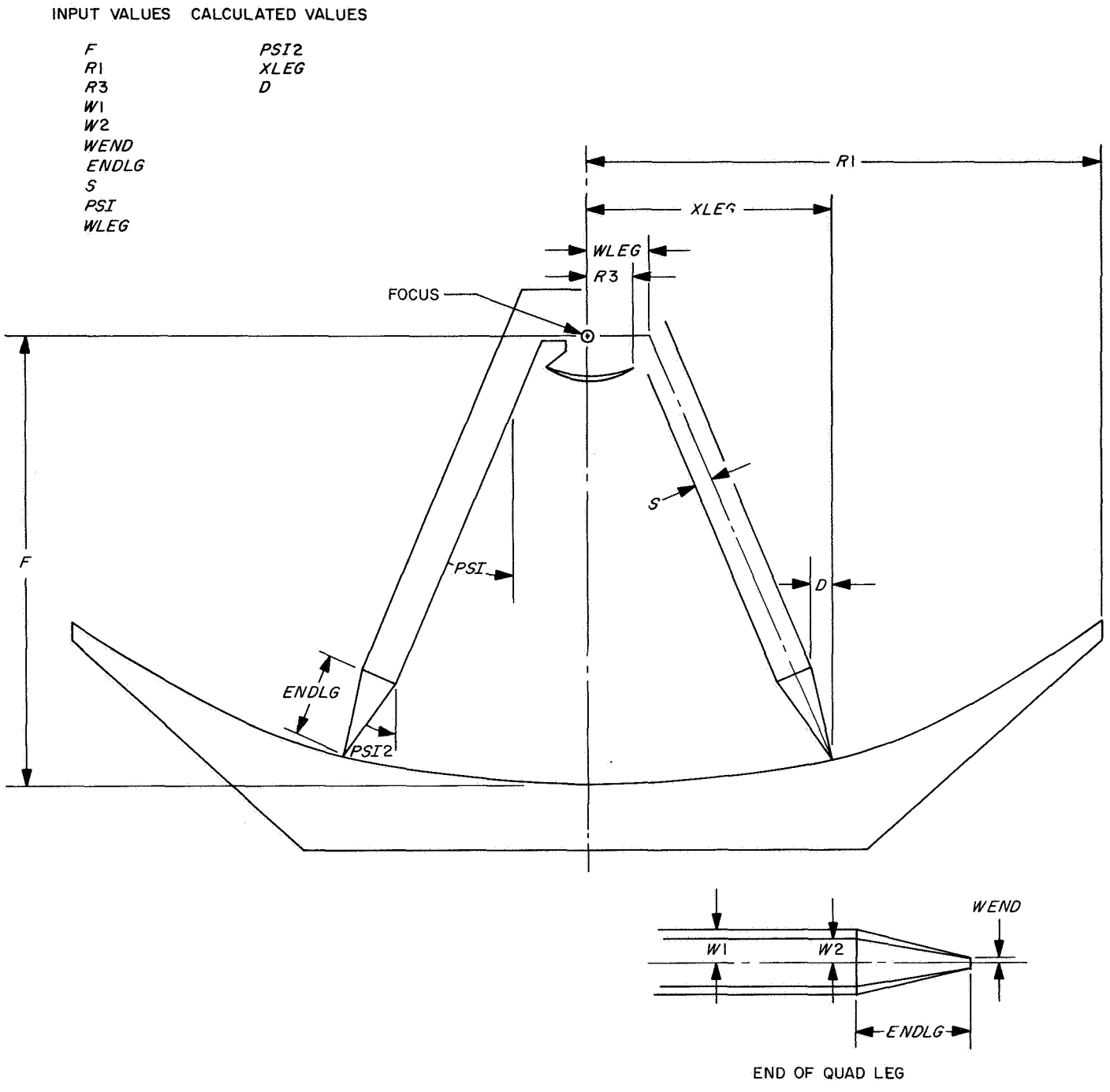

Fig. 15. Dimension names for 210-ft antenna blockage program

```
INPUT DATA

F= 88.94117
R1= 105.00000
R3= 11.00000
W1= 1.62500
W2= .87500
WEND= .27083
ENDLG= 18.74479
S= 4.00000
PSI= .47880
WLEG= 14.09909

COMPUTED CONSTANTS

PSI2= .68903
XLEG= 55.73464
D= 5.08580

OUTPUT DATA, CASE 1

AREA1= 200.16843 AREA2= 1.52151 AREA3= 380.13239 AREA4= 142.93333
TOTAL BLOCKAGE AREA= 2547.12700
PERCENT BLOCKAGE= 7.353
```

Fig. 16. Program printout

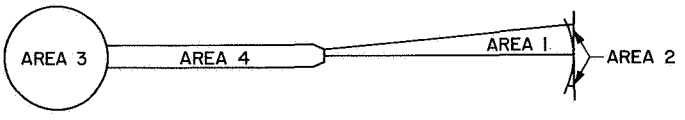

Fig. 17. Output areas for 210-ft az–el blockage program

program (DLN60). Figure 18 shows these plots for the nominal cases of both the 85- and 210-ft antennas. If detailed numerical information about the shape of the spherical wave blockage area is desired, sense switch 2 is turned on. The computer will print out the values of several variables at each increment in the integration. For instance, this sense switch is used if one wants to know whether the blockage by the inside or the outside width of the quadripod leg predominates. For the 210-ft antenna nominal case it is the inside width that predominates.

To simplify the calculations, the structure of the antenna was idealized in several ways, as illustrated by the differences between Figs. 13 and 14: (1) the edge of the dish is assumed to be a circle; it is actually a polygon, (2) the pipes in the subreflector assembly which project beyond the edge of the hyperboloid are neglected in the program, (3) the optical opacity of the quadripod and the subreflector are assumed to be equal. Actually, the opacity of the quadripod is less.

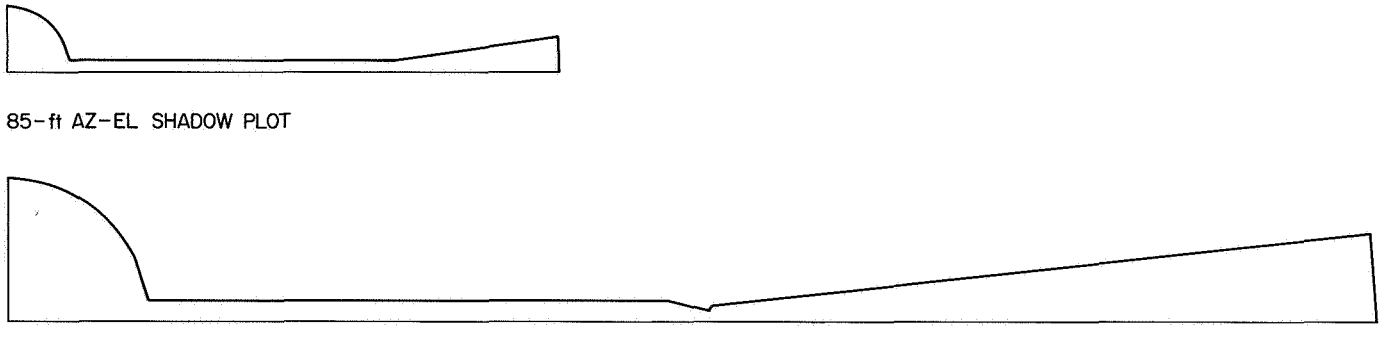

85-ft AZ-EL SHADOW PLOT

210-ft AZ-EL SHADOW PLOT

Fig. 18. 210- and 85-ft az–el shadow plots

The geometrical properties of the problem place restrictions on how much the input values may be changed from their nominal values. These restrictions are:

(1) The quadripod legs must touch the surface of the dish: $XLEG < RI$

(2) D must be positive:
$$(ENDLG)\sin(PSI) - (S)\cos(PSI) > 0$$

(3) The face of the quadripod leg toward the paraboloid axis must cross the axis above the focus:
$$\frac{WLEG}{\tan(PSI)} - \frac{S}{\sin(PSI)} > 0.$$

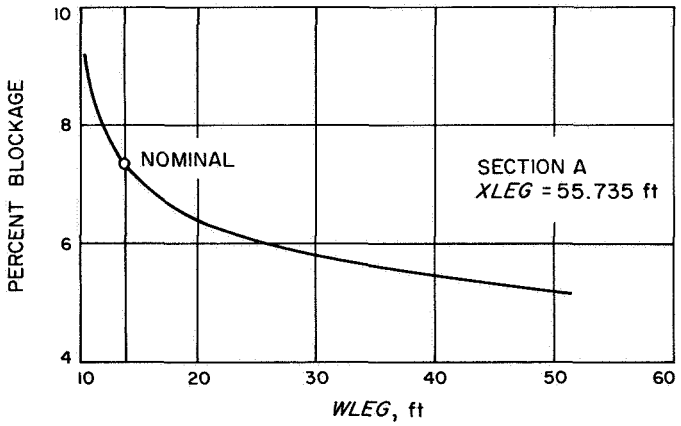

Fig. 19. 210-ft antenna blockage, section A

Assuming a fixed focal length, the position and angle of the quadripod leg is completely described by two lengths: *XLEG* and *WLEG*. The blockage as a function of length was calculated for two cases. In each case one length was allowed to vary while the other was held constant at its nominal value. *XLEG* is not an input value; it is determined by the input values of *PSI* and *WLEG*. *XLEG* was held constant by varying *WLEG* and *PSI* according to the function:

$$PSI = \arctan\left[\frac{(XLEG - WLEG)}{F - \frac{XLEG^2}{4F}}\right],$$

$$XLEG = 55.735\,\text{ft}$$

The two resulting graphs (Figs. 19 and 20) show that the change in blockage with respect to *WLEG* is greater than it is with respect to *XLEG*. This means that, for the 210-ft antenna, a greater reduction in blockage would result from changing the apex assembly than from changing the attachment position of the quadripod to the dish surface. In either case, the achievable reduction in blockage is small. Figure 21 shows how the curves in Figs. 19 and 20 can be thought of as sections through a 3-dimensional graph of the blockage.

The nominal percent blockage for the 210-ft antenna as calculated by the program is 7.353%. This is in good agreement with the percent blockage estimated by graphical methods.

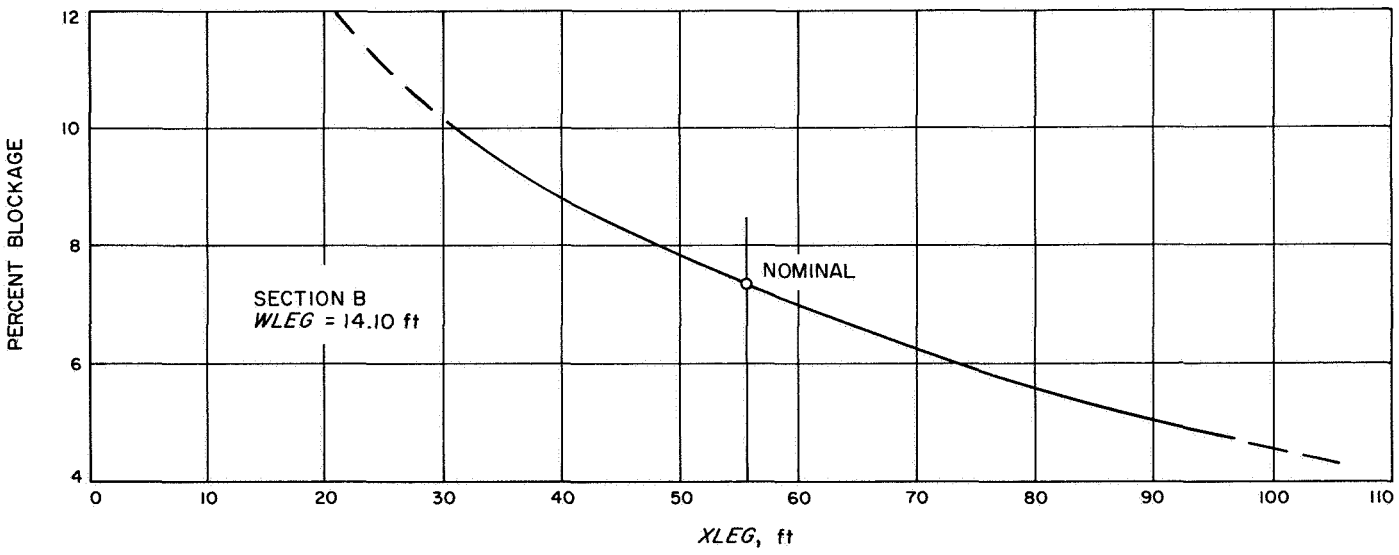

Fig. 20. 210-ft antenna blockage, section B

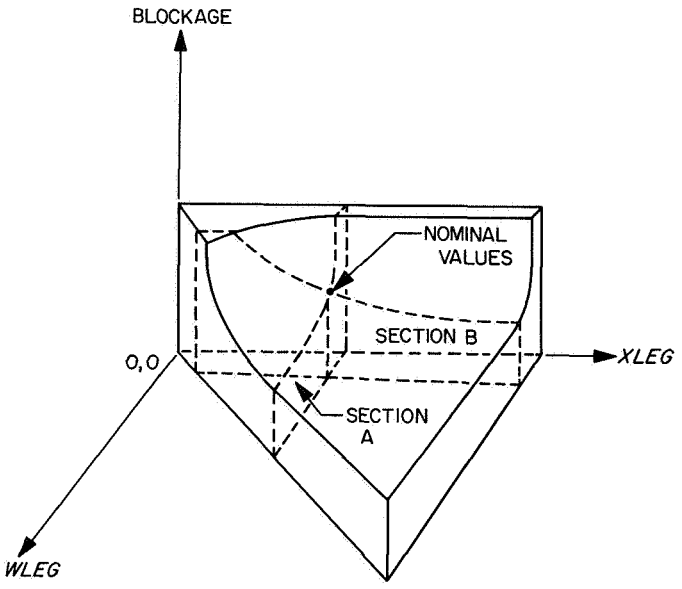

Fig. 21. Antenna blockage as a function of *WLEG* and *XLEG*

4. 85-ft Blockage Program

A relatively simple program to find the blockage of the 85-ft antenna was run with variations of quadripod position similar to the variations in the 210-ft program. Variations in the width of the quad legs were also tried. The results are shown graphically in Figs. 22 and 23. The nominal percent blockage was calculated to be 7.814%. Graphical methods of estimating the percent blockage confirm this value. As was found for the 210-ft antenna, the achievable reduction in blockage is again small.

5. Conclusion

Our present blockage programs do not include any explicit function which relates the optical blockage to the RF antenna efficiency. The rule by which we relate the percent blockage B and aperture efficiency η now is to say that, other factors remaining constant, $\eta \simeq (1-B)^2$, e.g., the efficiency is proportional to the square of the available area. It was mentioned that the intensity in the beam cross section is assumed to be uniform. Actually, the intensity is greater near the center of the cross section. This means that changing the plane wave blockage would have a greater effect on antenna efficiency than changing the spherical wave blockage by the same amount. In the case of the 210-ft antenna, where the blockage was calculated for different quadripod positions, most of the change in blockage came from changes in the spherical wave blockage, while the plane wave blockage remained constant. Thus, the efficiency to be gained by changing the quadripod position is even less than that suggested in Figs. 19 and 20.

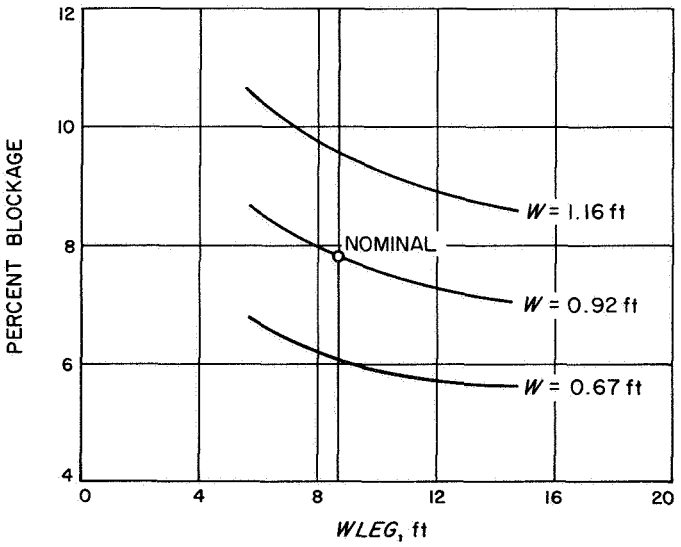

Fig. 22. 85-ft antenna blockage, *XLEG* = 29.8 ft

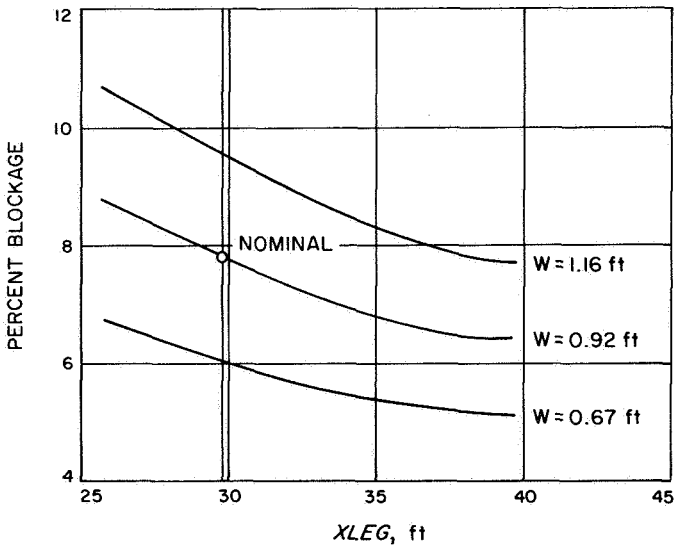

Fig. 23. 85-ft antenna blockage, *WLEG* = 8.8 ft

I. Special Equipment for *Mariner* Venus 67 Ranging System, *W. Martin*

1. Introduction

During construction of the *Mariner* Venus 67 ranging system, it became apparent that several special circuits would be required to complete the project. This special circuitry included (1) control cards for the multiplexer

and analog-to-digital converter (A/DC), (2) shapers for the various clock signals, and (3) a high-precision coaxial line driver with controlled transition times. Additionally, noise problems in the computer-to-ranging-rack signal lines necessitated the construction of a special set of amplifiers to buffer all digital signals entering the ranging equipment. Each of these special circuits is discussed here.

2. Multiplexer J-Cards

The control system for the multiplexer was designed and constructed using standard J-card techniques (SPS 37-39, Vol. III, pp. 52–65). Two cards are required: the parallel output (POT) card, for decoding the energized output medium (EOM) to command the multiplexer; and the parallel input (PIN) to gate the multiplexer channel address back to the computer.

The multiplexer requires three control signals that are supplied by the POT J-card: CLEAR, which causes the multiplexer to return to channel zero; STEP, which makes the multiplexer advance by one channel from its present location; and TRANSFER, which is used in conjunction with a POT to load the address of any channel into the multiplexer, thus providing a random access feature.

The PIN card serves to gate the multiplexer's current address into the computer's least-significant eight bits. Because these gates are connected directly to the multiplexer's address register, they provide an excellent check on the multiplexer's operation. This card is used in conjunction with the PIN card on the A/DC described below.

3. Analog-to-Digital Converter J-Cards

Like the multiplexer, the A/DC requires two cards for commands and data routing. Here, the purpose of the POT card is to generate *convert* signals and to provide an optional interrupt—or a *skip-if-external-signal-not-set* (SKS) instruction—to the computer when the conversion is completed.

Convert signals can originate in three ways. First, the computer can cause a convert pulse by supplying a specific EOM—called the programmed-convert mode. The multiplexer is the second source of conversion commands. When the multiplexer is instructed to move to a new channel, a 20-μs waiting period is begun to allow the output to become stable. At the end of this time, a signal is sent via the multiplexer's J-card, causing the A/DC to initiate a conversion. An external device is the third source of convert pulses. A phone jack located in the handle of the A/DC POT J-card can receive a *convert* signal from external equipment. These external commands are then shaped and timed to conform with the requirements of the converter.

When the conversion is complete, an *interrupt* is sent to the computer to indicate that the data are ready to be used. Additionally, an SKS flip-flop changes state immediately after the multiplexer has been commanded to switch to a different channel. Thus, an SKS will indicate *data not ready* through the multiplexer stepping sequence, as well as during the actual conversion. Only when the *end-of-convert* signal appears will it again return to the *data ready* condition.

Data input to the computer is accomplished through the PIN J-card. Two operational modes are available. The sign-extension mode puts the contents of the converter's register into the computer's least-significant twelve-bit positions, and the sign of this newly converted number is extended into the upper twelve bits. The multiplexer-address mode loads the converted number into the computer's upper twelve-bit locations and the multiplexer's address into the lower twelve bits. Selection of either mode is by the EOM which immediately precedes the PIN instruction. Thus, the programmer has complete freedom to change to alternate modes if he desires.

Because of their complexity, it is impossible to adequately cover the design and programming of these J-cards in a summary-type article. Therefore, both are to be covered more thoroughly in future publications.

4. Computer-to-Ranging-System Interface Amplifiers

Excessive noise levels (on the order of 2-V peak) at the ranging system end of the computer-to-ranging-system interconnection cables caused erroneous operation in some of the equipment. Terminating the POT signal cables reduced the problem, but occasional noise bursts still caused malfunctions. To alleviate the situation, a set of discrete circuit amplifiers that had very high noise thresholds (approximately 4 V) was designed. The amplifiers were noninverting, and nineteen were constructed on each of two identical cards. These were installed in the ranging rack to buffer all incoming signals from the computer. After installation, no further noise problems were encountered.

5. Clock-Shaper Card

Several analog signals were used in the ranging equipment; e.g., the RF and clock-doppler frequencies, the 1-MHz clock, and the command pulse from the tracking

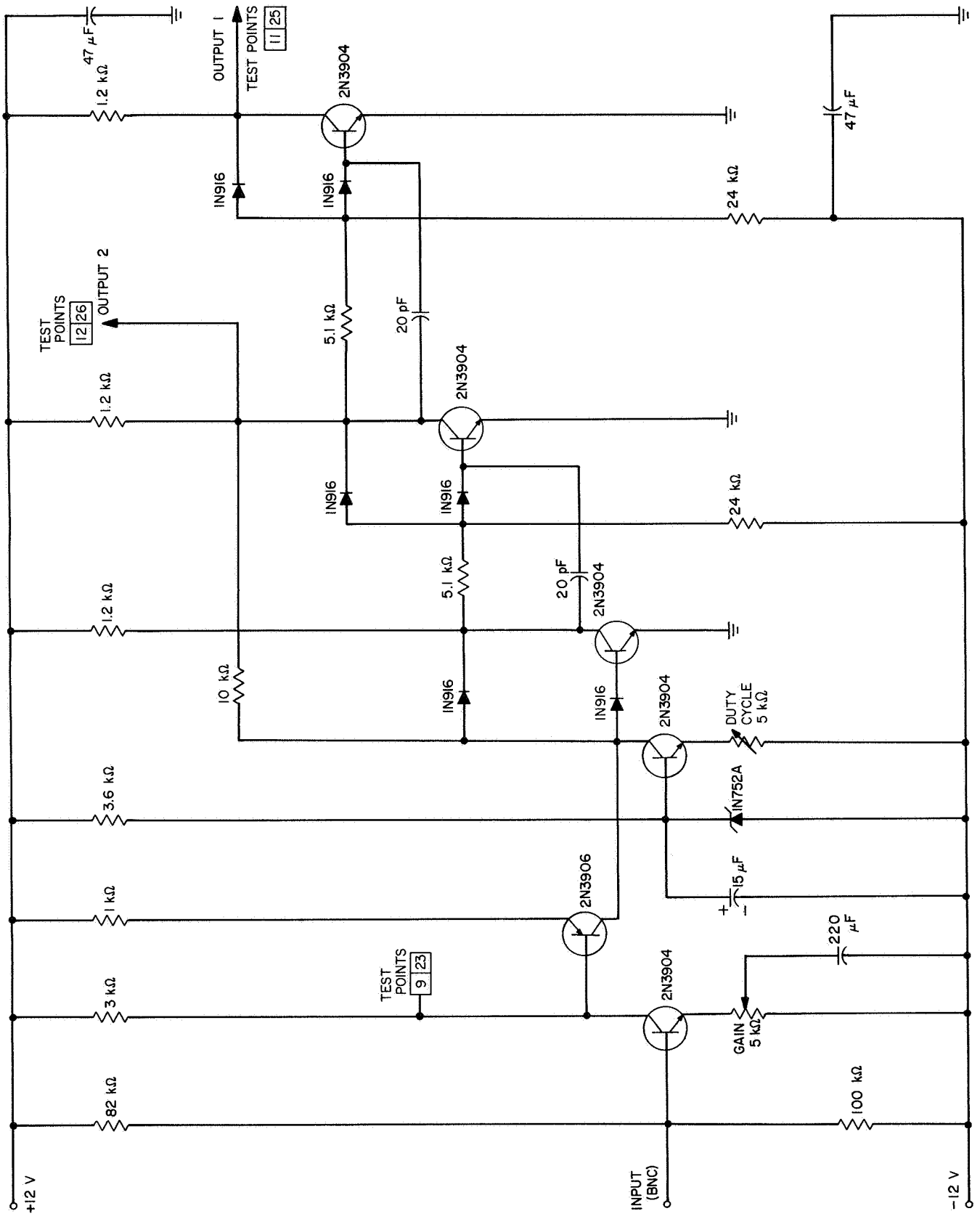

Fig. 24. Threshold detector

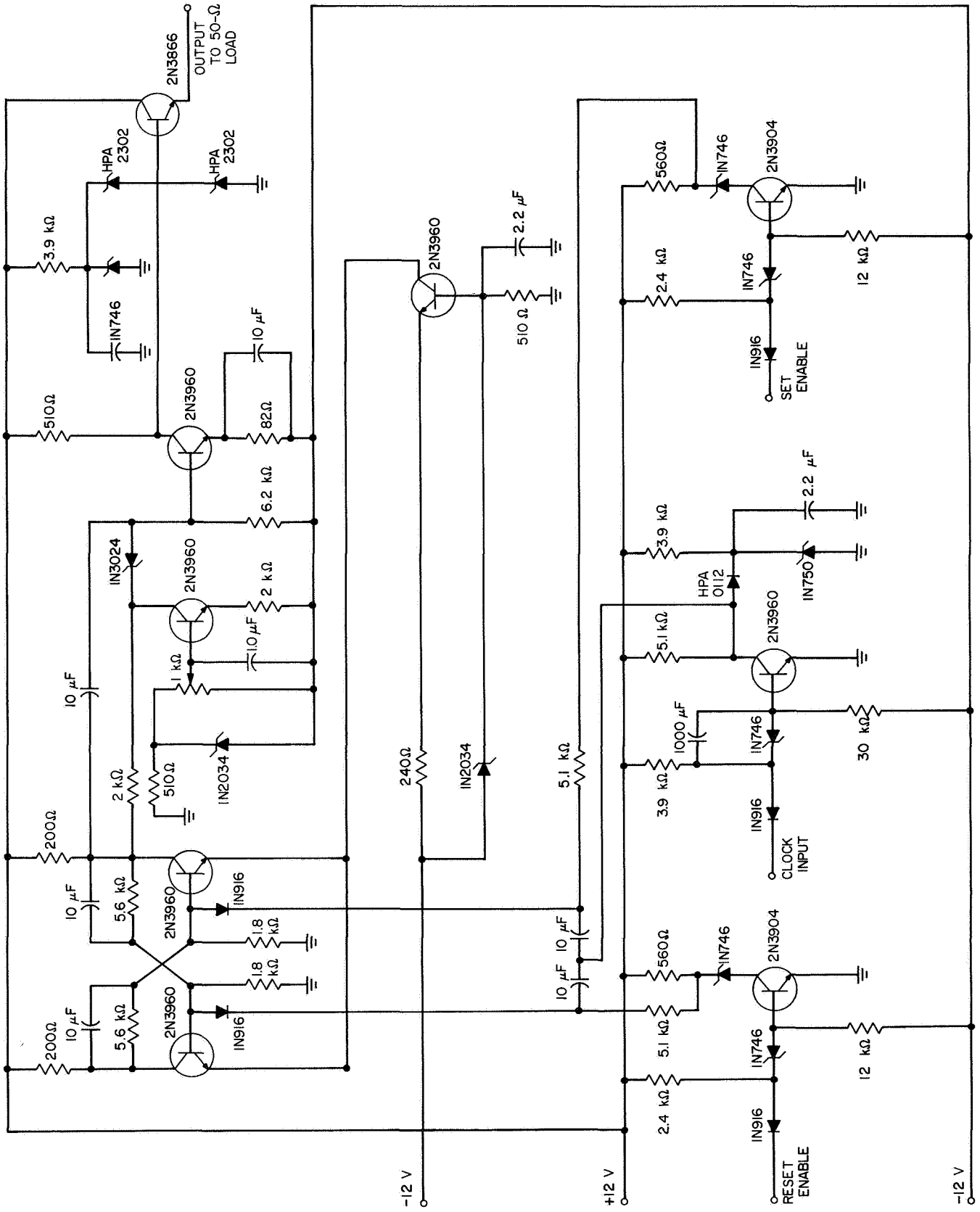

Fig. 25. High-precision, 50-Ω line driver

and data handling (TDH) system. Most were sinusoidal in character. However, some—notably the TDH commands —were single pulses approximately 20 V in amplitude. Even the doppler signals tended to vary in amplitude from one detector to another, depending upon the load. Thus, it was necessary to design a general-purpose threshold detector that could accommodate any of these signals and provide a clean square wave suitable for use in the standard digital modules.[4]

Figure 24 shows the threshold detector used in the ranging equipment. It not only provides a high input impedance (approximately 40 kΩ for small signals), but can also accommodiate a wide range of input amplitudes (from 0.1 to 7 V rms). Furthermore, a threshold adjustment is provided for the control of the output duty cycle. This threshold control changes the bias and, hence, the switching point on the first stage of a trigger circuit. Nonsaturating amplifiers were used throughout to facilitate high-speed operation.

Card alignment is accomplished by first setting the gain control to provide a 6-V peak-to-peak signal at the collector of the first linear amplifier, and then adjusting the threshold to provide the desired symmetry in the output waveform.

Two circuits are packaged on a single standard-module[4]-size card. Controls, as well as the BNC input connectors, are located to the rear of the card, while outputs are via the designated pins on the front.

6. High-Precision, 50-Ω Line Driver

To achieve the required carrier suppression, very rigid specifications were placed on the bit symmetry of the transmitted code. It was determined that a minimum *one–zero* asymmetry of less than 0.1% was necessary. Present line drivers were doing well to achieve 1%, and most fell into the 1 to 5% category. A development program was undertaken to design a circuit with the required characteristics.

A diagram of the line driver appears in Fig. 25. At the heart of the system is a high-speed, current-mode flip-flop employing transistors with a frequency cutoff f_T of 1800 MHz. Switching speeds are on the order of 2 to 3 ns, and loop delay is virtually nonexistent. The flip-flop is enabled in the conventional manner with the aid of isolation amplifiers whose inputs are connected to the ranging coders. A high-speed clock amplifier with a hot-carrier diode clamp provides a sharply defined trigger pulse.

[4]JPL Division 33 standard digital modules.

The flip-flop's output is amplified and clamped to provide the desired amplitude. An adjustable current source controls the bias and, hence, the dc output level from the amplifier. Changing the current setting alters the operating point of the amplifier and has a direct bearing on the symmetry of the output waveform. The circuit is designed to achieve virtually perfect symmetry with proper adjustment of the current source.

An emitter-follower current amplifier is used to provide a low output impedance for driving a coaxial cable. The unit has been tested with cable lengths up to 200 ft, with no apparent degradation in the signal quality.

7. Results

These circuits have been operating in the *Mariner* Venus 67 ranging equipment at DSS 14 (Goldstone Mars) since June 1967. Despite a rather hostile environment, all equipment has performed satisfactorily.

J. *Mariner* Venus 67 Ranging: DSS 14 RF Delay,

D. Sanger

1. Introduction

The *Mariner* Venus 67 R&D ranging system, which has recently been installed in the alidade room at DSS 14 (Goldstone Mars), is capable of measuring the range to *Mariner V* at planetary distances with very high precision. This accuracy, however, depends upon the precise determination of the station RF delay. At the standard 85-ft-diam antenna sites, this delay is obtained by ranging over a surveyed path to a collimation tower. However, this procedure cannot be used at DSS 14 since a collimation tower (if one existed) would be in the near field of the 210-ft-diam antenna. Therefore, an alternate method for measuring the station delay was developed, and is discussed in this report.

2. Analysis

The true (two-way) range R from DSS 14 to a spacecraft is defined as the linear distance measured from the station position to the spacecraft. The station position is defined as the intersection of the elevation and azimuth axes. Referring to Fig. 26,

$$R = 2(r + a + c) \tag{1}$$

When measured with the R&D ranging system, this range is a combination of several factors.

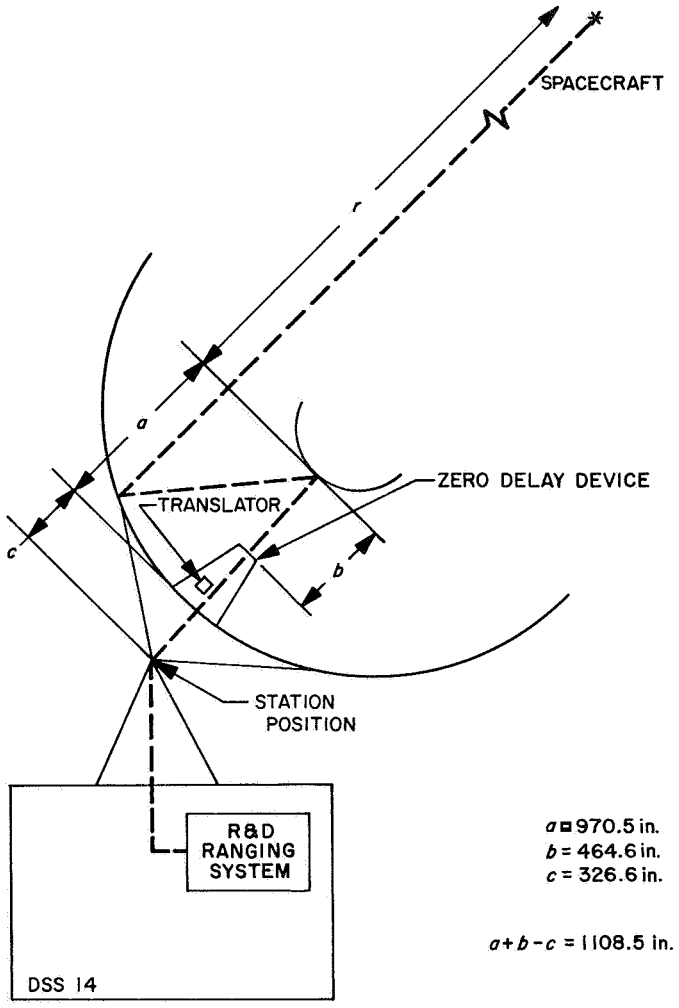

Fig. 26. Physical dimensions of DSS 14

If

R_c = two-way range from the ranging system (alidade room) to the Mylar protective window on the feed cone and return

R_m = two-way range to a spacecraft as measured by the R&D ranging system

then

$$R_m = R_c + 2(b + 2a + r) \tag{2}$$

The difference between the measured range and the true range is the station delay Δ:

$$\begin{aligned}\Delta &= R_m - R \\ &= R_c + 2(b + a - c)\end{aligned} \tag{3}$$

The station delay should be measured as part of the pre-pass calibration of the R&D ranging system. This requires measuring R_c by ranging to a frequency translator located on the Mylar protective window of the feed cone — a capability that does not exist with the present station configuration. However, since a DSS translator located near the base of the cone is a standard part of the station test equipment, the measurement of R_c may be divided into two segments:

Let

R_t = two-way range from the alidade room ranging system to the DSS translator

R_{tc} = two-way range from the DSS translator to the Mylar window on the cone

Then

$$R_c = R_t + R_{tc} \tag{4}$$

If this new definition is used for R_c in Eq. (3), the station delay can be redefined:

$$\Delta = R_t + R_{tc} + 2(a + b - c) \tag{5}$$

When the physical dimensions on the antenna are evaluated, assuming the free space velocity C (where $C = 2.997 \times 10^8$ m/s), Eq. (5) becomes

$$\Delta = R_t + R_{tc} + 188 \text{ ns} \tag{6}$$

R_t can be determined during the pre-pass calibration. The remainder of this report describes a test that was conducted at the Mars DSS to determine R_{tc}, which may be regarded as nearly constant for a fixed klystron power level.

3. Determination of R_t, R_c, R_{tc}

The frequency translator used in ranging to the Mylar surface of the feed is a battery-operated zero-delay device (ZDD) used to calibrate the Mark I ranging system. However, when used with an S-band test horn antenna, the ZDD provides ranging power in excess of the receiver threshold.

One of the requirements for ranging to the Mylar window is that the power output of the klystron be at 20 kW, since the delay through the klystron is a function of the beam voltage. However, the power at the crystal diode mixer in the ZDD cannot exceed 0.5 W without diode failure. The solution is to utilize the leakage across the

SWS-2 waveguide switch (60-dB isolation) into the horn antenna while the klystron is radiating into the water load. This test configuration is shown in Fig. 27.

This test was recently performed at the Mars DSS. The following values were measured for R_t and R_c:

$$R_t = 33 \text{ ns}$$

$$R_c = 190 \text{ ns}$$

Then, from Eq. (4),

$$R_{tc} = 157 \text{ ns} \quad (7)$$

and, from Eq. (6),

$$\Delta = R_t + 345 \text{ ns} \quad (8)$$

4. Error Analysis

If it is assumed that the ranging equipment can range on the station translator with a known accuracy, the probable errors in this method can be attributed to the measurement of R_{tc} (i.e., $R_c - R_t$) and the evaluation of the duplication in path length on the antenna ($b + a - c$).

With respect to errors in R_{tc}, the waveguide used over the path from the translator to the surface of the cone is WR 430. At 2115 MHz, the propagation velocity in the guide is 0.75684 C. R_{tc} was measured at 157 ns, which is a one-way distance of 58.4 ft. The waveguide run is approximately 45 ft in length and includes several switches and bends. In addition, the klystron amplifier is in this path, causing additional delay. This has not been measured at 20-kW power output, but is approximately 5 ns.[5] Thus, the measured R_{tc} (58.4 ft) is close to the approximate RF distance (50 ft).

Values for a, b, and c were obtained from the antenna structural drawings and are specified to the nearest inch.[6] In converting the distance to range time, the free space velocity of propagation was used. The error in this method should be negligible.

K. A Random-Number Package for the SDS 920/930 FORTRAN II and Real-Time FORTRAN II Systems, *J. W. Layland*

1. Introduction

Monte Carlo experiments, simulation of complex systems, and data generation for the testing of hybrid systems

[5]Private communication to the author from R. L. Leu, JPL Section 335.

[6]Private communication to the author from R. J. Wallace, JPL Section 335.

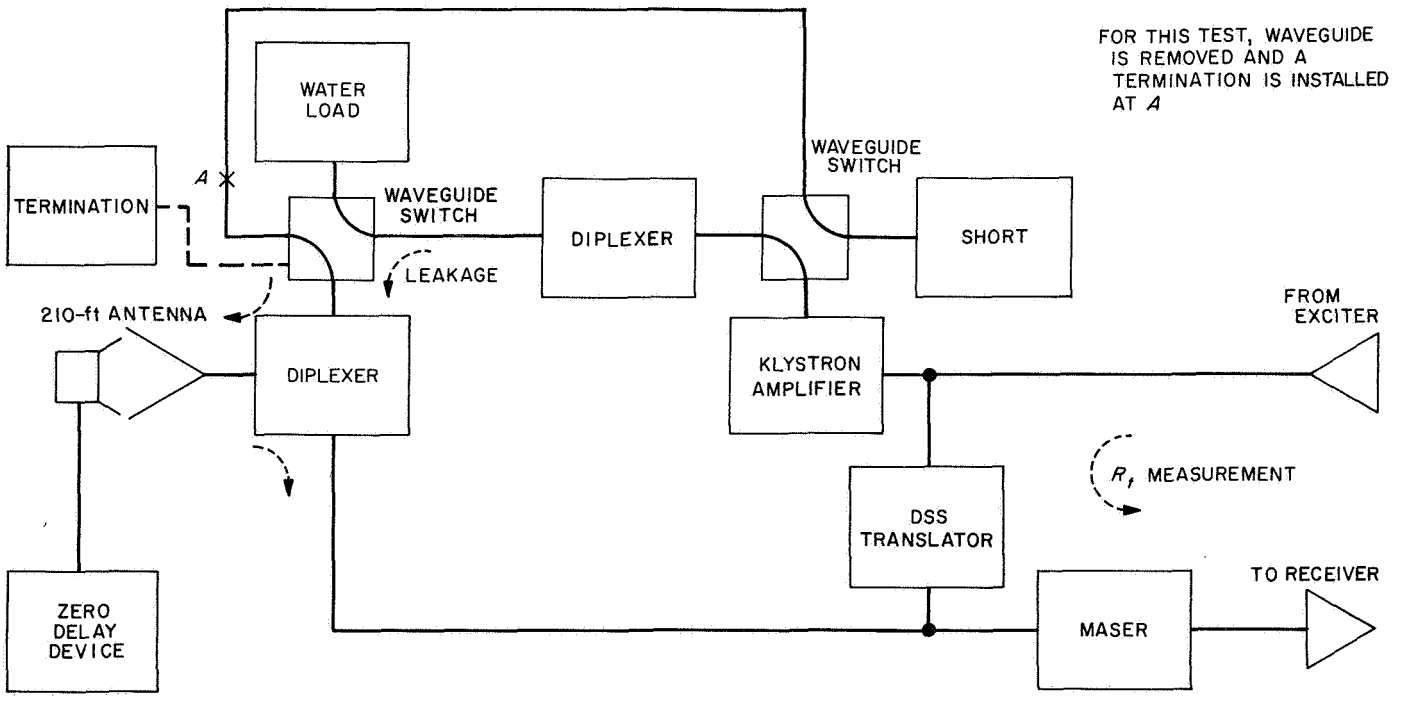

Fig. 27. DSS 14 transmitter and receiver

are all situations in which it is desirable to systematically generate large numbers of pseudorandom variables. Tausworthe (Ref. 5) has described a method for the generation of uncorrelated uniform (0,1) random variables using recurrence modulo-2, and Kendall (SPS 37-34, Vol. IV, pp. 296–298) subsequently developed an efficient program for the execution of one such random-number generator on SDS 900-series computers. This article describes a machine-language subroutine for the SDS FORTRAN-II systems which will generate either uniform or Gaussian pseudorandom numbers. The uniform numbers are generated using Kendall's program and are returned to the calling program in floating-point format. The transformation of Box and Muller (Ref. 6) is used to produce Gaussian variables of zero-mean and unit variance.

2. Program Calls

The random-number package may be addressed by any of the following calls:

CALL GAUSS(X) or X = GAUSS(D) (D is any dummy); X (and D) becomes a Gaussian random variable of zero-mean and unit variance.

CALL GAUS2(X,Y); X and Y become an independent pair of Gaussian random variables $N(0,1)$.

CALL PNRN(X,Y); X and Y become an indepent pair of 23-bit floating uniform (0,1) random variables.

CALL PNGN(X) or X=PNGN(D); X (and D) becomes a 38-bit floating uniform (0,1) random variable.

CALL PIX(K,L) and CALL PAK(K,L); PIX and PAK together enable the programmer to halt a sequence of random numbers and resume at the termination point when the program is reloaded. PIX gives K and L the values of the current numbers in the PN generator. PAK gives the PN generator the numbers K and L in place of the basic initialization.

3. The Numbers and Their Properties

The basic PN number generator uses the recurrence relation $a_k = a_{k-42} \oplus a_{k-47}$ to generate a pseudorandom sequence of binary digits $2^{47} - 1$ digits long. If any 47 consecutive digits are treated as the binary expansion of a real-number fraction, that fraction is uniformly distributed (0,1). The normalized correlation between any $[(2^{47} - 1)/47]$ consecutive fractions is $\approx -1.5 \times 2^{-46}$. Furthermore, if the 47 consecutive bits are divided into N disjoint sets, the N numbers obtained by treating these sets of bits as binary fractions form an N-vector which is uniform over the N-dimensional unit cube (0,1).

4. Program Operation

When the program is called to generate a random number, the current 47-bit number in the generator (the state vector) is obtained, and the mod-2 recurrence executed to obtain the next (disjoint) 47-bit number. This new number replaces the original state vector and is processed for output according to the particular call. For PNGN, the new PN number is normalized, the exponent loaded (destroying the least-significant 0–9 bits), and the floating result returned to the calling program. The mean value of these numbers is $\approx \frac{1}{2}(1 - \frac{1}{3} \times 2^{-38})$, their mean-squared value is $\approx \frac{1}{3}(1 - 2^{-46})$, and the correlation between any $[(2^{47} - 1)/47]$ consecutive numbers is $\approx -2^{-49}$. If the call is to PNRN, a round-off bit is appended to the first 23 bits of the new PN number, and these are floated to become the first call variable. The last 23 bits of the PN number are rounded and floated to become the second call variable. These two variables are independent, each with mean value ½ and mean-square value $\frac{1}{3}(1 + 2^{-47})$. Figure 28 is a two-dimensional scatter diagram of the paired numbers returned by PNRN(U_1, U_2). Correlation between numbers returned by $[(2^{47} - 1)/47]$ consecutive calls is $\approx -2^{-49}$.

Calls to GAUS2 are deferred to PNRN. Let U_1 and U_2 denote the two uniform numbers returned by PNRN, and N_1 and N_2 the numbers to be returned by GAUS2. The following transformation is performed (see Ref. 6):

$$\left.\begin{aligned} N_1 &= \sqrt{-2 \cdot \log(U_1)} \cdot \cos(2\pi \cdot U_2) \\ N_2 &= \sqrt{-2 \cdot \log(U_1)} \cdot \sin(2\pi \cdot U_2) \end{aligned}\right\} \quad (1)$$

Figure 29 is a scatter diagram of N_1 versus N_2. By virtue of their uniformity over the unit square, U_1 and U_2 independently take on all numbers of the form $2^{-23} \cdot (j + \frac{1}{2})$,

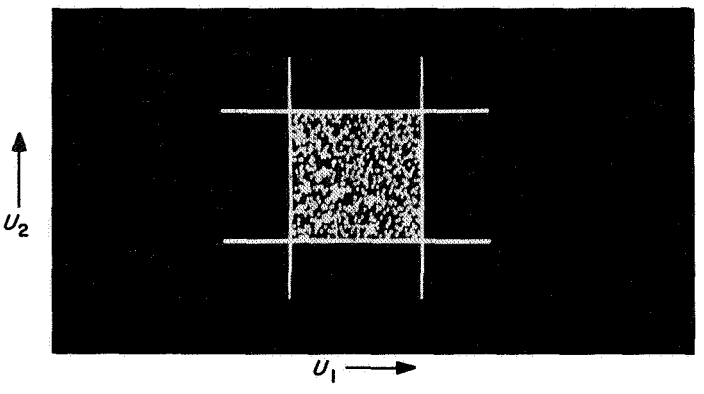

Fig. 28. Two-dimensional scatter diagram of U_1 and U_2, 1000 samples

$j = 0,1, \cdots, 2^{23} - 1$. Thus, the mean value of N_1 or N_2 is *zero* and the correlation between N_1 and N_2 is *zero*. The mean-squared value of either is given by:

$$N_1^2 = \left[2^{-23} \sum_{j=0}^{2^{23}-1} - 2\log\left(\frac{j+\frac{1}{2}}{2^{23}}\right)\right] \cdot \left[2^{-23} \sum_{k=0}^{2^{23}-1} \cos^2\left(2\pi \frac{k+\frac{1}{2}}{2^{23}}\right)\right]$$

$$= -2^{-23} \sum_{j=0}^{2^{23}-1} \log\left(\frac{j+\frac{1}{2}}{2^{23}}\right)$$

$$= 23\log(2) - 2^{-23}\log\left[\Gamma(2^{23}+\tfrac{1}{2})/\Gamma(\tfrac{1}{2})\right]$$

$$\approx 1 - 2^{-24}\log 2 - \tfrac{1}{3} \times 2^{-48} \qquad (2)$$

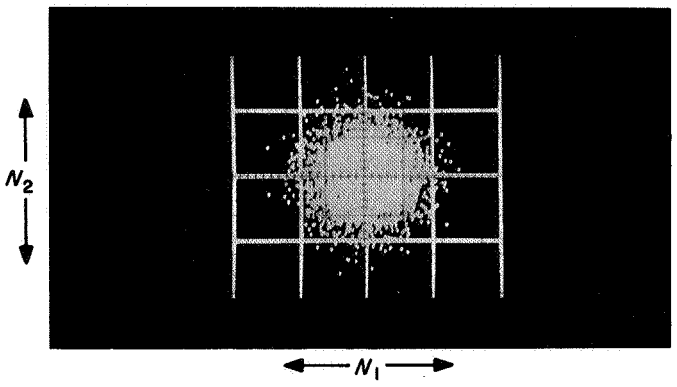

Fig. 29. Two-dimensional scatter diagram of N_1 and N_2, 5000 samples

Figure 30 is an experimental density function for the Gaussian numbers. The correlation between the Gaussian numbers returned by consecutive calls has been shown by experimentation to be small. Figures 31 and 32 are sample autocorrelation functions of the Gaussian numbers. The curve of Fig. 31 involves all numbers generated, while Fig. 32 was generated using only the first number of each pair. In addition, the four interesting plane projections of the four-dimensional distribution of N_1, N_2 and N_1', N_2', returned on two consecutive calls to GAUS2, are shown in Fig. 33. The planes shown are $N_1 \times N_1'$, $N_1 \times N_2'$, $N_2 \times N_1'$, and $N_2 \times N_2'$. N_1, N_2 and N_1', N_2' have been shown to be pairwise independent, and the evidence implies that, for all practical purposes, the same is true for the entire sequence of numbers, or for at least $(2^{47}-1)/47$ of them. The first eight moments of the Gaussian numbers have been estimated with a sample size of 10,000. A comparison of these estimates with the true values for a Gaussian variable is shown in Table 10. Subroutine GAUSS calls GAUS2 and returns the Gaussian numbers one at a time instead of pairwise.

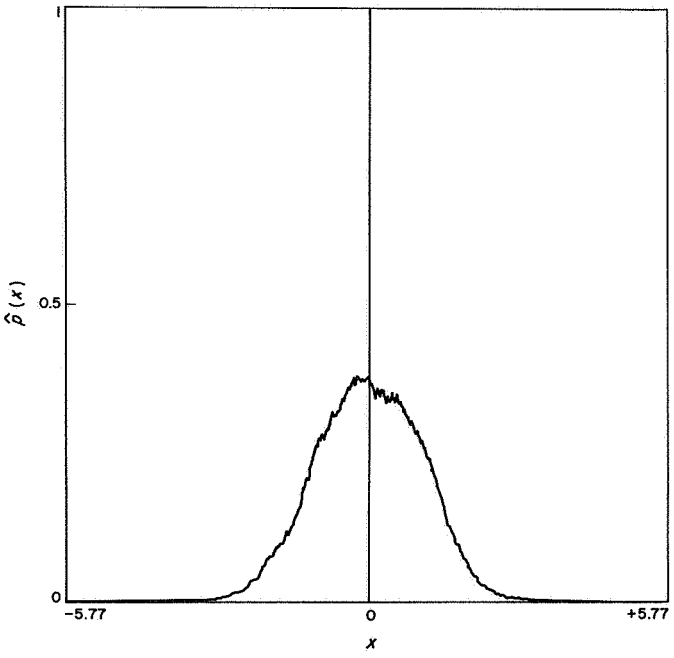

Fig. 30. Experimental density function for the GAUSS numbers, using 2500 samples

Table 10. Moments of the Gaussian numbers

Moment	10,000 sample estimate	True value
1	−0.014	0
2	1.02	1
3	0.004	0
4	3.1	3
5	0.106	0
6	15.5	15
7	0.28	0
8	105.9	105

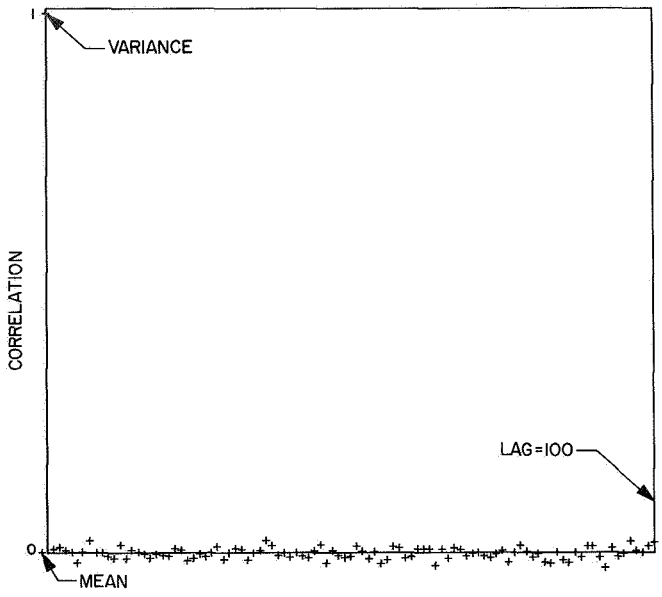

Fig. 31. Correlations of the GAUSS numbers for 10,000 samples: mean, variance, and covariance at lags to 100

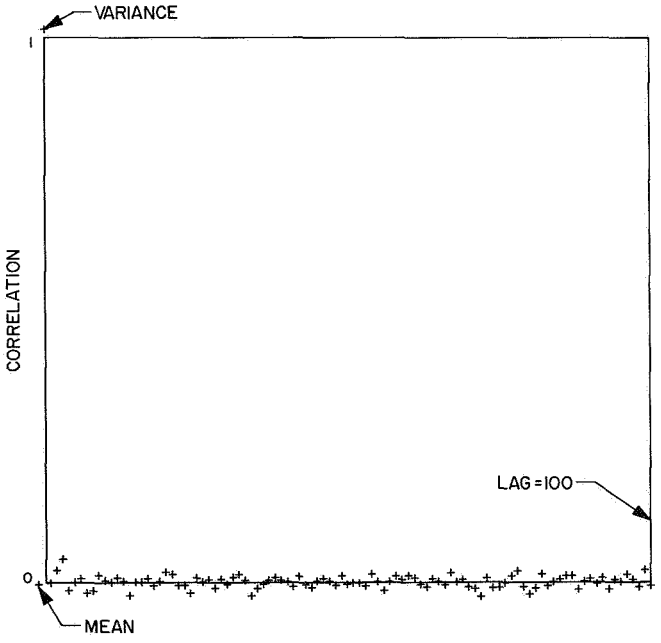

Fig. 32. Correlations of the GAUSS numbers for 10,000 samples: first of pair only

Timing for the generation of the Gaussian numbers is approximately 6 ms per pair on an SDS 930. Most of this time is consumed by the floating-point arithmetic and the library routines ALOG, COS, and SQRT used in the transformation (Eq. 1).

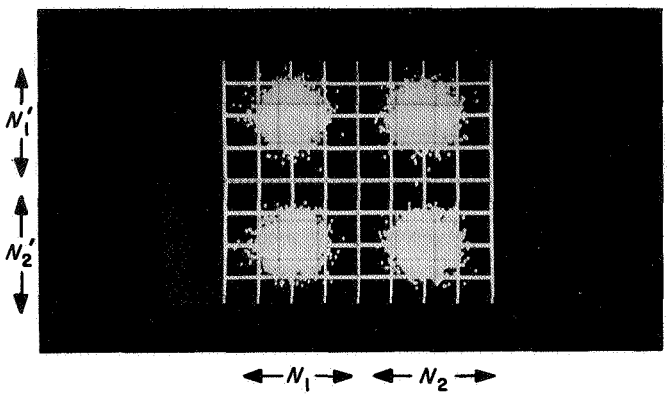

Fig. 33. Four projection planes of the four-dimensional scatter diagram of N_1, N_2, N_1', and N_2', 5000 samples

L. Planetary-Radar Spectrum Analysis Program, *G. Morris, Jr.*

1. Introduction

A program for automatic control of real-time planetary-radar spectrum analysis on the SDS 930 computer has been written in the SDS real-time FORTRAN (RTF-II) language. The advantages of using RTF-II to generate programs such as this are the great time savings in initial program writing and debugging, and the ease with which the program can be modified as requirements change.

The SDS 930 computer at DSS 13 controls a nine-channel autocorrelator (SPS 37-26, Vol. III, p. 37) and receives control signals from the Mod III stored program controller (SPC), as shown by a block diagram in Fig. 34. The correlator can be operated in a nine-channel mode with 51 lags per channel, or a single-channel mode with 459 lags per channel. The correlator accumulates the number of agreements between the present input level (either +1 or −1 limiter output) and previous input levels. The *zero*th lag compares the present signal level with itself (and, therefore, is always in agreement) and

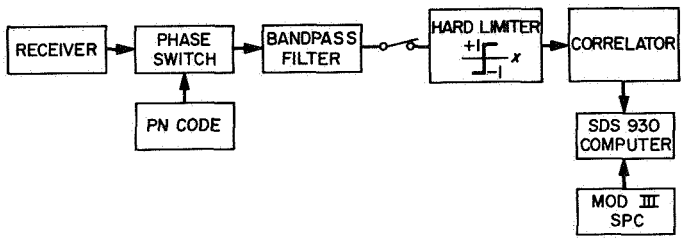

Fig. 34. Planetary spectrum analysis block diagram

merely records the number of samples taken. Lag 1 contains the number of agreements between the present sample and the last sample. The nine channels are used to correlate the signal against nine adjacent phases of a pseudo-noise (PN) code to determine the spectrum of energy in adjacent range zones, since the power correlated with adjacent phases of the PN code is separated in range by the corresponding time displacement of one bit of the PN code. A spectrum is computed for each channel, with adjacent channels corresponding to adjacent range zones on the planet. The SDS 930 computer can start, stop, and read the contents of the correlator. The signals sent to the SDS 930 from the Mod III SPC consist of the status of two output flip-flops whose states indicate the periods during which the correlator should be collecting noise and signal data.

2. Automatic and Manual Control

In the automatic mode, SPC flip-flops are tested 10 times per second by the SDS 930 program on interrupt from the SDS 930's real-time clock. The SDS 930 generates an interrupt to itself if a flip-flop has changed state since the last time tested.

Manual control of the program is effected by inserting control messages into the SDS 930 typewriter or by using two interrupt pushbuttons. All control messages are four letter combinations as shown and explained in Fig. 35. The interrupt pushbuttons allow the operator to (1) stop the correlator and inhibit the automatic mode of operation, and (2) start the automatic mode of operation. With these pushbuttons, the operator can quickly change control during operating difficulties such as programmed local oscillator off-frequency or antenna off-target. The *stop-correlator-and-inhibit-automatic-mode* pushbutton is connected through interrupts to the ABORT subroutine (see flow chart in Fig. 36). The *start-automatic-mode* pushbutton is connected to the RESTART subroutine (see flow chart in Fig. 37). It should be noted that messages indicating all action taken are automatically typed to maintain a permanent record of all operations.

```
C  CORI= CORRELATOR INITIALIZE
C  PLTC= PLOTTER CALIBRATE
C  ESFN=  ENTER SCALE FACTOR NUMBER
C  EIDN= ENTER ID NUMBER
C  SPUL= SET PLOTTER TO UPPER LEFT
C  ZERO= ZERO ACCUMULATED CORRELATOR NUMBERS
C  STOP= STOP CORRELATOR
C  INPN= INPUT NOISE RUN FROM CORRELATOR
C  INPS= INPUT SIGNAL RUN FROM CORRELATOR
C  DRIC= DRAW INCREMENTAL SPECTRUM
C  DRAC= DRAW ACCUMULATED SPECTRUM
C  INHD= INHIBIT DRAWING
C  TIAI= TRANSFER INCREMENTAL TO ACCUMULATED IMMEDIATELY
C  PACI= PUNCH ACCUMULATED CORRELATOR NUMBERS IMMEDIATELY
C  INHA= INHIBIT AUTOMATIC TRANSFER OF INCREMENTAL TO ACCUMULATED
C  PAZA= PUNCH AND ZERO ACCUMULATED CORRELATOR NUMBERS AUTOMATICALLY
C  IMD3= INHIBIT AUTOMATIC CONTROL FROM THE MOD 3
C  EMD3= ENABLE AUTOMATIC CONTROL FROM THE MOD 3
C  1CHL= ONE CHANNEL OF 459 LAGS
C  9CHL= 9 CHANNELS OF 51 LAGS
C  STRT= CORRELATOR START
```

Fig. 35. Manual control commands

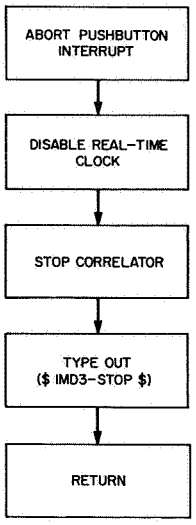

Fig. 36. ABORT subroutine

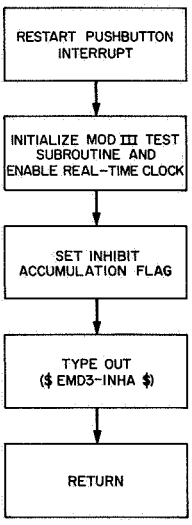

Fig. 37. RESTART subroutine

3. Program Operation

The flow of the program under normal automatic control is as follows: The SDS 930 computer program is put into the automatic mode by either depressing the *restart* pushbutton or typing *enable Mod III automatic control* (EMD3) shortly after starting a transmit cycle. The CLOCK subroutine (flow chart in Fig. 38) detects that the Mod III flip-flop indicating *collect noise data* has

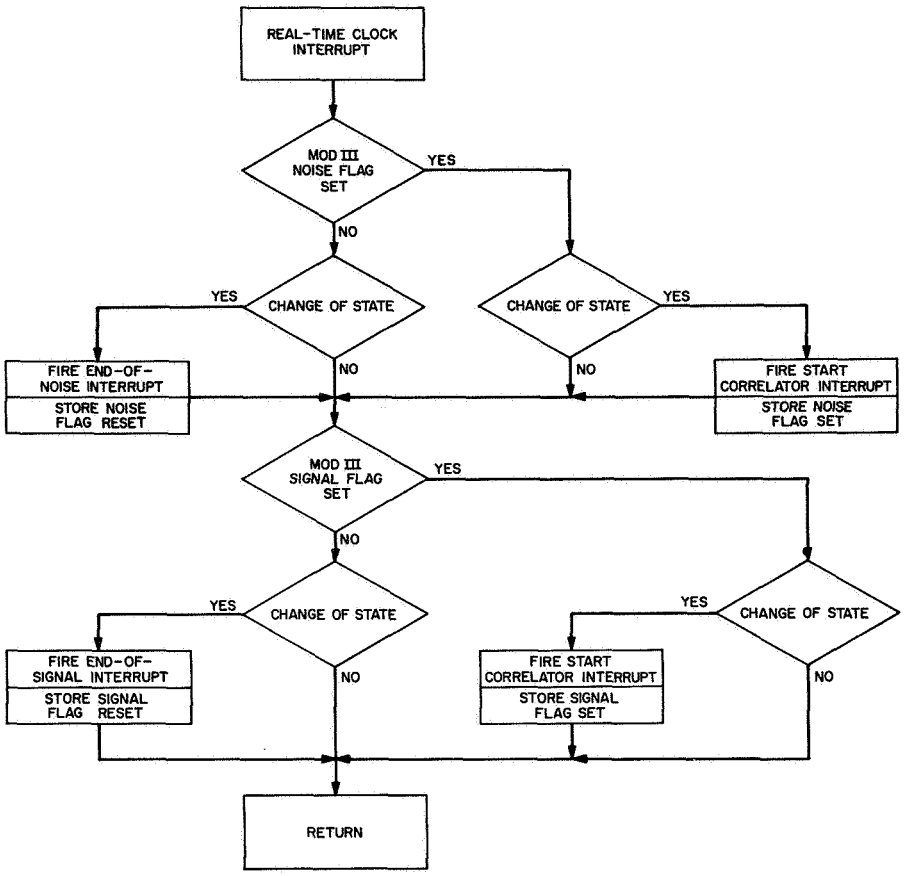

Fig. 38. CLOCK subroutine

changed from reset to set; therefore, the *start-correlator* interrupt is fired. The *start-correlator* interrupt is connected to the START-CORRELATOR subroutine (flow chart in Fig. 39) that starts the correlator. When the Mod III *noise* flip-flop resets, the CLOCK subroutine fires the *end-of-noise* interrupt. The *end-of-noise* interrupt is connected to the END-NOISE subroutine (flow chart Fig. 40). When the Mod III *collect-signal* flip-flop sets, the CLOCK subroutine again fires the *start-correlator* interrupt. When the Mod III *signal* flip-flop resets, the CLOCK subroutine fires the *end-of-signal* interrupt. The *end-of-signal* interrupt is connected to the END-SIGNAL subroutine (flow chart Fig. 41).

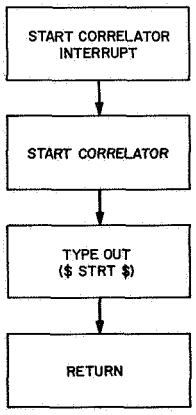

Fig. 39. START CORRELATOR subroutine

The subroutine that "reads" the correlator subtracts the last count read from the correlator from the present count to obtain the new correlation number. This technique does not require the correlator to be cleared to *zero* after each signal and noise run. If the differenced correlation number is negative, it is assumed that overflow has occurred in the correlator, and the lost carry bit is added in the SDS 930 to correct the overflow. In the initialization of the program, the correlator is read once to provide an initial count for the program so that it is never necessary to clear the correlator.

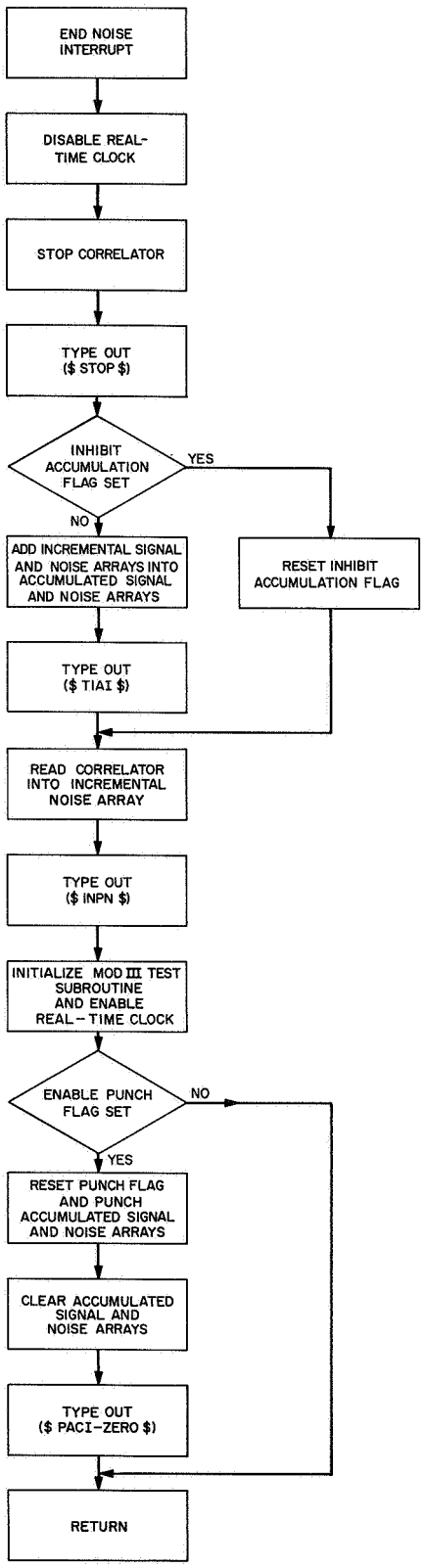

Fig. 40. END NOISE subroutine

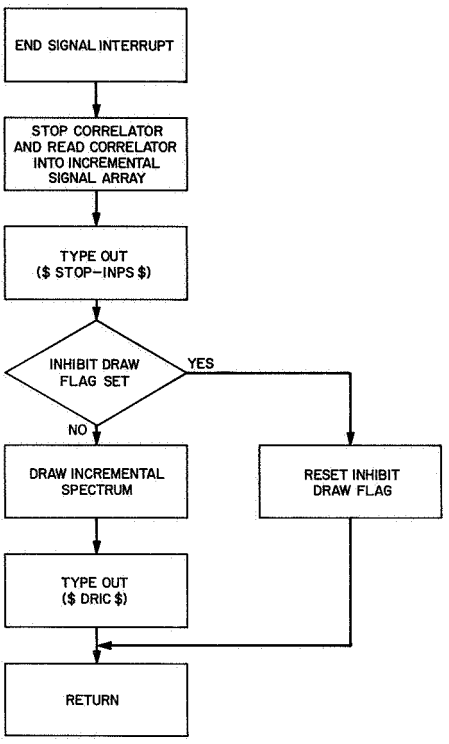

Fig. 41. END SIGNAL subroutine

There are five FORTRAN fixed-point arrays associated with numbers read from the correlator: One array contains the last count of the correlator, as explained above. The output numbers from the correlator (corrected for overflow, if necessary) are stored first into one of two *increment* arrays (one for signal, one for noise) that hold the data from one transmit-receive cycle. A spectrum from these incremental data is drawn on the *X-Y* plotter so it can be examined by the operator. If the data appear to be good, the operator does nothing, and the contents of the *increment* arrays will automatically be added into the accumulated signal and noise arrays at the end of the transmit cycle. If the incremental spectrum appears unsatisfactory, the operator types a command that inhibits the transfer of these data to the accumulated arrays. The operator may draw the spectra of the accumulated array at any time by typing the command DRAC. The accumulation of several transmit-receive cycles improves the signal-to-noise ratio and decreases the amount of data returned to the laboratory for further data processing.

While the program is operating in the automatic mode, each automatic operation is followed by automatic typed output of the corresponding manual control word that would have been used had the operator been operating

manually. The message automatically output is identical to the manual input control messages except that it is enclosed within ($\cdots$). This technique allows later reconstruction of the sequence in which data are taken, since all commands, automatic or manual, appear on the typewriter output. These typed output pages are retained for future reference should any question arise concerning the sequence of operations used to acquire data.

4. Real-Time FORTRAN

The SDS RTF-II language is basically the same as FORTRAN II, with the addition of special instructions to handle interrupts and interrupt subroutines.

The special instructions available in RTF-II include the following:

CONNECT subroutine (arg 1, arg 2, $\cdots$, arg m), n: This statement causes the subroutine named after the *connect* statement to be called when interrupt n occurs.

CALL RELEASE (n): This subroutine releases any subroutine that is set up to be called by interrupt n, and connects it to a do-nothing routine.

CALL ASSIGN (n): This subprogram assigns n as the maximum number of system interrupts above 0200 that will be used by the RTF-II system.

CALL ARM ($n_1, n_2, \cdots, n_j$): This subprogram arms the interrupts specified by $n_1, n_2 \cdots, n_j$. Here $0200 \leq n_i \leq 0217$.

CALL DISARM ($n_1, n_2, \cdots, n_j$): This subprogram disarms the interrupts specified by $n_1, n_2, \cdots, n_j$.

CALL CONDITION: This subprogram disarms all system interrupts and releases any subroutines connected to them. Input/output interrupts are not disturbed.

5. CARD OUTPUT Routine

This subroutine outputs the correlator numbers from the accumulated signal and noise arrays in a compact format. The single-channel output format and the nine-channel output format are shown respectively in Figs. 42 and 43, where the cards have been listed on a line printer.

In both formats, the correlator numbers are packed into the first 72 columns of the card. The numbers punched on the cards are not actually the accumulated numbers from the correlator except in the case of the *zero*th lag, which counts the number of samples taken. The other numbers punched are the actual numbers minus one-half the *zero*th lag number. This technique results in an excellent compression of data, because under low signal-to-noise ratios all the other lags are approximately one-half the *zero*th lag. Each number is preceded by a blank if positive and a minus if negative. If the number is *zero*, only a blank is punched for that number. A number may continue from column 72 of one card to column 1 of the next card. This packing technique reduces the average number of cards generated by approximately 40%. The last eight columns (73–80) are used to identify the data. In both modes, the letter in column 73 identifies the target, such as V for Venus. The experiment number is shown in columns 74–76. The accumulated noise array numbers are identified by an N in column 78. The signal numbers are identified by an S in column 78.

In the single-channel mode (Fig. 42), column 77 contains a C unless this card is the last card of the signal or noise array, in which case column 77 contains a D. Columns 79–80 contain the card count of either the signal or noise output.

In the nine-channel mode (Fig. 43), column 77 contains an A unless this card is the last card of the signal or noise array for that zone, in which case it contains a B. Column 79 identifies the zone number for signal or noise. Column 80 contains the card count for a single zone of signal or noise. The card count starts at *zero* in either mode.

By typewriter command, the operator may call for data to be punched. He can then clear the accumulated signal and noise arrays or not, as he chooses. There is an automatic feature in the program that punches cards and clears the accumulated arrays before overflow can occur. With a 100-Hz bandwidth, it would be possible to accumulate alternate signal and noise data for more than 23 hours before overflow could occur.

6. DRAW Routine

This subroutine draws out the spectrum of the received signal—either single channel or nine channel. In the single-channel mode, only the first 51 of the 459 lags are used in computing the spectrum.

The signal spectrum is divided by the noise spectrum to obtain the true received signal spectrum. This correction is computed separately for each channel in order to remove the response of the filter from the displayed

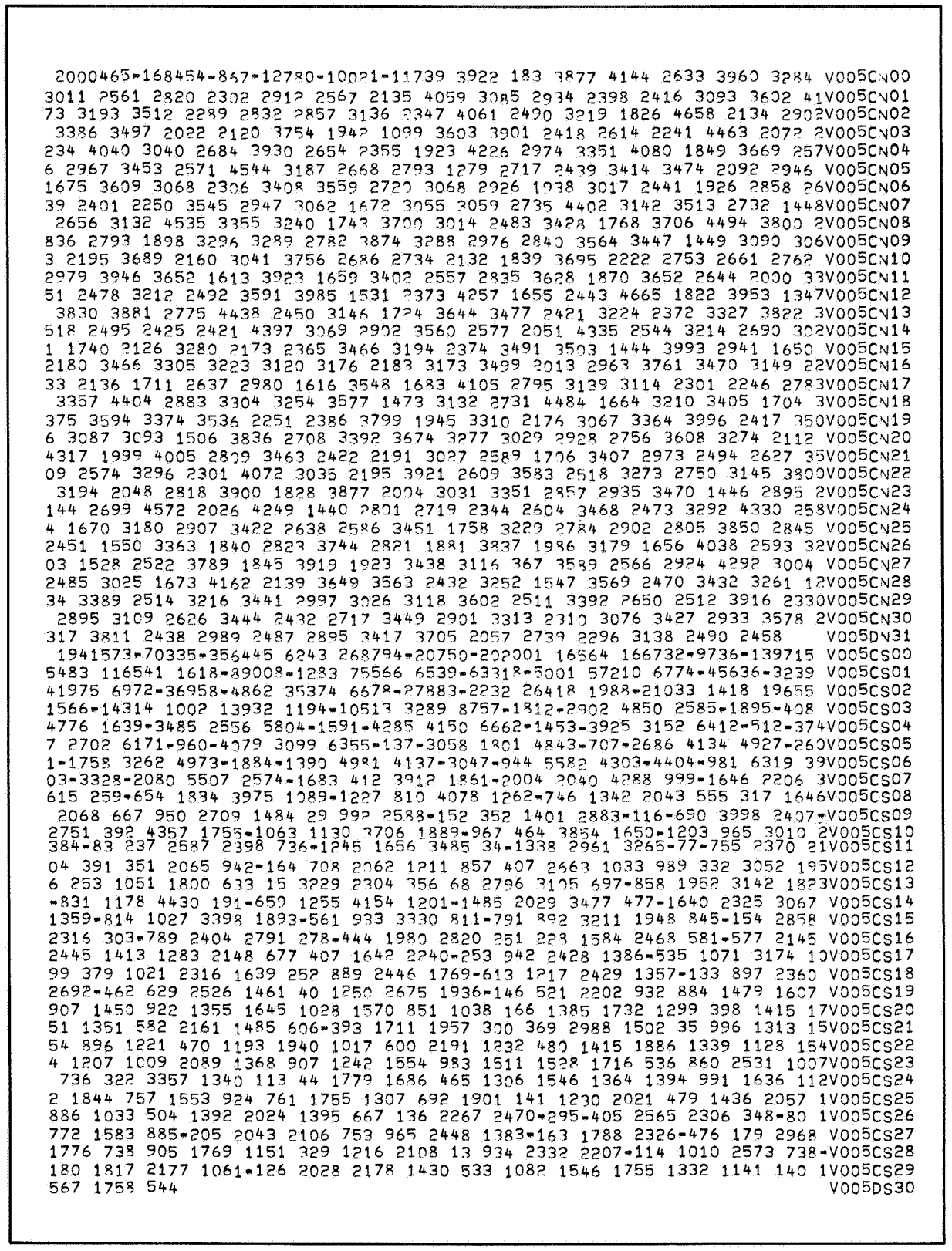

Fig. 42. Single-channel card format

```
 408559-11768-21476-8828-9371-5319-4022-275-12 4298 1928 2770 780 1082 1V397AN10
9 818-455 643 255 269 324 870 532 4 966 1072 259 265 236 660 50 448 1024V397AN11
 702 774 446 997-348 168 473 398 235 744 223 878 672 503 186 563 197 131V397AN12
8                                                                       V397BN13
 422417-12537-28389-5589-12532-6089 1687-961 2433 4609-2553 3756-1470 32V397AS10
 2276 289 1601 321-2087 274-1498 168 3068-100 2232 821-2091 581-330 480 V397AS11
1863 942 781-18-730-229-41 105 1631 280 2246 972-880-482-143 1208 1910-2V397AS12
27 386 1259-829                                                         V397BS13
 408559-10888-14994-7792-12611-3711-4656-2779-3548 2991-460 4342 288 294V397AN20
0 441 1275-244 1169 370 453 278 392 336 996 741 473 313 1096 716 284 602V397AN21
 701 1029 421-43 370 734 460 718 972 809 701-334 357 876 350 198 727 402V397AN22
 435 865                                                                V397BN23
 422417-10954-21074-5595-17258-3074-1566-3713 507 2133-1576 4183-2259 29V397AS20
86 687 1083 1786-37-281 746-2568 656 429 178 3091 449-153 948-1024-268 2V397AS21
18 379 1745 315 1428-63-281 93-250 319 1410 1003 543 146-189 389-102 666V397AS22
 784 614 516                                                            V397BS23
 408559-10541-21378-7601-9939-5237-4888-603-579 2544 663 2651 823 1138 4V397AN30
50 193 254 299 88-137 286-44 60 161-20 477 330 281 570 565 1034-262 77 7V397AN31
84 400-260 110 316 43 167 634 698 614 670 393 395-207 499 285 232 449   V397BN32
 422417-10038-25139-5951-15410-5192-3404-822 2753 2566 1829 2906-2196 11V397AS30
82-1647-259 2112 563 1530 308-1518-221-1274-1 1219-44 1727-44 390 815-87V397AS31
0 487-509-293 1327 820 1035 50-621 919-14 148-58 294 1123-337-223 174-51V397AS32
1 637 54                                                                V397BS33
 408559-3894-18661-4167-11239-2131-7467-239-6734 2388-1711 2052-154 1549V397AN40
 916 774 823 701 732-208 770-331-2 575-75 425 658 558-7 363 315 345 282 V397AN41
354-139 122 412 275 514 476-43 357 515 613 292 820-120 620 301 500 614  V397BN42
 422417-5354-21402-1899-15700-1631-7167-1099-3786 1293 278 2734-2103 191V397AS40
1-1333 1698 1466 624 2205-300 853-311-153 380-1180 430 1095 670 1577 256V397AS41
 262 271-363-23-716 150 1423 662 1191 210-362-126 265 527-849 546 1105 7V397AS42
4 1295 383-164                                                          V397BS43
 408559-17656-17197-12654-5698-8011-1930-1454 4229 2614 3657 2099 996-31V397AN50
4-88-252 239-151 741 247 760 684 717 380 437 90 516 1040 426 477 710-47 V397AN51
368 686 260 319 591 475 567 382 149 872 926-26 143 639 739 796 144 692 5V397AN52
40                                                                      V397BN53
 422417-17079-19227-12300-9776-6885-2748-1660 5192 1886 6747 1834-86-804V397AS50
-1556 581-1096 58 1399-82 1963-517 525 523-638 1106 213 240 1009-155 176V397AS51
2-139 1010 59-32 129-4 430 523-273 762-83 933 603 527 166-902 371-24 635V397AS52
 985                                                                    V397BS53
 408559-15315-13359-12184-7244-6833-3086-1194 1037 1620 1130 1180 1336 5V397AN60
45 395 264 129-88 239-122 267 646 398 646 293 924-49 90 253 36 369-179 4V397AN61
22 701 411 137 44 939 315-98 146-530 409 421 32 213 365 506 152 743 172 V397BN62
 422417-15044-15641-12326-11281-4382-3520-1669 1169 1675 5366 1613 498-1V397AS60
190-1639 1387-1219 368 49-359 1066 135 979-54 277 151-490 1016-1017 131 V397AS61
599-134 982-8 404 724-692-376-260 268 202 300 335 83 764 238 882 132-208V397AS62
-129-1                                                                  V397BS63
 408559-12159-15597-14197-10484-2916-4822 4136-928 4240-833 2515-489 104V397AN70
2-272-296-434 433-63 37 566 118 242 384 916-201-402 442 263 380-233 73 4V397AN71
75 275 819 55-362 70 78 516 201-268 10 357 359 83-344 35 429 614 671    V397BN72
 422417-11166-17206-15525-13088-853-5835 2935-1599 3718 1839 2201 574-16V397AS70
2-1112 1281-847 902-1686-157 517 486 874-516 936 294 62-282-540 363 203 V397AS71
395 206-713 435 210 636 136-225 69 309 494-106-336-464 42 1161 283 986-2V397AS72
27-344                                                                  V397BS73
 408559 12360-20420-6130-10375-15775 4073 5665-3212 3873 252 2195-677 44V397AN80
36-77 3673 1589 2981 956 2363 847 1076 2121 2375 1782 1828 1378 1480 142V397AN81
8 2032 1938 1429 1734 1573 1790 1731 2525 1955 1499 1817 2131 1982 1892 V397AN82
1913 1400 1489 2132 1972 1563 1924 1667                                 V397BN83
 422417 13155-22201-9119-14353-15073 3812 4690-5218 3037 858 2423 1067 4V397AS80
137-922 2826 242 2719-1524 1259-331 2025 1434 842 2009 1124 2150 1693 19V397AS81
96 1181 490 556 605 1438 769 1455 1854 1307 1934 1670 559 1181 348 548 1V397AS82
156 1291 1415 886 1539 1327 1533                                        V397BS83
 408559-11366-19766-11270-7169-9239-5034 310-416 4340 1383 3097-2 1323-9V397AN90
45 634-1625 465-416 621-84 628 99 331 284-261-259 398 68 325 211 394 215V397AN91
-111 482 362 196 514-323 285 275-85 467 226 266 836 475 428-731 140 273 V397BN92
 422417-10690-20088-13018-10195-6959-6416 494-2116 4503 3059 4431 495 15V397AS90
3-16 326-918 179-1483 860-528 186-60 476 746-121 1150 48 88-729 123-96 5V397AS91
62-237-477 425 481 468-370 989 293-145 374-221 404 946-966 65-279 797 84V397BS92
```

Fig. 43. Nine-channel card format

spectrum. A constant is also subtracted from the divided spectrum to give a *zero* average spectrum outside the bandwidth of the signal. This constant is also used to obtain the signal-to-noise ratio, which is recorded on the typewriter for each zone. These calculations to give a *zero* average baseline outside the signal bandwidth are necessary, since the limiter in the signal path causes both the signal and noise to have the same total power at the correlator.

The program plots four single-channel spectra or four groups of nine-channel spectra on a page, and provides automatic positioning and chart advance. The operator may call a CALIBRATE subroutine from the typewriter, whenever necessary, to calibrate the *X-Y* plotter. A breakpoint test in the plot routine allows the operator to stop plotting and return to the control program at any time by setting breakpoint 4. The operator may change the scale of the plot to adjust for large or small signals by entering a scale factor number through the typewriter.

M. Clock Calibration via Quasar, *R. Goldstein*

This report describes an experiment designed to calibrate the time difference between distant clocks in the DSN by means of the noise radiation from a radio star. Such use of a radio star was first suggested in 1953.[7] The received noise from two deep space stations is brought together and, after allowance for the time-of-flight between the stations, is correlated. Any additional time delay required to obtain maximum correlation may be attributed to the two clocks.

[7] Goldstein, S. J., JPL internal report.

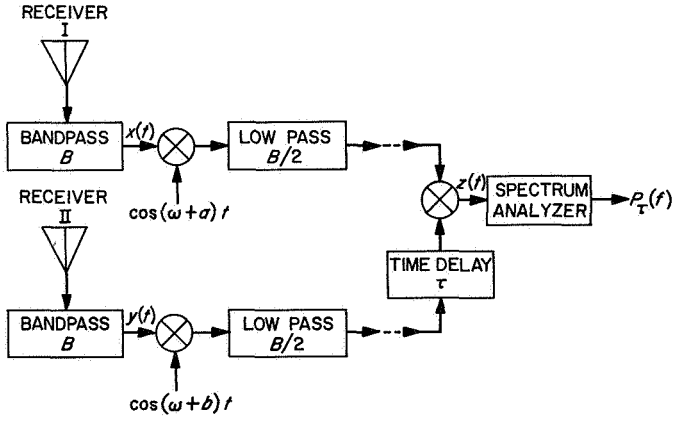

Fig. 44. System block diagram

The correlation obtained will not, in general, be at dc, but will be at the frequency that is the sum of the doppler difference and the frequency-standard difference between the two stations. Signal processing is therefore not straight correlation but, rather, spectral analysis.

Figure 44 shows a block diagram of the system. For this experiment, receiver I was DSS 11, and receiver II was DSS 12. To simplify the experiment, the signals were not recorded on tape (along with timing marks), but were brought together in real time via the microwave link. However, the local oscillators of the two stations ran independently from separate frequency standards. The filters of the standard telemetry channels were used (bandwidth 4.5 kHz).

The multiplication, time delay, and spectral measurements were made at DSS 13 with equipment borrowed from the planetary radar experiments.

It can be shown (Ref. 7) that the angular diameter of the radar source must be less than λ/D, where λ is the wavelength and D is the projection of the spacing between antennas. Quasar 3C 273 was used for this experiment, since it is a relatively strong radio source and is known to be an effective point source for λ/D ratios of less than 10^{-6}.

Figure 45 shows the resulting spectrograms, taken on September 18, 1967, for three different values of time delay. The correlation peak occurs at 8.6 Hz. The doppler shift for quasar 3C 273 was 4.07 sin (h + 2^h18^m) Hz, where h is the hour angle of the source. At the time these spectrograms were taken, the doppler shift was only 1.14 Hz. The receivers were purposely offset to obtain a more convenient operating frequency.

It can be seen that the correlation peak drops rapidly with time delay. The time-setting accuracy of this experimental configuration was easily 30 μs. Increasing the system bandwidth past 4.5 kHz would increase the time-setting accuracy proportionally.

In this paper, the performance of the system is analyzed from the signal-to-noise ratio, or detectability, point of view. Time delays of zero are assumed so that the correlation is maximized. The signal of receiver I, $x(t)$, is characterized (see Fig. 44) by the equation

$$x(t) = [n(t) + s(t)] \cos \omega t + [m(t) + r(t)] \sin \omega t \quad (1)$$

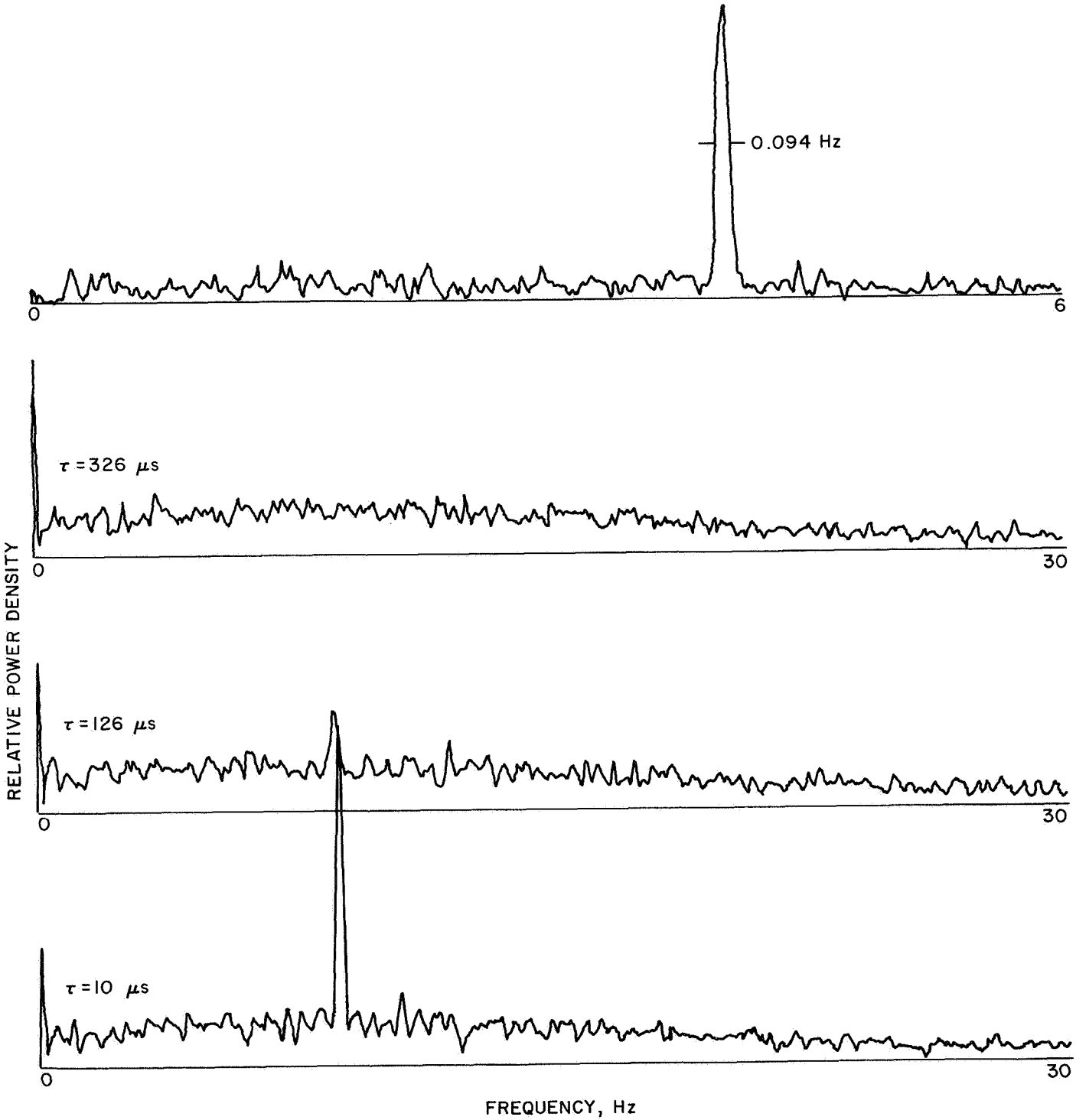

Fig. 45. Data spectrograms

where $n(t)$ and $m(t)$ are independent signals due to the system noise of receiver I, and $s(t)$ and $r(t)$ are independent signals due to the radio star. Their spectra are sketched in Fig. 46. Equation (1) is a valid way of representing a narrow-band Gaussian noise waveform with a symmetrical spectrum centered at frequency $\omega/2\pi$.

The signal at y is then characterized by the similar equation

$$y(t) = [p(t) + s(t)] \cos \omega t + [q(t) + r(t)] \sin \omega t \quad (2)$$

where $p(t)$ and $q(t)$ represent the independent system noise from receiver II. The signals due to the radio star are, of course, the same as in Eq. (1).

The autocorrelation function at point z (Fig. 44) is computed in a straightforward manner, assuming the noise sources are Gaussian. The result is

$$R_z(\tau) = 2[R_n(\tau) + R_s(\tau)]^2 \cos a\tau \cos b\tau + [R_s^2(\tau) + R_s^2(0)] \cos (a - b)\tau \quad (3)$$

where $R_n(\tau)$ and $R_s(\tau)$ are the autocorrelation functions of the noise and the signal, and $a/2\pi$ and $b/2\pi$ are the frequency offsets of receivers I and II.

It follows from Eq. (3) that, for low frequencies, the spectrum at point z (which is measured by the spectrum analyzer) is noise with a density of

$$N_z = 2[2(N + S)^2 + S^2]B \text{ watts/Hz} \quad (4)$$

(where N and S are the spectral densities of the system noise and the radio star noise, respectively) and a total signal power [at the frequency $(a-b)/2\pi$] of

$$P_s = S^2 B^2 \text{ watts} \quad (5)$$

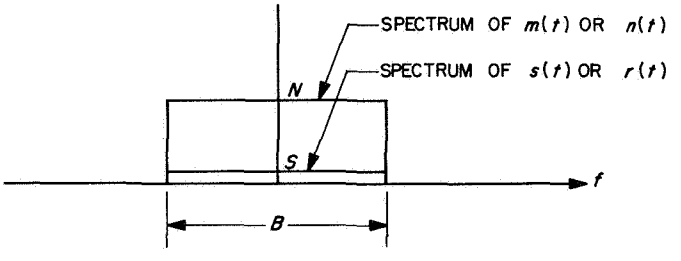

Fig. 46. Signal and noise spectra

These are the spectra plotted in Fig. 45.

The ratio of signal power to noise density is

$$\frac{P_s}{N_z} = \frac{S^2 B}{4(N + S)^2 + 2S^2} \text{ Hz} \quad (6)$$

which, for weak radio sources, becomes

$$\frac{P_s}{N_z} = \frac{S^2 B}{4N^2} \text{ Hz} \quad (6a)$$

From Fig. 45, it is estimated that P_s/N_z equals 2.11 Hz. Using 46°K for the system temperature and Eq. (6), one finds that the antenna temperature of quasar 3C 273 is

$$S = 2.1°\text{K}$$

The flux of quasar 3C 273 has been estimated[8] at about 25 flux units, which converts to 2.8°K for the DSS antennas. Hence, it is seen that there was very little loss, such as decorrelation caused by nonmatching filters, in the system.

In order for the signal to be detected, it is necessary that the peak of the spectrum be significantly larger than the fluctuations. An adequate number for this post-detection signal-to-noise ratio SNR is ten. It has been shown (Ref. 8) that

$$SNR = \frac{S^2 B}{4N^2} \left(\frac{T}{\Delta f}\right)^{1/2} \quad \text{for } T > 1/\Delta f$$
$$= \frac{S^2 BT}{4N^2} \quad \text{for } T < 1/\Delta f \quad (7)$$

where T is the integration time and Δf is the smallest bandwidth that contains the signal.

The upper trace of Fig. 45 was made in order to estimate the bandwidth of the signal. The half-power bandwidth was 0.094 Hz, part of which was caused by the changing doppler during the four minutes of integration used to produce these spectrograms. This part amounted to about 0.068 Hz and can be completely compensated; the balance is attributed to frequency drift and jitter in the oscillators of the system.

For an $SNR = 10$, an integration time

$$T = 8.5 \text{ s} \quad (8)$$

[8] Moffet, A. T., personal communication to the author, 1967.

is required, assuming the measured values of P_s/N_z and Δf.

The total number n of data samples is an important design consideration. The sampling rate is B samples/s, so that

$$n = BT$$

Equation (7) becomes

$$SNR = \frac{S^2}{4N^2}\left(\frac{Bn}{\Delta f}\right)^{1/2} \qquad \text{for } T > 1/\Delta f$$

$$= \frac{S^2 n}{4N^2} \qquad \text{for } T < 1/\Delta f \qquad (9)$$

For the parameters used here, adequate detection can be obtained with

$$n \geq 19000 \qquad (10)$$

If the system bandwidth is made wider, these samples will be obtained more quickly, with a corresponding increase in the accuracy of the time difference measurement.

It is concluded that the distant DSN clocks can be calibrated quite accurately by this technique, with only a modest amount of recorded data. This conclusion is conditional, of course, on finding a suitable radio star that remains an effective point source over the very much longer base line used by the DSN.

References

1. *Microwave Theory and Measurements,* Hewlett-Packard Engineering Staff, Prentice-Hall, 1962. This text contains all the material in H-P Application Note No. 38, *Microwave Measurements for Calibration Laboratories* (now out of print).
2. Holmes, J. K., *System Identification From Noisy Measurements,* PHD thesis. University of California, Los Angeles, Calif., 1967.
3. Stelzried, C. T., Reid, M. S., and Petty, S. M., "A Precision DC Potentiometer Microwave Insertion Loss Test Set," *IEEE Transactions on Instrumentation and Measurement,* Vol. IM-15, No. 3, p. 98, Sept. 1966.
4. Stelzried, C. T., and Reid, M. S., "Precision Power Measurements of Spacecraft CW Signal Level with Microwave Noise Standards," *IEEE Transactions on Instrumentation and Measurement,* Vol. IM-15, No. 4, p. 318, Dec. 1965.
5. Tausworthe, R. C., "Random Numbers Generated by Linear Recurrence Modulo Two," *Math. Comp.,* Vol. 19, No. 90, pp. 201–209, Apr. 1965.
6. Box, G. E. P., and Muller, M. E., "A Note on the Generation of Random Normal Deviates," *Ann. Math. Statist.,* Vol. 29, p. 610, 1958.
7. Brown, R. H., and Lovell, A. C. B., *The Exploration of Space by Radio,* Chapter III. John Wiley & Sons, Inc., New York, 1958.
8. Goldstein, R. M., "A Technique for the Measurement of Power Spectra," *IRE Trans. Space Electron. Telem.,* Vol. SET-8, No. 2, pp. 170–173, June 1962.

IV. High-Rate Telemetry Project

A. Introduction, *M. Easterling*

1. Purpose

The high-rate telemetry (HRT) project is an advanced engineering project with three main objectives:

(1) To meet the requirements of the *Mariner* Mars 1969 project by designing, building, verifying, integrating, and operating equipment at DSS 14 to receive data from the *Mariner* Mars 1969 spacecraft at 16,200 bits/s.

(2) To develop prototype high-rate ground telemetry equipment for the DSN which has multiple-mission capability.

(3) To advance the technology of deep space communications.

The first objective includes flight/ground system verification testing at DSS 21 and DSS 71. The second objective includes the establishment of the ranges of the parameters that may be encountered in future missions, e.g., data rate and subcarrier frequency, and the design of equipment to handle these ranges. The third objective includes working out all of the techniques of system analysis and verification testing required to support the first two objectives.

2. History

The HRT project uses techniques and theories which have been developed over many years at JPL, but it was instituted as a direct result of a *Mariner* Mars 1969 spacecraft system design review held in November 1966. That design review established that the telemetry system, which was adapted with only minor changes from that used on the *Mariner IV*, was inadequate for the *Mariner* Mars 1969 mission. Accordingly, the telemetry system was redesigned, and the HRT project was established to support one part of the redesigned system.

A major objective of the *Mariner* Mars 1969 mission is to obtain television pictures of Mars. The pictures are to be stored at high speed by an analog tape recorder, played back at a lower speed through an analog-to-digital converter and re-recorded by a digital tape recorder. A second playback at a still lower speed will then produce a data stream at a rate which can be transmitted to earth over the telemetry channel. The use of two tape recorders in tandem was recognized as being a somewhat unreliable situation, and the question was raised as to whether it would be possible to devise a special channel which could transmit the data at the rate from the analog tape recorder and avoid one of the tape recorders, at least. A study was made which showed that

such a channel could be devised using the DSS 14 210-ft-diameter antenna if certain operational constraints were accepted. The constraints, principally the one that the ground antenna must operate above a certain minimum elevation angle, proved to be acceptable, and the project was established formally on April 4, 1967. The intervening time has been devoted to the analysis, design, and assembly of a prototype version of the system to verify the concept and design and to the preparation for testing with the breadboard spacecraft equipment. This article is the first formal report on the project, but it is anticipated that further reports will appear regularly.

B. Project Description, *M. Easterling*

1. Technical Description

The HRT system is a modificatin of the basic digital telemetry system that was used on *Mariners IV* and *V*. It differs from that system in that the data is block coded, there is no sync channel, and the detection process is more efficient. A very functional block diagram of the HRT system is shown in Fig. 1. The data from the data source is block-encoded into binary symbols. The symbols, in the form of a binary waveform, biphase-modulate the squarewave subcarrier. The modulated subcarrier in turn phase-modulates the carrier, which is then amplified and radiated from the antenna. On the ground the DSIF receiver tracks the carrier and provides a reference for synchronously demodulating the carrier. The subcarrier loop tracks the subcarrier and provides a reference for synchronously demodulating the subcarrier. The symbol loop tracks the transitions in the data waveform and provides the symbol timing to the word timer, which triggers the crosscorrelation detector. The output of the detector is the recovered bit stream, which is recorded for the data user. In the actual hardware, the functions are slightly rearranged, and in some cases combined, to simplify the equipment, but the functions performed are exactly those described.

The HRT project is responsible for the design and construction of the ground portion of the system. The *Mariner* Mars 1969 project is responsible for the design of the spacecraft portion of the system. Accordingly, the reporting here will be concerned only with the ground portion except where necessary to discuss the interrelations between the parts.

The equipment being developed is intended to fit into a standard DSIF tracking station. It will connect into the S-band receiver, which will require only a minor modification to accommodate it. It will also utilize the computer that is part of the telemetry and command data subsystem, with no change being made to the computer. A functional block diagram of the ground portion of the system starting with the 10-MHz IF signal in the receiver is shown in Fig. 2. The receiver operates to produce at this point a 10-MHz version of the received signal which is fixed in both frequency and phase. The equipment whose functions are shown acts to extract the data from this signal and record it on a magnetic tape. The first step in the process is to synchronously demodulate the subcarrier. To facilitate the design of the equipment, it is convenient to do this before demodulating the carrier. After further amplification and filtering in the 10-MHz IF amplifier, the data waveform is recovered by synchronously demodulating the carrier. The data waveform is integrated symbol by symbol, and the symbol

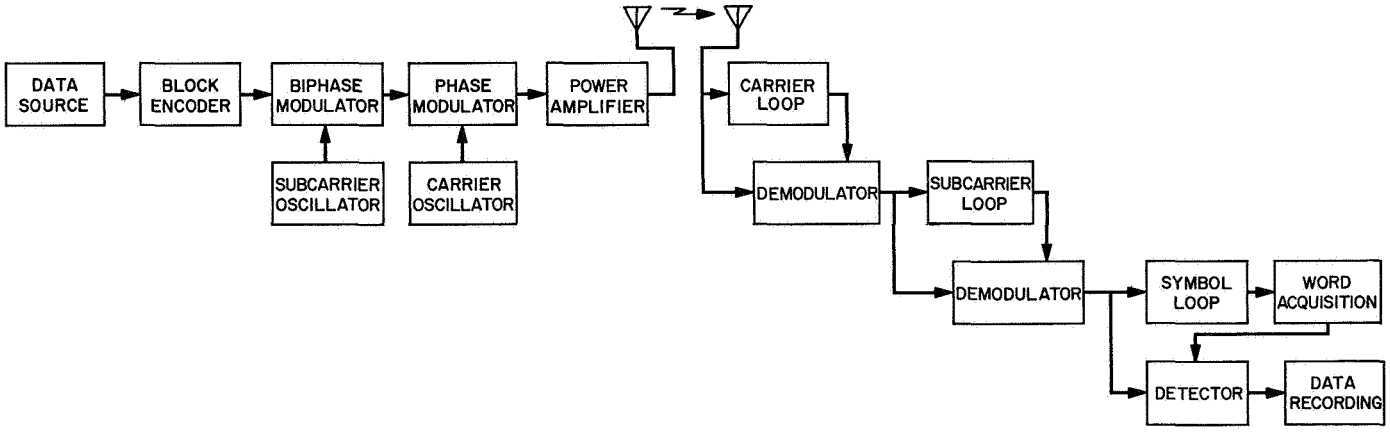

Fig. 1. High-rate telemetry system block diagram

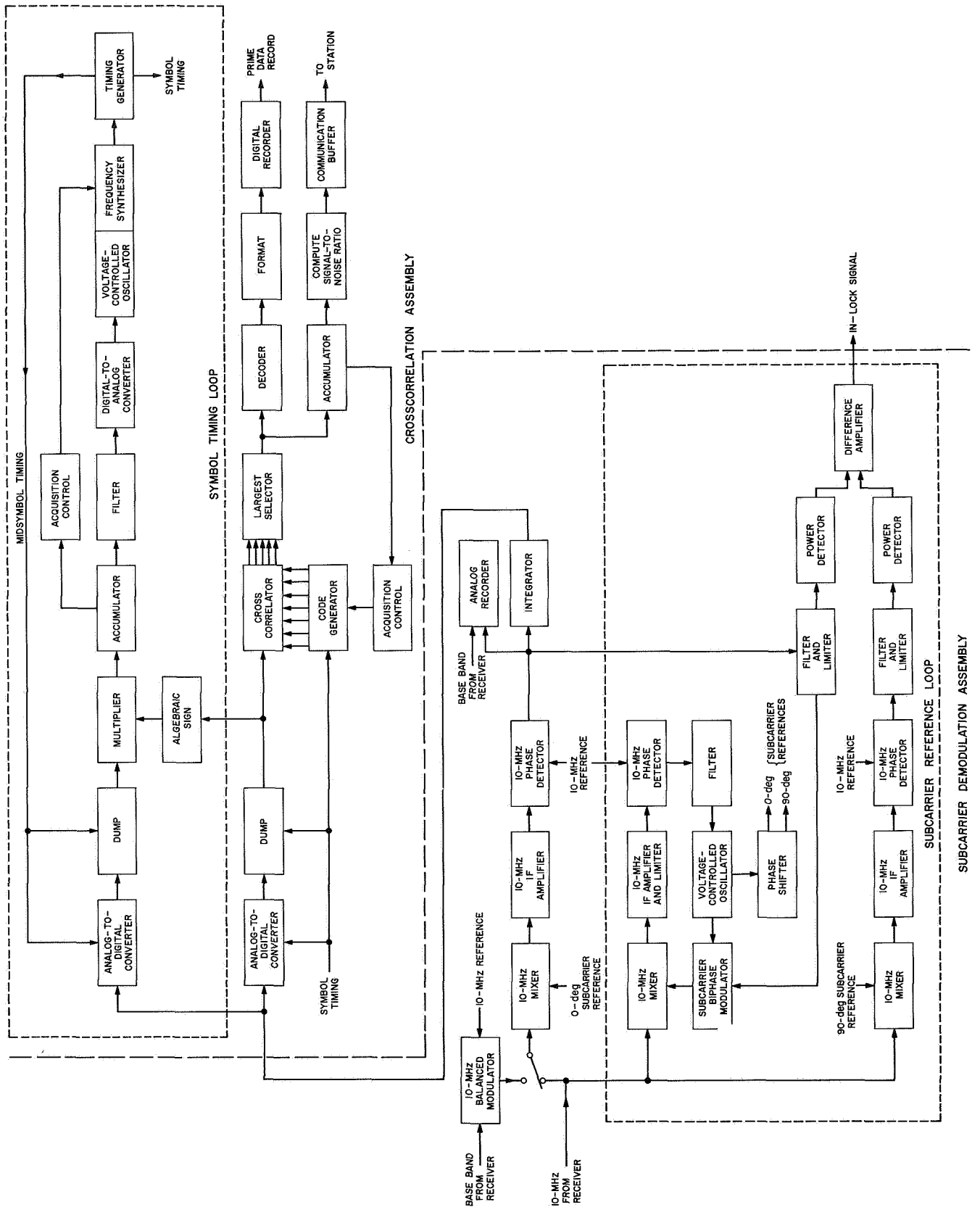

Fig. 2. High-rate ground telemetry block diagram

integrals are combined in the crosscorrelator to produce the 64 crosscorrelations over each word-time of the data waveform (plus noise) with every possible data waveform (without noise). The largest of the crosscorrelations is selected, and the corresponding 6 bits are determined and sent to the recorder. The crosscorrelation detection is thus a standard maximum likelihood detection.

The reference that is used to demodulate the subcarrier is provided by the subcarrier reference loop which tracks the subcarrier. Because the subcarrier is biphase-modulated, it is necessary to provide an estimate of the data to partially demodulate it and obtain a signal for the loop to track. This is provided by the filter and limiter acting on the signal from the carrier demodulator in the data channel. In the subcarrier reference loop, it is convenient to do the carrier demodulation after the subcarrier phase detection in a manner similar to that employed in the data channel. An inlock signal is obtained by demodulating the signal with a subcarrier shifted 90 deg and by comparing the power obtained with that obtained from the data channel. When the subcarrier reference loop is in lock, the power from the data channel contains components due to the signal as well as noise, but the power from the quadrature channel contains only noise. The two channels are constrained to have the same gain and bandwidth so that the noise components are equal and are rejected by the difference amplifier which passes only signal components. When the subcarrier loop is out of lock, the phase of the voltage-controlled oscillator is unrelated to the phase of the subcarrier, and the outputs of the data channel and the quadrature channel are the same so the output of the difference amplifier is zero.

The timing for both the symbol integrator and the crosscorrelator is provided by the symbol tracking loop which tracks the transitions in the data waveform. Essentially, the loop operates to maintain a zero value for the integrals of the data waveform from the middle of one symbol period to the middle of the following one, whenever a transition occurs. The occurrences of a transition and its direction are determined by a comparison of the signs of the integrals over the two symbol periods. Thus, if the midsymbol timing tends to drift away from the center of the symbol period, an error signal is generated which controls the voltage-controlled oscillator to correct the midsymbol timing. Since the symbol timing is derived from the midsymbol timing, it is also corrected and made to coincide with the symbol transitions in the data waveform.

The primary output of the equipment is the digital data on magnetic tape, and this is the form in which the data is normally delivered to the user. The two analog records are backup in case of a failure.

The equipment which performs the functions shown in Fig. 2 is divided into two major assemblies. One is the subcarrier demodulator assembly which contains the data channel down through the integrator and the subcarrier reference loop. This assembly is primarily analog equipment and will be part of the receiver subsystem. The other assembly is digital equipment and is constructed as peripheral equipment for the computer in the telemetry and command data subsystem. The digital recorder (actually there are two) is also a peripheral to the computer which acts as the overall control device for both the symbol tracking process and the data detection and recording. The analog recorder is an existing device in the analog instrumentation subsystem. Initial reporting on the details of the equipment is in Section C of this article.

2. System Analysis for *Mariner* Mars 1969

As part of the system study that indicated it was feasible to construct a channel which would transmit data from the spacecraft at the rate at which it is to be played back from the analog tape recorder in the spacecraft, it was necessary to look into a number of factors. The approach was to take the design control table that had already been developed for the *Mariner* Mars 1969 telecommunications system and determine which factors could be changed to increase the capability the requisite amount. It should be emphasized that this could be done only because the high-rate channel was required to operate for a limited period of time and could use the DSS 14 210-ft-diameter antenna whereas the standard telecommunications system was designed to operate continuously using a network of 85-ft-diameter antennas spaced around the earth. Specifically, at 16,200 bits/s, the analog tape recorder in the spacecraft will play back all of the recorded data in slightly less than 3 h. As will be shown, this allowed a number of changes.

The results of the study are summarized in Table 1, which is a comparison of simplified design control tables for the 270- and the 16,200-bit/s channels with the 8⅓-bit/s channel from *Mariner IV* included to extend the comparison. The quantities in Table 1 are related by the standard communication equation

$$S = P_T M G_T L_S G_R L_R \quad (1)$$

Table 1. Comparison of channels

Parameter	1. *Mariner IV* 8⅓-bit/s channel		Δ	2. *Mariner* Mars 1969 270-bit/s channel		Δ	3. *Mariner* Mars 1969 16,200-bit/s channel	
P_T	8.9 W	+39.5 dBmW	+3.10 dB	18.2 W	+42.60 dBmW	—	18.2 W	+42.60 dBmW
M		−5.3 dB	+3.50 dB		−1.80 dB	+0.46 dB		−1.34 dB
G_T		+20.1 dB	+0.11 dB		+20.21 dB	—		+20.21 dB
L_S	216 × 10^6 km	−266.2 dB	+6.84 dB	97 × 10^6 km	−259.36 dB	—	97 × 10^6 km	−259.36 dB
G_R	85 ft	+52.5 dB	—	85 ft	+52.5 dB	+8.50 dB	210 ft	+61.00 dB
L_R		−3.4 dB	+2.26 dB		−1.14 dB	+0.70 dB		−0.44 dB
S		−162.8 dBmW	+15.81 dB		−146.99 dBmW	+9.66 dB		−137.33 dBmW
T_B	8⅓ bits/s	−9.2 dB-s	−15.11 dB	270 bits/s	−24.31 dB-s	−17.79 dB	16,000 bits/s	−42.10 dB-s
ST_B		−172.0 dBmW-s	+0.70 dB		−171.30 dBmW-s	−8.13 dB		−179.43 dBmW-s
N_0	65°K	−180.5 dBmW/Hz	—	65°K	−180.50 dBmW/Hz	+4.10 dB	25°K	−184.60 dBmW/Hz
ST_B/N_0		+8.5 dB	+0.70 dB		+9.20 dB	−4.03 dB		+5.17 dB
Required ST_B/N_0	5 × 10^{-3} BER[a]	+5.2 dB	—	5 × 10^{-3} BER[a]	+5.20 dB	+2.20 dB	1 × 10^{-2} WER[b]	+3.00 dB
Margin		+3.3 dB	+0.70 dB		+4.00 dB	−1.83 dB		+2.17 dB

[a] BER = bit error rate.
[b] WER = word error rate.

where P_T is the power produced by the transmitter, M is the modulation loss, i.e., the factor which relates the power in the sidebands to the total power, G_T is the gain over isotropic and includes both circuit and pointing losses as well as antenna gain, L_S is the space loss $\lambda^2/(4\pi)^2 r^2$, in which λ is the wavelength and r is the range, G_R is the receiving antenna gain, L_R is the receiver loss, and S is the received sideband power.

The received sideband power is multiplied by the duration of a bit T_B to give the received signal energy per bit. The receiver system noise temperature is multiplied by Boltzmann's constant to give the receiver noise spectral density. Dividing the receiver energy per bit by the noise spectral density yields the appropriate figure of merit for a digital communication system ST_B/N_0. Dividing the figure of merit achieved by that required for a specified bit error rate gives the margin. The two columns labeled Δ give the change from one system to the next with the change considered as positive if it favors the second system.

The increase in capability from 8⅓ bits/s on the *Mariner IV* to 16,200 bits/s for the high-rate channel on the *Mariner* Mars 1969 is due to many factors. These are discussed for each line in Table 1.

The transmitter power has been approximately doubled since the *Mariner IV*. This factor, of course, results in a doubling of the capability.

The modulation index was changed to increase the sideband power from −5.3 to −1.80 dB relative to the total power, in going from column 1 to 2 in Table 1. This was possible for two reasons. First, the *Mariner* Mars 1969 telemetry system does not use a separate synchronizing channel, so the power which was devoted to that in *Mariner IV* is available for the data signal. The second reason has to do with providing enough power in the carrier for the receiver to track in order to produce a reference signal for synchronous demodulation. If the data rate is comparable to the bandwidth of the carrier tracking loop, the power allocated to the carrier must be comparable to that allocated to the data signal. That, of course, was the case for *Mariner IV*, which used a 12-Hz carrier loop bandwidth. In the 270- and 16,200-bit/s channels the carrier loop used still has a bandwidth of 12 Hz, so much less relative power must be allocated to the carrier. This point is treated more fully in SPS 37-45, Vol. IV, pp. 276-289.

The design control table does not show a significant change in the antenna gain even though a larger antenna is used for the *Mariner* Mars 1969 mission. This is mostly because the increased antenna gain was traded off against some other factors, such as using a single pointing angle for the antennas on two spacecraft even though they arrive at Mars on different days.

The range at encounter for *Mariner* Mars 1969 will be about half what it was for *Mariner IV*. This increases the communications capability by 6.84 dB even though it is not a change in the communications technology per se.

The antenna gain does not change from column 1 to 2 in Table 1 because both *Mariners* are designed to operate with a network of 85-ft-diameter ground antennas. The 16,200-bit/s channel is intended to operate only with the 210-ft-diameter antenna at DSS 14. The increase in gain of 8.50 dB is slightly more than the area increase because of the way that tolerances are handled. In the detailed design control table each parameter is assigned a nominal value and a favorable and an unfavorable tolerance. The system design is constrained to provide adequate performance with all of the parameters having their full unfavorable tolerances. This is the same philosophy that is usually followed in engineering work, e.g., in designing a structure where all elements are derated by an appropriate factor. The unfavorable tolerances are included in all parameters in Table 1. Because there is only one 210-ft-diameter antenna, and it is under the direct supervision of the JPL antenna engineers, it has a lower unfavorable tolerance than that which must be used in dealing with the worst of a network of antennas located around the world. There is another reason why the tolerance is less in this particular case. When an antenna is moved from pointing at the zenith to pointing at the horizon, the sag due to gravity changes and the gain changes. The reflector plates are usually set at an elevation angle of 45 deg, and a tolerance is assigned to cover the effects of sag at both higher and lower angles. When the 85-ft-diameter antennas are used, continuous operation must be provided and tolerances are assigned to cover the effects of sag down to within a few degrees of the horizon. In the case of the 16,200-bit/s channel, the total time required to play back the data from the analog recorder in the spacecraft is less than 3 h. Moreover, the playback time can be selected to take place when the antenna angle is above 25 deg, which further reduces the required unfavorable tolerance. In addition, if there were an unusually high wind, say above 45 mph, on the day when playback was desired, the playback could be delayed for a day. This also allows a lower unfavorable tolerance than that required for an 85-ft-diameter antenna which must operate continuously. The effect of these several factors is to give the 210-ft-diameter antenna a higher useable gain. The cost of this gain is a set of restrictions on the operations. Since the playback time is both short and selectable, the restrictions are acceptable.

The entry in Table 1 labeled receiver loss includes several factors. The most important is the degradation in the process of demodulation from the carrier due to the fact that the carrier tracking loop provides a noisy reference. The *Mariner IV* was constrained to have a low signal-to-noise ratio in the carrier tracking loop, and even though the power allocation was optimized, the effect was equivalent to a loss of more than 2 dB. In the 270-bit/s channel, even though the power allocation is reoptimized with proportionately less power in the carrier, the carrier has more absolute power, and the effect of the reference produced by the carrier loop is equivalent to a loss of less than 0.5 dB. The effect of the carrier loop is similarly small in the case of the 16,200-bit/s channel. A second factor is the signal-to-noise ratio in the bandwidth of the subcarrier tracking loop. In the case of the *Mariner IV*, this loop was constrained to have a poor signal-to-noise ratio. In addition, although a squarewave subcarrier was used, the demodulation process recovered only the power that was carried in the fundamental of the squarewave. The total result was equivalent to a loss of more than 1 dB. In the *Mariner* Mars 1969, a different method of tracking the subcarrier is used; this method uses the entire sideband power, and thus inherently has a higher signal-to-noise ratio. In addition, the demodulation process recovers the power in all of the harmonics of the subcarrier up through at least the fifth and thus loses very little. The combined result is to have a much smaller equivalent signal loss for either channel. Finally, there are small losses associated with bit or symbol tracking, data detection, and circuitry imperfections in all three channels. In summary, the higher ratio of data rate to carrier loop bandwidth permits the reduction in effective loss due to a noisy carrier reference, and improved methods of tracking the subcarrier and bits or symbols and of detecting the data permits the recovery of more of the sideband power.

The system temperature is decreased significantly in the case of the 16,200-bit/s channel. This is due to two factors. The first is that, because the 210-ft-diameter antenna will not be required to transmit during the short time while it is receiving the high rate data, no diplexer is required and a listen-only feed system of advanced design can be used. The second is that, since the minimum elevation angle is 25 deg, the antenna need not look obliquely through the atmosphere. It should be noted that this also implies some operational restrictions, namely, the antenna cannot be used for transmitting during the reception of high-rate data and the channel is operable only above a 25-deg elevation angle. The latter restriction is the same as that imposed by the antenna gain tolerance. There is an additional restriction: the temperature of the receiving system will begin to rise if the rainfall rate exceeds 0.1 in./h, but this is unlikely in the Mojave desert in August.

The final factor to be considered is the required ST_B/N_0. In all cases the channel is required to transmit data with an error rate not exceeding 5×10^{-3}. If bit by bit detection is used, the required ST_B/N_0 is 5.20 dB after all losses or equivalent losses are considered. If the data is encoded into a biorthogonal code in blocks of 6 bits, the required ST_B/N_0 is reduced to 3.0 dB for a word error rate of 10^{-2}, which is equivalent to a bit error rate of 5×10^{-3}. Thus, all other factors being equal, the block coding reduces the signal level required by 2.2 dB.

The margin shown for each channel is the margin at encounter. The margin generally decreases after encounter. Sufficient margin must be provided to maintain a positive margin over the playback period. Since the 16,200-bit/s channel recovers the data in 3 h, only a small margin is required even if it is desired to play the data back on several successive days.

The purpose of this discussion has been to show the rationale that was used in the study which indicated that a 16,200-bit/s channel for *Mariner* Mars 1969 was feasible and to enumerate the several factors that were important. Equally important was to define the operational constraints under which the channel can be used. The numbers in Table 1 must now be considered as only illustrative. Since the study was concluded, the numbers have been subjected to continuous refinement. The current values of the various parameters, together with their tolerances, are published in the appropriate planning document. In addition, the situation is somewhat more complex than indicated in Table 1 because there is a second low data rate channel on a separate subcarrier present when either the 270- or 16,200-bit/s channel is used. The effect of the second channel is to reduce the performance slightly. This effect was not considered when Table 1 was constructed, but the detail system design does, of course, consider it. The conclusions to be drawn from Table 1 are not changed.

3. Equipment and Schedule

Since the primary objective of the HRT project is to support the *Mariner* Mars 1969 flight project, certain equipment must be produced on a time scale which is consistent with the schedule of the flight project. Although the operation date is not until after encounter in mid-1969, equipment must be produced as early as January 1968 to assist in the testing of the proof-test-model spacecraft. Moreover, the high-rate system is experimental in that it involves both new equipment and, to some extent, new techniques in the area of subcarrier tracking and data synchronization. For that reason, it was deemed desirable to construct a prototype system before constructing the actual field systems. However, since time was very short, it was decided to support the initial spacecraft testing with the prototype system. The way in which this is to be handled can be best explained with reference to Fig. 3, which is a simplified version of the project schedule showing only the most important milestones and periods of required support.

The first seven lines of the schedule show several flight project milestones of importance to the HRT project and the support required from the HRT project. The rest of the schedule shows the activity of the HRT project which is intended to provide the requisite support.

When the project was first organized, it was recognized that techniques for testing the system would have to be devised. Therefore, the team which had the responsibility for system verification designed and constructed a slow speed laboratory version of the system and began to run various tests while the prototype system was under development. The results of that testing are reported below.

The prototype system (set A) was designed and constructed, and system assembly and checkout was begun during the first week in October 1967. It is intended that the system will be completely checked out and verified by the first of January 1968. This will include a preliminary compatibility test with the breadboard spacecraft communications equipment, which is scheduled for delivery in October 1967.

Beginning in January 1968, the HRT project is committed to support the flight project by maintaining equipment in the flight project/tracking and data acquisition interface laboratory (DSS 21) to test the proof-test-model spacecraft. Set A will provide that support.

In May, June, and July 1968, the flight spacecraft are scheduled for delivery and must be supported in a test program by DSS 21. To provide that support, the first of two field sets will be installed. The field sets will be functionally the same as set A, but advantage will be taken of the experience gained to produce more fieldworthy equipment. The additional time available will also be helpful in achieving a better piece of equipment.

Approximately the first of November 1968, the prelaunch operations at Cape Kennedy will begin. To support this activity, the first field set will be installed there. To maintain the capability in DSS 21, the second field set will be installed there.

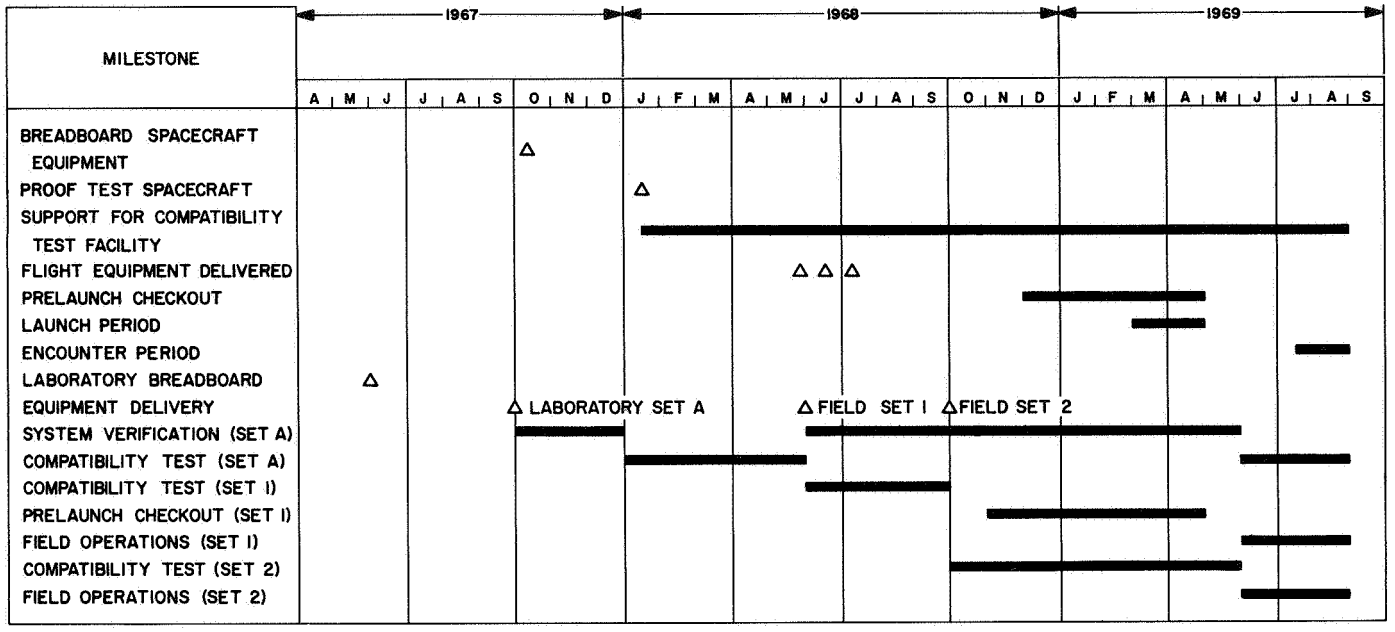

Fig. 3. High-rate telemetry project schedule

After launch, both field sets will be moved to DSS 14 and used to support the operation at encounter. Two field sets are provided so that there will be a completely redundant ground system.

After set A is removed from DSS 21, it will be used in additional laboratory tests to further develop the techniques. When both field sets are sent to DSS 14, set A will be reinstalled in DSS 21 to provide a complete capability there for testing with the proof-test-model spacecraft should any problems arise with the flight spacecraft during the flight.

While the two field sets to be provided are intended to be fieldworthy equipment in every respect, they will be considered as experimental and maintenance responsibility will be retained by the HRT project. The equipment will be operated by the regular station operations personnel, however, as part of the receiver and telemetry and command data handling subsystems. No additional operators will be required.

4. Project Organization

The high-rate telemetry project is an advanced engineering project with several engineering teams drawn from various parts of the JPL Telecommunications Division. The project organization is shown in Fig. 4. As noted in the introduction, the *Mariner* Mars 1969 flight project has the responsibility for producing the spacecraft portion of the HRT system. The dashed line in Fig. 4 indicates the engineering liaison function between the HRT project and the *Mariner* Mars 1969 spacecraft system organization which is intended to assure compatibility between the encoder used in the spacecraft and the detection equipment on the ground. A similar liaison function exists between the HRT project and the multiple-mission telemetry project (SPS 37-46, Vol. III, pp. 175–243), which is developing the ground equipment for the other telemetry channels to be used in the *Mariner* Mars 1969 mission. When the HRT project was organized, and even when the article on the multiple-mission telemetry project was written, it was intended that the HRT project would develop a subcarrier demodulator assembly. It was an objective to make the device as similar to that being developed by the multiple-mission telemetry project as possible, but it was felt, because the subcarrier frequencies and the data rates in the two systems were very different, that the devices would also have to be somewhat different. Recently, however, it has been found possible to modify the design of the subcarrier demodulator assembly so that it can be used for both kinds of channels. Therefore, the multiple-mission telemetry project is developing the subcarrier demodulator assembly for the HRT project and an engineering liaison function is required to assure that the device as developed is suitable. It should be noted that the device is somewhat modified from that reported in SPS 37-46, Vol. III, and this modification will be reported in a subsequent issue of this volume of the SPS.

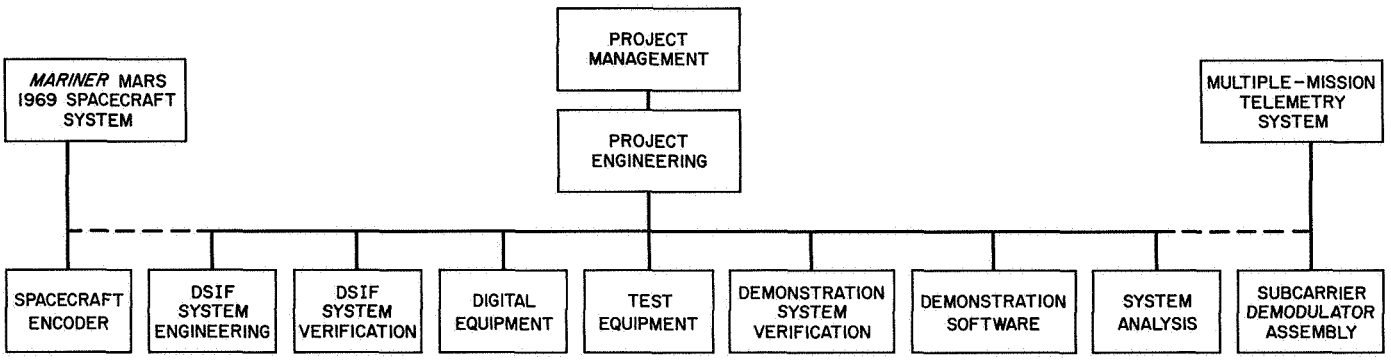

Fig. 4. High-rate telemetry project organization chart

The functions of the engineering teams which make up the HRT project proper are as follows:

DSIF system engineering. Performs the engineering work necessary to install the HRT equipment in DSS 21, DSS 71, and DSS 14, including station layouts, cable design, and documentation. An important part of this work is the preparation of necessary engineering change requests and obtaining approvals for them.

DSIF system verification. Performs the performance verification testing of the high-rate ground telemetry system as installed in the tracking stations, including the effects of other equipment, such as the receiver. This includes developing the verification test procedures and the additional test procedures required by the station operating personnel to maintain the performance of the system after it has been initially verified.

Digital equipment. Develops, produces, and maintains the digital equipment. This is essentially the equipment shown in the right side of Fig. 2, exclusive of the computer.

Test equipment. Develops, produces, and maintains the test equipment, which is a device to produce appropriate signals to test the HRT system.

Demonstration system verification. Performs the system verification testing on a demonstration system consisting of a laboratory version of an RF link, a laboratory computer, and the prototype HRT equipment, set A. This includes devising the testing techniques and locating any design flaws which impair performance.

Demonstration software. Designs and develops the demonstration software, i.e., the software that is used in the demonstration system. Since the system is an advanced engineering system, there will be no operational software developed. Instead the demonstration software will be used during spacecraft testing and during the receipt of actual data.

System analysis. Performs the analyses needed for the design of the ground equipment and to predict its performance when operating in the system. This does not include the overall performance of the *Mariner* Mars 1969 high-rate channel, which is the responsibility of the *Mariner* Mars 1969 spacecraft system organization.

C. System Development, *M. Easterling, P. H. Schottler, R. A. Winkelstein, J. C. Springett, F. L. Larson, G. L. Fultz, and M. H. Brockman*

1. Status of Development, *M. Easterling*

According to the project schedule (Fig. 3), set A should be completed and undergoing system verification testing. This has been mostly accomplished. The demonstration software and the digital equipment have been completed and are in the process of being checked out with the laboratory computer. A breadboard version of the subcarrier demodulator assembly has been assembled and is now being modified to incorporate the changes attendant upon using the same device for all channels of *Mariner* Mars 1969 telemetry. It will be available for the verification testing about the middle of the testing period. The prototype test equipment has been built and is undergoing final checkout.

DSIF system engineering is well underway. The interfaces between the several pieces of equipment have been established, station layouts have been made, and cable design and procurement have begun. DSIF system verification is just beginning. Enough system analysis has been done to establish preliminary values of system parameters.

Initial reports on the work done in the development of the prototype equipment are in the following sections. The demonstration software is first because the computer acts as the control element for the symbol tracking, word acquisition, and data detection processes. The software reported is prototype software in the same sense that the hardware is prototype, and will be further developed for use with the field equipment. The section on the digital equipment is self-explanatory. The test equipment is just being completed, and will be reported in a later issue of this volume. The section on demonstration system verification covers work that was done on the laboratory breadboard in preparation for the verification testing of the prototype equipment. Finally, a first-order analysis of the subcarrier demodulator loop is provided which establishes preliminary values of the parameters required for *Mariner* Mars 1969. The reporting on the subcarrier demodulator assembly itself will be done in subsequent issues of this volume under the multiple-mission telemetry system.

2. Demonstration Software, *P. H. Schottler*

a. Introduction. The system of documentation for the high-rate telemetry project software is based upon a hierarchy of drawings. The top drawing in the hierarchy is called the software mode diagram. In general terms, a mode may be defined as a body of coding which directs the computer to perform a particular set of functions during a prescribed interval of time. A mode is usually designated by the name of the most important function performed in that mode.

It is characteristic of real-time programs that not all functions are required in each mode of operation. For example, in general, a different set of functions is performed in an acquisition mode from that performed in a tracking mode. The purpose of the software mode diagram is to define the several modes of operation of the program and the permissible transitions between modes together with the criteria for the transitions. This drawing displays the overall structure of the program and is derived from the system block diagram.

The second level of drawings consists of a sequencing chart for each mode shown in the software mode diagram. A sequencing chart has somewhat the same form as a conventional flow chart, but it is concerned with how the several functions required in a given mode are called up when required. The functions are shown only as blocks, and the chart shows the queueing scheme, the links to other modes, and the operation of the interrupts, including arming and disarming. In cases where the timing is tight, the sequencing chart is accompanied by a timing diagram.

The final level of drawings consists of a flow chart for each of the functions to be performed in each mode. The coding is derived from these flow charts, and, as a result, there is a great deal of reciprocity between the coding and the flow charts. It is clear, then, that the final level of documentation is in no sense finished until the coding itself is finished. Furthermore, it is entirely possible that one or more of the sequencing charts can be finalized only after enough coding has been done to establish that a particular sequence of functions can, in fact, be performed within the time available.

The sections which follow describe in detail the software mode diagram and the sequencing charts for the high-rate telemetry project software. The diagrams given are largely self-explanatory, but several points deserve comment: (1) Transitions between modes are shown by large triangles with the transition number inside. Both incoming and outgoing transitions are shown in this manner. (2) Each block in each diagram is numbered, and the coding for a particular block is labeled by the block number. For example, the first instruction in block 4 of mode 3 data interrupt routine DIRA is labeled DIRA4. Coding by blocks provides a direct correspondence between the block diagrams and the assembly listing. (3) The data interrupt is armed very early in mode 0 and remains armed thereafter, unless the interrupt system is disarmed and disabled as a result of a manual restart. Each mode, however, requires several different data interrupt routines. The program selectively links to the required data interrupt routine by changing the BRM instruction[1] in the interrupt location. Selective linking to a data interrupt routine is indicated on the block diagrams by a block labeled DIR=, followed by the mnemonic of the interrupt routine linked to.

b. Software modes. The overall block diagram for the software is the software mode diagram (Fig. 5). Four modes of program operation are defined in this block diagram, viz., an initialization mode, a symbol acquisition mode, a word acquisition mode, and finally, a data mode. Transitions between the modes of operation are indicated by arrows, the solid arrows indicate those transitions which occur under normal operating conditions, and the dashed arrows those transitions which occur in response to system malfunctions or manual intervention.

[1]BRM = mark place and branch.

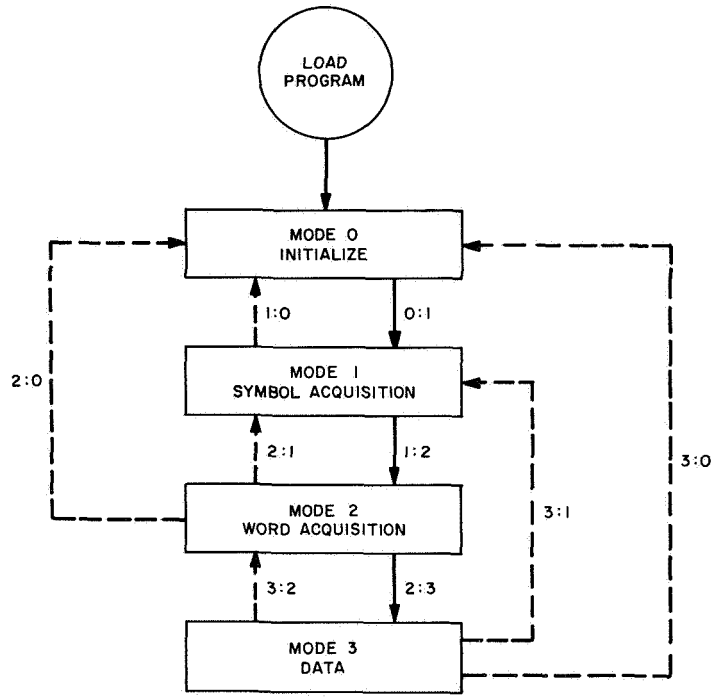

DASHED LINES INDICATE PROGRAM RESPONSES TO MALFUNCTIONS

CONDITIONS FOR TRANSITIONS

0:1 INITIALIZATION COMPLETE AND CARRIER LOOP IN-LOCK AND SUBCARRIER LOOP IN-LOCK	1:0 CARRIER LOOP LOSES LOCK OR SUBCARRIER LOOP LOSES LOCK OR MANUAL RESTART
1:2 CARRIER LOOP IN-LOCK AND SUBCARRIER LOOP IN-LOCK AND SYMBOL LOOP IN-LOCK	2:0, 3:0 MANUAL RESTART
2:3 CARRIER LOOP IN-LOCK AND SUBCARRIER LOOP IN-LOCK AND SYMBOL LOOP IN-LOCK AND WORD SYNC ACQUIRED	2:1, 3:1 SYMBOL LOOP LOSES LOCK AND CARRIER LOOP RETAINS LOCK AND SUBCARRIER LOOP RETAINS LOCK
	3:2 WORD SYNC LOST AND CARRIER LOOP RETAINS LOCK AND SUBCARRIER LOOP RETAINS LOCK AND SYMBOL LOOP RETAINS LOCK

Fig. 5. Software mode diagram

A transition between two modes of operation occurs in response to a certain set of conditions. The software mode diagram enumerates the particular set of conditions which leads to each of the transitions defined in the diagram. For example, the transition between modes 0 and 1 (0:1) occurs after initialization is complete and the carrier and subcarrier tracking loops are both in-lock.

It should be clearly understood that the program can be in only one of the four modes at any particular time. Furthermore, under normal operating conditions, the program (following loading) progresses sequentially through modes 0, 1, and 2 until mode 3 is reached, in which mode the program remains until data reception is terminated.

Of the four syncs which must be acquired prior to the start of data detection, two are under program control, viz., symbol sync and word sync, and two are not, viz., carrier sync and subcarrier sync. The program responds to the lock status of the carrier, subcarrier, and symbol tracking loops via computer SKS lines[2] which are connected to analog lock detectors on these loops. The program remains in mode 0 until the carrier and subcarrier loops are in-lock. The program then proceeds, in mode 1, to acquire symbol sync, and, in mode 2, to acquire word sync. In mode 3, data is recorded in real time on magnetic tape, estimates are computed for μ and σ, and the status of each loop is continuously monitored.

c. Mode 0 (Figs. 6, 7, 8, 9, and 10). Mode 0 is entered directly upon loading of the program into the computer. While in this mode, the program generates and stores any constants which may be required in subsequent operations, initializes the special-purpose digital equipment which is connected to the computer, and checks for carrier loop and subcarrier loop in-lock. The generation of program constants involves data inputs to the computer via the console typewriter.

The main routine for mode 0 is the initialization routine (IR) (Fig. 6). Data interrupt routine DIRH (Fig. 7) uses the SKS lines to test the lock status of the carrier loop and subcarrier loop over intervals of 1024 consecutive data interrupts (equivalent to one record in mode 3). Data interrupt routine DIRG (Fig. 8) and the interrupt routines for power off (POF) (Fig. 9) and power on (PON) (Fig. 10) are included as part of mode 0, but, in fact, these routines are common to all four modes of operation.

[2] SKS = skip if external signal not set.

d. Mode 1 (Figs. 11, 12, and 13). In the symbol sync acquisition mode, the program has two functions to perform: (1) implementation of the loop filter in the symbol tracking loop, and (2) control over the acquisition of symbol sync.

The algorithm for the loop filter implements a transfer function of the form

$$F(s) = G\left(\frac{1 + \tau s}{s}\right)$$

where G and τ are constants. The corresponding time domain differential equation is

$$\dot{y} = G\tau\dot{x} + Gx$$

where x and y are the input and output to the filter, respectively. Rewriting the differential equation as a difference equation, viz.,

$$\frac{y_n - y_{n-1}}{\Delta} = G\tau\left(\frac{x_n - x_{n-1}}{\Delta}\right) + \frac{G}{2}(x_n + x_{n+1})$$

gives

$$y_n = y_{n-1} + k_2(x_n + k_1 x_{n-1})$$

where the constants

$$k_2 = G\left(\tau + \frac{\Delta}{2}\right)$$

$$k_1 = -\left(1 + \frac{\Delta}{2\tau}\right)^{-1}\left(1 - \frac{\Delta}{2\tau}\right)$$

depend upon the choice of τ, G, and the sample interval Δ. Successive values of x_n are input to the computer from the special-purpose digital equipment, and computed values of y_n are output to the symbol loop voltage-controlled oscillator via a digital-to-analog converter. A value for x_n is input once every four channel word times, representing integration over $4 \cdot 32 = 128$ channel symbols.

The algorithm which controls acquisition of symbol sync may be described as follows. Briefly, there are two (at least) pairs of filter constants (k_1, k_2) such that one pair implements a wide bandwidth loop while the other pair implements a narrow bandwidth loop. The narrow bandwidth loop has been designed so that the variance of the loop phase error produces less than 0.1-dB degradation in the data signal-to-noise ratio. The program starts with the wide bandwidth pair and sweeps the

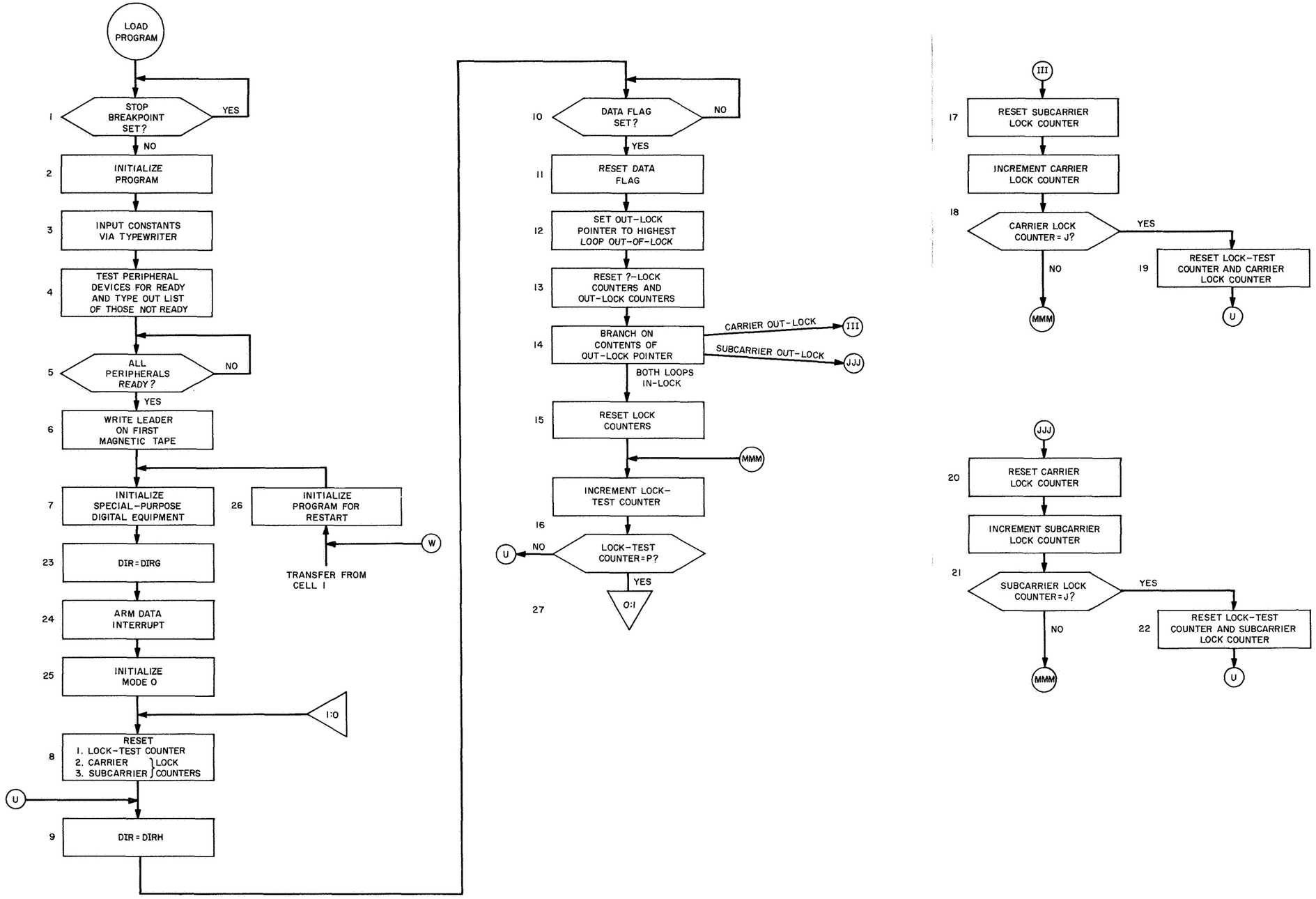

Fig. 6. Mode 0: initialization routine (IR)

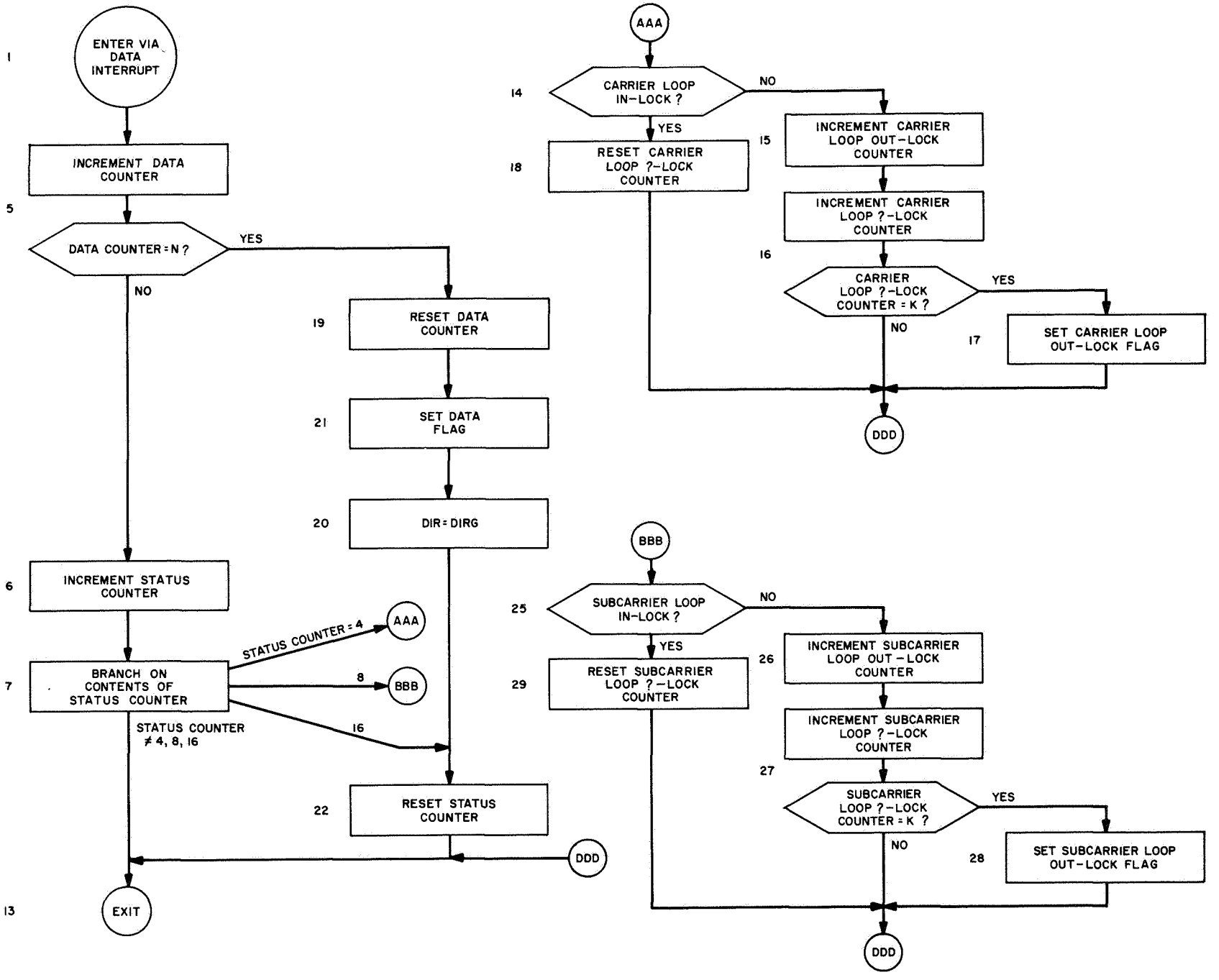

Fig. 7. Mode 0: data interrupt routine (DIRH)

frequency of the frequency synthesizer–voltage-controlled oscillator until an in-lock condition is achieved. At that point, the program implements the narrow bandwidth loop. If the symbol loop should lose lock when the narrow bandwidth loop is implemented, the program reverts to the wide bandwidth loop in order to reacquire lock.

The main routine for mode 1 is the symbol acquisition routine (SAR) (Fig. 11), which implements the acquisition algorithm. The filter is implemented in the two data interrupt routines for mode 1, DIRE (Fig. 12) and DIRC (Fig. 13).

e. Mode 2 (Figs. 14 and 15). Assuming that symbol sync has been acquired, there are 32 possible phases at which a word may start, corresponding to the 32 symbols in each channel word. The word-sync algorithm searches through all of these phases in a sequential fashion starting with phase 0, which is taken as the phase of the local symbol waveform at the initiation of the search.

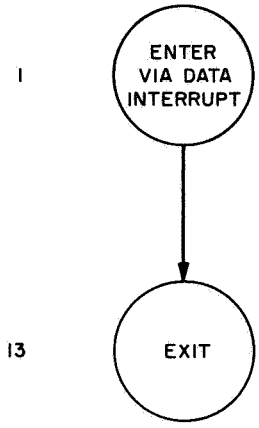

Fig. 8. Mode 0: data interrupt routine (DIRG)

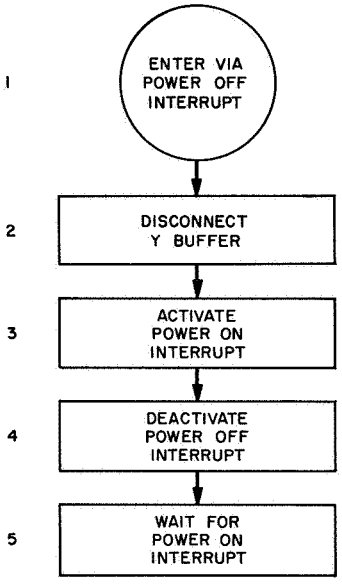

Fig. 9. Mode 0: power off interrupt routine (POF)

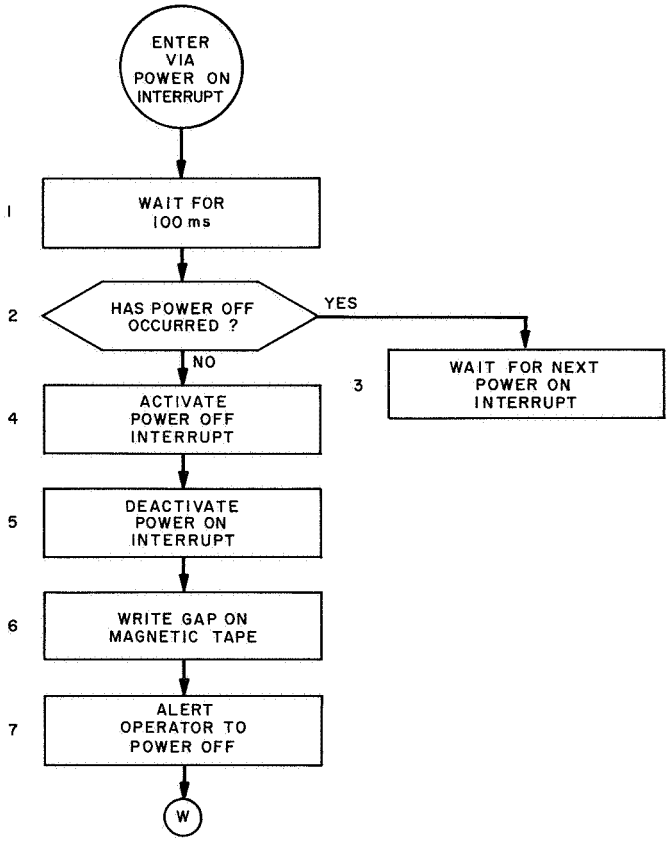

Fig. 10. Mode 0: power on interrupt routine (PON)

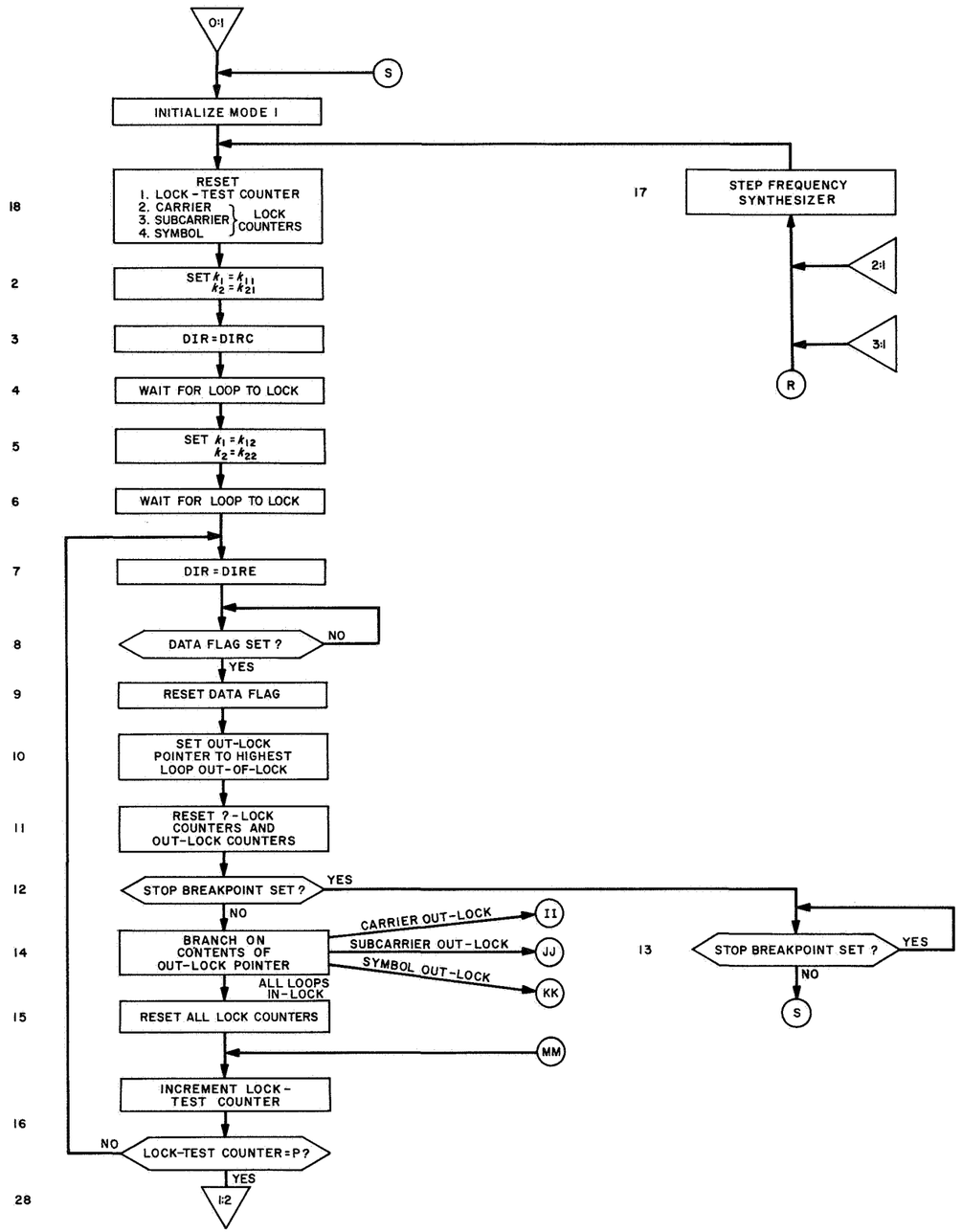

Fig. 11. Mode 1: symbol acquisition routine (SAR)

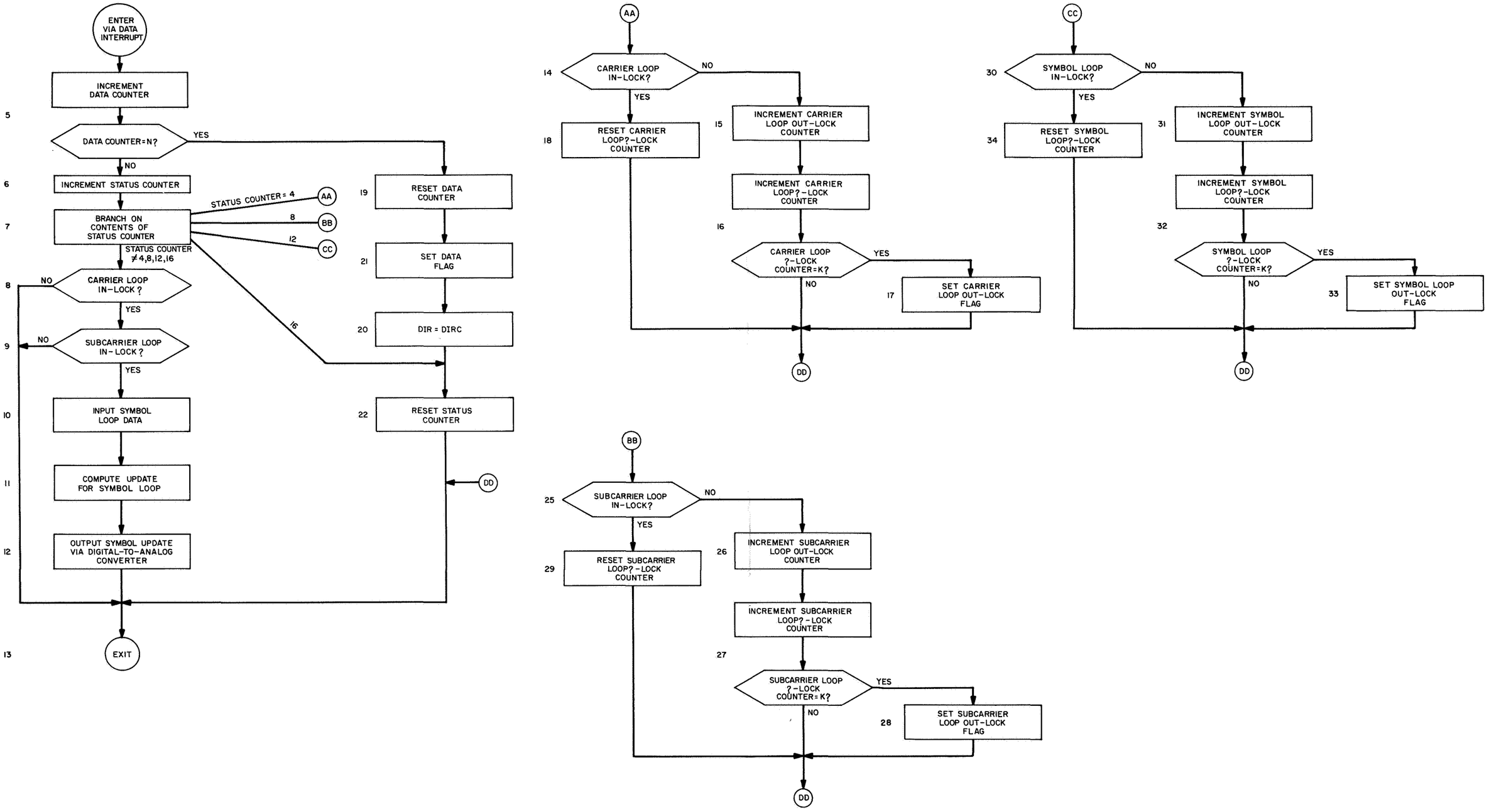

Fig. 12. Mode 1: data interrupt routine (DIRE)

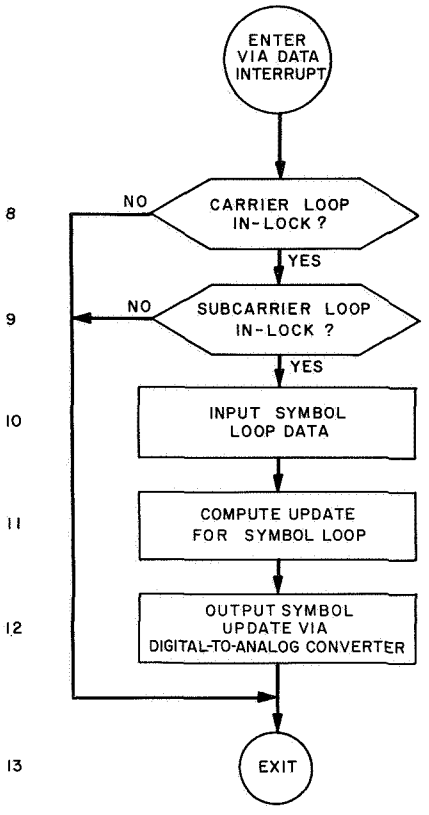

Fig. 13. Mode 1: data interrupt routine (DIRC)

The search algorithm for an arbitrary phase i is as follows. The algorithm assumes that phase i is the correct phase, and M successive channel words, each containing 32 channel symbols, are detected at that phase. The decoding process for each of the M channel words consists of cross-correlating that word with each word in one half of the biorthogonal dictionary and retaining the largest absolute value of correlation. The M correlation values obtained are added together to form the correlation number corresponding to phase i. The local code is then shifted by one symbol period and the process is repeated for phase $i + 1$. After M words are detected at each of the 32 phases, the algorithm selects that phase corresponding to the largest correlation number and shifts the local code to that phase. The value of M determines the probability of false sync. It is expected that $M \approx 24$ will yield a probability of false sync of less than 10^{-3}.

Detection of the channel words and determination of the largest absolute value correlations are done by special-purpose equipment external to the computer. A data interrupt, generated by the special-purpose digital equipment, occurs once every four channel word times. The data input consists of two numbers, viz., the sum of the maximum and non-maximum absolute value correlations over the previous four channel words. Thus, at any phase i, the number M is counted up to in increments of four.

The word acquisition routine (WAR) (Fig. 14) controls the acquisition of word sync. The data interrupt routine for mode 2, DIRD (Fig. 15) inputs the data and computes the update for the symbol tracking loop.

f. Mode 3 (Figs. 16, 17, 18, and 19). When all syncs have been acquired, the program enters mode 3, the data mode. In this mode, the program performs a number of functions simultaneously and in real time.

One function is to record data words, which are brought into the computer via a data interrupt, onto magnetic tape. The data words are input in groups of 4 six-bit words and written on tape in groups of 4096 six-bit words (1024 24-bit words), each group comprising one record on magnetic tape. The program handles the incoming data in the following manner. Two tables are reserved in memory, each the length of one record on magnetic tape. During data recording, the program is simultaneously filling one table while the other is being emptied onto magnetic tape. The magnetic tape recording rate is approximately five times the data input rate, so that recording of one table is completed well ahead of a table-full indication for the other table. When a table-full indication does occur, the program immediately switches over and begins to store data in the empty table while simultaneously initiating recording of the table just filled.

Data is brought into memory via the data interrupt routine. Data interrupts are generated by the special-purpose digital equipment and occur at the rate of one each four channel word times. Writing of a record on magnetic tape is under control of the computer interlace. An end-of-record interrupt is generated after each record has been written. The end-of-record interrupt routine (MEOR) (Fig. 18) sets a flag to notify the program that a write operation has been completed. If a write error is made during the writing of any record, that record is rewritten once on a new section of tape.

In addition to recording data on magnetic tape, the program is responsible for implementation of the filter in the symbol tracking loop, computing estimates for μ and σ, and monitoring the lock status of the carrier, subcarrier, symbol, and word loops. The estimates for

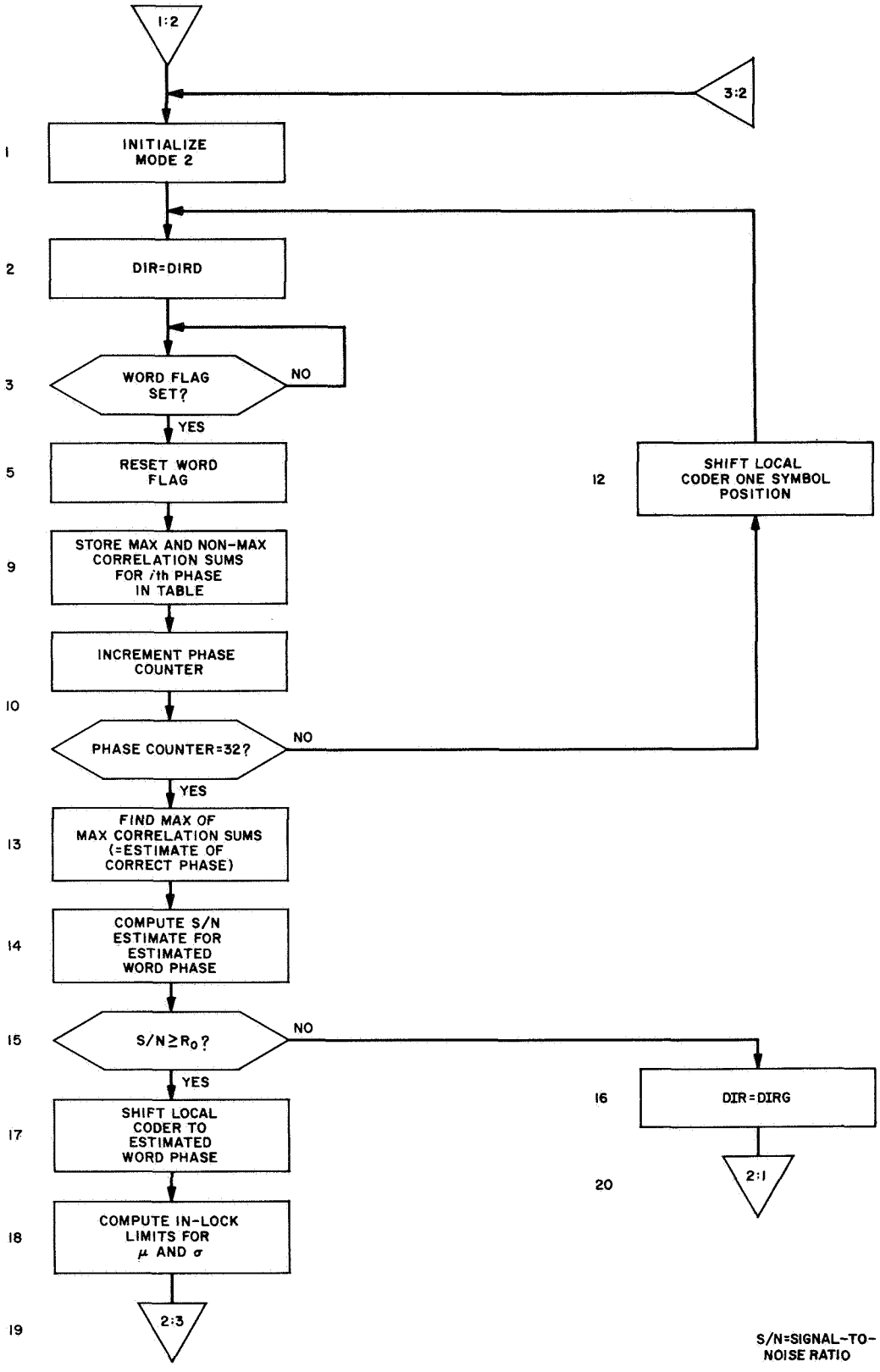

Fig. 14. Mode 2: word acquisition routine (WAR)

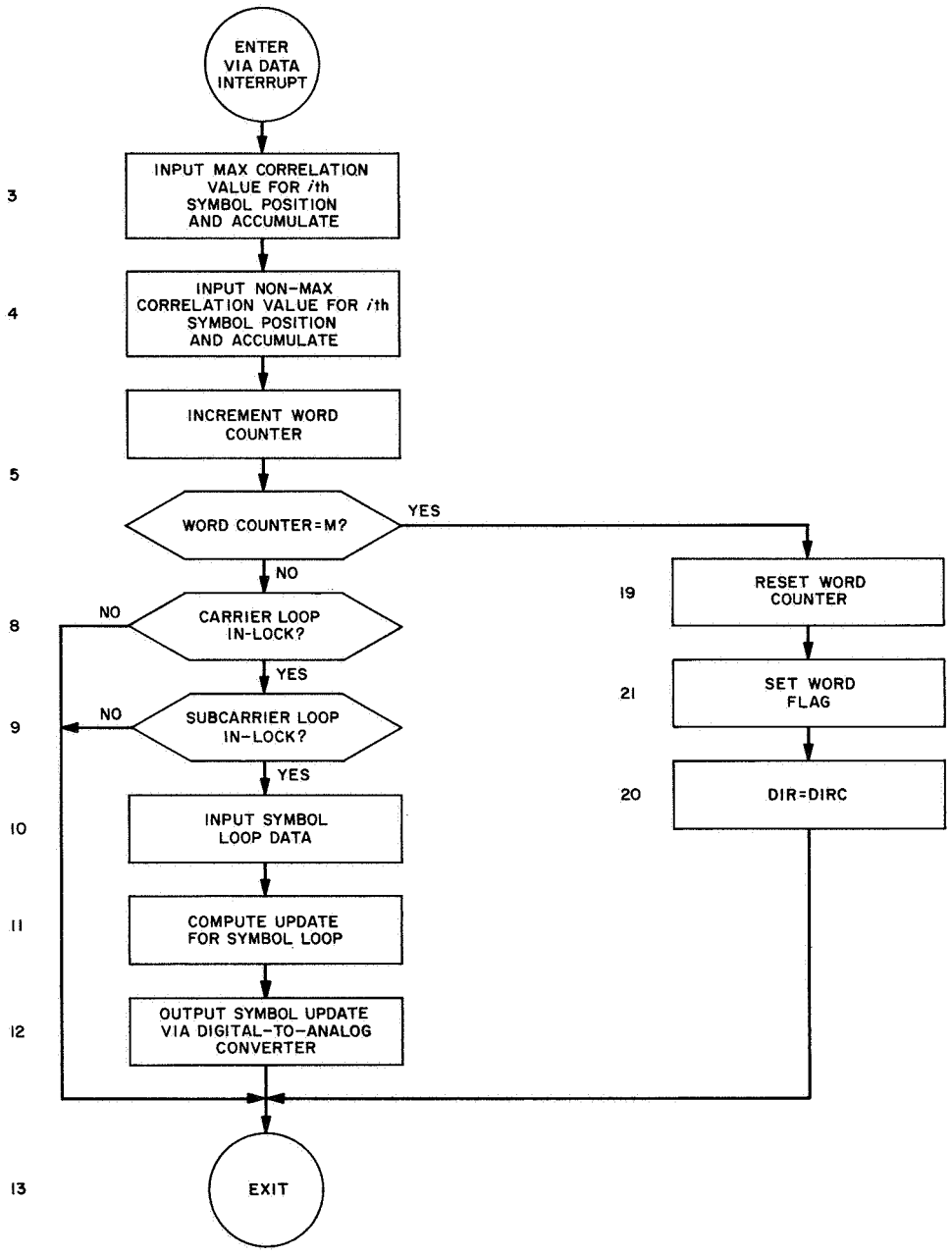

Fig. 15. Mode 2: data interrupt routine (DIRD)

μ and σ, and monitoring the lock status of the various loops, are performed in the main cycle of the data processing routine (DPR). The data processing routine (Fig. 16) is entered directly from mode 2 and, except for time spent processing various interrupts, the program remains in the data processing routine while in mode 3. The program waits in block 3 of the data processing routine until a table-full indication is received from the data interrupt routine. The program then completes one pass through the data processing routine while simultaneously loading data into the empty table in memory. When the pass is completed, the program returns to block 3 to await the next table-full indication.

The functions performed by data interrupt routines DIRA and DIRB (Fig. 17) are the following:

(1) Input packed data word and store.

(2) Input maximum correlation value and accumulate single precision.

(3) Input non-maximum correlation value and accumulate single precision.

(4) Input symbol data and update symbol tracking loop.

(5) Check carrier loop lock status.

(6) Check subcarrier loop lock status.

(7) Check symbol loop lock status.

(8) Augment μ and σ double precision accumulations.

Because of a severe timing problem in mode 3, however, only a subset of these functions is performed in response to any particular data interrupt. There are, in fact, five types of data interrupt responses which may be distinguished:

$$A = (a, b, c, e)$$

$$B = (a, b, c, f)$$

$$C = (a, b, c, g)$$

$$D = (a, b, c, h)$$

$$E = (a, b, c, d)$$

where A = (a, b, c, e) means that the functions a, b, c, and e only are performed in a type A response to a data interrupt.

The manner in which the data interrupt routine responds to a given data interrupt is determined by the contents of the status counter in the interrupt routine. The status counter increments by 1 each time a data interrupt occurs and resets after every 16th data interrupt. The table which follows gives the type of response corresponding to each of the 16 states of the status counter. From the table, it may be seen that the lock status of the carrier (subcarrier, symbol) loop is checked once every 16 data interrupts. Since data interrupts occur approximately 1.5 ms apart, a lock status check is made approximately once every 24 ms. Furthermore, since 1024 data interrupts are required to fill one record with data, it follows that there are 64 lock status checks per record for each of the three loops.

Contents of status counter	Response to data interrupt
$a + 1$	E
$a + 2$	E
$a + 3$	E
$a + 4$	A
$a + 5$	E
$a + 6$	E
$a + 7$	E
$a + 8$	B
$a + 9$	E
$a + 10$	E
$a + 11$	E
$a + 12$	C
$a + 13$	E
$a + 14$	E
$a + 15$	E
$a + 16$	D
$a + 1$	E
$a + 2$	E
.	.
.	.
.	.

a = arbitrary bias in counter.

The interaction of the various routines in mode 3 can best be understood by reference to the timing diagram for mode 3 (Fig. 19). Several different situations are illustrated in this diagram. Line 1 shows operation following entry into mode 3 when initially neither table contains data. The data interrupt routine is the only active routine as table A is being filled, and execution of this routine takes approximately one-half the total

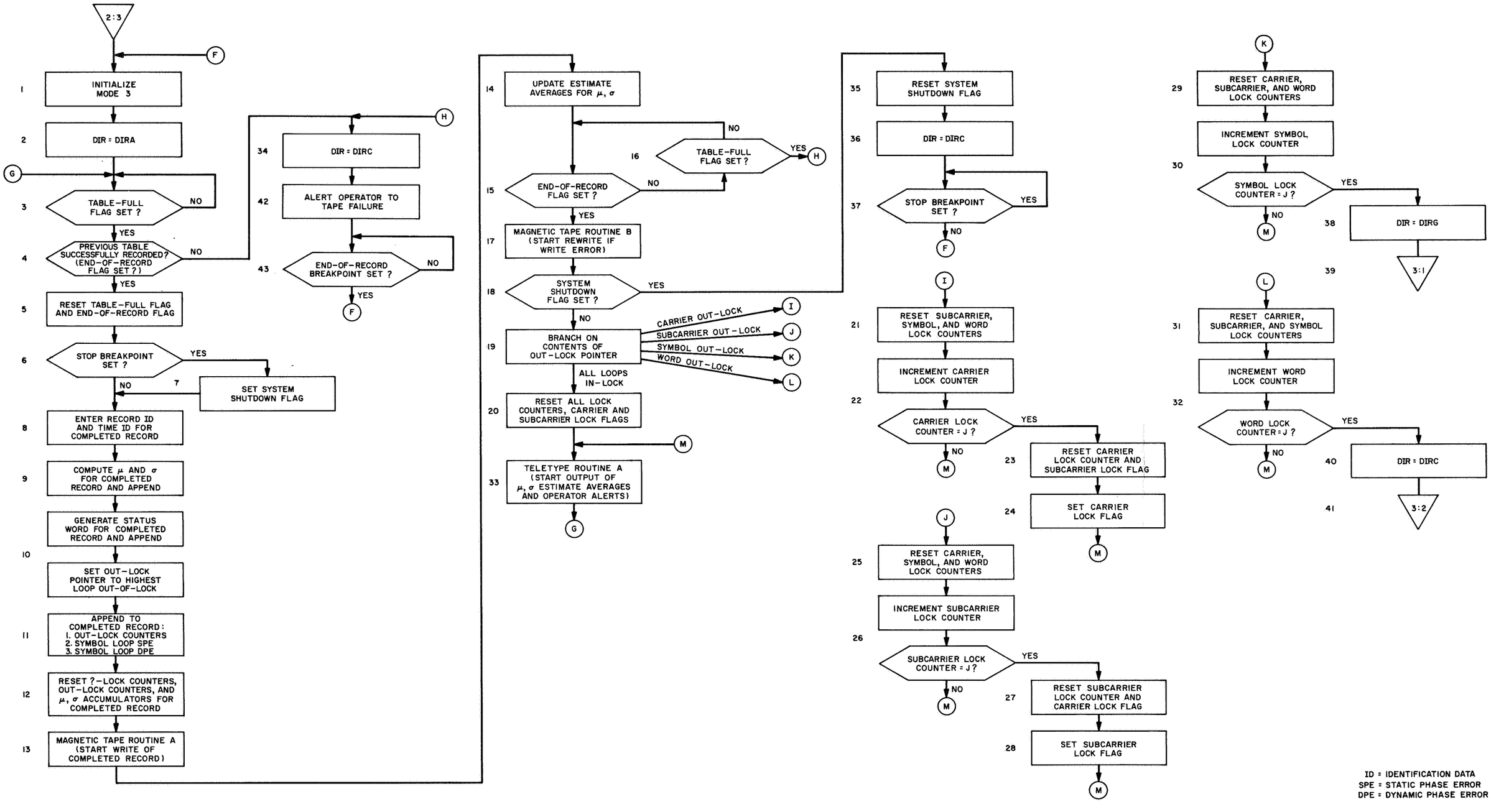

Fig. 16. Mode 3: data processing routine (DPR)

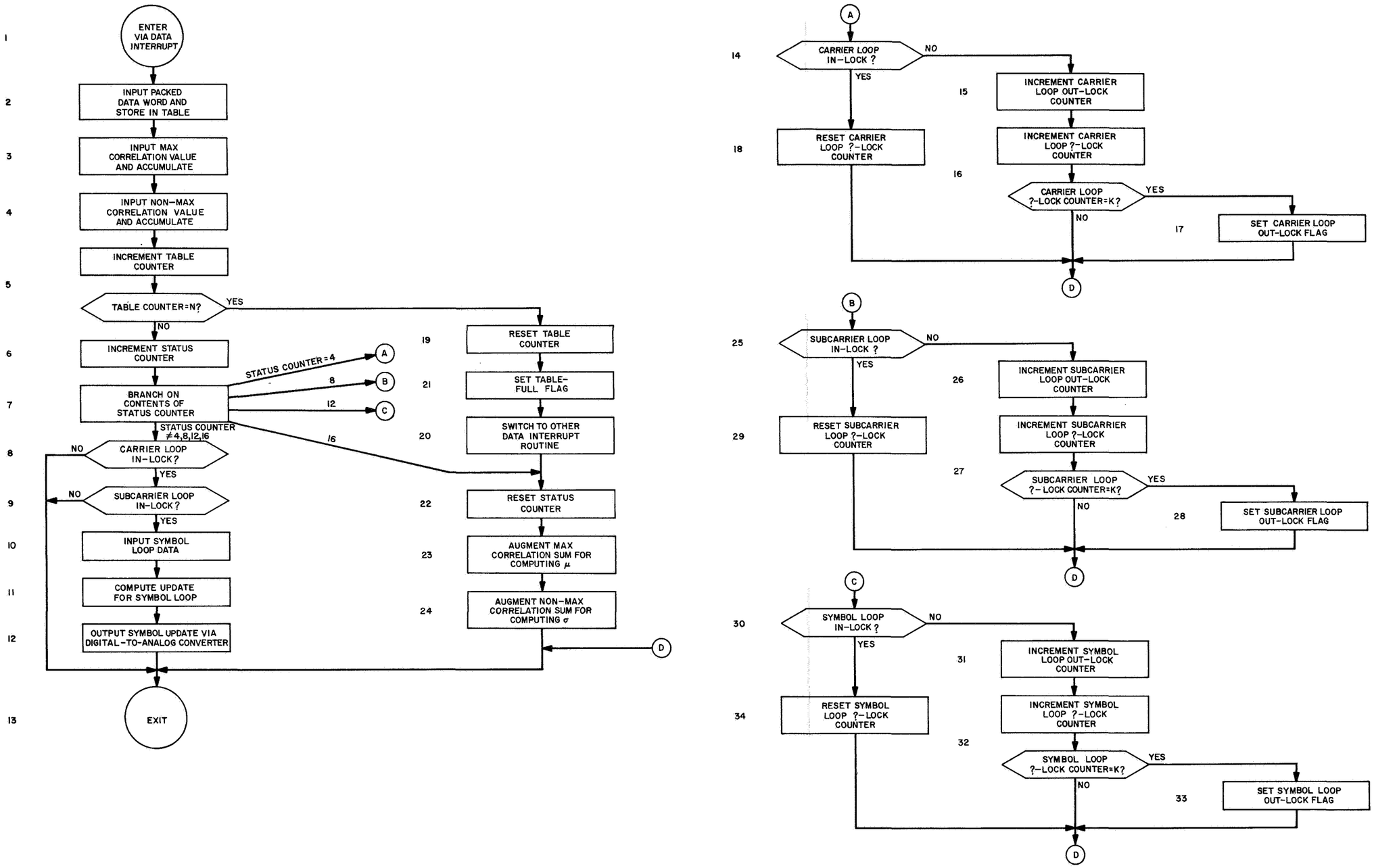

Fig. 17. Mode 3: data interrupt routines (DIRA, DIRB)

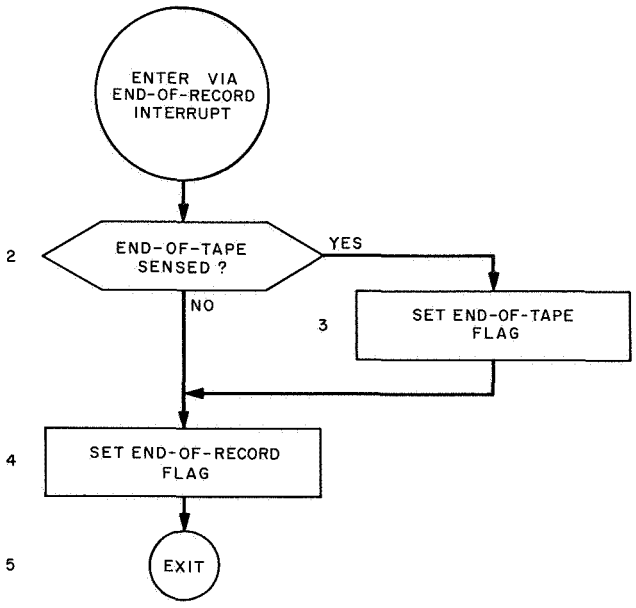

Fig. 18. Mode 3: end-of-record interrupt routine (MEOR)

time between successive interrupts. Line 2 shows operation following insertion of the final entry into table A. The data interrupt routine then starts to fill table B, and the time between successive data interrupts not devoted to processing the interrupt routine is used to execute the main loop of the data processing routine. Line 3 shows operation after the main loop of the data processing routine has been completed, and the program is waiting for table B to fill. The interrupt routine is decimated because the interlace, which controls the writing of table A onto magnetic tape, requires memory accesses, and it has a higher priority than does the central processor.

g. Software status. A preliminary version of the high-rate telemetry project software has been coded and assembled. This version is preliminary in the sense that coding for some of the blocks is incomplete, notably teletype routine A in mode 3, and the program has not yet been debugged. The work which remains to be done in order to produce a finished program consists of: (1) completion of the coding, (2) program checkout, and (3) additional documentation.

3. Digital Equipment, *R. A. Winkelstein*

The digital equipment for the high-rate telemetry project consists of two logical subsystems, namely, (1) the symbol timing loop, and (2) the cross correlation detector. The following describes these subsystems and details some unusual system design concepts.

a. Coding and timing format. The function of the digital equipment is to detect the information transmitted from a spacecraft in the high-rate telemetry channel. The digital equipment operates in conjunction with the Scientific Data Systems 920 computer. This system computer controls both logical subsystems as well as recording the detected telemetry information on magnetic tape. Information from the spacecraft is transmitted in consecutive two-valued units call symbols. For wide-range applicability, the digital equipment is being designed to receive symbols at rates as high as 200,000 symbols/s, although the initial requirement for *Mariner* Mars 1969 is only 86,400 symbols/s. Consecutive groups of symbols form code words. The equipment may be controlled by the system computer to process code words whose symbol length is either 16, 32, or 64. Each code word is equivalent to a block of telemetry information bits. The number of bits per code word is determined by the number of dictionary words for the given code length. Table 2 lists this relationship for the three modes of equipment operation.

Table 2. Relationship of three modes of operation

Information bits/word	Symbols/ word	Dictionary words/code	Correlation stage No. output	Words accumulated for computer
5	16	32	4	4
6	32	64	5	4
7	64	128	6	3

The correlation stage output number refers to the internal equipment connection for the given mode of operation. The number of words processed before information is given to the computer depends upon the computer word length, which is 24 bits. Thus, for *Mariner* Mars 1969, which uses a six-bit code word, the output will be taken from correlation stage No. 5 and four words will be accumulated for each read-in operation.

Symbol time is further subdivided into digit times for internal equipment serial representation of numerical values.

b. Symbol timing loop. The symbol timing loop generates the precise timing pulses needed to demark the block coding symbols of the received telemetry signal. One pulse, called the symbol sync, is generated at the end of each symbol time and is used by the cross correlation detector to obtain the integral of the symbol voltage.

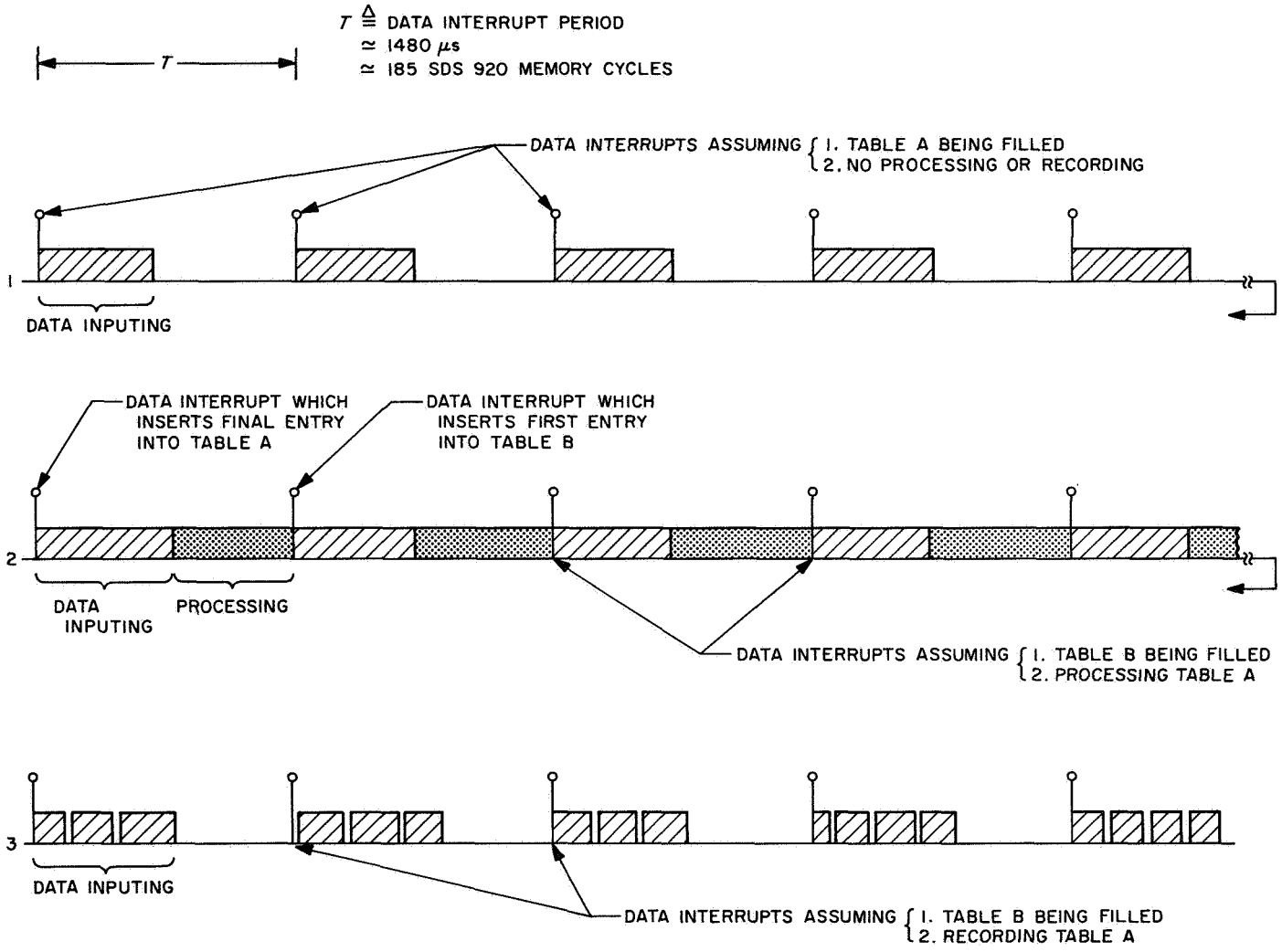

Fig. 19. Mode 3: timing diagram

In order to accomplish its function, the symbol timing loop operates as a phase-locked loop. Values of the integrated signal are obtained using sync pulses which are midway between the symbol sync. An accumulation of these values, suitably modified, results in zero output when the mid-symbol sync pulse occurs exactly at the midpoint of the signal symbol time. Deviations from this midpoint timing produce an error signal which corrects the sync pulse generating circuitry for proper phasing with the input signal.

A block diagram of the symbol timing loop is shown in Fig. 20. The integrated signal from the filter is sampled by means of the analog-to-digital converter (1) and the dump (2). Since these blocks are controlled by the mid-symbol sync, the resulting value is the sum of the last half of one symbol and the first half of the succeeding symbol. Block (3) modifies these values as follows: The unmodified value is given to the accumulator (5) when a positive transition occurs between the adjacent symbols. The complemented value is given to the accumulator (5) when a negative transition occurs between the adjacent symbols. When the adjacent symbols are of the same sign, a zero is given to the accumulator (5). Symbol sign information is obtained by block (4) from the cross correlation detector. 128 samples are summed by the accumulator (5), and the result is given to the system computer (6). The accumulator (5) is immediately reset to zero and the process is repeated.

Loop information given to the computer is digitally filtered by the computer program and used to control the output frequency of a Hewlett-Packard frequency synthesizer (8). Fine frequency control is accomplished by means of the digital-to-analog converter (7) controlling the search oscillator within the synthesizer. Coarse frequency control required during acquisition of symbol sync is accomplished through the interface (9) and the drivers (10) acting upon the pushbutton decades of the synthesizer. The output of the synthesizer (8) is used by the timing (11) to generate symbol and mid-symbol sync pulses.

c. Cross correlation detector. The cross correlation detector receives consecutive code words of information and cross-correlates each received word with all code words of the code dictionary. Information bits of the dictionary word with the highest correlation value are packed into a 24-bit register. A second register accumulates this highest correlation value, and a third register accumulates a typical non-highest correlation value. Information in these last two registers enables the computer to determine the signal-to-noise ratio of the received telemetry signal. After processing the number of words as shown in Table 2, the cross correlation detector transfers the register information to the system computer, the registers are reset to zero, and the process repeated for the next batch of code words.

Figure 21 is a block diagram of the cross correlation detector. Timing for the detector is done by blocks (1), (2), and (3). The digit counter (1) counts 10 clock pulses which come from the clock generator (4) at a 2-MHz rate. Use of double rail logic permits serial numerical

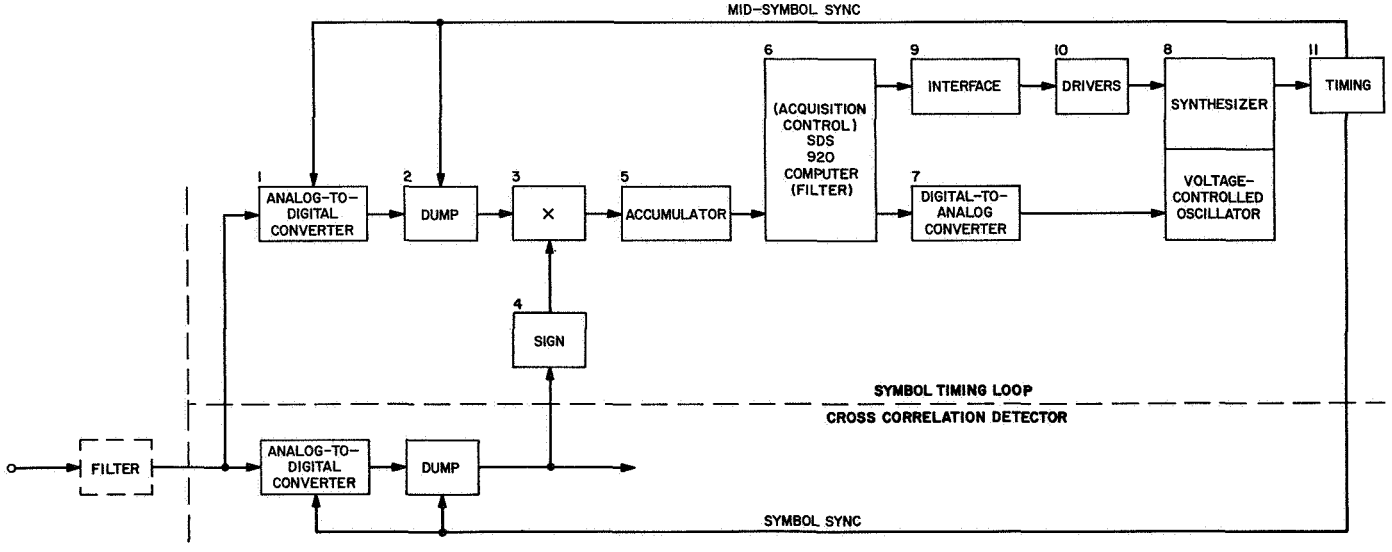

Fig. 20. Symbol timing loop block diagram

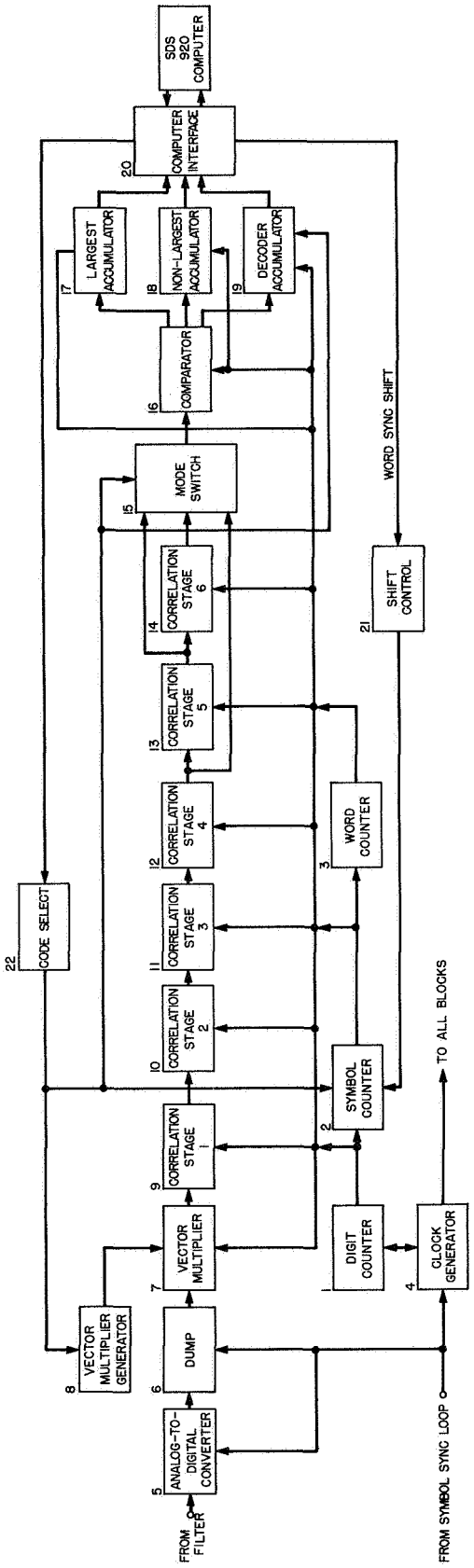

Fig. 21. Cross correlation detector block diagram

representation of 19 binary digit numbers plus sign. The symbol counter (2) counts symbols during each word time and operates the correlation stages in the correct sequence. At the end of each word a pulse is sent to the word counter (3), which keeps track of the number of words processed before being sent to the computer.

The same integrated signal that goes to the symbol timing loop also goes to the cross correlation detector. Sampling of the signal is performed by the analog-to-digital converter (5) and dump (6) under control of the symbol sync pulses from the symbol timing loop. The comma-free code vector is removed by the vector multiplier (7) and vector multiplier generator (8). The signal code, now biorthogonal, is cross-correlated with half the code dictionary in correlation stages 1 through 6, blocks (9) through (14). A high positive correlation value indicates the correct dictionary word. A high negative correlation value indicates the one's complement of the selected dictionary word. The mode switch (15) selects the output from the proper correlation stage as listed in Table 2. The results of the correlation go to the comparator (16), which puts the largest correlation value into the largest accumulator (17), the corresponding information bits into the decoder accumulator (19), and a typical non-largest correlation value into the non-largest accumulator (18). This non-largest correlation value is equal to the correlation between the code word and the last word in the code dictionary. If this last correlation value is the largest, then the non-largest value is set to zero. After the required number of words have been processed as determined by the word counter (3), the information is transferred to the system computer via the computer interface (20).

The ratio of the largest correlation value to the typical correlation value is used in synchronizing the symbol counter (2) to the incoming signal. This ratio should be much greater for the in-phase condition than for any of the out-of-phase conditions. Accordingly, in the word acquisition mode, the computer periodically shifts the symbol counter (2) via the computer interface (20) and shift control (21). After each shift, the computer calculates and records the signal-to-noise ratio. All possible phases will have been examined when the number of shifts equals the number of symbols in a code word. After examining its table of ratios, the computer again shifts the word counter (3) to that phase which has the highest ratio. The code select (22) under control of the computer establishes which of the three code modes listed in Table 2 will be utilized.

d. Digital dump. To facilitate equipment design, two unusual system concepts have been utilized. First of these is the digital dump, which forms the basic data quantities to be processed by the remaining system. Each quantity is the integral of the demodulated signal over a time T equal to the symbol period of the incoming data. In the cross correlation detector subsystem, T starts with the beginning of a symbol and ends with the beginning of the next symbol. In the symbol timing loop subsystem, T starts at the midpoint of a symbol and ends at the midpoint of the next symbol.

Normally, at low data rates, this function is accomplished by an analog integrate-and-dump circuit which then feeds an analog-to-digital converter for the remaining digital processing. At high data rates, the disadvantages of the dump inaccuracy and lost time might be avoided by replacing the integrate-and-dump circuit with a perfect integrator and digitally subtracting the previous output of the analog-to-digital converter from the present output to obtain the desired integral over the past period. Exact implementation of this scheme is not feasible for two reasons. First, noise and drift would saturate the integrator, and second, the effect of the finite levels of quantization in the analog-to-digital converter would cause high system degradation at low signal-to-noise ratios (SPS 37-45, Vol. IV, p. 290).

Therefore, the input to the digital equipment is the output of an imperfect integrator, which is a simple low-pass RC filter. After analog-to-digital conversion, the digital dump logic calculates an approximation to the required integral ΔE from:

$$\Delta E = E_n - \alpha E_{n-1} \tag{1}$$

where E_n = the present voltage sample, E_{n-1} = the previous voltage sample, and α = a positive constant less than unity.

The constant α, the filter time constant RC, and the sample or symbol period T are interrelated as follows: Assuming a step input voltage E to the filter, the output voltage E_n is

$$E_n = E(1 - e^{-T/RC}) + E_{n-1} e^{-T/RC} \tag{2}$$

where e is the Naperian logarithmic base. Substituting Eq. (2) into Eq. (1) gives

$$\Delta E = E(1 - e^{-T/RC}) + E_{n-1}(e^{-T/RC} - \alpha)$$

To eliminate the dependence of ΔE on E_{n-1}, α is

$$\alpha = e^{-T/RC}$$

For ease of digital implementation, α is made to be

$$\alpha = 1 - 2^{-N} \tag{3}$$

where N is a positive integer.

Table 3 shows the relationship between N and T/RC, as well as the degradation from theoretical, using various numbers of analog-to-digital conversion bits. These values are obtained from SPS 37-45, Vol. IV, p. 290, and assume that the range of the digital-to-analog converter is $\pm 3 \times$ the rms value of the input signal plus noise. The starred value of N equal to 3 is used because the corresponding value of T/RC gives least degradation for 7- and 8-bit conversion and negligible degradation for higher bit conversions. Thus, the resultant equation implemented in the digital dump is found by substituting Eq. (3) into Eq. (1).

$$\Delta E = E_n - E_{n-1} + 2^{-3} E_{n-1}$$

For the *Mariner* Mars 1969 mission, the symbol period T for a symbol rate of 86,400 symbols/s is 11.574 μs. Dividing this by 0.134, the value of T/RC found in Table 3, gives the required value for the filter time constant to be 86.4 μs.

e. Correlation method. The second unusual system concept utilized by the digital equipment is the method of correlation. Correlation of the incoming signal code word with a particular dictionary word consists of the multiplication of each symbol integral with its corresponding dictionary word symbol. These products are then summed to give the correlation value. Since the dictionary word symbols are assigned values of either $+1$ or -1, the correlation process reduces to one of simple addition or subtraction of the signal integrals according to the rules of the dictionary code word. The codes detected by the digital equipment are Reed–Muller biorthogonal (q,n) binary codes which have 2^n dictionary words and q symbols equal in number to 2^{n-1}. A biorthogonal code dictionary may have its words divided into two groups, a word in one group being the complement of a word in the second group. Therefore a signal word need only be correlated with the 2^{n-1} words in one group. A large negative correlation value would indicate that the dictionary word corresponding to the signal word is the complement of the dictionary word giving the negative correlation.

Table 4a shows a (2,2) code with the two dictionary words used for decoding. Y_0 is the value of the first symbol integral of the incoming signal word, and Y_1 is the value of the second symbol integral of the incoming word. For the (2,2) code there are only two symbols per code word. The code word rules for forming the correlation values from the incoming symbol integrals are $(Y_0 + Y_1)$ for dictionary word 0, and $(Y_0 - Y_1)$ for dictionary word 1. Similarly, the following signal word has correlation values $(Y_2 + Y_3)$ and $(Y_2 - Y_3)$, etc.

Figure 22 is a block diagram of equipment used to obtain the (2,2) code correlations in real time (SPS 37-39, Vol. IV, p. 247). The input is serialized values of the Ys as might be obtained from the digital dump logic described above. Starting with the switch in position 1, the serial value of Y_0 enters and fills the shift register. The switch is then placed in position 2, and Y_0 comes out of the register while Y_1 appears on the input line. The adder output $Y_0 + Y_1$ goes out of the equipment while the subtractor output $Y_0 - Y_1$ goes into the shift register right behind Y_0 as Y_0 is coming out. At the completion of this operation, the switch is returned to position 1, and the value $Y_0 - Y_1$ comes out of the register and out of the equipment. Simultaneously, Y_2 from the next incoming word fills into the shift register right behind the value of $Y_0 - Y_1$, and the next cycle is begun. There is a one-to-one correspondence between incoming symbol

Table 3. DB degradation for digital-to-analog bits

N	T/RC	6	7	8	9	13
1	0.693	0.1791	0.1716	0.1697	0.1693	0.1961
2	0.288	0.0542	0.0360	0.0314	0.0303	0.0299
*3	0.134	0.0728	0.0232	0.0107	0.0075	0.0065
4	0.0645	0.1974	0.0513	0.0140	0.0046	0.0015
5	0.0317	0.5961	0.1571	0.0401	0.0103	0.0004

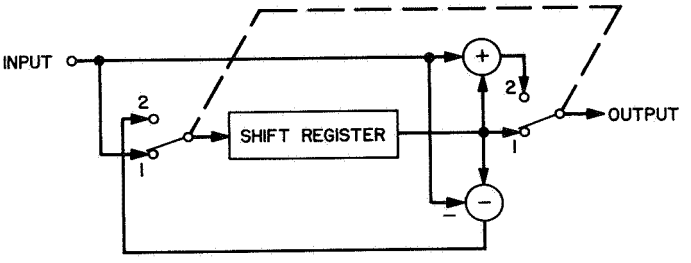

Fig. 22. Correlation stage

Table 4. Reed–Muller codes

Type	Dictionary word	Code	Correlation values	
			Current word	Next word
		Y_0 Y_1		
a. (2,2) code	0	1 1	$Y_0 + Y_1$	$Y_2 + Y_3$
	1	1 −1	$Y_0 - Y_1$	$Y_2 - Y_3$
		Y_0 Y_1 Y_2 Y_3		
	0	1 1 1 1	$(Y_0 + Y_1) + (Y_2 + Y_3)$	$(Y_4 + Y_5) + (Y_6 + Y_7)$
b. (4,3) code	1	1 −1 1 −1	$(Y_0 - Y_1) + (Y_2 - Y_3)$	$(Y_4 - Y_5) + (Y_6 - Y_7)$
	2	1 1 −1 −1	$(Y_0 + Y_1) - (Y_2 + Y_3)$	$(Y_4 + Y_5) - (Y_6 + Y_7)$
	3	1 −1 −1 1	$(Y_0 - Y_1) - (Y_2 - Y_3)$	$(Y_4 - Y_5) - (Y_6 - Y_7)$
		Y_0 Y_1 Y_2 Y_3 Y_4 Y_5 Y_6 Y_7		
	0	1 1 1 1 1 1 1 1		
	1	1 −1 1 −1 1 −1 1 −1		
	2	1 1 −1 −1 1 1 −1 −1		
c. (8,4) code	3	1 −1 −1 1 1 −1 −1 1		
	4	1 1 1 1 −1 −1 −1 −1		
	5	1 −1 1 −1 −1 1 −1 1		
	6	1 1 −1 −1 −1 −1 1 1		
	7	1 −1 −1 1 −1 1 1 −1		

values and outgoing correlation values with an appropriate delay since the equipment cannot start calculating correlation values for a particular word until receipt of the last symbol of that word.

The next code in the hierarchy of Reed–Muller codes is the (4,3) code shown in Table 4b. It is formed by four groups of the previous (2,2) code. The lower right-hand group is the complement of the (2,2) code, just as the lower right-hand symbol of the (2,2) code is the complement of the other symbols. Signal words have four symbols labeled Y_0 through Y_3 for the incoming word, Y_4 through Y_7 for the next word, etc. Correlation values for two words are formed following the rules of the code as before, but are shown with a particular grouping. This grouping shows that the correlation values of the (4,3) code are formed by operating on values obtained from the equipment shown in Fig. 22.

Equipment for calculating (4,3) code correlation values is thus formed by cascading two stages of equipment, each stage being equivalent to that shown in Fig. 22. The first stage operates as described for the (2,2) code. The second stage has a shift register twice as long as the previous stage, and the switch dwells at each switch position for two symbol times. Operation of the second stage begins at switch position 1 when $Y_0 + Y_1$ appears on the input line. $Y_0 + Y_1$ goes into the register followed by $Y_0 - Y_1$, which also goes into the register. The switch then goes to position 2 and $Y_2 + Y_3$ appears at the input while $Y_0 + Y_1$ comes from the register. The output line has the adder output $(Y_0 + Y_1) + (Y_2 + Y_3)$ while the subtractor output $(Y_0 + Y_1) - (Y_2 + Y_3)$ goes into the register right behind $Y_0 - Y_1$. Next, $Y_2 - Y_3$ appears on the input line, and the output line contains the adder output $(Y_0 - Y_1) + (Y_2 - Y_3)$ while the subtractor output $(Y_0 - Y_1) - (Y_2 - Y_3)$ goes into the register behind $(Y_0 + Y_1) - (Y_2 + Y_3)$. The switch then returns to position 1. As the correlation values $(Y_0 + Y_1) - (Y_2 + Y_3)$ followed by $(Y_0 - Y_1) - (Y_2 - Y_3)$ come out of the register to the output line, $Y_4 + Y_5$ followed by $Y_4 - Y_5$ of the next word comes into the register starting the next cycle of operation.

Table 4c shows the (8,4) code which is constructed from the (4,3) code in the same way that the (4,3) code was constructed from the (2,2) code. Real-time detection is mechanized by cascading a third stage to the previous

two stages where the register length is twice as long as in the preceding stage and the switch dwell time is twice as long as in the preceding stage. Thus the (16,5) code uses four stages, the (32,6) code uses five stages, and the (64,7) code requires six stages. As shown in Fig. 21, the digital equipment can detect code words in either the (16,5) code, the (32,6) code, or the (64,7) code merely by selecting the output of the proper stage.

4. Demonstration System Verification, *J. C. Springett, F. L. Larson, and G. L. Fultz*

a. Introduction.

Task objectives. The primary objective of the demonstration system verification task is to continually test the laboratory set A high-rate system, or portions of the system, as it evolves, in order to establish system performance relative to the parameters to be used in the design control table. Since the system is intended to be a high-performance system used in situations where margins are small, e.g., in *Mariner* Mars 1969 where the margin is approximately 2 dB, considerable care must be taken to ensure that losses due to improper design or malfunctioning elements do not significantly degrade the performance.

A secondary objective of the effort is to build a functional breadboard of the high-rate detector early in the program, in order to: (1) gain experience in working with block-coded detection techniques, (2) establish testing criteria and procedures, and (3) obtain performance parameters from testing the functional breadboard which can subsequently be used for establishing a base for the tests on laboratory set A. The word "functional" is used to connotate a detector which performs, in a statistical sense, as the actual high-rate system design, but which is not necessarily constructed (hardware and software) in the same manner.

A third objective of the verification work will be to conduct analytical and experimental studies of basic concepts and mechanizations in order to refine the design of the system. Items scheduled to be investigated include: (1) the matched filter with a digital dump, (2) the minimum number of analog-to-digital levels required to give good performance, and (3) hardware–software tradeoffs.

Task approach. The approach to be taken for construction of the laboratory breadboard has been one of using existing on-hand equipment so that a working breadboard could be realized in as short a time as possible. As a result, the laboratory breadboard operates at a bit rate much lower than 16.2K bits/s. This, however, does not in any way impair the establishment of the desired statistical parameters, since the establishment and maintenance of word sync, and the probability of error as a function of ST_B/N_0, are independent of data rate. A detailed discussion of the breadboard appears in Part *c*.

During the first three months the laboratory set A is being tested, it will undergo the identical tests that have been made on the laboratory breadboard. Any difference in test results between laboratory set A and the breadboard will be investigated, and corrective action will be recommended as necessary.

Finally, the special studies will primarily be analytical in nature with verification via computer simulation.

b. Methods for obtaining accurate experimental results.

Measurement techniques and statistical estimators. The results of testing the breadboard and laboratory set A will only be as good as the accuracy by which the experiment is set up and run. Since the theoretical system margin is only 2 dB, it does not take many errors on the order of tenths of a dB to cause this margin to approach zero, or even become negative. As a result, it is imperative that very accurate measurements be made in order that mean errors and their standard deviations be held to a minimum.

Measurement errors can occur due to a large number of causes, such as:

(1) Improper signal and noise levels at any point within the system.

(2) Not operating system elements at their design points, e.g., having too large a static phase error in a tracking loop.

(3) Failure to check for problems associated with grounding signal lines, and loading of one element by another.

(4) And perhaps the most critical cause of all is the set-up, measurement, and maintenance of signal-to-noise ratio (S/N).

Testing of the laboratory detector breadboard has provided an excellent means of establishing accurate measurement techniques. For example, it has been found that proper scaling of the signal and noise voltages into the

analog-to-digital converter, accurate knowledge of the *RC* time constant, and the elimination of dc offsets in the system are all very important to obtaining optimum operation. To check these parameters, special test software has been produced to enable the computer to perform diagnostic evaluations prior to each test run.

The establishment of S/N is done via statistical estimators. A "rough" S/N is first set up using calibrated filters, attenuators, and rms meters. The accuracy here may be only within several tenths of a dB. The computer is then used to calculate the mean and variance of sample values of signal-plus-noise, and establish a S/N estimate (an introduction to this technique, SNORE, may be found in SPS 37-27, Vol. IV, pp. 169–184). This measurement is made just prior and subsequent to the test, and the average value taken to be the S/N for that test. Over a number of tests, the standard deviation on the S/N estimate may also be obtained. Using this technique, accuracies to better than 0.1 dB are obtained.

The RF test console. Generally, baseband S/N testing can be accomplished with absolute accuracies of about 0.1 dB. Testing with an RF system, however, is typically a different story because such factors as instability, RF leakage, inadequate measurement equipment, inability to set attenuations to within a fraction of a dB over a wide dynamic range, all contribute significantly to measurement error. In many cases, accuracies to no better than 1 or 2 dB are possible, and repeatability is very poor.

This problem of testing through RF systems was realized several years ago, and as a result, a contract was awarded to the Westinghouse Corp., Surface Div., to study this problem, build an RF system simulator, and develop appropriate accurate measurement techniques. The resulting simulator, called the RF test console (RFTC), was to provide an overall accuracy an order of magnitude better than that obtainable from an operational DSIF transmitter/receiver pair. Figure 23 shows the completed RFTC.

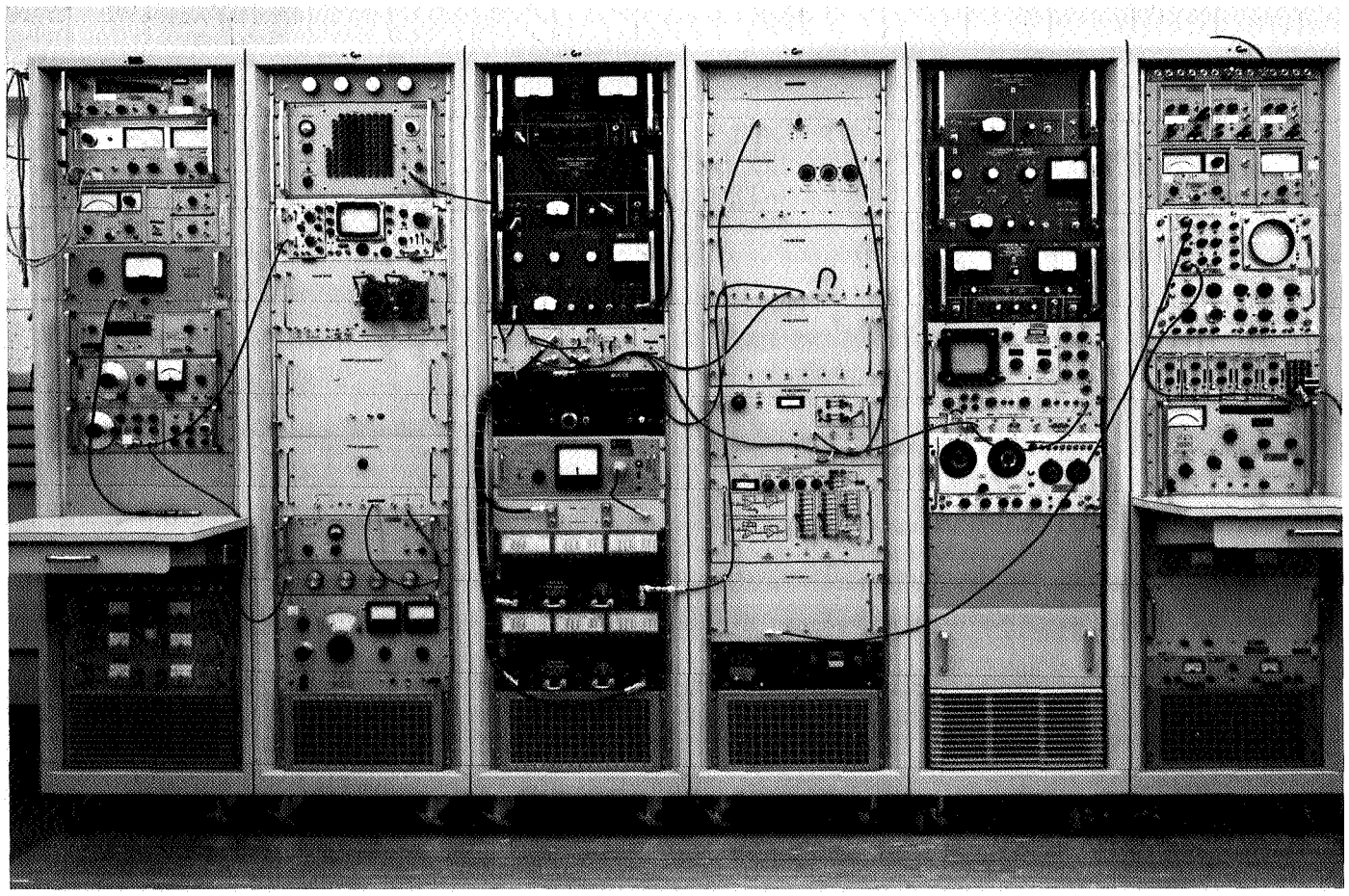

Fig. 23. RF test console

The RFTC has capability for all forms of modulation (AM, FM, PM),[3] however, this article will be confined to the PM subsystem.

The PM subsystem is outlined in Fig. 24. The PM subsystem consists of the PM modulator and PM receiver. Each of these units was fabricated to its own specification; however, several specifications pertain to the performance of the transmitter/receiver pair. Table 5 presents the principal PM subsystem specifications. The frequency and phase stability specifications pertain to not only the PM transmitter/receiver pair but also the transmitter and receiver frequency synthesizer.

The PM subsystem short- and long-term frequency stability parameters, as defined by the specifications, are determined by the transmitter reference oscillator, located in the transmitter frequency synthesizer. The design plan indicated that the transmitter/receiver frequency stability specification required proportional temperature control of the oscillator's crystal.

The PM subsystem phase stability is a function of the phase stability of the transmitter frequency standard, the PM receiver reference oscillator, the carrier tracking loop voltage-controlled oscillator, the system frequency multipliers, amplifiers, and receiver noise figure. The measured system phase noise was 0.25 deg rms in $2B_{LO}$ of 3.0 Hz. The PM subsystem fidelity specification is a function of the PM modulator linearity, the phase linearity of the receiver input amplifier, mixer, and wideband 10-MHz IF amplifier. The PM modulator was implemented using a phase-locked loop as shown in Fig. 25. Principal specifications are given in Table 6.

Specifications on the PM receiver appear in Table 7, and a detailed block diagram is shown in Fig. 26. The receiver input amplifier and wideband IF amplifier were designed to exhibit maximally flat group delay or linear phase response. The receiver mixer and limiters were designed as broadband units that exhibit a linear phase response over the band of interest. The receiver demodulation channel phase detector is a nonlinear sinusoidal unit (as required by DSIF simulation), and the phase

[3]AM = amplitude modulation, FM = frequency modulation, PM = phase modulation.

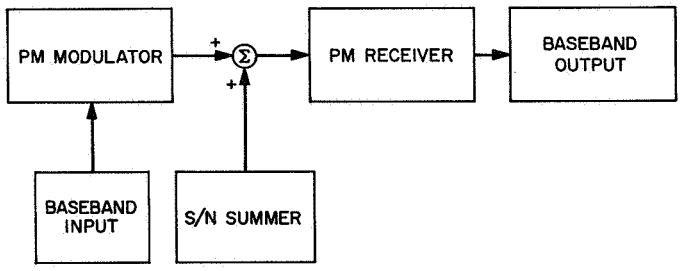

Fig. 24. PM subsystem

Table 5. PM subsystem specifications

Parameter	Specification
Frequency stability Transmitter frequency source Receiver reference oscillator	Shall have a short-term stability measured over a 1-min period of 1 part in 10^7 Shall have a long-term stability measured over a 4-h period of 5 parts in 10^7
Phase stability Transmitter/receiver	Shall cause no more than 1-deg rms phase error in 2 B_{LO} of 3.0 Hz
Fidelity Transmitter/receiver	All spurious sidebands within the modulation passband are 30 dB (40-dB design goal) below the modulated carrier or 40 dB (50-dB design goal) below unmodulated power when the transmitter is modulated with two pure sinusoids of any frequency and at modulation indices within the phase modulator design limits

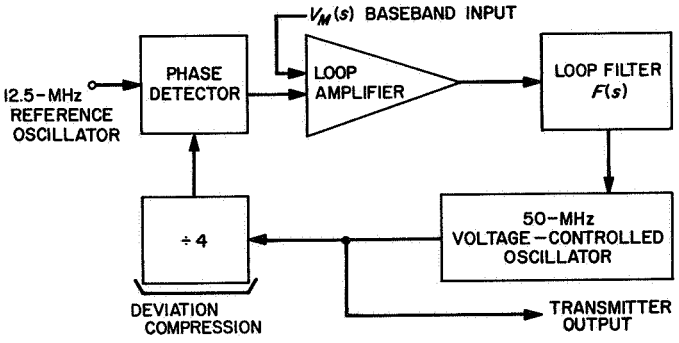

Fig. 25. PM modulator

Table 6. PM modulator specifications

Parameter	Specification
Carrier frequency	50 MHz, tuneable ±500 Hz
Phase modulator	
Frequency response	±0.1 dB to 500 kHz ±0.5 dB to 500 kHz–1.0 MHz
Phase deviation	±3.0 rad dc to 500 kHz ±1.0 rad dc to 1.5 MHz

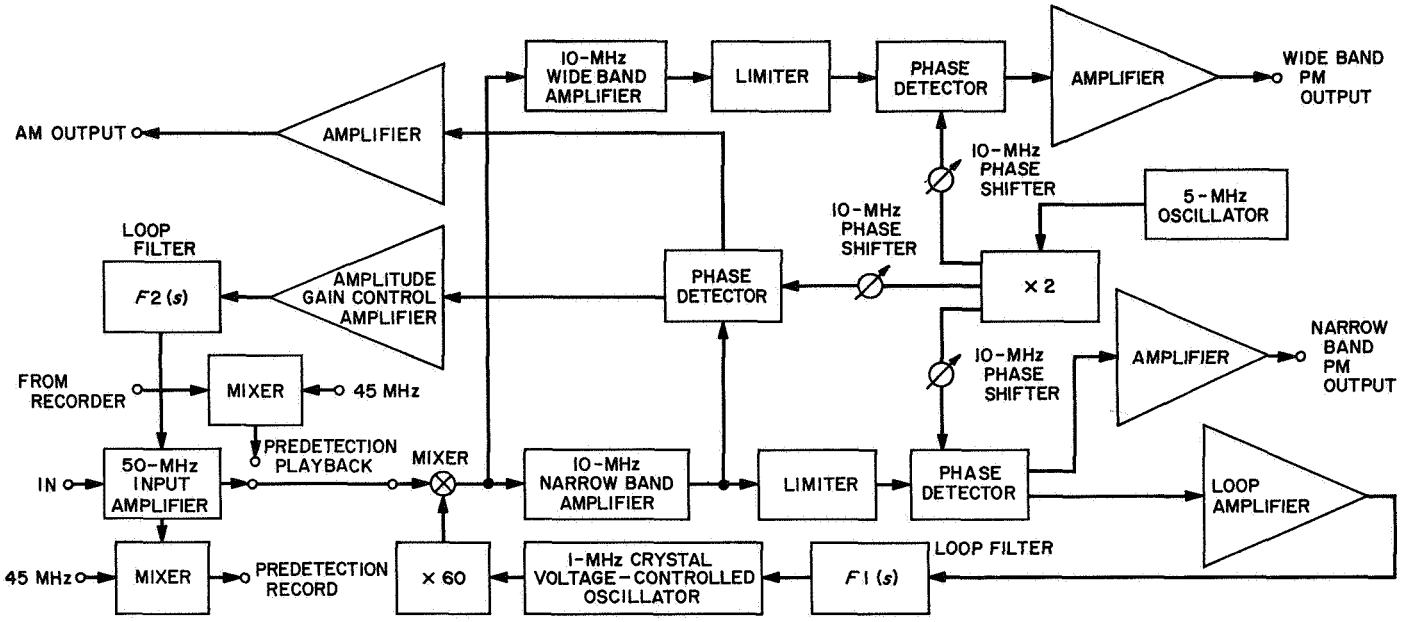

Fig. 26. PM receiver

Table 7. PM receiver specifications

Parameter	Specification
Carrier frequency	50 MHz
Input amplifier	
Bandwidth	3 dB, 10 MHz min flat within ±0.25 dB, within ±2 MHz of 50 MHz
Phase linearity	Compatible with PM subsystem linearity specification
Amplitude gain control range	30 dB
Narrow band IF	
Center frequency	10 MHz
Bandwidth	2 kHz (3 dB)
Phase symmetry	±5 deg for frequencies, ±1 kHz of center frequency (±6 kHz design goal)
Wideband IF	
Center frequency	10 MHz
Bandwidth	6 MHz (3 dB), ±0.5 dB within 1.5 MHz of center frequency
Phase symmetry	±5 deg over 6-MHz passband

Parameter	Specification
Wideband phase detector	
Video 3-dB bandwidth	5 MHz
Dynamic range	40 dB
Fidelity	Compatible with PM subsystem linearity specification
Carrier tracking loop	
No noise loop gain	Constrain static phase error 1 deg, transmitter detuning ±500 Hz
Loop bandwidths $2B_{L0}$	3.0, 12.0, 20.0, and 48.0 Hz, variable 1.0 Hz to 1 kHz
Loop filter	Active and passive, 1% resistors, 3% capacitors
Loop gain stability	±3% over transmitter tuning range
Amplitude gain control loop	
Min loop gain	20
Loop noise bandwidths	0.01, 0.1, 1.0, and 10 Hz
Loop filter	Passive, 1% resistors, 2% capacitors

detector output filter exhibits a Butterworth amplitude response with an inherent nonlinear phase response.

The heart of the entire RFTC is the linear signal-to-noise summer which mixes the output of the transmitter with bandpass noise centered at 50 MHz. Specifications on the summer, and the measured performance of the summer, appear in Table 8. Figure 27 shows the block diagram of the S/N summer. The primary function of the S/N summer is to enable the operator to change relative signal-to-noise ratios accurately over a wide dynamic range.

Table 8. Linear S/N summer specified and measured values

Parameter	Value	
	Specified	Measured
S/N dynamic range	0 to 100 dB (+30 to −70 dB)	100 dB
Absolute accuracy	±0.3 dB over 4-h period	±0.156 dB
S/N ratio repeatability	±0.05 dB over 4-h period	±0.024 dB
Precision noise and signal attenuators	Resolution of 0.1 dB with ±0.1-dB uncertainty	—
Power monitor	Resolution better than 0.05 dB with ±0.1-dB uncertainty	—
Noise power stability	Resolution of 0.1 dB with ±0.1-dB uncertainty	±0.013 dB
Noise bandwidth	46 to 54 MHz ±0.05 dB	46 to 54 MHz ±0.05 dB
Noise amplitude	Linear up to 5 σ Vrms	—
Noise power spectral density	Constant within ±0.05 dB from 48 to 52 MHz	±0.05 dB

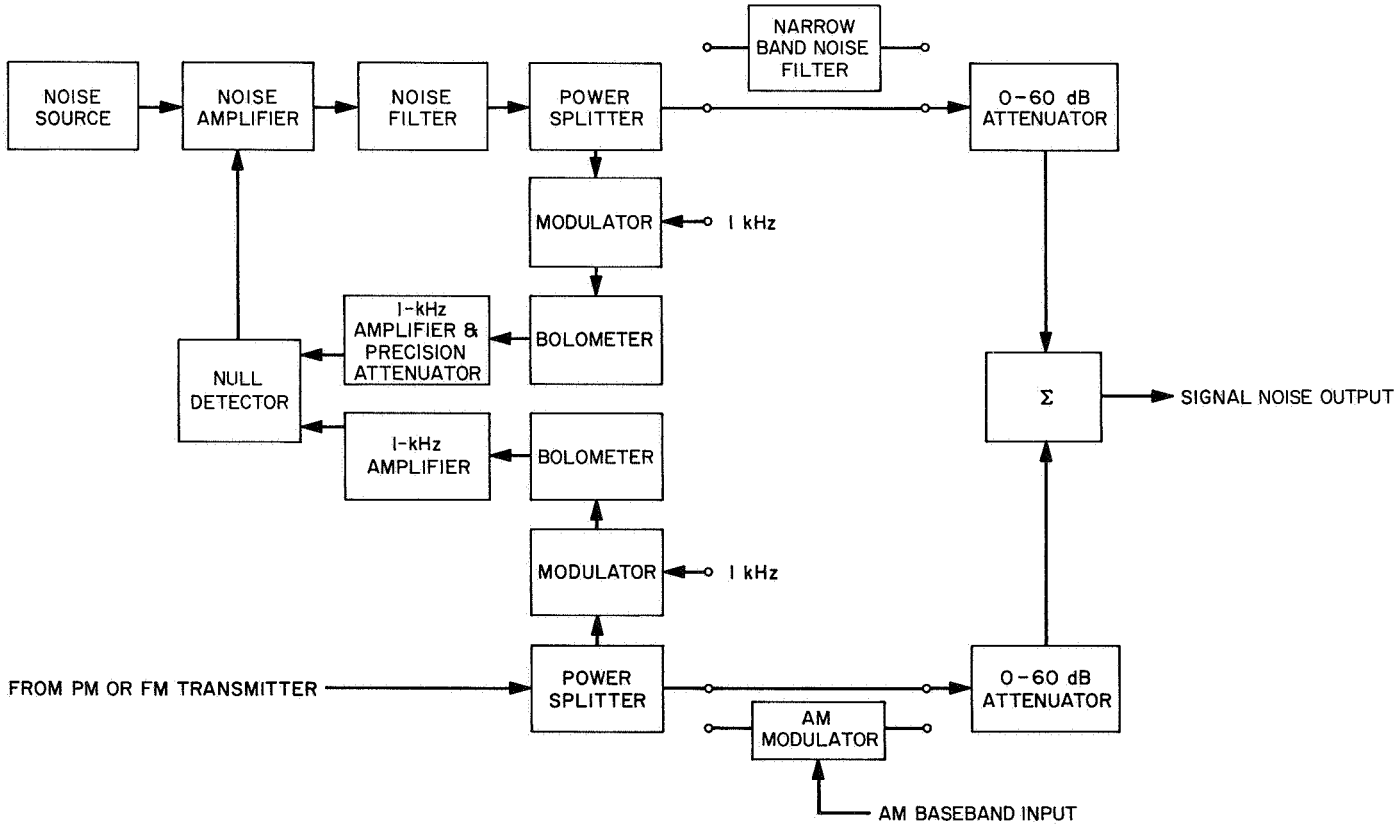

Fig. 27. S/N summer

The S/N summer is a closed-loop system whereby the angle modulated carrier input serves as a power reference. A portion of the input carrier power is compared to a portion of the noise power generated within the summer. If an error exists between the compared signal and noise power, the resulting error voltage controls the noise power such that it is forced to equal the signal power. In this manner, the magnitude of the noise power is slaved to the signal power by the control loop. Note that the signal power may change (for example the transmitter power output may change slightly); however, the relative signal-to-noise ratio established by the summer does not change because of the loop's correction. Outside the control loop, the signal and noise paths have fixed precision attenuators or pads that determine the relative levels of the signal and noise. Further, the signal and noise paths have separate precision variable attenuators (variable from 60 dB in 0.1-dB increments) such that the relative signal and noise power may be precisely varied. After the carrier and noise signals traverse their respective variable attenuators, they are linearly summed in a precision resistive power adder. Signal-to-noise ratios are established by a second closed loop (not shown in Fig. 27) by sampling the signal power and the output of the summer.

The noise bandwidth is established by the noise filter in the oven assembly. The noise amplifier and filter frequency response do not exhibit sufficient amplitude stability without temperature control; therefore, the noise amplifier and noise filter are packaged in a temperature controlled oven. The amplifier filter combination has been carefully tuned for proper response at an oven temperature of 40°C.

A recent test made using SNORE techniques showed that the absolute accuracy of the entire PM system was 0.19 dB with a standard deviation of 0.03 dB over a continuous 66-h period.

The RFTC will play a major role in determining the actual performance of the high-rate system.

c. Laboratory breadboard.

Functional description. A simplified block diagram of the 360-bits/s word detection laboratory breadboard is

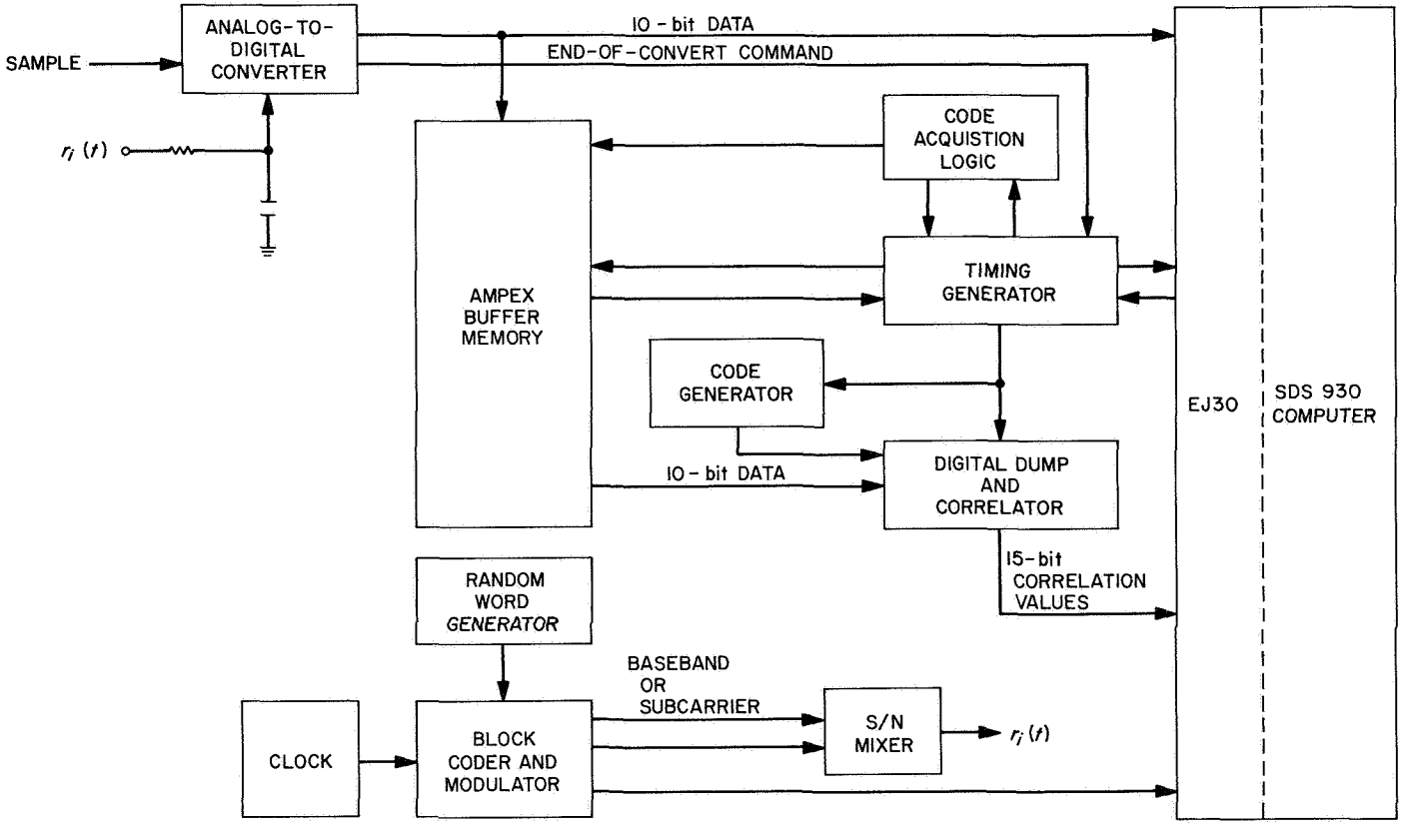

Fig. 28. Word detection system laboratory breadboard

shown in Fig. 28. Since all of the hardware external to the computer, with the exception of the core memory, was implemented with readily available 1-MHz logic, a data rate of only 360 bits/s could be realized without exceeding the maximum operating frequency of the logic.

The design philosophy utilized in the construction of the laboratory breadboard was to:

(1) Simulate the basic functional performance characteristics of laboratory set A without being required to operate at 16.2K bits/s or to utilize the "Green" algorithm (see SPS 37-39, Vol. IV, pp. 247–252) for decoding.

(2) Implement as many laboratory breadboard hardware functions with computer software programs as feasible.

The laboratory breadboard was originally implemented as a baseband modulator–demodulator/detector pair, with an expansion capability for simulating the entire system utilizing the RF test console. In this article, only the features of the baseband system hardware and the measurement of its performance are considered.

The major functional requirements of the baseband breadboard system are to:

(1) Acquire word synchronization using the comma-free properties of the code.

(2) Perform word detection.

(3) Compute various statistical parameters of the system to determine its performance relative to acquisition and word probability of error.

In order to understand how the laboratory breadboard operates, refer to Fig. 29, which shows a block diagram of a correlation receiver operating at baseband on a (32, 6) biorthogonal code. The detector performs the following operations (assuming word synchronization):

(1) The comma-free vector $C(t)$ is removed from $S_i(t)$ to form $r(t)$.

(2) The following statistics are formed:

$$r_i = \int_0^{32T_s} r(t)W_i(t)dt, \qquad i = 0, \cdots, 31$$

where T_s = symbol time period and $W_i(t)$ is the ith locally generated code word.

(3) Select max $| r_i |$ and save sign of the maximum.

(4) The decoded word then becomes W_i, if the sign is positive, and W_{i+32}, if the sign is negative.

(5) Map the code word W_j into the data word j.

Since the code words $W_i(t)$ may be thought of as binary waveforms of amplitude ± 1 during each T_s second interval, the statistics may be rewritten as

$$r_i = \sum_{J=1}^{32} W_{ij} \int_{(J-1)T_s}^{JT_s} r(t)dt$$

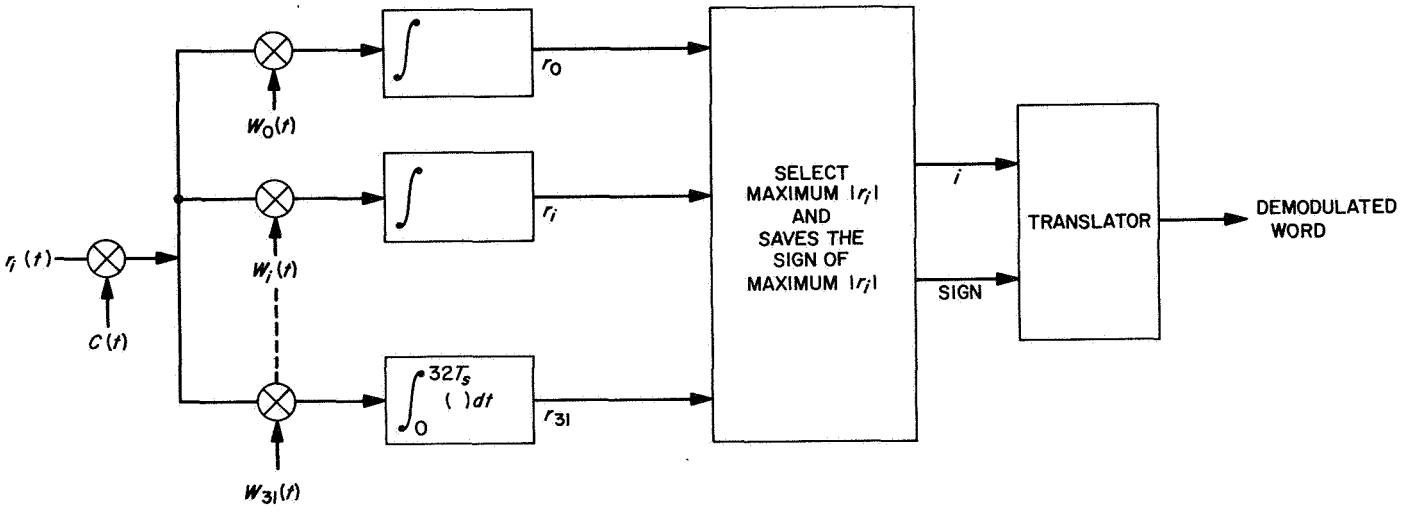

Fig. 29. Correlation receiver operating at baseband on a (32,6) biorthogonal code

Let

$$Z_j = \int_{(J-1)T_s}^{JT_s} r(t)dt$$

then

$$r_i = \sum_{J=1}^{32} W_{ij} Z_j$$

If Z_j is represented as a digital number, then the statistic r_i may be formed by addition and subtraction of the Z_js according to whether $W_{ij} = +1$ or -1. If the sequence of Z_js is stored serially in a buffer memory, then each r_i may be computed sequentially in a digital manner. This method, with a slight modification, is the underlying mechanization for the laboratory breadboard.

Consider the mechanization shown in Fig. 30. The Z_js may be generated by the following dump function:

$$Z_j = Y_i - \exp\left(\frac{-T_s}{RC}\right) Y_{j-1}$$

without a significant loss in word-error performance of the system providing $RC > T_s$. If we select the RC product of the low-pass filter so that

$$\exp\left(\frac{-T_s}{RC}\right) = 1 - 2^{-k}$$

then

$$Z_j = Y_i - Y_{j-1} + 2^{-k} Y_{j-1}$$

which can be easily computed by a combination of simple shifts, additions and subtractions, rather than requiring a multiplication operation. However, since the received signal $r_i(t)$ still contains the comma-free vector $C(t)$, the computational algorithm for the r_is must be modified to obtain

$$r_i = \sum_{J=1}^{32} (C_j^* W_{ij}) Z_j$$

$$= \sum_{J=1}^{32} (C_j^* W_{ij}) (Y_j - Y_{j-1} + 2^{-k} Y_{j-1})$$

The factor $C_j^* W_{ij}$ may be determined basically from a mod 2 operation of C_j and W_{ij}. With this background the detailed operation of the laboratory breadboard can now be discussed.

The core memory is divided into two buffer areas (Buf_A, Buf_B), consisting of 32 words each. Let us assume word sync is known and begin to fill Buf_A with the Y_ns. This action is initiated by the timing generator upon the receipt of an end-of-convert command from the analog-to-digital converter. Let us also assume Y is held in a storage register. When Buf_A is filled, the next Y_n will be stored in the first position of Buf_B. Once this has happened, the correlation goes into operation to form r_0, which is then stored in the SDS 930 computer. The correlation then halts until the receipt of the next analog-to-digital converter end-of-convert command. This operation continues until Buf_B is filled and r_{31} has been inputed to the computer. At this time, the SDS 930 computer computes max $| r_i |$ and subsequently determines the received data number. This sequence of operations continues, alternating between Buf_B and Buf_A.

Now let us assume that word sync is unknown. Since word sync is not directly transmitted, the receiver must examine all 32 possible phase positions of the received code and determine the true word sync phase position. The receiver performs the following basic operations:

(1) Forms the set $\{r_i\}$ as is done during word detection at a fixed phase position ϕ_k $(k = 0, \cdots, 31)$.

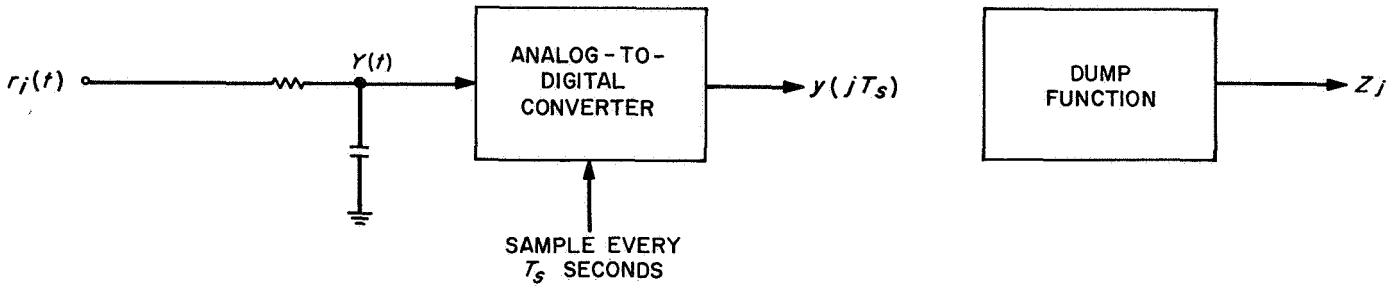

Fig. 30. Mechanization for word detection system laboratory breadboard

(2) Computes and stores max $|r_i|$ (called the largest selector) and one of the other non-maximum values (called the other selector).

(3) Performs steps 1 and 2 a total of N times.

(4) Computes the mean $\mu_L(\phi_i)$ and the variance $\sigma_L^2(\phi_i)$ of the largest selector, and the square $S_0^2(\phi_i)$ of the other selector.

(5) Repeats steps 1 through 4 for each of the 32 possible received phases. This is accomplished by dropping a Y_i value from the $\{Y_i\}$ before they are stored in the Ampex memory. By this method, the group of Y_is contained in Buf_A and Buf_B has been moved one T_s time segment in relation to the time base.

(6) Computes a statistic of the form

$$\ell = \hat{f}(\mu_L(\phi_k), \sigma_L^2(\phi_k), S_0^2(\phi_k)), \qquad (k = 0, \cdots, 31)$$

and estimates and checks the true word sync position ℓ.

(7) Informs the timing generator and code acquisition logic to drop ℓ Y_is from the $\{Y_i\}$ before they are stored in the Ampex memory.

Supporting software package. The software package written for the SDS 930 computer contains four modes and some associated monitoring functions.

Mode 1 is concerned with acquisition of word sync. The operation of the word sync algorithm has already been discussed, with the exception of the statistic $\ell = f(\cdot)$. Three statistics were proposed and tested for word sync acquisition properties:

(1) ℓ = subscript k of max $(\mu_L(\phi_k))$ (the maximum likelihood estimator)

(2) ℓ = subscript k of max $(S/N_L(\phi_k) = \mu_L^2(\phi_k)/\sigma_2^2(\phi_F))$

(3) ℓ = subscript k of max $(S/N_0(\phi_k) = \mu_L^2(\phi_k)/S_0^2(\phi_k))$

ℓ is then compared to the true word sync index for a prescribed number of acquisition attempts and finally the probability of false word sync acquisition PE^{ACQ} is computed.

Mode 2 is concerned with performing word detection. The algorithm for word detection has already been described. Once the receiver has performed the detection operation, the received word is compared to the transmitted word for a prescribed number of transmitted words, and then the probability of word error PE^w is computed. Using the value of PE^w, the theoretical equation for PE^w versus ST_B/N_0 is solved, and this signal-to-noise ratio is compared to the actual S/N to obtain the effective loss in ST_B/N_0.

Mode 3 is concerned with monitoring loss of word sync.

Mode 4 is used to monitor the input ST_B/N_0 to the system by performing operations directly on the $\{Y_N\}$ when a known data sequence is transmitted through the system. This allows precise measurement of the input ST_B/N_0 to the system for set-up purposes and for automatically monitoring ST_B/N_0 during long tests.

d. Analytical and experimental results.

Probability of word error versus ST_B/N_0. The theoretical performance of a (32,6) biorthogonal word detection system is given by the following equation:

$$PE^w = 1 - \frac{1}{(\pi)^{1/2}} \int_{-(ST_w/N_0)^{1/2}}^{+\infty} e^{-\alpha^2} \frac{1}{(\pi)^{1/2}} \left\{ \int_{\beta - (ST_w/N_0)^{1/2}}^{\beta + ST_w/N_0} e^{-\beta^2}\, d\beta \right\}^{31} d\alpha$$

where S = signal power, T_w = transmission time/word (seconds), and N_0 = one-sided noise spectral density/Hz. A plot of PE^w versus ST_B/N_0 is given in Fig. 31 where T_B = time per information bit ($T_w/6$).

PE^w performance for the laboratory breadboard was determined by transmitting 100,000 words through the system and comparing the received words against the transmitted words. The results of these tests are plotted against the theoretical curve (Fig. 31). For ST_B/N_0 = 1, 2, 3, 4, and 5 dB, the loss in effective ST_B/N_0 was found to be

ST_B/N_0, dB	Loss, dB
1	0.48
2	0.55
3	0.63
4	0.81
5	1.17

The laboratory breadboard and ST_B/N_0 measurement techniques were investigated to determine the source of loss in ST_B/N_0 performance. To date, no deficiencies in either the hardware or measurement techniques have been found which would cause the observed loss in performance.

One particular test which was performed indicates that a problem does exist in the system—a fixed code word was transmitted, instead of random words, at an $ST_B/N_0 = 5$ dB

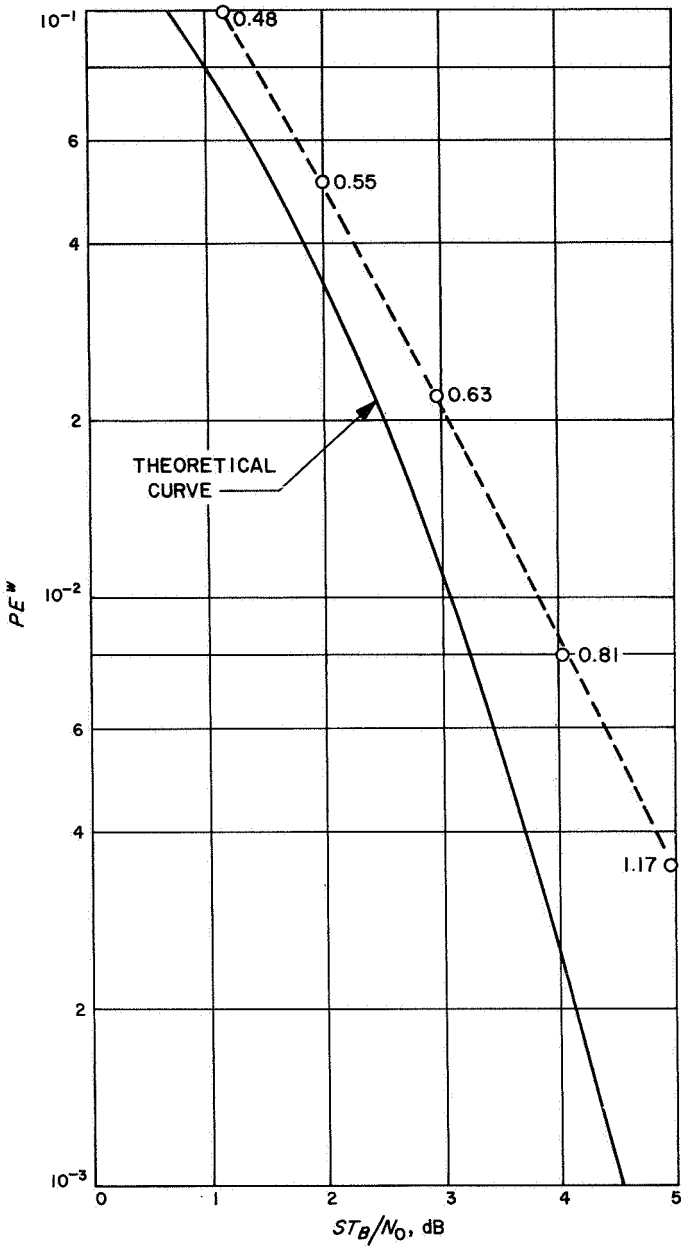

Fig. 31. PE^w versus ST_B/N_0

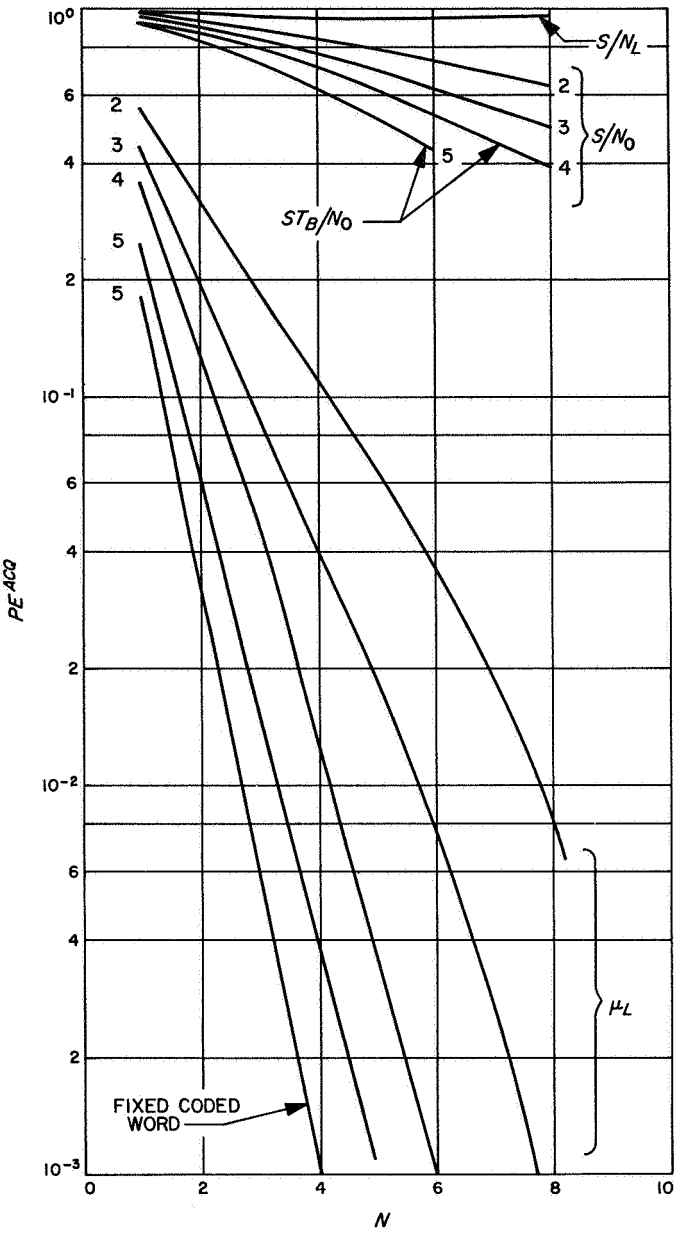

Fig. 32. Word sync acquisition

and the loss in effective ST_B/N_0 decreases from 1.14 to 0.77 dB (0.37 dB difference). Previous theoretical work did not indicate that this problem should arise. Therefore, it must be concluded that there is an unsolved problem concerning the laboratory's breadboard operation which requires further investigation.

Probability of word sync acquisition. Since no theoretical equations can be easily derived to determine PE^{ACQ} versus ST_B/N_0 and N, experimental results were collected on the performance of the three proposed statistics, μ_L, S/N_L, and S/N_0, which are shown in Fig. 32.

The experimental results indicate that the μ_L statistic should be used for word sync acquisition since it requires a much smaller N than the other two statistics.

Effects of the number of analog-to-digital converter bits on performance. The experimental results described in the preceding paragraphs concerning PE^w and PE^{ACQ} were run with a 10-bit analog-to-digital converter. Thus, each sample of $y(t)$ was quantized into 2^{10} levels. As the number of analog-to-digital converter bits was reduced, both PE^w and PE^{ACQ} increased slowly and then finally reached a threshold where the system performance

Table 9. Results of PE^{w} tests

Analog-to-digital converter bits	Loss in ST_B/N_0, dB	Signal component quantization levels
10	0.81	28
8	0.85	7
6	0.94	1.75
5	2.41	0.875
4	2.53	0.44

was drastically reduced. Table 9 summarizes the loss in effective ST_B/N_0 as a function of the number of analog-to-digital converter bits for a system input $ST_B/N_0 = 4$ dB.

It was found that the observed threshold phenomenon can be basically explained by examination of the statistics Z_j. The value of each Z_j is composed of two components—one due to the signal and one due to the noise. The threshold phenomenon occurs when the signal component of the Z_j drops below one quantization level of the analog-to-digital converter.

Effects of dc offset on performance. Tests were conducted to determine the loss in effective ST_B/N_0 versus a dc offset voltage contained in the received signal $r_i(t)$. The dc offset ratio was measured by the following method:

$$\text{dc offset ratio} = \frac{\text{voltage dc}}{\text{peak symbol voltage}}$$

where voltage dc = dc offset voltage into matched filter, and peak symbol voltage = peak voltage of a symbol into the matched filter. The results of one such test run at an $ST_B/N_0 = 4$ dB is shown in Fig. 33.

In order to determine if the effect of a dc offset on performance could be minimized, a series of tests was conducted. The system was tested with a large dc offset ratio with and without a 1-Hz high-pass filter preceding the low-pass filter (matched filter) shown in Fig. 30. The results, shown in Table 10, indicate that performance loss

Table 10. Results of dc offset ratio test with and without 1-Hz high-pass filter

DC offset ratio	Loss with no dc blocking, dB	Loss with 1-Hz high-pass filter, dB
0.005	0.89	0.97
1.59	4.8	0.94

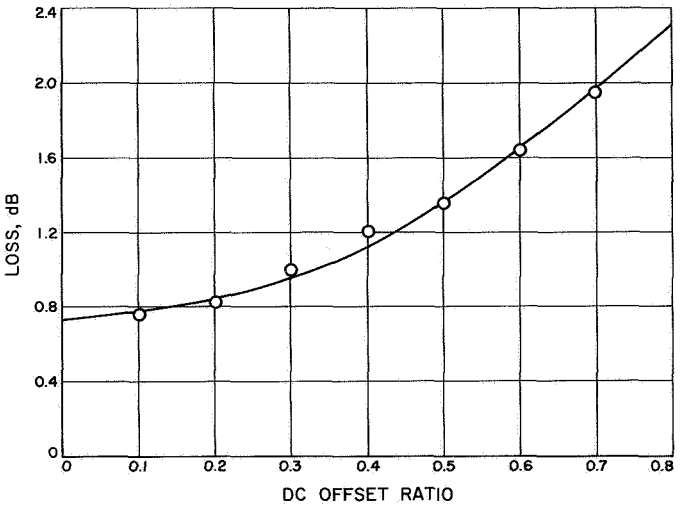

Fig. 33. Effect of dc offset on word detection system laboratory breadboard performance

to dc offsets can be eliminated by an appropriate high-pass filter.

5. Analysis of the Subcarrier Demodulator,

M. H. Brockman

a. Design considerations. The hi-rate telemetry system utilizes biorthogonal block coding for reasons outlined in A. Introduction. In the overall telecommunications system design for block coding, a 1% word error rate is specified as the minimum operating condition (moc) which determines ST_B/N_0 (moc) for any given coding. In examining the design and performance of the telemetry subcarrier demodulator, this ST_B/N_0 (moc) must be transformed into ST_{SY}/N_0 (moc) (ratio of signal energy per symbol to noise spectral density at minimum operating condition). In particular,

$$\frac{ST_{SY}}{N_0} = \frac{1}{l} \times \frac{ST_B}{N_0} \qquad (1)$$

where $l = 2^{k-1}/k$ symbols/bit (biorthogonal coding) and k represents bits/word.

In the design of the telemetry subcarrier demodulator, the concept of design point is established so that performance can be specified at signal levels below minimum operating conditions. At design point (dp), a 10% bit error rate is specified which determines ST_B/N_0 (dp) for any given coding. This ST_B/N_0 (dp) determines in turn ST_{SY}/N_0 (dp) from Expression (1). A detailed analysis of performance at design point will be presented in a later article.

At the nominal minimum operating condition, a fraction of a dB degradation in ST_{SY}/N_0 is allocated to the subcarrier telemetry demodulator in the overall telecommunications system design. Degradation in demodulated ST_{SY}/N_0 (due to the subcarrier demodulator) results from the rms phase noise error in the subcarrier tracking loop and/or from the phase error due to doppler shift on the received subcarrier frequency and its attendant doppler rate.

b. Effect of subcarrier tracking loop phase error on demodulated ST_{SY}/N_0. An analysis of the telemetry subcarrier demodulator presented in SPS 37-46, Vol. III, pp. 189–201, provides reference material for the following analysis. The demodulated data signal-to-noise voltage ratio can be written as

$$\frac{V_S}{V_N} = \left(\frac{ST_{SY}}{N_0}\right)^{1/2} \times \left(\frac{2}{\lambda}\right)^{1/2} \times \left[1 - \frac{2}{\pi}(\theta - \hat{\theta})\right] \tag{2}$$

where the predemodulation filter noise bandwidth ($NBW_{F_{A_1}}$) for the data is related to the time duration of the data symbol by

$$NWB_{F_{A_1}} = \frac{\lambda}{T_{SY}} \tag{3}$$

and $\hat{\theta}$ is the loop estimate of θ, the subcarrier input phase. It is assumed here that the predemodulation filter produces negligible attenuation of the data spectrum.

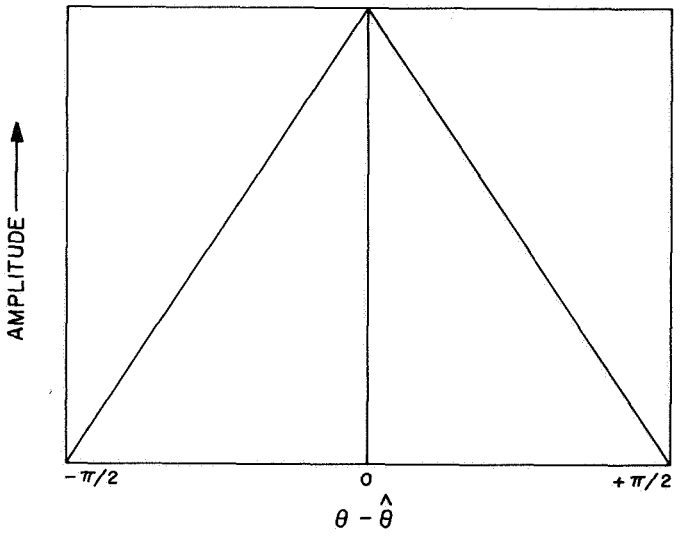

Fig. 34. Demodulated data symbol amplitude vs $\theta - \hat{\theta}$

Figure 34 shows the demodulated data symbol amplitude as a function of $\theta - \hat{\theta}$, which is obtained from Expression (9) of the referenced SPS. Designate $\Delta\theta = \theta - \hat{\theta}$ as the phase error due to doppler shift and/or doppler rate on the received subcarrier frequency. Then, degradation in ST_{SY}/N_0 due to doppler is

$$\frac{\text{demodulated } \dfrac{ST_{SY}}{N_0}}{\text{input } \dfrac{ST_{SY}}{N_0}} = \left[1 - \left(\frac{2}{\pi}\right)\Delta\theta\right]^2 \tag{4}$$

Expression (4) is shown plotted in Fig. 35.

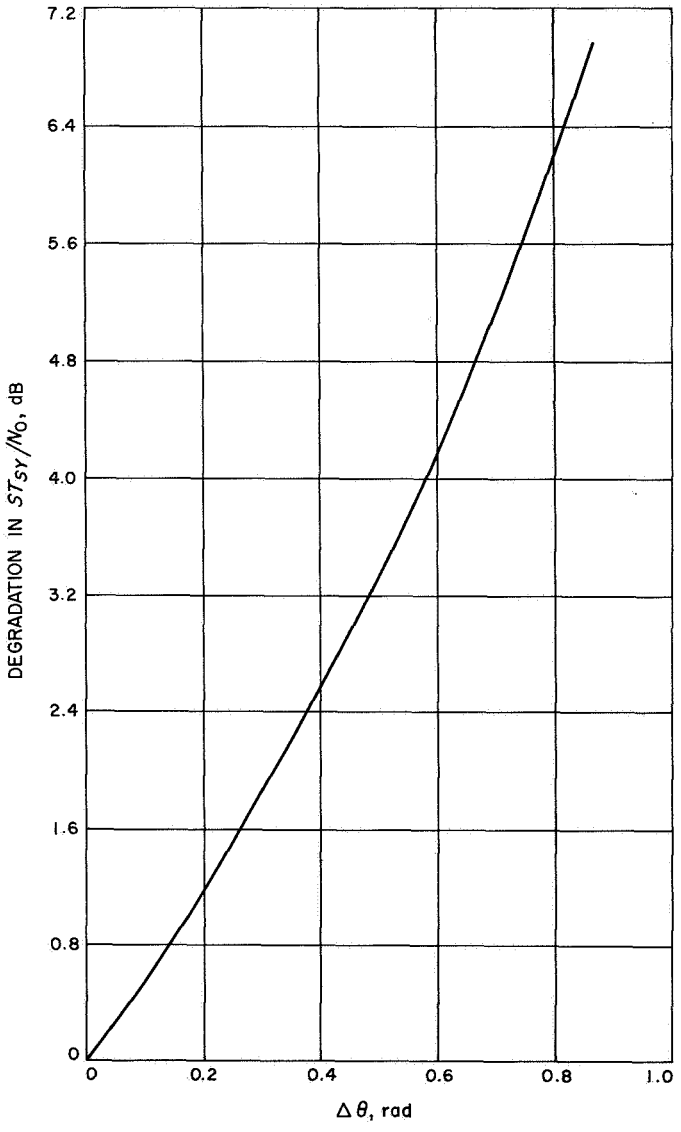

Fig. 35. Degradation in demodulated ST_{SY}/N_0 vs phase error due to doppler shift/rate

Consider next the effect of the rms phase noise error ($\sigma_{\theta\eta}$) on ST_{SY}/N_0. Designate $\psi = \theta - \hat{\theta}$ as the phase error due to noise. ψ is Gaussian and has a probability density function

$$p(\psi) = \frac{1}{(2\pi)^{1/2}\,\sigma_{\theta\eta}} \times \exp\left(\frac{-\psi^2}{2\sigma^2_{\theta\eta}}\right) \tag{5}$$

Expression (2) can be written in this case as

$$\left(\frac{\text{demodulated } \dfrac{ST_{SY}}{N_0}}{\text{input } \dfrac{ST_{SY}}{N_0}}\right)^{1/2} = \left[1 - \left(\frac{2}{\pi}\right)|\psi|\right] \tag{6}$$

Since degradation in $(ST_{SY}/N_0)^{1/2}$ is a function of ψ and the probability density function is defined in Expression (5), the statistical average (expectation) is

$$E\left(\frac{\text{demodulated } \dfrac{ST_{SY}}{N_0}}{\text{input } \dfrac{ST_{SY}}{N_0}}\right)^{1/2} = \frac{2}{(2\pi)^{1/2}\,\sigma_{\theta\eta}} \int_0^{\infty} \left[1 - \left(\frac{2}{\pi}\right)\psi\right] \exp\left(-\frac{\psi^2}{2\sigma^2_{\theta\eta}}\right) d\psi$$

which becomes

$$E\left(\frac{\text{demodulated } \dfrac{ST_{SY}}{N_0}}{\text{input } \dfrac{ST_{SY}}{N_0}}\right)^{1/2} = 1 - \left(\frac{2}{\pi}\right)^{3/2} \sigma_{\theta\eta} \tag{7}$$

For the case considered here, degradation in $(ST_{SY}/N_0)^{1/2}$ is defined over $\pm\pi/2$ rad. However, since $3\sigma_{\theta\eta} < \pi/2$ rad, effectively all of the probability density function of ψ is contained within $\pm\pi/2$ rad. Therefore, integrating from zero to infinity gives the same result as integrating from zero to $\pi/2$. Consequently, degradation in ST_{SY}/N_0 due to rms phase noise error in the subcarrier tracking loop is

$$\frac{\text{demodulated } \dfrac{ST_{SY}}{N_0}}{\text{input } \dfrac{ST_{SY}}{N_0}} = \left[1 - \left(\frac{2}{\pi}\right)^{3/2} \sigma_{\theta\eta}\right]^2 \tag{8}$$

Expression (8) is shown plotted in Fig. 36.

Finally, consider degradation in demodulated $(ST_{SY}/N_0)^{1/2}$ due to phase error due to both doppler and Gaussian noise. The statistical average (expectation) in this case becomes

$$E\left(\frac{\text{demodulated } \dfrac{ST_{SY}}{N_0}}{\text{input } \dfrac{ST_{SY}}{N_0}}\right)^{1/2} = \frac{1}{(2\pi)^{1/2}\,\sigma_{\theta\eta}} \int_{-\infty}^{0} \left[1 + \left(\frac{2}{\pi}\right)\psi\right] \exp\left[-\frac{(\psi - \Delta\theta)^2}{2\sigma^2_{\theta\eta}}\right] d\psi$$

$$+ \frac{1}{(2\pi)^{1/2}\,\sigma_{\theta\eta}} \int_0^{+\infty} \left[1 - \left(\frac{2}{\pi}\right)\psi\right] \exp\left[-\frac{(\psi - \Delta\theta)^2}{2\sigma^2_{\theta\eta}}\right] d\psi \tag{9}$$

which becomes

$$E\left(\frac{\text{demodulated }\frac{ST_{SY}}{N_0}}{\text{input }\frac{ST_{SY}}{N_0}}\right)^{1/2} = 1 + \left(\frac{2}{\pi}\right)\int_{-\infty}^{0} \exp\left[-\frac{(\psi-\Delta\theta)^2}{2\sigma_{\theta\eta}^2}\right]\frac{(\psi-\Delta\theta)}{(2\pi)^{1/2}\,\sigma_{\theta\eta}}\,d\psi$$

$$+\left(\frac{2}{\pi}\right)\frac{\Delta\theta}{(2\pi)^{1/2}\,\sigma_{\theta\eta}}\int_{-\infty}^{0} \exp\left[-\frac{(\psi-\Delta\theta)^2}{2\sigma_{\theta\eta}^2}\right]d\psi$$

$$-\left(\frac{2}{\pi}\right)\int_{0}^{+\infty} \exp\left[-\frac{(\psi-\Delta\theta)^2}{2\sigma_{\theta\eta}^2}\right]\frac{(\psi-\Delta\theta)}{(2\pi)^{1/2}\,\sigma_{\theta\eta}}\,d\psi$$

$$-\left(\frac{2}{\pi}\right)\frac{\Delta\theta}{(2\pi)^{1/2}\,\sigma_{\theta\eta}}\int_{0}^{+\infty} \exp\left[-\frac{(\psi-\Delta\theta)^2}{2\sigma_{\theta\eta}^2}\right]d\psi \qquad (10)$$

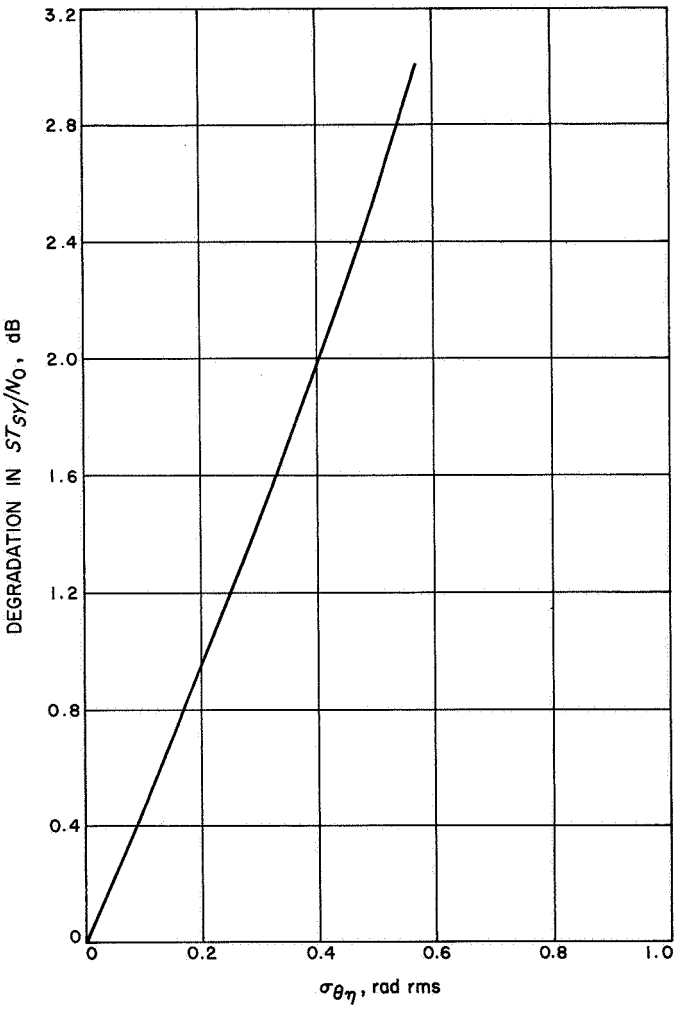

Fig. 36. Degradation in demodulated ST_{SY}/N_0 vs rms phase noise error

Integration of Expression (10) provides

$$E\left(\frac{\text{demodulated } \frac{ST_{SY}}{N_0}}{\text{input } \frac{ST_{SY}}{N_0}}\right)^{1/2} = 1 - \left(\frac{2}{\pi}\right)^{3/2} \sigma_{\theta\eta} - \left(\frac{2}{\pi}\right) \Delta\theta \operatorname{erf}\left(\frac{\Delta\theta}{(2)^{1/2}\sigma_{\theta\eta}}\right) \tag{11}$$

where erf is the error function. Consequently, degradation in ST_{SY}/N_0 due to phase error ($\Delta\theta$) and rms phase noise ($\sigma_{\theta\eta}$) is

$$\frac{\text{demodulated } \frac{ST_{SY}}{N_0}}{\text{input } \frac{ST_{SY}}{N_0}} = \left[1 - \left(\frac{2}{\pi}\right)^{3/2} \sigma_{\theta\eta} - \left(\frac{2}{\pi}\right) \Delta\theta \operatorname{erf}\left(\frac{\Delta\theta}{(2)^{1/2}\sigma_{\theta\eta}}\right)\right]^2 \tag{12}$$

It should be pointed out that using the expected value of ST_{SY}/N_0 as developed in the above analysis to determine bit or word error probability from the curves in Ref. 1 will provide a good approximation to the correct error probability since the variance on $S^{1/2}$ in demodulated ST_{SY}/N_0 is small at minimum operating conditions.

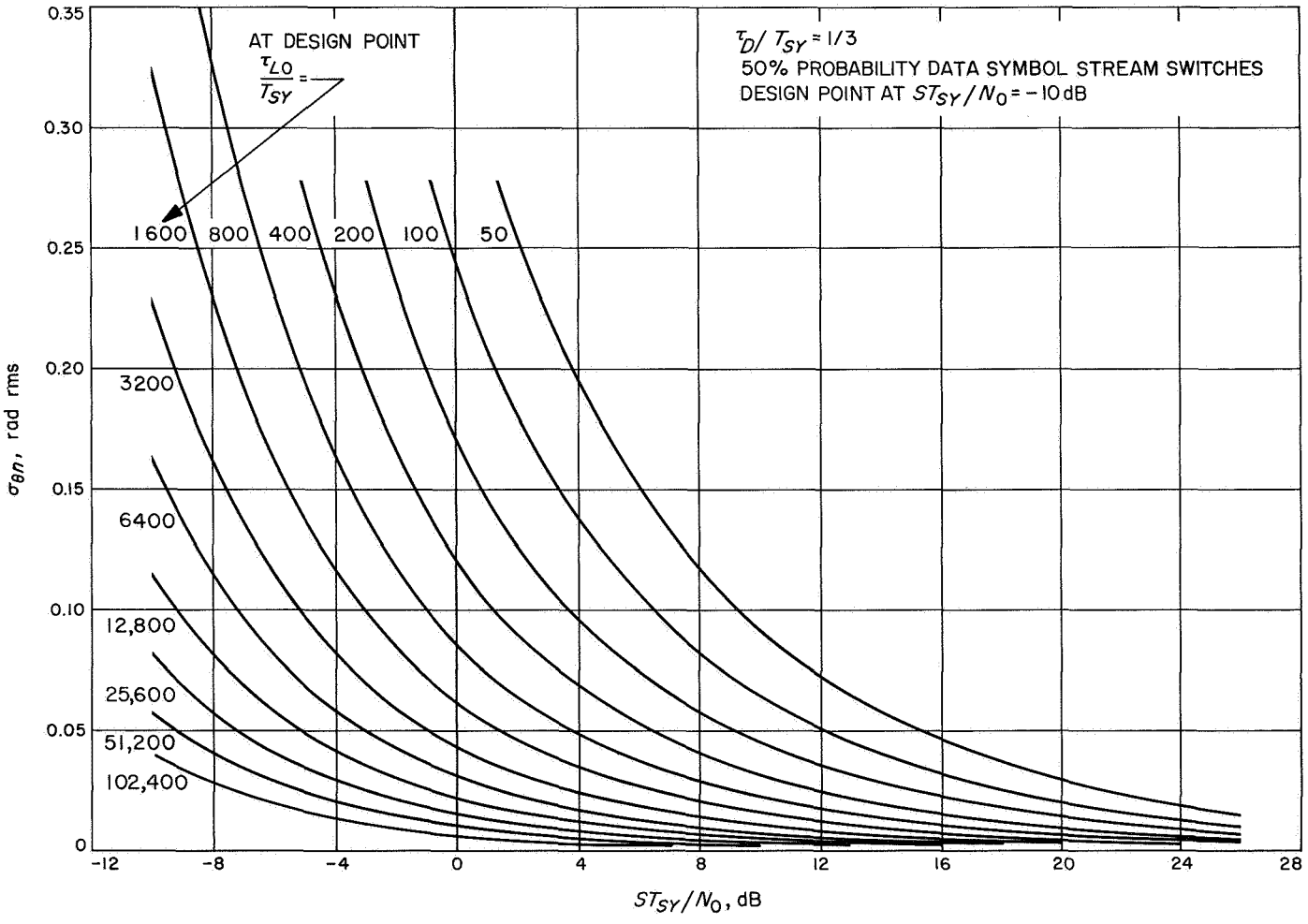

Fig. 37. Subcarrier demodulator first-order loop rms phase noise error vs ratio of signal energy per symbol to noise spectral density

c. Subcarrier loop noise bandwidth. The hi-rate telemetry for the *Mariner* Mars 1969 mission will use biorthogonal block coding with 6 bits/word and a data rate of 16.2K bits/s. At minimum operating condition (1% word error rate), ST_B/N_0 (moc) is +3 dB (Ref. 1). The resultant ST_{SY}/N_0 (moc) is (from Expression 1) 1/2.67 or −4.3 dB. Consider application of the first-order loop analysis presented in SPS 37-46, Vol. III, to hi-rate telemetry for the case of 6 bits/word. (Note that the procedure can be applied to other codes.) Figure 37, which is essentially a duplicate of Fig. 20, p. 202, SPS 37-46, Vol. III, shows rms phase error versus ratio of signal energy per symbol-to-noise spectral density for a first-order loop with design point at $ST_{SY}/N_0 = -10$ dB, $\tau_D/T_{SY} = \frac{1}{3}$, and 50% probability that the data symbol stream switches on successive symbol periods (see referenced SPS for definition of terms).

From Fig. 37, the curve for $\tau_{LO}/T_{SY} = 51{,}200$ provides an rms phase noise error ($\sigma_{\theta\eta}$) of 0.02 rad rms at an $ST_{SY}/N_0 = -4.3$ dB. Proceeding as in the SPS reference (using Fig. 16 and Expressions 58, 59, and 60),

$$BW_{SCL}\,(\text{moc}) \times \tau_{SY} = \frac{1}{2 \times 51200} \times \frac{0.36}{0.193}$$

$$= 1.82 \times 10^{-5}$$

From Fig. 36, a $\sigma_{\theta\eta} = 0.02$ rad rms represents 0.1-dB degradation in ST_{SY}/N_0 in the subcarrier demodulator.

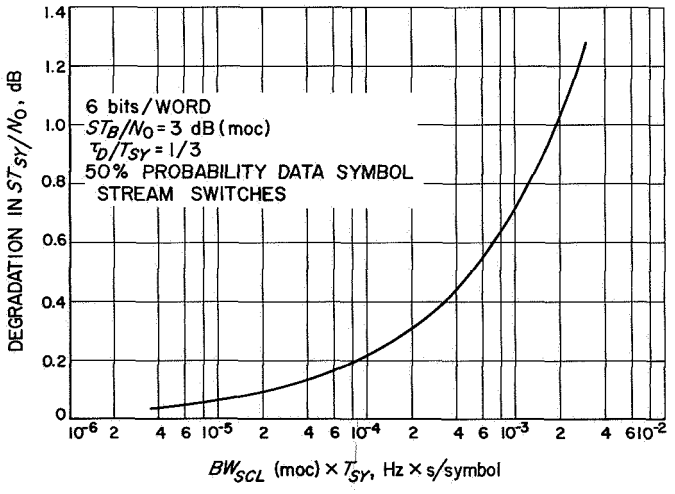

Fig. 38. Degradation in demodulated ST_{SY}/N_0 due to phase noise error at minimum operating condition vs subcarrier loop two-sided noise bandwidth × symbol period

Proceeding in this manner at an $ST_{SY}/N_0 = -4.3$ dB and selecting a number of τ_{LO}/T_{SY}s, degradation in demodulated ST_{SY}/N_0 due to noise only at minimum operating condition is obtained as a function of the product of subcarrier two-sided noise bandwidth [BW_{SCL} (moc)] and symbol period (T_{SY}). This characteristic, which is shown plotted in Fig. 38, represents a general design curve for biorthogonal block coding with 6 bits/word (based on a first-order subcarrier tracking loop analysis).

d. Application to Mariner Mars 1969. Since the data rate for hi-rate telemetry for *Mariner* Mars 1969 is 16.2K bits/s with 6 bits/word (biorthogonal block coding), the symbol rate ($1/T_{SY}$) is (from Expression 1 above) 86.4K symbols/s. Applying this symbol rate, the general design curve shown in Fig. 38 provides the characteristic shown in Fig. 39 of degradation in demodulated ST_{SY}/N_0 as a function of subcarrier tracking loop two-sided noise bandwidth at minimum operating condition ($ST_{SY}/N_0 = -4.3$ dB). It should be noted that the total degradation in demodulated ST_{SY}/N_0 due to phase error resulting from doppler and noise is obtained from Expression (12) above.

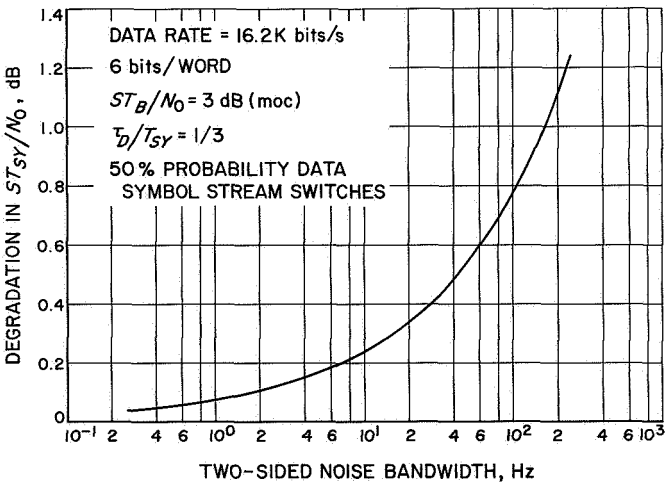

Fig. 39. Degradation in demodulated ST_{SY}/N_0 due to phase noise error at minimum operating condition vs subcarrier loop two-sided noise bandwidth

D. Work in Progress, *M. Easterling*

The most important work in progress is the demonstration system verification in preparation for the first tests with the proof-test-model spacecraft early in 1968. The DSIF system engineering and system verification work to prepare for those tests is also under way.

Refinement of system analysis is also being done, particularly in the operation of the subcarrier tracking loop. Design and construction of field equipment is just beginning.

Reference

1. Golomb, S. W., Baumert, T. D., Easterling, M. F., Stiffer, J. J., and Viterbi, A. J., *Digital Communications.* Prentice-Hall, Inc., Englewood Cliffs, N.J., 1964.

V. Antenna Engineering

A. Resonant Frequency Analysis for 85-ft Az–El Antenna, *M. Kron, R. Levy, V. Lobb, and F. Stoller*

1. Introduction

An analytical study was performed to predict vibratory characteristics of the 85-ft-diam az–el antenna. The particular configuration studied included the proposed modification to the existing antenna now operating at the Goldstone Venus Station. The objectives of this study were: (1) to develop a mathematical procedure that could be applied to this antenna, or with minor modifications, to similar structures; and (2) to obtain an estimate of performance to be expected for the modified antenna.

2. Procedure

The procedure developed was to strike a balance in complexity between a readily postulated mathematical model of several hundred degrees of freedom that would tax available computer facilities and require extensive programming, and on the other hand, the cursory models of two or three degrees of freedom that typically consider hypothetically rigid reflectors attached to one-dimensional mounts and gear trains. The objection to the first model is the effort and time required in data preparation and computation. The second model, although capable of being applied with a relatively minute effort, is objectionable because it depends for validity almost entirely upon the intuition of the analyst. A compromise procedure was developed, which although moderately complex, has sufficient mathematical basis to minimize the reliance upon intuition of the analyst.

The great problem in forming the analytical model of the antenna system is the typically enormous number (from a computational standpoint) of junctions used in the reflector construction. For example, there are almost 800 such junctions in the 85-ft reflector. Even by invoking symmetry to restrict the problem to half the size, the associated 1200 degrees of freedom makes the use of a classical eigenvalue solution procedure impractical. Therefore, it is necessary to use some condensation procedure

to drastically reduce the degrees of freedom until it comes within the capacity of standard programs and computers, and preferably fits within core storage. For example, the SAMIS and STIFF-EIG programs are presently limited to handle 130 degrees of freedom for vibratory problems, although much larger problems can be solved statically.

Any condensation procedure to be applied to the reflector will almost certainly be some variation of Rayleigh–Ritz approach. In fact, it could be argued that modeling the reflector by establishing three to six degrees of freedom at every one of the actual physical nodes of the structure is, in itself, a variation of a Rayleigh–Ritz approach because the members of the structure really are continuous between, and not lumped at, the nodes. The approach is to generate or assume sets of mode shape functions that describe the set of displacements for all the original degrees of freedom. Since the displacements of the original degrees of freedom are no longer independent, but are now prescribed by the mode shape functions, there remain only a restricted number of degrees of freedom, that is, one degree of freedom for each displacement function.

The problem then reduces to one of how to choose the restricting displacement functions. One method is the "consistent mass" method of Archer, or some variation of this, which is based upon using a condensed stiffness matrix and generating an appropriate associated mass matrix. Another way is to choose displacement functions that are the result of applying unit loads at critical locations of the structure; this is equivalent to choosing particular columns of the flexibility matrix for the functions. Both of these methods, which have been advanced and used successfully at JPL, are theoretically and practically attractive. The difficulty is that they are applied only within the framework of some procedure that requires modeling of the antenna by a specific program such as SAMIS.

Although there was the possibility of converting available STAIR input data to SAMIS data for the reflector, it was considered to be more efficient to use an existing model of the reflector and exploit the reuse of a successfully executed STAIR program.

The STAIR program was used to generate displacement functions for the reflector, one at a time, by an almost classical application of the Rayleigh method. That is, displacement functions were constructed as the static response to various orientations of the gravity vector.

Combining 6 selected reflector displacement functions with additional degrees of freedom that were considered necessary to represent the mount, led to totals of 19 and 21 degrees of freedom to be handled in solving the eigenvalue problem. No difficulty arose in obtaining the solutions, and in fact, it is probable that considerably larger problems could be handled the same way.

The theoretical justification for this procedure is founded upon experience that the Rayleigh method, which was used for the reflector, almost always leads to a close approximation to the fundamental mode frequency. The Rayleigh–Ritz method, which was used to represent the mount, can lead to solutions indistinguishable from "mathematically exact" solutions, depending upon how consistent and detailed the application. Combination of reflector and mount was done by an "equivalent mass" mathematical approach, which in the limit, tends to a rigorous theoretical basis. Although the theoretical justification for the method described depends more upon intuition than do either the consistent mass or unit load displacement function methods, the present advantage is expedience, minimum usage of computer time, and simplicity of procedure in that the analyst is never involved in either the generation or manipulation of stiffness or flexibility matrices for the reflector. An important by-product of the procedure could be that the way of separating and then combining reflector and mount might be developed into a realistic method of preparing specifications for the acceptance and design of reflector and mount from separate suppliers.

Free vibration analysis of the antenna requires an inertia (mass) matrix and a matrix describing the elastic properties, such as either the stiffness or the flexibility (influence coefficient) matrix. The antenna system here was considered as the combination of two major components: the reflector, and the mount (combination of pedestal and alidade). The flexibility matrix was constructed initially, and when needed, the stiffness matrix was obtained by inversion of flexibility.

The most difficult part of the analysis is the development of the elastic properties needed to describe the system. In contrasting simplicity, the inertia properties for the lumped mass model of the mount can be arrived at by a rational process of assigning inertias to the adjacent displacement indices of the model for the several components. The inertia properties for the reflector were generated automatically by a mathematical process used in establishing an "equivalent" reflector mass.

Development of the flexibility matrix for the mount follows the conventional procedures of developing matrices of flexibility coefficients for elemental members of the subassemblies and combining these coefficients by triple product multiplications of equilibrium, geometry, or coordinate transformation matrices. The elemental flexibility matrices have been obtained from separate STRESS program analyses for the alidade and for the pedestal. Additional transformations and modifications to the STRESS program outputs were performed either manually, by desk calculator and slide rule, or within the computer program "ALID."

Analysis of the reflector elastic and inertial properties was founded upon the existing STAIR program (set up by S. Katow of JPL) that has been used to describe the static response of the reflector to various gravity and live loadings. A subsequent procedure was developed to approximate the 1200 degrees of freedom used in the STAIR program. This procedure generated six "equivalent" mass and spring constants that represent six condensed degrees of freedom for the reflector.

Theory of the condensation procedure is based upon a Rayleigh method analysis of the reflector and also upon variations of a condensation procedure suggested by R. Bamford, which is used to approximate normal modes of a system by so-called "equivalent" single degree of freedom oscillators. Following is an outline of the procedure used for the reflector:

(1) Static loadings that were assumed to generate principal vibratory mode shapes were applied to the reflector via the STAIR program. For example, loads were applied separately in the X, Y and Z coordinates at each of the 400 reflector joints to generate corresponding reflector translatory mode shapes. In addition, loads were applied antisymmetrically (positive and negative) about the three reflector coordinate axes in order to simulate possible rotational vibratory modes. Magnitude of joint loads was equal to the static weight tributary to each joint, as developed within the STAIR program.

(2) FORTRAN statements within the "STAIR," "SLOP," "DEFSOL" and "CHETA" subprograms were added so that joint weights, displacements, and coordinates were correspondingly punched out on data cards.

(3) A FORTRAN IV program (RAQC and RAQV) was written to read in the STAIR punched card output and compute natural frequencies, effective masses and other properties pertinent to subsequent analyses for the

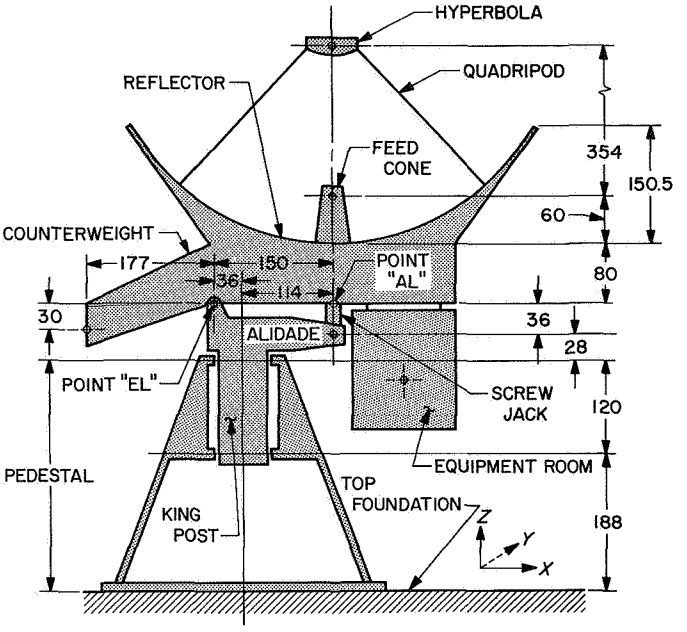

Fig. 1. Analytical model of 85-ft az–el antenna system

"effective" single degree of freedom equivalent reflector oscillators. Output of the FORTRAN programs was converted manually to statics transformation and inertia coefficients for the supporting mount. This was converted to additional punched cards and entered into continuing FORTRAN programs for the assembly of mount and reflector.

Figure 1 shows the major components of the antenna assembly depicted in the zenith (90-deg) elevation position. The STAIR program included the counterweight, feed cone, hyperbola, quadripod, and equipment room subassemblies. The mount (alidade and pedestal) included the screw jack, bearings, and drives. Figure 2 shows the general flow of the procedure and names the major computer programs used. Of these, only the STRESS and STAIR programs are standard, the others were designed specifically for the present problem.

The programs described have just been completed and operated. Consequently it is now possible to consider improving the efficiency of program operation, reductions of present storage requirements so that considerably larger systems could be handled within core, and reducing the number of intermediate manual operations by performing more of these within the computer. Another modification of the programs would be to replace by data card entries the data that is presently entered by source program statements.

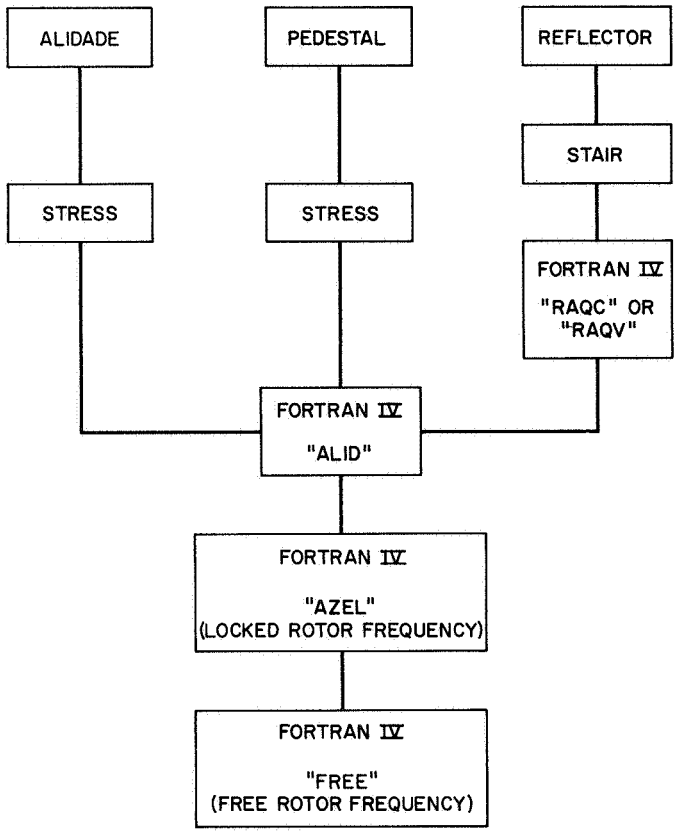

Fig. 2. Primary flow chart

There are two procedures that have not been included to date because of time limitations. These are the development of a free rotor model for the elevation drive system, and the computation of the displacements for specific joints of the reflector. The latter procedure can be developed by relating dynamic displacements for the equivalent reflector oscillators to the STAIR program joint displacements.

Solutions have been found for the proposed modification to the 85-ft az–el antenna for locked and free rotor frequencies and mode shapes, and for the frequency response in the azimuth drive mode. These have been obtained for the 90-, 45-, and 0-deg elevation angles and for both third and fourth trial reflector inertia lumpings. Frequencies for the 90-deg elevation (zenith attitude), which were the lowest frequencies, are given in Table 1.

The frequency response results exhibit the expected phenomena; that is, as frequency increases, the motor reaches an antiresonance at slightly below the locked rotor frequency (the frequency is less because the hydraulic oil compliance is not included for locked rotor)

Table 1. First two mode natural frequencies, Hz, at 90-deg elevation angle

Calculation	Locked rotor		Free rotor	
	First mode	Second mode	First mode	Second mode
Third trial	1.637 (torsion)	2.407 (bending)	2.407 (bending)	2.913 (torsion)
Fourth trial	1.621 (torsion)	2.452 (bending)	2.452 (bending)	3.106 (torsion)
Third trial, azimuth gear compliance tripled	1.139 (torsion)	2.519 (bending)		
Third trial, azimuth gear and motor compliance doubled			2.371 (torsion)	2.407 (bending)

and then peaks sharply at the free rotor resonant frequency. At low frequencies, computations show that the reflector torsional rotation approaches the expected rigid-body amplitude and also that the resonant amplitude is equal to the rigid-body amplitude, divided by twice the damping ratio, which is typical of lightly damped systems.

There is some information available from SPS 37-19 and -20, Vol. III, for dynamic tests performed on the existing antenna.

Nevertheless, in comparing the tested antenna with the proposed modification, it is to be noted that the modification will be considerably heavier due to the equipment room and counterweight additions. Some reduction in natural frequency is anticipated because of the added weight. This will be partly offset by stiffening the reflector and by an improved geometrical arrangement that has been developed for the counterweight trusses. One set of test procedures determined a locked rotor frequency of 1.25 Hz (zenith position) from variable frequency excitation about the azimuth axis. In this test, all of the azimuth drive backlash effect was present, and furthermore, it is possible that the inertia and compliance of the excitation rig, which consisted of a cable, spring, and ground-supported excitation drive, could have participated with the structure, influencing the results.

Another set of locked rotor tests, but not described in the SPS reports, was performed by driving the system in azimuth and observing the frequency after a sudden application of the brakes. This test indicated natural frequencies from 2.2 to 2.5 Hz. A third group of tests with servo-motor excitation is stated in the reports to have indicated a fundamental frequency of 1 Hz. However, this should not be compared with the free rotor frequency

computed here because, according to the report, the system during the test was "grounded" at the servo valve.

In reviewing the analytical results, assumptions made to expedite the computation should be considered. Principal assumptions were the omission of backlash, severe simplifications in idealization of components (including the reflector within the STAIR program), and the assumptions made in deriving mount inertia coefficients from approximate, rather than carefully developed information. The pedestal foundation was also taken to be rigid, neglecting possible soil compliance. It would be important to determine the validity of the assumptions by use of field tests and measurements, and further, to correct the analysis accordingly.

B. 85-ft HA–dec Antenna Dish Resurfacing (DSS 51), *J. Carpenter*

Resurfacing of the 85-ft HA–dec antenna at Johannesburg Station is now in progress and is being accomplished on a noninterference basis. Parity error rates on *Pioneer VII* spacecraft from June 1 to 30, 1967, are now available.

Figure 3 illustrates the decrease in error rates and apparent increase in gain as the original expanded aluminum mesh panels (with 70% porosity and extensive damage from hailstones—Fig. 4) are replaced with a panel surface which affords better performance. Of 224 panels, 63 had been replaced in the inner dish area as of October 16, 1967.

The new surface panels are 0.080-in.-thick, perforated aluminum sheets, having 25% porosity for the inner three-quarters of the dish area, and 50% porosity for the remaining dish area (Fig. 5).

The replacement panels are secured with self-tapping screws at ¾-in. centers (more than 70,000 screws are required).

The over-all effect of the resurfacing to DSS 51 is not yet known since this task has not been completed, and final measurements have not been made. However, data obtained from two previous antennas that were resurfaced, in the same manner, show an increase in gain of at least 0.6 dB and a decrease in system temperature of at least 4°K.

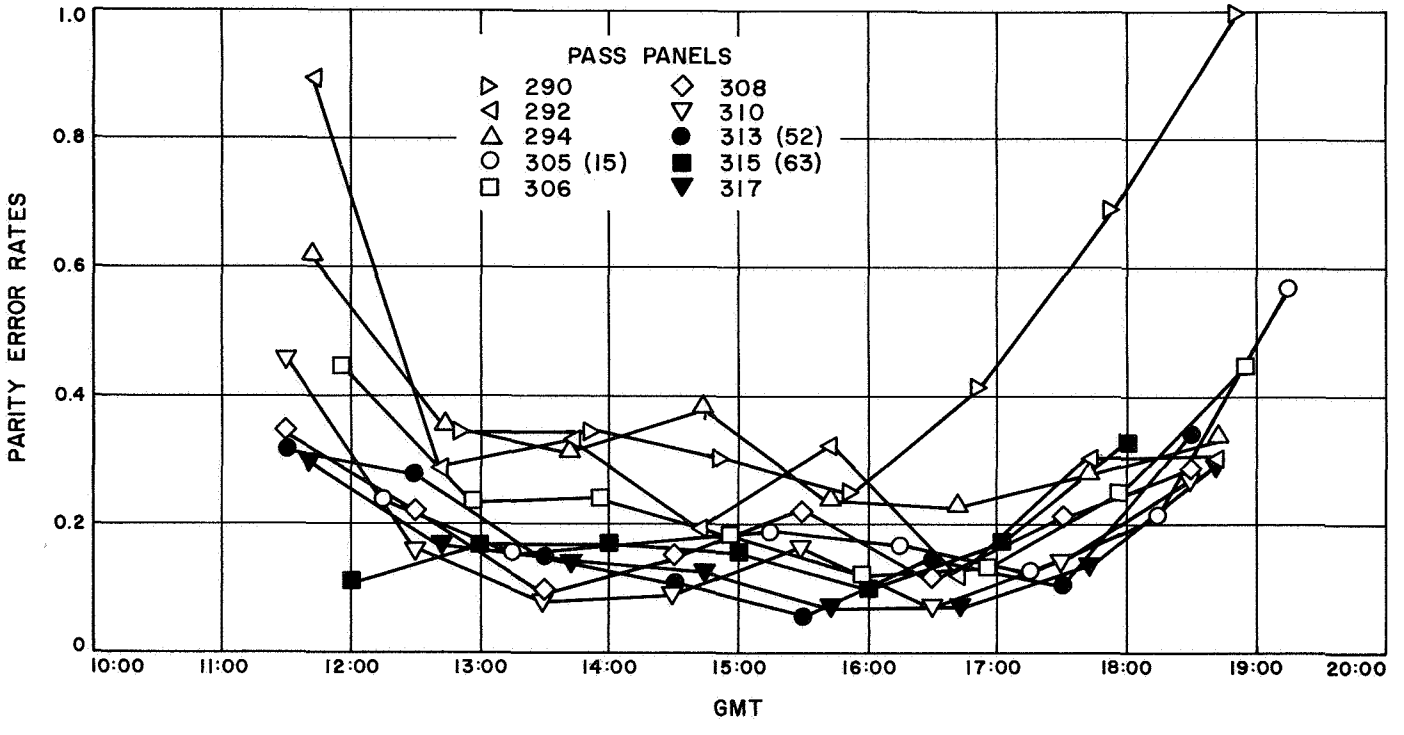

Fig. 3. Parity error rates (June 1 to 30, 1967)

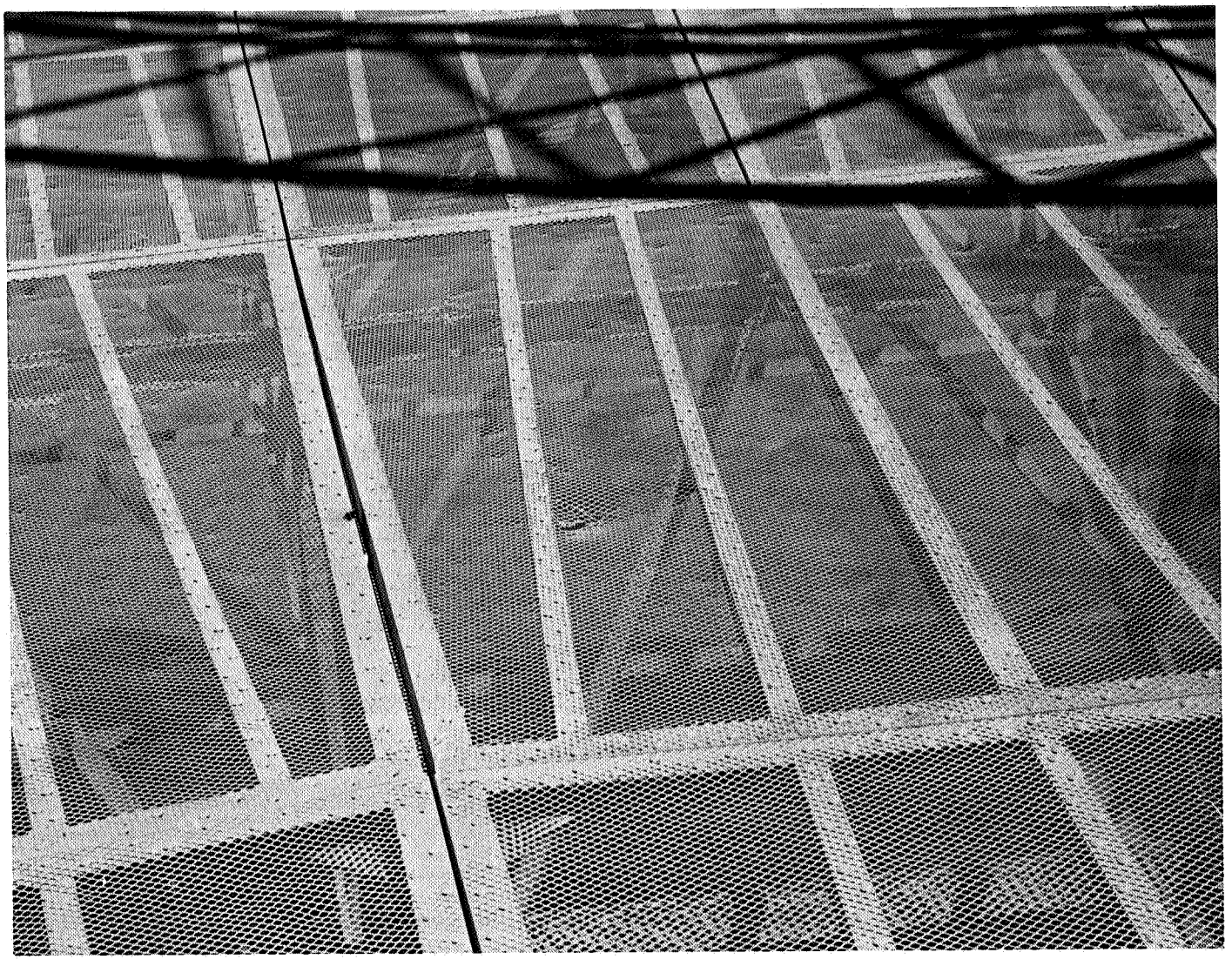

Fig. 4. Hailstone-caused surface rupture

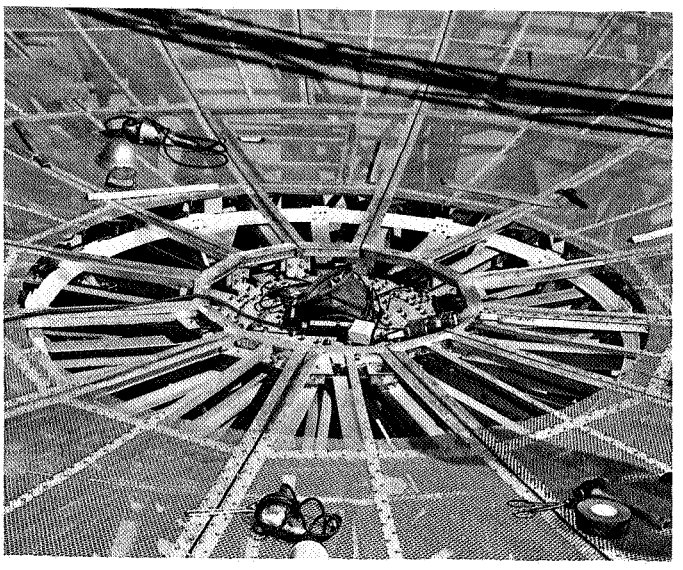

Fig. 5. Panels installed

C. Measurement of Unpainted Dish Surfaces Temperature Effects, *C. Lundy and D. Lambdin*

Because a paraboloid's reflecting surface can concentrate solar energy (especially with new shiny skins), and so endanger feed assemblies and components, it is now the practice to cover all focusing surfaces with a special white paint. This paint reflects most of the sunshine diffusely, and is also a good radiator of long-wave radiation.

The surfaces of the paraboloid on the older three-legged 85-ft HA–dec antennas at DSSs 11, 12, and 41 have never been painted. Years of weathering have turned the paraboloidal surfaces dull and gray. The hyperboloids and their supports are painted. To resolve design requirements and ascertain whether it would be necessary to paint these surfaces to stay within acceptable tolerances, temperature rises were measured. This was accomplished on a bright summer day using representative points within the Pioneer Station dish. These data were compared with corresponding temperature rises on the 30-ft research antenna at Venus Station where the whole antenna has a coat of white paint, to establish both relative and true values.

All temperatures were measured with thermistors. The air was nearly still; probably no gust of wind exceeded 10 mph. Air temperature rose from 22.5°C at 8:12 a.m. to 26.5° at 9:40 a. m. The thermistors were distributed as follows:

No. 1. On the hyperboloid, midway between center and edge, facing the dish.

No. 3. Close to No. 1, but attached to a thin disk which was coated with black lacquer. The back was insulated with plastic foam.

No. 5. On a quadripod leg near the hyperboloid.

No. 7. On a quadripod leg near the dish.

No. 8. On the plastic cover of the cassegrain cone. A refrigeration system keeps the cone cold. This explains the low temperatures read when the dish faced the sun, because then the cone was shaded by the hyperboloid.

Free air temperatures, measured by a shaded thermistor, were subtracted from the temperatures of the above five points and plotted as shown in Fig. 6. These data show the moderate rise in temperature of the quadripod leg, a much higher rise in the hyperboloid (which is near the focus of the dish), and the still higher rise of a blackbody near the focus.

A similar set of data was taken at the 30-ft antenna. Temperature rises are substantially less for both the hyperboloid and the blackbody, as shown in Fig. 7. The effectiveness of the special white paint shows up plainly.

The data shown in Figs. 6 and 7 illustrate that the aged low performance S-band panels constituting the surfaces at DSSs 11, 12, and 41 do not contribute significant temperature rises at their focal planes and, therefore, are not a source of hazard to hardware and do not require painting.

D. Surveillance Television at DSS 14, *C. Lundy*

The antenna surveillance television prototype has been installed at DSS 14. This instrumentation affords operating personnel located in the pedestal the ability to observe or detect external obstacles when the antenna is moving. Failure to detect items such as vehicles improperly parked, etc., can cause significant damage to the rotating parts of the antenna. The absence of direct observation by antenna control personnel can also constitute a serious hazard to personnel and their test equipment.

The prototype configuration at present affords two television cameras for watching the antenna. They are connected to monitors within view of the servo operator. Both cameras mount on pan-and-tilt supports that are controlled from the servo rack,enabling the operator to sweep the camera left or right, and up or down. The lenses zoom from wide angle to extreme telephoto, a ten-to-one range.

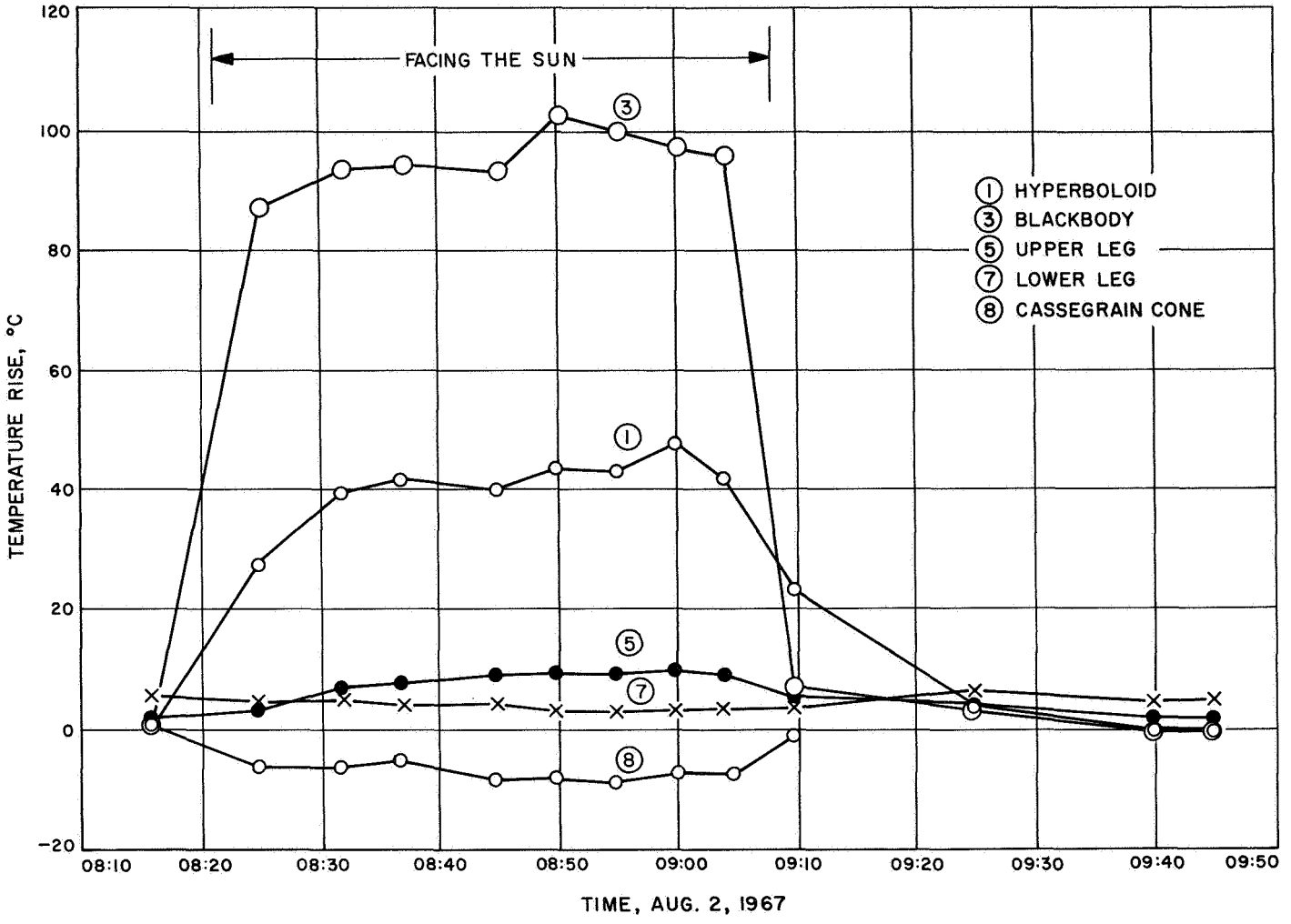

Fig. 6. Temperature rise on 85-ft antenna

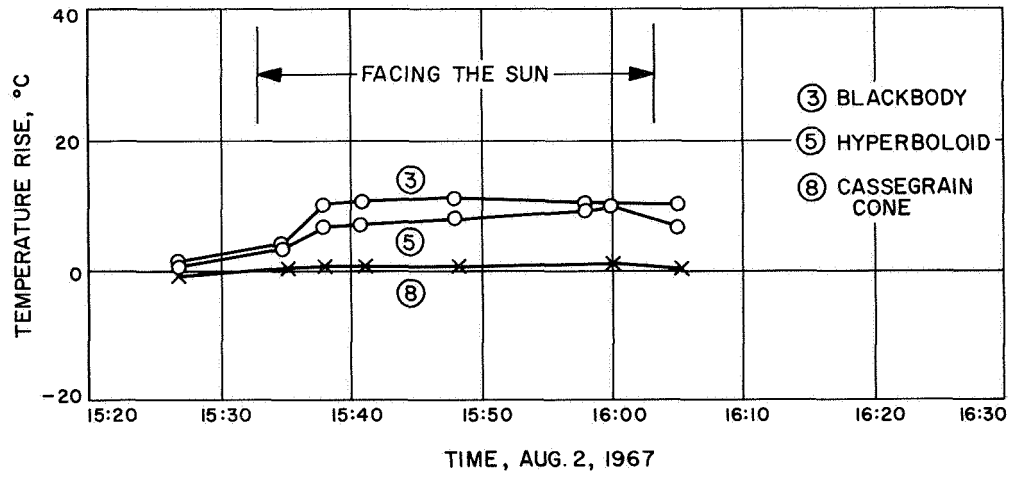

Fig. 7. Temperature rise on 30-ft antenna

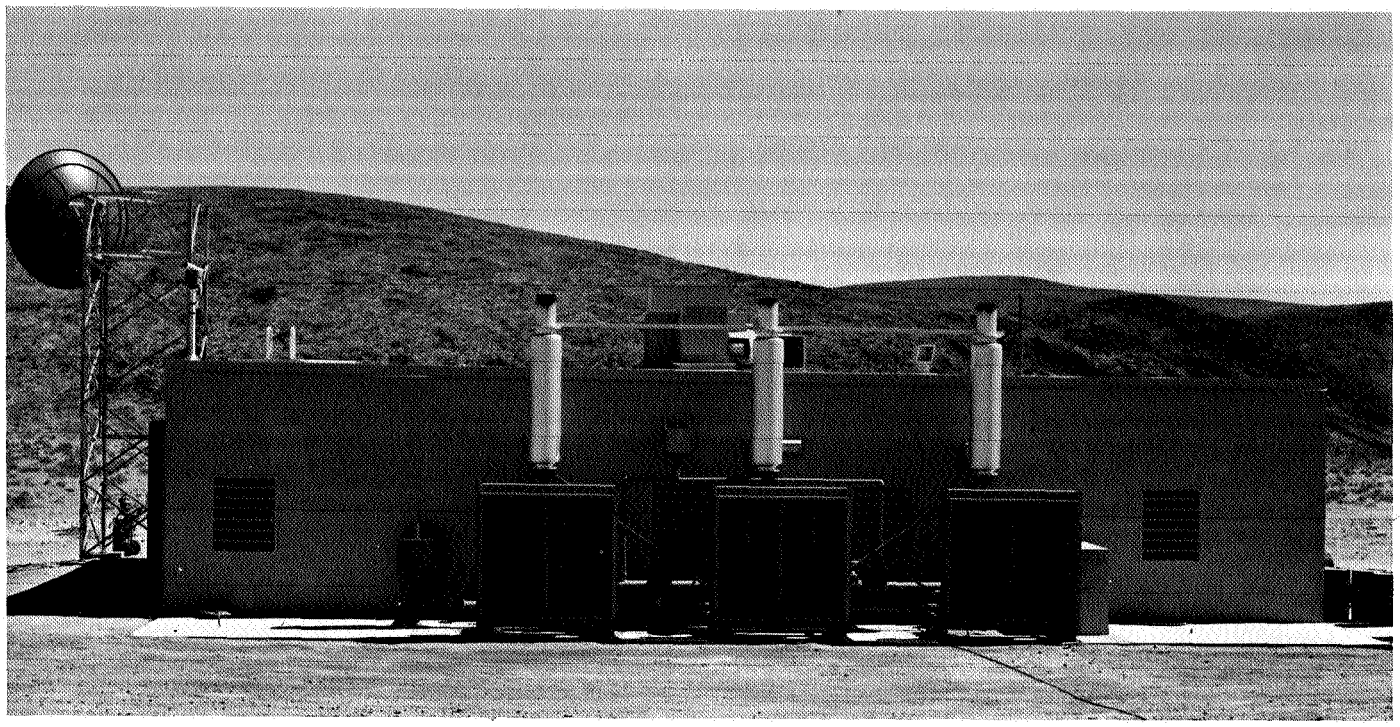

Fig. 8. Typical camera setup on roof of generator building

This flexibility allows the servo operator to view the whole antenna and its neighborhood, or to see a close-up of any part.

The two cameras now in use are on the roofs of the generator building and the hydromechanical building, respectively. They see the antenna from two nearly opposite locations so as to minimize blind areas. Two more cameras and their accessories have been purchased and will be placed high in the alidade, one over each elevation bearing. From these high bases they can watch most of the work areas on the antenna structure, and so reduce the dangers to working personnel.

Figure 8 shows a typical camera setup on the roof of the generator building.

E. Installation of a 4-ft Time Synchronization Antenna at National Bureau of Standards Facility, *M. Kron*

During the latter part of July, 1967, a time synchronization system was installed at the National Bureau of Standards Facility, Boulder, Colorado.

The purpose of this installation is to check synchronization of the DSN clocks with the cesium standard at the National Bureau of Standards, and also to evaluate the JPL time synchronization system.

The 4-ft-diam HA–dec receiving antenna was installed on top of the National Bureau of Standards radio building. A modified "H" frame roof foundation was used. The design of the "H" frame (Fig. 9) was tailored to the structural configuration of the building.

Prior to the final installation of the foundation frame, an astronomical survey was conducted by JPL personnel, since survey data were not available. Astronomical latitude, longitude, and north were established by setting up a theodolite on the roof of the radio building and sighting on Polaris.

The antenna mount was positioned and aligned according to procedures and methods developed for the installations already completed at DSSs 11 and 42. Figure 10 shows the final installation with service platform.

F. Decelerations, Impact Damage Investigation, *V. Lobb*

1. Introduction

The existing three-legged 85-ft HA–dec tracking antennas of the DSIF were originally limited capability

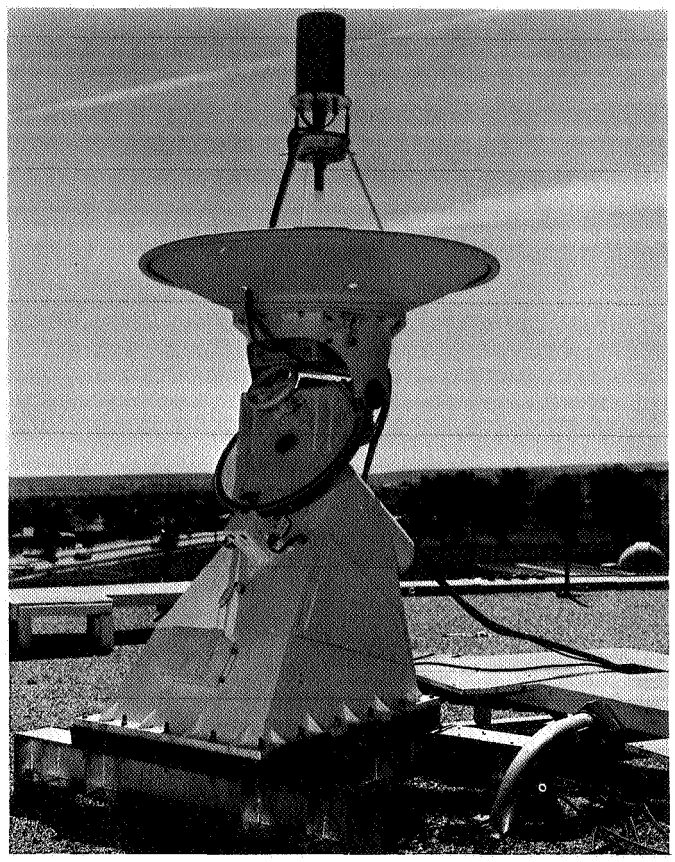

Fig. 9. 4-ft-diam time synchronization antenna showing "H" frame design

instruments, bought off the shelf for L-band operation, with an expected low duty cycle service life of 10 yr.

However, as a result of increased tracking commitments, they have since been upgraded, in requirements, to S-band instruments with vastly increased duty cycle levels, with more complex and sophisticated testing, simulation, and training operations.

As a result of these increased duty cycle levels and more complex operational procedures having more severe dynamic inputs (higher velocity rates, greater inertia values, high acceleration or deceleration inputs, etc.), investigations were undertaken to resolve possible future or existing areas of mechanical or structural damage.

2. Investigations

The investigations revealed structural clip damage and failures developing in the (HA) polar wheel counterweight cage support areas of DSSs 11, 12, 61, and 51.

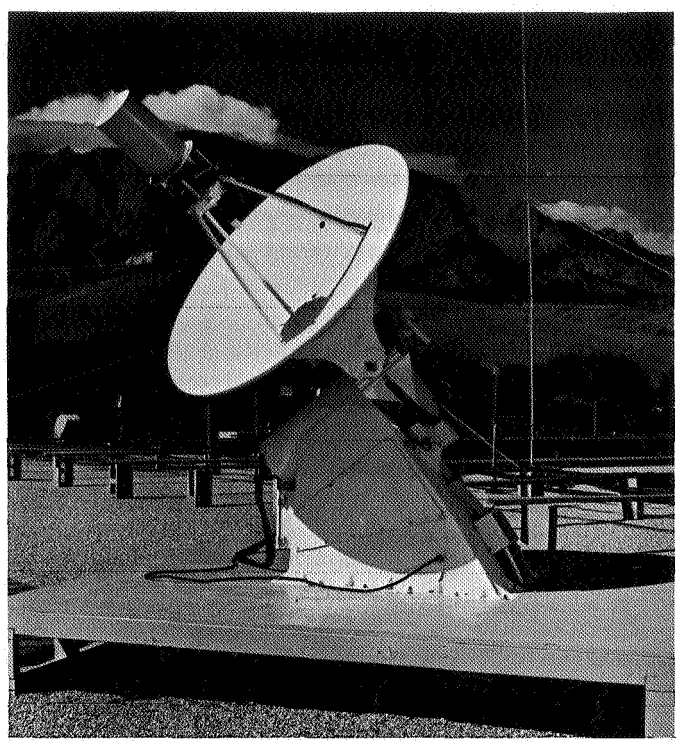

Fig. 10. 4-ft-diam time synchronization antenna final installation with service platform

Investigations revealed the problem was related to current operational procedures—high-speed collimation tower snap-on tests and high-speed stops with their large deceleration inputs.

a. Failures. Failures were found in the counterweight area of the hour angle axis. Clips and bolts holding the counterweight were sheared. Bolts in the hour angle speed reducer skid supports and its main bracing members were found to be broken by tension. Further inspection revealed that the bolts in the counterweight support members were sheared or distorted and, in addition, many others were badly brinelled (Figs. 11 and 12).

b. Repairs. Hydraulic jacks were used to restore the dropped counterweight to its original position and the structural clips were repaired and reinforced to return and maintain the load at the original load points. Additional counterweight support was achieved by the tie-in of the counterweight front plate to the radial wheel members, with A-325 high-strength structural bolts. Sufficient hour angle bull gear running clearance was achieved by this repair to alleviate previous excessive gear tooth wear.

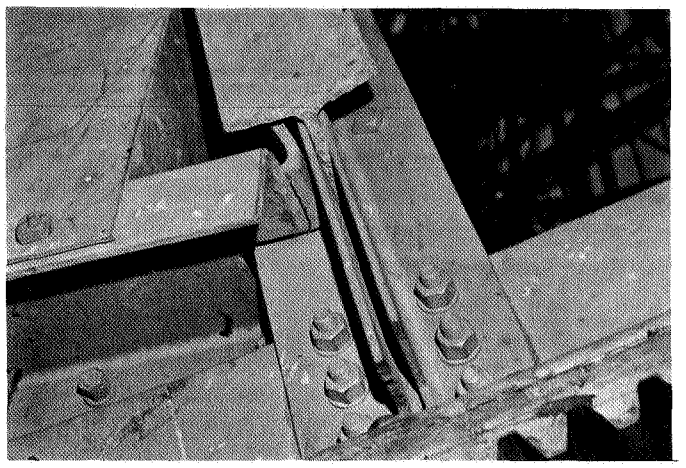

Fig. 11. Broken polar counterweight clip, DSS 11

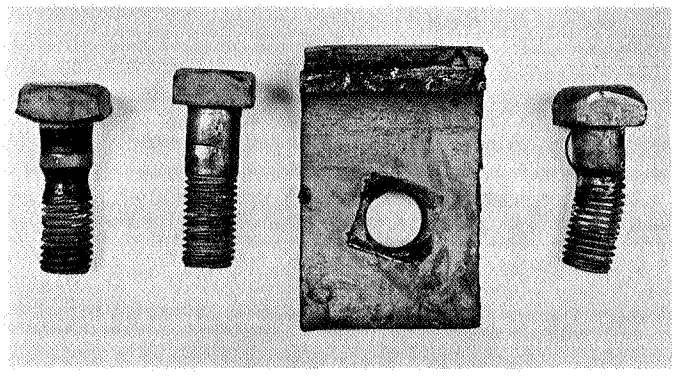

Fig. 12. Damaged bolts and broken polar clip, DSS 11

3. Discussion

Bearing in mind the possibility that the antennas during operation could have been subjected to inertial loads exceeding the working stress of the structure, the antenna operating procedures were reviewed with the following findings:

On the basis of previous antenna deceleration test data, no antenna design parameters would be exceeded in low-speed drive, acceleration and decelerations. High-speed drive accelerations appeared acceptable; however, high-speed rapid decelerations and applications of brakes or speed reversals could be harmful.

As a result of these findings, it was decided to experiment on a repaired antenna to get current data for the investigation. An experiment was performed at DSS 11 May 5, 1967, to compile engineering data relating to the structural failure problems, as follows:

A recording accelerometer was placed on the HA counterweight supports at the clip junction, and the antenna was exercised from both the MSFN and DSN control rooms. Accelerometer and tachometer recordings obtained during MSFN test program, program tape, high-speed brake, and normal brake operation along with DSN normal and emergency brake operations are on file with JPL Systems Engineering Section. All tests were performed at high-speed servo drive mode, and data were obtained at the hour angle counterweight area, which was the region of failures.

During normal DSN and emergency MSFN braking, the measured stresses at the hour angle clip positions exceeded the yield point of the original steel clip configuration and the working levels of the modified (repaired) clip members. During high-speed MSFN program test mode direction reverses, normal high-speed braking, acquisition tracking and acquisition track/auto track transfer, the measured stresses were above the working levels of the steel but below the yield point. Sample calculations are shown in Figs. 13 and 14.

4. Summary and Conclusions

The antennas, because of improper operational procedures, were subjected to decelerations in excess of the allowable design specifications. This caused long-term (1 yr or less) fatigue failures in the counterweight clip and bolt area.

To prevent possible future structural failures, the following changes to the antenna operational procedure and techniques were recommended and adopted.

(1) Braking at high speeds should be avoided. This can be accomplished in two ways: by using this brake for actual emergency situations only, and by modifying the brake with an incremental servo brake to lessen the deceleration. An engineering change requirement has been submitted for the latter to provide a proper long-term resolution; the former is being implemented as a short-term solution.

(2) High-speed directional changes can be eliminated by operator instructions in usage of MSFN digit switches.

(3) Sudden stops can be eliminated by modifying MSFN program tapes to better agree with actual antenna velocities.

(4) Acquisition tracking high-speed changes can be lessened by changing to auto track as quickly as possible after acquisition.

(A) TACHOMETER DATA — EMERGENCY BRAKE

Recorded data: $V_o = 0.92\,\text{deg/s}$

$t = 0.25\,\text{s}$

Find a in deg/s²: $V = V_o + at$

Final velocity $V = 0$

Solve $V = V_o + at$

$$-V_o = at - a = \frac{V}{t}$$

$$-a = \frac{0.92}{0.25} = 3.68\,\text{deg/s}^2$$

(Reducer shaft deceleration)

(B) ACCELEROMETER DATA — EMERGENCY BRAKE

Recorded data: 0.33-g Deceleration

Find α: $a_t = R\alpha$

$R = 24\,\text{ft}$

$a_t = 0.33\,(32.2) = 10.6\,\text{ft/s}^2$

$$\alpha = \frac{a_t}{R} = \frac{10.6\,\text{ft/s}^2}{24\,\text{ft}} \times \frac{57.3\,\text{deg/rad}}{24\,\text{ft}}$$

$\alpha = 25.4\,\text{deg/s}^2$ (cwt. deceleration)

(C) ACCELEROMETER DATA — NORMAL BRAKE AND HIGH-SPEED REVERSE

Recorded data: 0.15-g Deceleration

$$a = \frac{0.15}{0.33}\,(25.4)$$

$= 13.1\,\text{deg/s}^2$ (cwt. deceleration)

From tachometer: $t = 1/4\,\text{s}, V = 0.7\,\text{deg/s}$

$\alpha = 2.8\,\text{deg/s}^2$ (Reducer shaft deceleration)

Fig. 13. Sample deceleration calculations

Previous stress calculations indicate clip stress of 53,000 for a 0.39-g deceleration (on file with Antenna Structure Group).

For 0.33 g (measured) the clip stress would be:

$$\left(\frac{0.33}{0.39}\right) \times (53{,}000) = 45{,}000\,\text{psi}$$

which exceeds yield of 33,000; but is less than 60,000 to 70,000 ultimate strength of the material (ASTM-A7).

Measured 0.15 g maximum for high-speed direction changes, tape mode would give stress of:

$$\left(\frac{0.15}{0.39}\right) \times (53{,}000) = 20{,}400\,\text{psi}$$

which is below yield and very near the normal working stress of the material of 20,000 psi.

Fig. 14. Sample stress ratios

Also, acquisition track at high speeds should be used only when required by the project and should be kept to a minimum.

The type of repairs instituted, the tie-in of the counterweight front plate as a shear plate, the use of A-325 bolts in lieu of A-394s, and modifications of the clip angles at DSSs 11, 41, and 51 will allow the actions noted in (1)–(4) to be carried out at a minimal level, because the stresses are below the yield point but above the working levels of the steel members involved. The brake modification, plus data from the current 85-ft HA–dec characteristics study, incorporated in the antenna upgrades, will eliminate this present need for minimal application of the changed procedures, because of excessive levels of deceleration and impact forces.

G. Control System Performance for the Advanced Antenna System's Master Equatorial,

W. M. Peterschmidt

1. Introduction

The master equatorial (ME) is the precision angle reference instrument for the 210-ft diam advanced antenna system (AAS). The relationship of the ME to the other components of the AAS has been summarized in SPS 37-26, Vol. III, pp. 66–72 and 37-27, Vol. III, pp. 133–136.

The design of the AAS placed two major design goals on the ME control system. The first was a servo tracking error of less than 5 s of arc peak. The second was to provide a completely redundant drive system.

The ME structural design (SPS 37-26, Vol. III, pp. 73–79) is similar to historical optical telescope configuration and for the same reasons the preferred choice for the drive was worm gearing. A typical optical telescope polar axis drive is shown in Fig. 15. The synchronous motor moves the axis at sidereal rate and the servo motor is controlled by an operator to correct for any errors. This type of open-loop drive is accurate because the worm gearing can be made with high accuracy in a large ratio, single mesh. This feature reduces the accuracy requirements of succeeding meshes so that the accuracy of the axis motion depends almost entirely on the stability of the frequency source and the accuracy of the main worm gear.

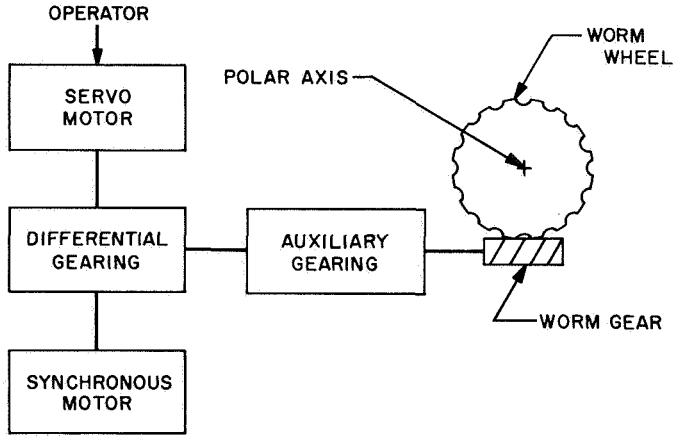

Fig. 15. Typical optical telescope polar axis drive

A worm gear drive can be made redundant because it can also be servo-controlled. However, it presents two problems to the servo design. Worm gears have high breakaway and running friction and have nonlinear dynamic characteristics. The friction characteristic is an impediment to the first design goal of low tracking error, as the pointing error is directly proportional to the friction for constant loop gain.

For the primary drive motor the choice was between a servo motor with further gear reduction and a dc torquer motor mounted on the worm shaft. The dc torquer motor was picked because it is basically more efficient, does not require more gear reduction and has a wider dynamic range. Motor efficiency was considered for the purpose of minimizing system thermal problems. Additional gear reduction was avoided because of the twin problems of backlash and friction. A schematic of the final drive configuration for the polar axis is shown in Fig. 16.

Backlash was eliminated in the worm wheel mesh by providing a constant torque on the axis by means of a spur gear mesh in parallel with the worm wheel and a dc torquer supplied with a constant voltage.

The ME control system provides many modes of operation with its redundant drives. The prime mode of operation is the computer command where the antenna pointing subsystem (APS) generates the error signals needed by the

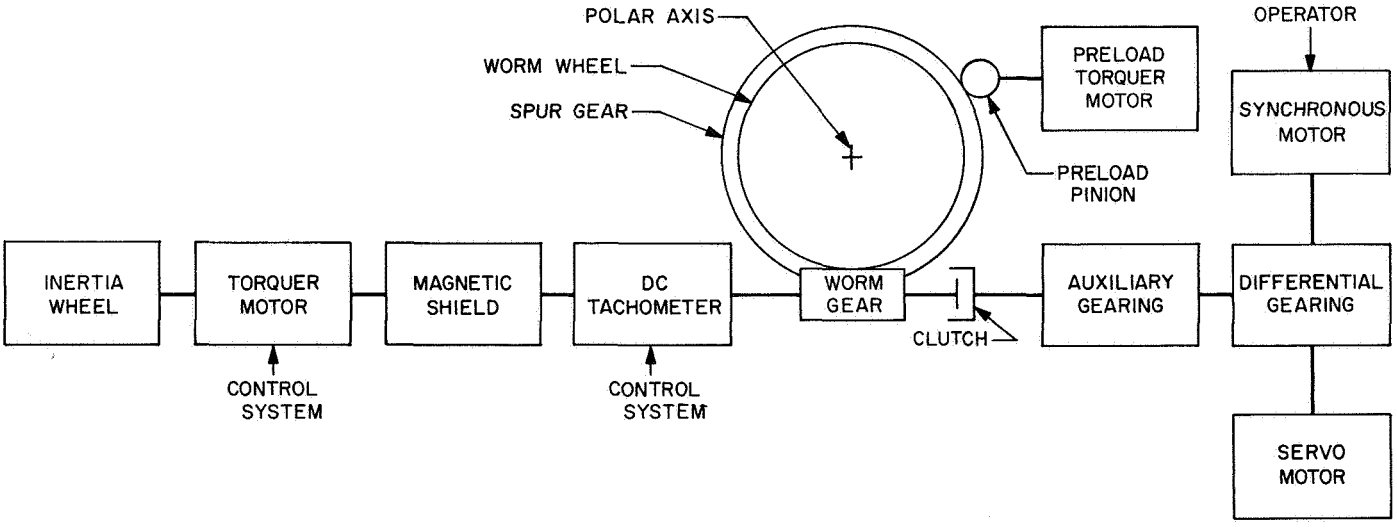

Fig. 16. Master equatorial polar axis drive schematic

servo loops to point the ME. The antenna is then slaved to the ME by means of the optical link. The second mode is optical slave where the error signals are generated by the automatic autocollimator which is part of the optical link and the ME is slaved to the antenna. The slew mode is provided for convenience in moving the ME rapidly. The redundant drive provides the last mode which is sidereal drive. In this mode, the clutch on the HA worm shaft is engaged and the synchronous motor is turned on. In both axes a rate offset speed selection is provided.

2. Servo Loop Design

The analysis of the servo loop with the constraint of a nonlinear element, the worm gear, became of necessity a major analysis project. A dynamic mathematical model of the worm gear drive was started, as was a library search for applicable work accomplished by others. The mathematical model consists of the following differential equations with an inequality equation to determine which set of equations applies for each instant of time.

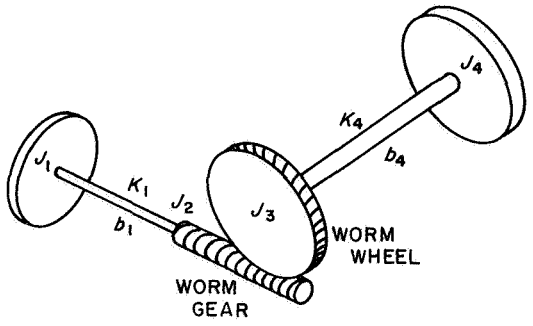

$$J_1\ddot{\Theta}_1 = -k_1(\Theta_1 - \Theta_2) - b_1(\dot{\Theta}_1 - \dot{\Theta}_2) + T_1(t) \tag{1}$$

$$J_4\ddot{\Theta}_4 = -k_4\left(\Theta_4 - \frac{\Theta_2}{n}\right) - b_4\left(\dot{\Theta}_4 - \frac{\dot{\Theta}_2}{n}\right) + T_4(t) \tag{2}$$

$$J_2\ddot{\Theta}_2 = -A + \frac{(A-D)\cos\phi\tan\alpha - H\mu|A-D|}{\left(1-\frac{n^2}{\beta}\right)\cos\phi\tan\alpha + H\mu\left(\frac{n^2\tan^2\alpha}{\beta} - 1\right)\frac{(A-D)}{|A-D|}} \tag{3}$$

where

$$A = k_1(\Theta_2 - \Theta_1) + b_1(\dot{\Theta}_2 - \dot{\Theta}_1)$$

$$D = \frac{1}{\beta}[k_4(\Theta_2 - n\Theta_4) + b_4(\dot{\Theta}_2 - n\dot{\Theta}_4)]$$

$$H = \dot{\Theta}_2/|\dot{\Theta}_2|$$

with the inequality equation

$$\frac{-\beta}{n^2}\frac{(\mu\cos + \alpha + \cos\phi)}{(\cos\phi - \mu\tan\alpha)} < \frac{A}{D} < \frac{\beta}{n^2}\frac{(\mu\cos + \alpha - \cos\phi)}{(\cos\phi + \mu\tan\alpha)} \tag{4}$$

Equations (1), (2), and (3) apply when $|\dot{\Theta}_2| > 0$ or inequality Eq. (4) is not valid.

Equations (1) and (2), together with $\ddot{\Theta}_2 = 0$, apply when $|\dot{\Theta}_2| = 0$ and inequality Eq. (4) is valid.

An analog study was started to verify the mathematical model and a mechanical model was built for experimental investigations. In the meantime, the library reported the results of the search which contained no usable references. The analog study was not completed because of the lack of time to properly develop the switching characteristics. The mechanical model showed that the large worm friction could best be controlled by a very wide bandwidth rate loop and that a large inertia added to the drive point eliminated most nonlinear effects. The design of the ME proceeded on that basis.

In order to achieve a wide bandwidth rate loop, an inner current loop was designed to raise the frequency of the inductive lag of torquer and power amplifier combination and to reduce the deadband of the power amplifier. The block diagram of the current loop is shown in Fig. 17. Because of the bridge-type output stage of the power amplifier, a differential amplifier is used to reject the common mode component of the current signal.

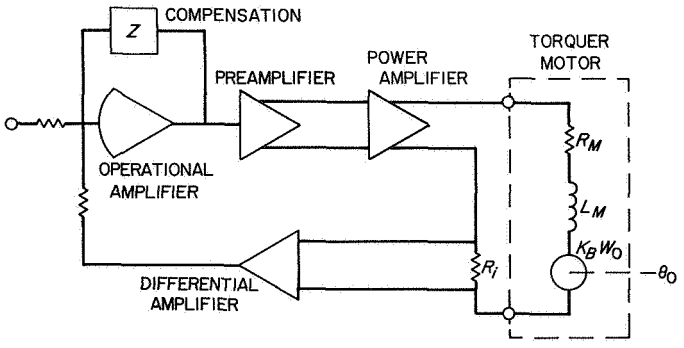

Fig. 17. Current loop

The transfer friction (TF) of the open current loop is shown in Fig. 18 as a Nichol's plot. The compensation for this TF contained in Z of Fig. 17 is a lag-lead-lag at 10, 200 and 4000 Hz, respectively. This results in a closed loop bandwidth of about 500 Hz. The open-loop TF for the rate loop is shown in Fig. 19. The compensation for the rate loop summation consists of another lag-lead-lag network at 0.5, 5, and 100 Hz. The closed rate loop bandwidth is not a simple single-valued function but depends on gimbal velocity. This is caused by the large inertia, added to the worm drive, which limits the acceleration capability. The rate loop has a bandwidth in excess of 70 Hz

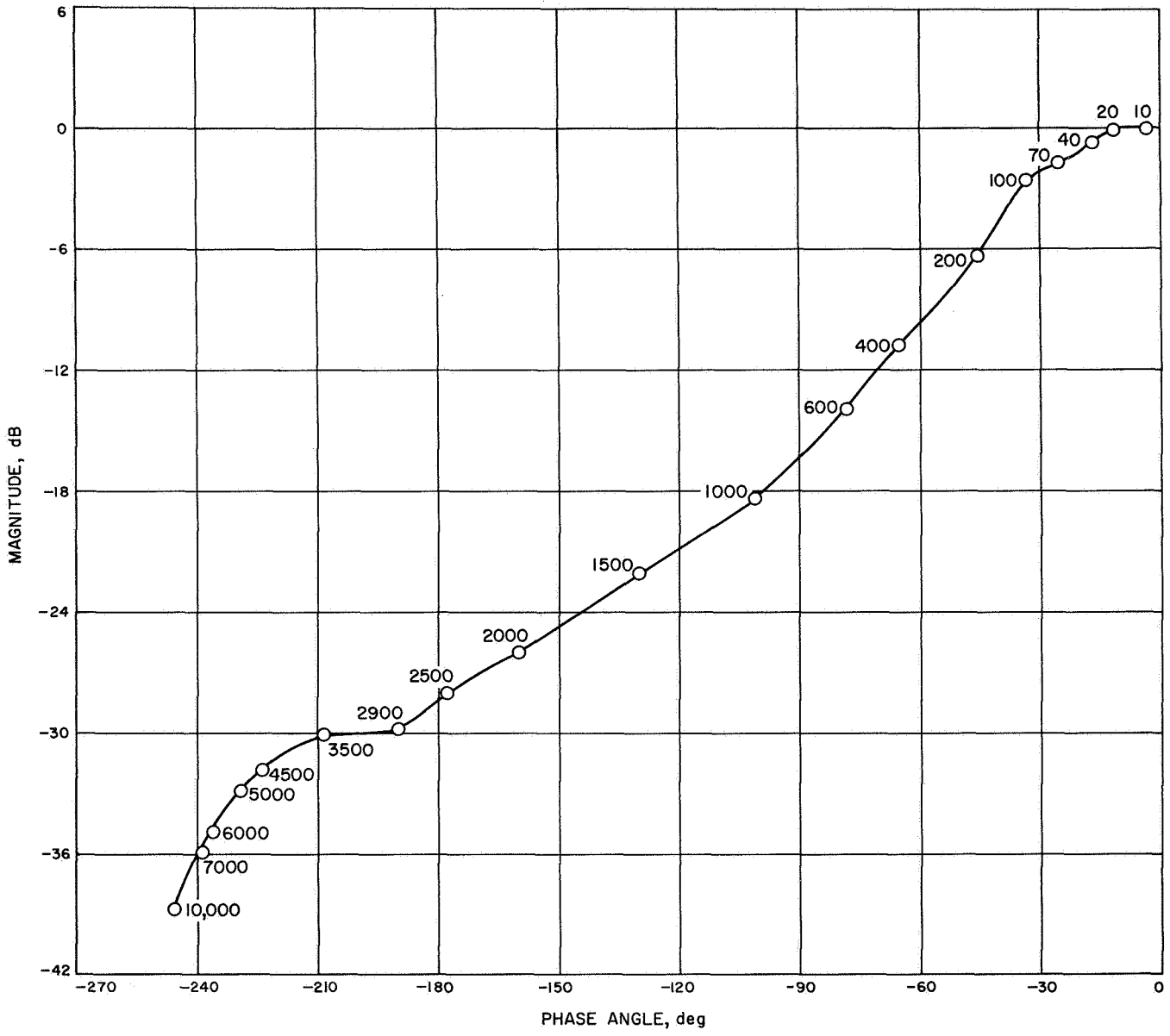

Fig. 18. Open current loop transfer function

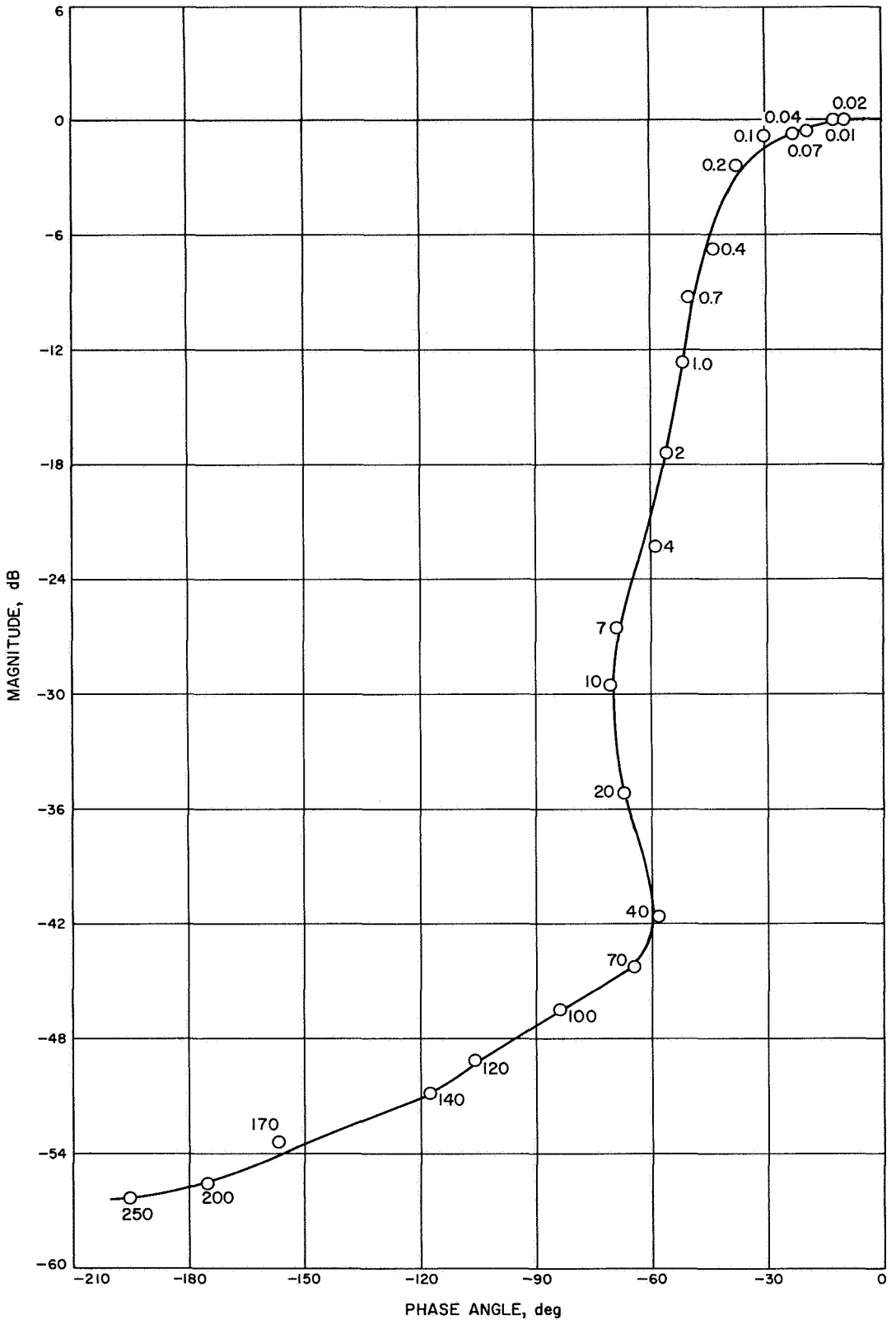

Fig. 19. Open rate loop transfer function

at small signal levels and not less than 8 Hz at a torque saturated condition.

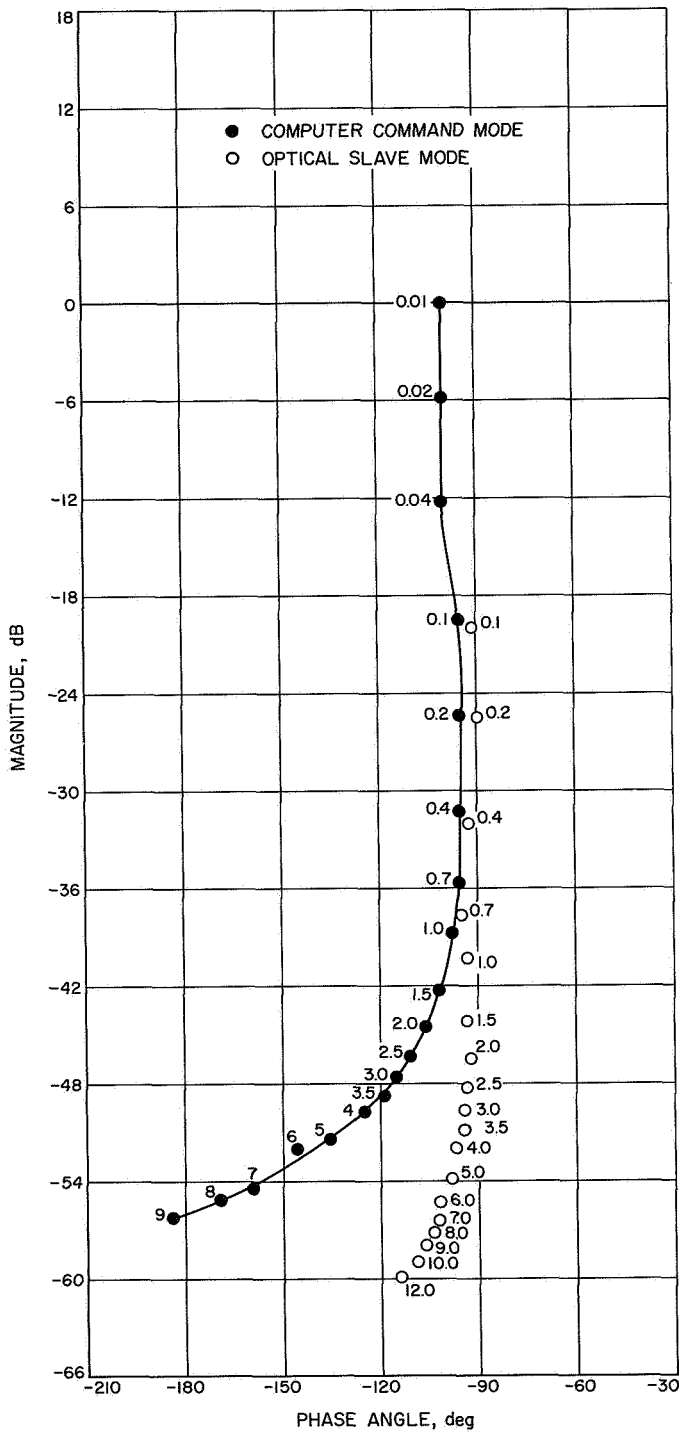

Fig. 20. Open position loop transfer functions, computer command and optical slave modes

The position loop transfer functions are shown in Fig. 20. The corresponding closed loop bandwidth is approximately 3 Hz for the computer command mode of operation and approximately 6 Hz for the optical slave mode. The explanation for this disparity in bandwidth is found by examination of the systems which provide the error signal in the two modes of operation. The automatic autocollimator used in the optical slave mode has less than 5 deg of phase lag at 5 Hz. However, the computer command mode has a series of phase-lag generating components. The Datex encoder system is a servo repeater type and its phase shift is approximately 5 deg lag at 5 Hz. The antenna pointing subsystem (APS) has two sources of phase shift. The first is the sample and hold function itself, which for a sampling rate of 50/s accounts for 18 deg of lag at 5 Hz.

The other source is the time delay between the interrogation of the encoders and the output of the error signals to the control system. The time delay is approximately 2 ms, which at 5 Hz gives a 4-deg phase lag. Therefore, the difference in phase lag at 5 Hz is at least 22 deg for the APS. Note that in Fig. 19 the actual difference in phase shift is 37 deg at 5 Hz, which is greater than the predicted difference by about 15 deg. This may be accounted for by a difference in amplitude which may cause acceleration limiting.

One problem that developed with the position loop was a limit-cycling condition when the loop was adjusted for best tracking. This could be brought about by a large step in position. The cause of the trouble was the acceleration-limiting effect of the inertia wheel. Since it was desirable to retain the inertia wheel, the problem was solved by an addition of a switching circuit to the position loop. This switching circuit sensed the size of the error signal and changed the configuration of the compensation from a type II for best tracking to a type I for better response. The resultant control loop block diagram is shown in Fig. 21.

The position loop bandwidth is adequate in the computer mode to assure a servo following error of ± 1 bit which is equivalent to ± 1.24 s of arc. The servo following error for the optical slave mode is about 0.5 s of arc at sidereal rates where the resolution of the autocollimator is approximately 0.25 s of arc.

The rate loop has adequate gain and bandwidth to provide smooth speeds from 3 to 0.001 deg/s. The mount can be readily positioned using these rate controls to within 0.001 deg.

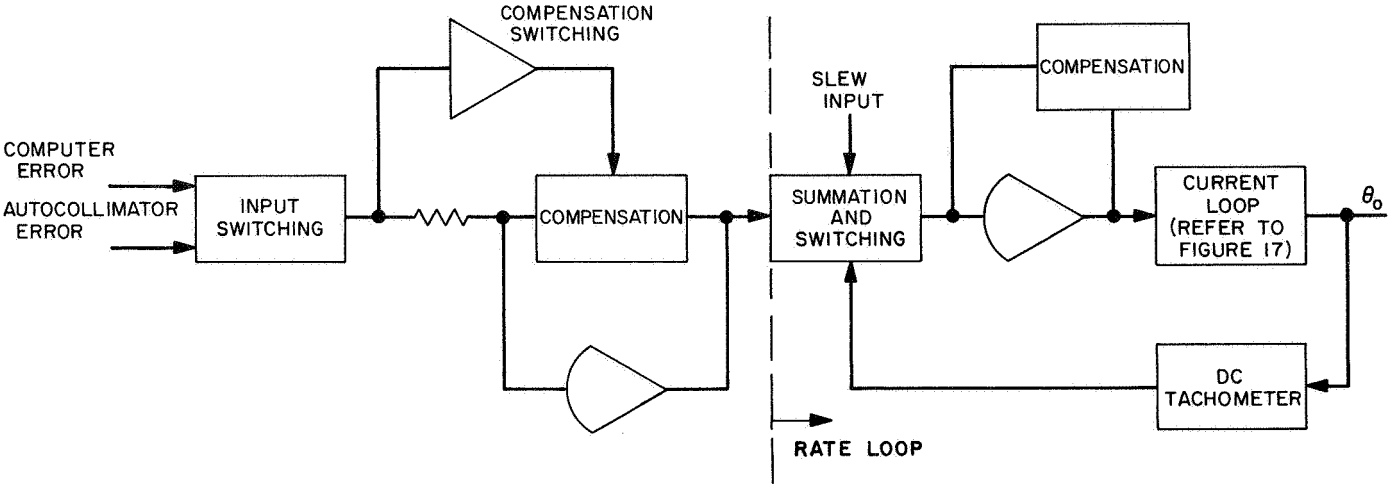

Fig. 21. Control loop

VI. Facility Engineering and Operations

A. Flight Project Support, *R. Cuberly*

1. *Lunar Orbiter* Missions

The *Lunar Orbiter V* photographic mission has been completed. The Echo DSS performed periodic tracking of *Lunar Orbiters II* and *III* until their transmitted data commands for impact on October 11 and October 9, respectively. The Echo DSS continued to track *Lunar Orbiter V* and to transmit data commands for engineering and scientific experiments.

2. Pioneer Missions

The stations are alternately tracking *Pioneers VI* and *VII* on a noninterference basis with other missions. The Pioneer and Echo DSSs are providing telemetry and command support for Mars DSS tracking.

3. *Mariner* Missions

a. Mariner IV. The Mars DSS transmitted data commands for a second burn on flight day 1061, October 25, and on October 26 for a retransmission of photographic data stored in the spacecraft. The Echo DSS provided back-up for the burn period and processing of the photographic data.

b. Mariner V. The spacecraft encounter with the planet Venus occurred on October 19. The Mars DSS provided primary tracking and data command transmissions. The Echo DSS processed the engineering and scientific data transmitted by the spacecraft. Other DSN stations provided back-up support during the encounter, and tracking support during their respective view periods. Routine tracking of the spacecraft continues.

4. Surveyor Mission

a. Surveyor V. The spacecraft was launched on September 8, 1967 (GMT). The Pioneer DSS provided primary tracking and data command transmissions and processed photographic, engineering, and scientific data transmitted by the spacecraft. The station processed more than 15,000 video frames. The Mars DSS provided back-up support until spacecraft landing. Pioneer DSS project support continues into the second lunar day.

b. Surveyor F. The Pioneer DSS is performing configuration verification testing in preparation for the mission.

5. Special Tests and Experiments

a. Voice relay experiments. On October 2 the Echo DSS participated with Langley Research Center in performing a voice relay via the orbiting *Lunar Orbiter V*. A technical description of the procedure is given in SPS 37-47, Vol. II, pp. 143 to 145.

b. Star-track experiments. The Pioneer DSS provided support for two experiments as follows:

(1) The lunar occultation experiment of a galactic source.

(2) The measurement of the scintillation effect on stars 3C273 and 3C279 as they approached the sun.

c. Goldstone-Venus bistatic experiments. The Mars DSS provided tracking facilities for Venus DSS experiments with the planets Venus, Mars, and Mercury. Venus DSS receivers, located at the Mars DSS, processed the return signals.

d. DSIF tests and experiments. The Goldstone DSCC continued to support various DSIF projects by conducting tests and experiments, such as antenna pattern experiments on a far field source, time-correlation experiments, periodic confidence tests, celestial mechanics tests, and equipment tests and experiments.

B. Venus DSS Operations, *J. D. Campbell, R. M. Gosline, M. A. Gregg, E. B. Jackson, R. B. Kolbly, A. L. Price, and H. C. Holeman*

1. Experimental Activities

During the period of August 16 through October 15, 1967 the 30-ft antenna at the Venus DSS continued to be used in a time-synchronization experiment, and the 85-ft antenna continued to be used in planetary radar experiments, both monostatic and bistatic. Additionally, the 30-ft antenna was extensively used for passive observations of Venus with a 23-GHz radiometer, and the 85-ft antenna was tested with an ultra-low-noise cone for reception of the *Mariner V* spacecraft (this cone was employed by the Venus DSS during the *Mariner V* encounter on October 19 with the planet Venus).

Time synchronization, via the moon as a reflector, has continued with the National Bureau of Standards (NBS) at Boulder, Colorado. NBS was able to measure, with good resolution, the rate at which the Venus master clock is drifting (100 μs in 60 days). Unfortunately, failures of the tunnel diode amplifier have kept the Canberra, Australia, and Pioneer DSSs from receiving the time-synchronization transmissions.

The planetary radar experiment, with Venus as the target, has been producing excellent data, particularly the bistatic experiments. Significant amounts of data have been accumulated on the various modes (total spectrum, cross and matched polarization, and mapping with various clock periods varying from 10 to 800 μs).

2. Subsystem Performance

a. Receiving system. During this period the Mod IV receiver (2388 MHz) was used in the Venus radar experiment. Reception was accomplished in both the bistatic mode and in the monostatic mode. Phase-locked operation as well as the normal open-loop operation was attained.

b. Servo system. System performance of the 85-ft antenna servo system has been degraded to some extent in the elevation axis due to removal of counterweight. This modification is in preparation for the transmitter-electronics room (SPS 37-46, Vol. III, pp. 138 to 144) to be installed during the next scheduled shut-down period. However, the tracking error is well within limits, and normal planetary tracking has continued during this time.

c. Transmitting systems. The R&D transmitter, operating for the Venus monostatic and bistatic radar experiments, has had only a few interlock failures and other minor problems.

The X-band transmitter has been operated for a total of 182.4 beam hours for the time-synchronization experiments.

3. System Improvements

a. Antenna systems. A special feed cone for the 30-ft antenna was installed to allow cassegrain feed to be achieved on either 8.45 GHz (X-band transmitter) or on 22.4 GHz (K-band) with a switched radiometer.

The original X-band feed horn/polarizer assembly, with its associated switches, was removed from the existing cassegrain cone structure and modified for installation in a new cone. Design and installation of the modified X-band waveguide system were done at the Antenna Range facility of the Goldstone development support group.

On either side of the X-band feed (located on the antenna axis) is a 22.4-GHz conical horn (Fig. 1). These are connected by runs of WR-42 waveguide to the

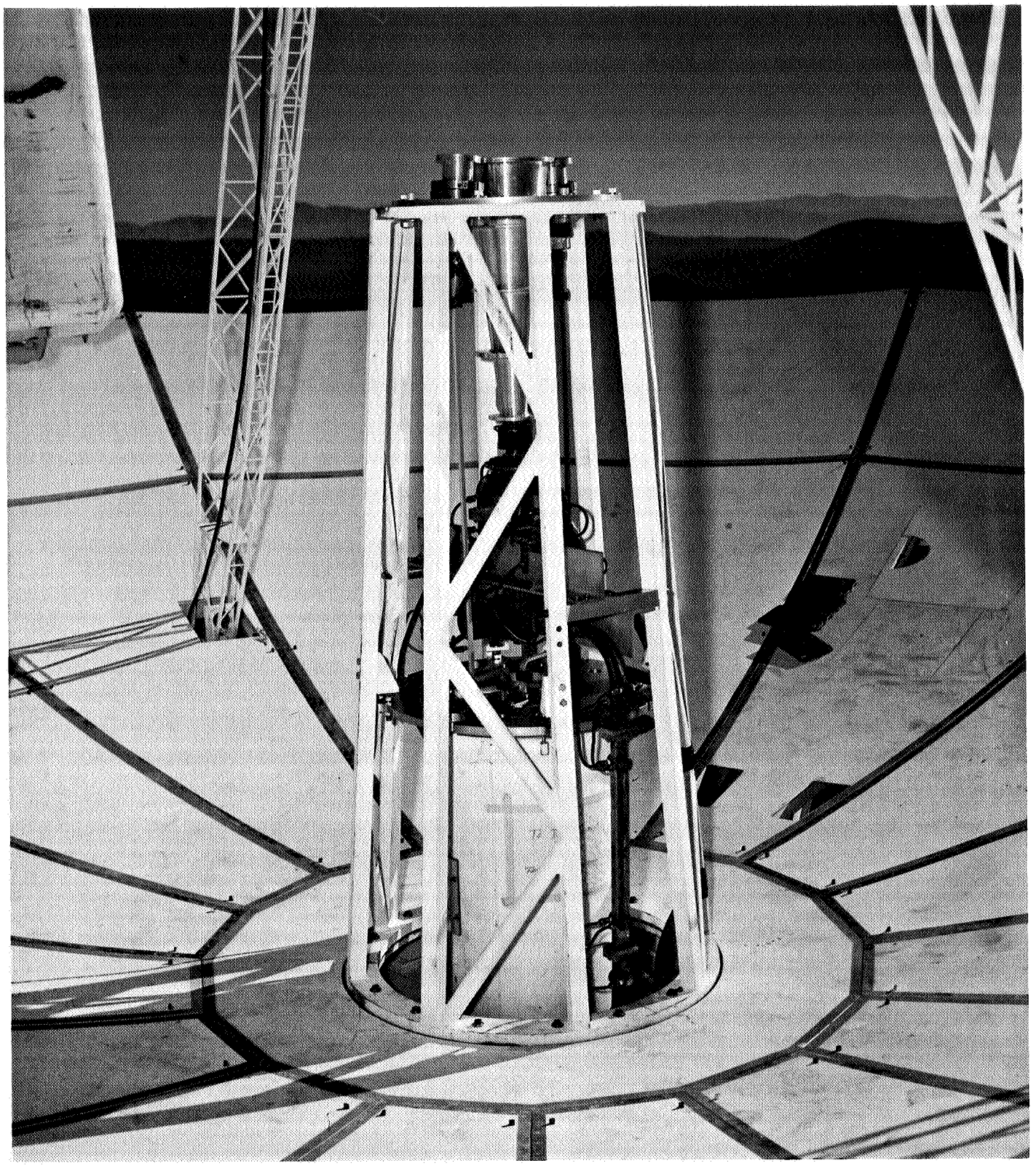

Fig. 1. Modified cassegrain feed cone, 30-ft antenna

switched radiometer package, located in the bottom of the cone structure. These two feed horns are not on the antenna axis, hence the K-band beams have an angular offset. One beam measures the temperature of the object under observation, and the other observes the adjacent sky.

Both the X-band transmitter system and the K-band radiometer have performed satisfactorily. It is now possible to go immediately from an X-band mission (e.g., time synchronization) to a K-band radiometer experiment with no time lost for feed system change-over. The two systems are independent (except the antenna and associated pointing system). No degradation of either system has been detected as of this writing.

b. Digital systems

Ephemeris Update Tracking Program. Early and accurate angle ephemerides for tracking missions are not always obtainable. A method of tracking a spacecraft or radio source from an approximate ephemeris is being implemented. The method is to use a digital computer to generate a small circular scan modified by signal power feedback to maximize the signal strength.

It was desired to use common equipment so that utilization at other sites would be simplified. The antenna pointing subsystem (APS), incorporating an SDS 910 computer, was chosen over the faster SDS 930, which is not available at other sites. The implementation therefore involves mainly software.

Referring to the functional diagram (Fig. 2) an HP 431B power meter converts the noise and signal power from the 30-MHz IF to a dc voltage suitable for an analog-to-digital converter (A/DC). A circular scan function is generated for the antenna by addition of a sine and cosine function to the azimuth and elevation drive channels, respectively. Provision is made for changing the amplitude and period of the scan while operating. The signal is sampled at a 50-Hz rate and correlated with the circular scan function each second. After suitable filtering and gain control, the correlated signal power and scan function is applied to the drive channels to cause the antenna to follow the point of higher signal power.

To minimize the amount of new software required, it was decided to use the existing basic Antenna Drive Program and integrate it with the Ephemeris Update Program. Numerous problems arose interfacing the two programs, and although they are now compatible, a better program could be written with the antenna drive portion incorporated with the ephemeris update portion as a unit.

The system has reached the trial stage and experimentation is needed to optimize parameters and evaluate the performance on moving targets. Initial tests indicate the antenna is able to lock on to a collimation tower signal with a scan amplitude as large as 1 deg. Initial tests also

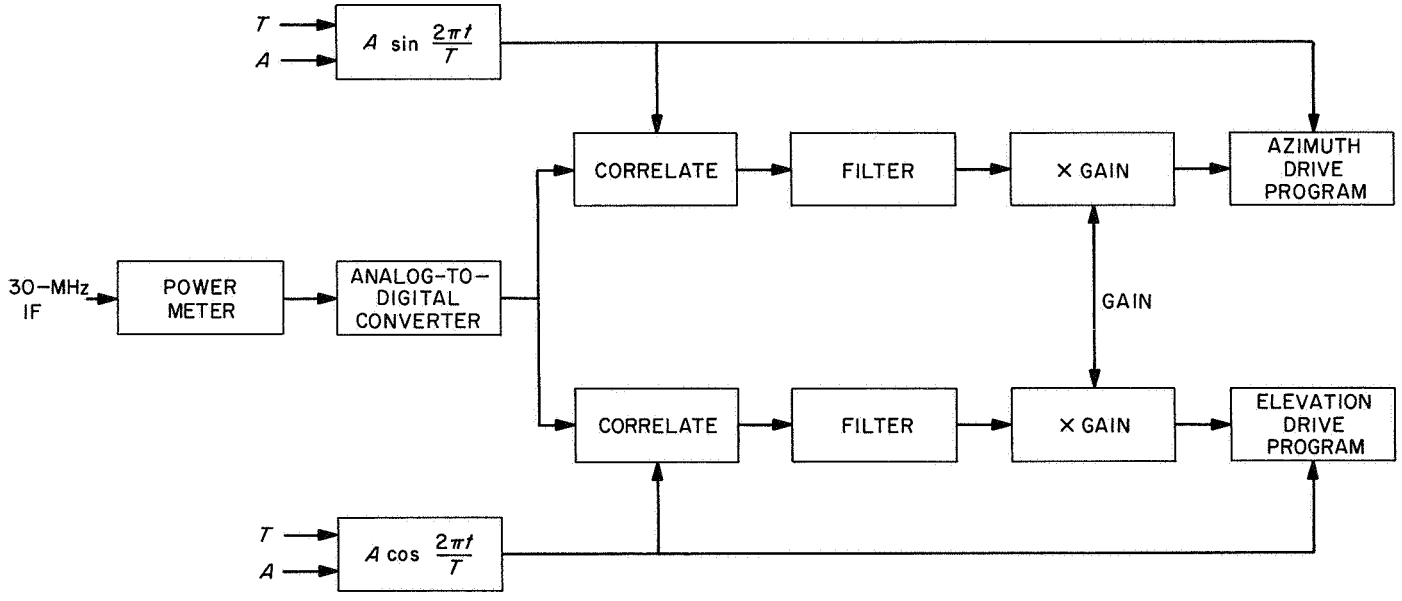

Fig. 2. Ephemeris Update Tracking Program functional diagram

indicate that some method of automatic gain control would be desirable.

A more detailed evaluation will be possible after additional experimentation and refinements in the implementation.

Stored program controller. The rebuild of the stored program controller (SPC) is continuing somewhat behind schedule, due to time necessary for correcting the following problems:

(1) The size of all interblock connectors had to be increased to allow for additional conductors.

(2) All interblock cable harnesses were rebuilt to contain additional conductors and correct a binding problem when opening the slide-out bays.

(3) Additional logic was provided to rectify module fan-out loading problems.

(4) The cabinets were unbolted and rearranged for more convenient operation and maintenance.

(5) Inadequate ground bars were replaced by copper braid.

(6) All interface connections were relocated to a common panel adequate for the number of conductors.

Other digital system improvements. An additional APS control panel is being constructed so that both the 85- and 30-ft antennas may be simultaneously controlled by the APS system. A new offset panel for the digital differencing junction (DDJ) is also under construction to allow for decimal offsets and replacement of the codebar switches with a more reliable type.

c. Receiving system. During this period, the 2295-MHz converter and its associated cabling were installed in the ultra-cone. Ground testing was accomplished by using the previously installed cables running from the antenna to the cone storage area. The cone was subsequently installed on the 85-ft antenna and used in the phase-locked reception of signals from the *Mariner V* spacecraft. Since the *Mariner* receiver, in its present configuration, has no phase-locked channel, phase-locked operation was attained by feeding 30 MHz from the *Mariner* receiver into the 30-MHz portion of the Mod IV receiver. Then by offsetting the programmed local oscillator to place the received signal in the center of the passband of the receiver, the special 455-kHz locked loop in the Mod IV receiver can be used.

The *Mariner* receiver (2295 MHz) has been modified for operation in the Venus occultation experiment. This modification involved the addition of a wideband (100 kHz) channel consisting basically of a 30-MHz amplifier, a 30-MHz mixer, and an output amplifier driving two FR-1400 tape recorders. The mixer uses a 30-MHz reference.

The local oscillator drive can be supplied from either of two sources. One source is derived from a frequency synthesizer. This will be used during occultation. The other source is the programmed local oscillator. This will be used for premission testing.

The 2295-MHz receiver was also used in a cw power calibration experiment. In order to perform this test, the 2295-MHz test transmitter was modified to supply 30 dB more output power. This change was necessary because of the high coupling losses (66 dB) in the ultra-cone. The modification will be retained through the occultation experiment.

The 8448 to 30 MHz converter and power supply were removed from the X-band feed cone and installed in the Venus DSS control room. The X-band receiver will be used to monitor the X-band transmitter output and to facilitate adjustment of the transmitter phase modulator. The modulation adjustment will be accomplished by observing the receiver range channel output (1050 Hz) through a 10-Hz filter. The signal input for the converter is obtained from a probe antenna mounted in the 30-ft antenna.

The planetary radar maser instrumentation was improved by the addition of a new 30-MHz detector bias panel and a shielded precision IF attenuator. The new equipment features improved shielding to reduce errors in noise power measurements due to signal leakage at the 30-MHz intermediate frequency.

Ground versus on-antenna facilities were expanded with the addition of a helium compressor and maser instrumentation equipment near the cone storage area. This allows operation of a cassegrain feed cone on the ground with instrumentation to monitor maser performance. Daily system temperature measurements were made on the

ultra-cone after its delivery to the Venus DSS and prior to its installation on the antenna.

During the period September 15 through 22, an S-band cassegrain ultra-cone was tested on the 85-ft az–el antenna. These tests consisted of daily system temperature measurements, radio source temperature calibration, and system temperature profiles as a function of elevation and azimuth angle.

System temperature was measured by comparing the noise output of the receiving system when alternately switching the maser input from the antenna feed horn to an ambient temperature waveguide termination (SPS 37-46, Vol. III, p. 72). The results of nine sets of measurements indicate a system temperature (antenna pointed at zenith) of 16.41 $\pm$0.34°K probable measurement error. This represents a nominal 1.3-dB improvement over the zenith system temperature of the planetary radar cone.

d. Servo systems

The 85-ft az–el antenna. Stability checks are continuing on the solid-state servo amplifier and power supply installed in the servo system during July. A modification has been added to the system to allow the antenna to be slaved to either the DDJ or the SDS 910 computer. This change will provide a back-up pointing system and allow the 85-ft antenna to be used in evaluating the Ephemeris Update Tracking Program.

Hydraulic test facilities. Installation and checkout has been completed on the hydraulic test console and power supply to be used for antenna hydraulic component testing. Manifold adapter subplates, hydraulic hoses and fittings which will allow full static and partial dynamic testing of most components now used on the present hydraulic systems have been ordered.

e. Transmitting systems. A new instrumentation cabinet was assembled to house the cone instrumentation for the klystron cabinet. Wiring modifications were made to the klystron cabinet to make the circuitry compatible with the new control cabinets installed for control of the new 100- and 500-kW transmitters.

Installation of the new 1-MW solid-state power supply, modifications to the crowbar cabinet for upgrading the capability of the beam voltage to 70 kV, and to effect compatibility with the new control system were also completed.

C. DSIF Station Control and Data Equipment,

E. Bann, R. N. Flanders, A. T. Burke, H. B. Paris, and E. Garcia

1. Introduction

The DSIF station control and data equipment consists of the antenna pointing subsystem (APS), digital instrumentation subsystem (DIS), the telemetry and command processor (TCP), the frequency and timing subsystem (FTS), and the multiple-mission support equipment (MMSE).

2. Antenna Pointing Subsystem

The APS has been implemented in the DSIF stations to provide the capability of pointing the station antenna via computer control.

The APS Phase I, in addition to its function of controlling the antenna, has been designed to provide monitoring information to the digital instrumentation subsystem phase II (DIS-II).

The function is accomplished by providing a 24-bit buffer register within the APS which can be updated by the APS program. This 24-bit register is connected via a system cable to one of the negative true inputs of the DIS which is at all times available to the DIS monitor program. These 24-bits of information are referred to as the "APS data monitor word." The function of the monitor word is to provide the DIS-II with the current operational status of the APS. The following information is supplied to the DIS-II:

(1) APS failure.

(2) APS ready.

(3) Diagnostic failure.

(4) Drive tape sample failure.

(5) Change in APS status.

(6) Antenna pointing angle errors.

APS Phase I is scheduled for installation at 1-mo intervals, starting in February 1968.

3. Digital Instrumentation Subsystem Phase II

The DIS-II, operating under the control of the DSIF Phase I Monitor Program, directs the monitoring functions within the various stations of the DSIF. The DIS-II, together with the station control and monitor console phase II (SMC-II), is responsible for system performance

and status monitoring, alarm monitoring, preparation of a permanent record of station performance for real-time or postmission analysis, and the generation of alarm and status messages for transmission to the SFOF.

Present activities are concerned with the implementation of the DIS-II within the DSIF and the establishment of a compatible format for alarm messages and periodic reports between each deep space station and the SFOF. The messages are to be transmitted via the high-speed data channel of the Ground Communications Facility. As such, the DSIF monitor reports are to be multiplexed with the telemetry and engineering messages of the telemetry and command processor phase II (TCP-II) which shares this same channel.

The DIS-II periodic report will utilize one 600-bit high-speed data block, while the alarm messages will utilize a second block. The alarm messages are to be by exception only, with the absence of any data in the alarm portion indicating satisfactory performance. The periodic report will output gross station performance indicators to the SFOF. The DSIF Monitor Program will process the high-resolution parameters provided to the station by merging related functions to produce the lower resolution periodic report. Parameters selected for transmission to the SFOF are to consist of those mutually selected by the DSN monitor project personnel. This will primarily include those for which processing and display requirements exist within the SFOF.

Interface compatibility with subsystems to be monitored is being established. This entails the definition of new and reassigned system cables, and the identification of new parameters not previously monitored. New interfaces will exist with the telemetry and command processor phase II (TCP-II), Ground Communications Facility, frequency and timing subsystem phase II (FTS-II), and the subcarrier demodulator of the multiple-mission telemetry project. Additional subsystems for which new parameters are to be monitored include the receiver, transmitter, antenna pointing subsystem and station control and monitor console. Digital and analog input signals from the monitored subsystems are inspected, converted to digital form if required, and stored for processing and recording. The processing for each input parameter is currently being defined as a part of the DSIF Phase I Monitor Program implementation.

4. Telemetry and Command Processor Phase II

The TCP-II provides the DSIF with a mission-independent telemetry and command data-processing capability for real-time operation. The TCP-II assembly interfaces with the mission-dependent project equipment and provides the capability to decommutate, process edit, alarm monitor, and format spacecraft telemetry data for transmission to the SFOF, and to process and verify command data, received at the DSIF station from the SFOF for transmission to the spacecraft.

The TCP-II is in the process of expansion to further its capabilities of digital recording of telemetry and station data (TCP-II-B) and telemetry processing support to the mission-independent telemetry demodulation (TCP-II-C).

The A/DC at DSS 12 has been aligned, checked out, and is now operational. Installation of the A/DCs for DSS 41, 42, 61, 62 and 71 will be made in mid-November 1967.

The SDS 920 computer and magnetic tape unit from the DSS 72 TCP-II arrived at JPL in mid-September 1967 and have been installed in the SFOF for use in DSIF computer program checkout in support of *Mariner* Mars 1969. The communications buffer from the DSS 72 TCP-II has now been installed in the digital instrumentation subsystem (DIS) at DSS 72, and TCP-II functions will now be performed in the DIS for support of the *Surveyor E* mission.

The purchase order for the prototype TCP-II-B-C expansion kit was placed and equipment delivery schedule is March 1, 1968. This first expansion kit will be installed at DSS 21 for system compatibility test. The purchase order for additional TCP-II-B-C expansion kits for DSS 14, 51, 61, and 71 is pending.

Functional and cabling interfaces with mating equipment have been designed. Software interfaces, including the format and content of data message, and special input/output equipment addresses are defined. The high-speed data line (HSDL) register of the TCP-II will be modified to interface with the high-speed block multiplexer (BMXR)/error detection encoder decoder (EDED)/HSDL modem in the DSIF ground communication system.

5. Station Monitor Console

A Block I version of the station monitor console has been installed to be used in the development of the Block II SMC.

Prototype versions of the program alarm panel and countdown clocks will be constructed and installed in the

prototype console as soon as the JPL standard modules are delivered.

An evaluation criteria specification is being generated to allow completion of the X-Y plotter evaluation.

6. Frequency and Timing Subsystem Phase II

Division 33 standard digital modules will be used which are built from components screened to flight equipment specifications. The component screening procedures will eliminate marginal components, significantly improving the initial and long-term reliability.

The FTS project is currently conducting an evaluation of the module types to identify those performance characteristics which will contribute to the overall FTS goals and to allow a more quantitative evaluation of the expected reliability. In addition to the use of these modules, triple redundant circuitry will be used in such critical assemblies as the frequency divider chain.

The FTS II design is currently being evaluated for the possible inclusion of a monitoring and automated status and operational configuration assembly.

7. Multiple-Mission Support Area (MMSA)

a. Mission support recording. Various changes have occurred in the MMSA's mission support recording capabilities at the stations due to the completion of the *Lunar Orbiter* project video recording requirements and the increased need for recorders during *Mariner V* Venus encounter.

The FR-900 video recorders previously located at DSS 12, 41, and 62 have been removed and two of them installed at DSS 11 and 42. The FR-900s will be used to back up the FR-800s supporting the *Surveyor* Project. The third unit will be sent to Langley Research Center for processing of *Lunar Orbiter* video tapes.

The mission support recording assembly, FR-1400s previously implemented at DSS 12 to support the *Pioneer* Project, has been temporarily removed and installed at DSS 14 to support the bistatic radar astronomy experiment.

In the interim period of October 4, 1967 to November 7, 1967, the *Pioneer* Project will share DSS 12's station recording equipment with *Lunar Orbiter* and *Mariner V*.

b. Communications interface assembly. The Communications Interface Assemblies (CIA) have been previously implemented at DSS 11, 12, 14, 61, and 62. The CIA provides the necessary signal conditioning required to interface the mission-independent low-frequency and DC signals to the intrasite microwave during remote tracking support of a project.

With the addition of the high- and low-data-rate demodulators, as mission independent equipment, the CIA will be expanded to handle two additional signals.

Procurement has been started for the purchase of plug-in modules to expand the CIA at DSS 12 and 14 to meet the requirements defined above.

In addition to the expanded capability, a monitor and test panel is under procurement. This panel is designed to provide access to the various signal-conditioning modules during test and calibration of the CIA.

c. System simulation assembly. All time code translators and spares have been delivered and will be implemented at the end of November 1967.

D. DSIF System Integration, *E. Thom*

1. Introduction

The early DSIF evolved as a network of four stations which were equipped with L-band equipment. Two of these were located at Goldstone and one each at Woomera, Australia, and Johannesburg, South Africa.

In 1963 it became a requirement to abandon the L-band frequencies and design new equipment to operate at S-band. Masers and digital computers were added to the DSIF to meet the growing need for increased communication range and data rates. The forthcoming *Surveyor* and *Lunar Orbiter* programs required additional stations to handle the heavy tracking and testing load that would be necessary.

As the DSIF grew from the initial four to ten operational stations and the equipment became more complex, it became necessary to organize the integration of the new equipment into stations and the new stations into the planned tracking network. This integration effort falls into several areas which will be discussed individually.

2. System Block Diagrams

The initial S-band system block diagram was released in September 1963, approximately six months prior to the implementation of the first station. Subsequently, the stations have evolved into five separate types: 85-ft GSDS, 85-ft Mutual (MSFN/DSN), 30-ft Guidance and Command, 4-ft Spacecraft Monitor, and 210-ft GSDS.

In order to retain a history of the development of the stations, a block diagram for each type station will be provided which will be updated yearly. This method will provide three or more block diagrams for each type station as follows:

(1) Historical. The block diagrams will show in discrete steps the development of the configuration of a system at the end of a calendar year.

(2) Working. The block diagram will show the latest revision for the current calendar year as equipment is added at the stations.

(3) Detailed Planned Implementation. These block diagrams will show planned configuration at the start of the designated calendar year. The block diagram will be similar to a working block diagram; however, planned implementations which are both scheduled and funded will be shown.

Typically, each type station would have a 1966 historical diagram, a 1967 working diagram, and a 1968 planning diagram. At the end of a year, the working diagram is retired to historical; the planning diagram becomes the working diagram; and a new planning diagram is generated based on the upgrades and changes scheduled and funded for the next year.

3. Equipment Layouts

A study was performed in late 1963 in an attempt to find an optimum layout for the S-band control rooms. Since the stations are becoming saturated as new equipment is being added, a new study is currently being performed to analyze the requirements for the next five years. Layout drawings are also prepared for the antenna, electronics cage, and hydromechanical building at each station.

4. Reference Designations

A system of reference designations has been implemented to provide a method of identifying each item of equipment at the stations. Although similar to military and other techniques of identifying equipment, the DSIF system has incorporated some unique details to satisfy its special requirements. Reference designators are required to identify every item of equipment from a major subsystem down to a given component. They are used for trouble and failure reporting, reliability studies, etc. The method of assigning the identifiers is readily adaptable to computer techniques of data analysis.

5. System Cabling and Interface Compatibility

Each DSIF station is composed of an assortment of semi-autonomous subsystems. This has been caused by each subsystem being developed at a different point in time and by a different development engineer. It has been found necessary to define and record the input and output signal interfaces for each subsystem and the details of interconnection at each station. The S-band signal interface list defines the connector type, pin assignment, function, level, impedance, frequency, and bandwidth of every signal provided by and required for each subsystem. These are arranged by system cable number in the document such that the output signals from the supplying subsystem can be readily compared with the input requirements of the recipient subsystem.

References to each output connector are maintained in computer data storage form and are readily available when the interfaces for a new or revised subsystem are being established. A system cable interconnect diagram is generated and maintained for each station.

6. Standard Design Control Documents

In an effort to equip the DSIF with equipment of uniform appearance, quality, and performance, several Standard Design Control Documents are being prepared. Each of these deals with a specific area, such as environmental requirements, grounding and shielding requirements, radio frequency interference suppression, general construction requirements, quality control requirements, etc. As each station is provided with equipment designed to meet these standards, it will become a more efficient operating entity.

E. DSN (MSFN *Apollo* Wings) Backup System Acceptance Tests, *F. M. Schiffman and W. J. Kinder*

1. Introduction

This article presents a summary of the results of the system acceptance testing and analysis performed from November 1, 1966 to April 1, 1967 on the Pioneer,

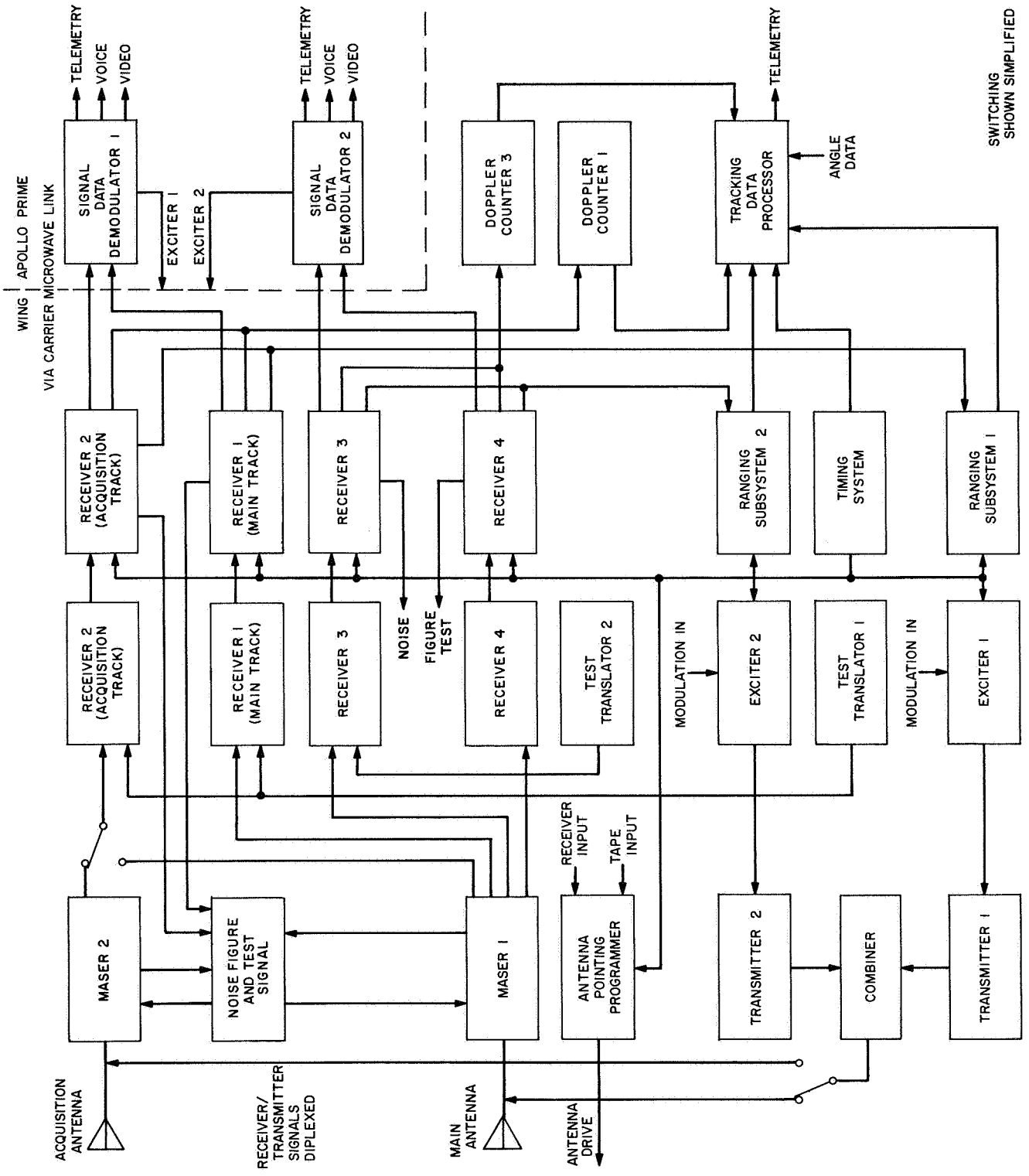

Fig. 3. Test configuration for 85-ft antenna system

Robledo, and Canberra DSSs' 85-ft antenna tracking and communication DSN/MSFN *Apollo* wing system[1].

The test objective was to verify the compatibility of the various subsystems and the overall operational capability of the system and to compile data necessary for analysis of system errors. The system tests are categorized into three general phases, namely:

(1) Static functional tests, consisting of configuration verification, system temperature, dual transmitter/combiner, up-link and down-link data.

(2) Static tracking (stationary target), in determination of angle tracking error gain slope and accumulation of star track data.

(3) Dynamic tracking utilizing aircraft tracking. A simplified diagram of the overall test configuration is shown in Fig. 3. Table 1 summarizes applicable tests.

Table 1. System tests

Test	Static	Static track	Dynamic track
Configuration verification	✓		
System temperature	✓		
Dual transmitter/combiner	✓		
Up-link data	✓		
Down-link data	✓		
Error analog		✓	
Star tracks		✓	
Aircraft tracks			✓

2. Configuration Verification

This test (Fig. 3) was to confirm the system configuration of all DSS (MSFN wings) and to verify equipment operational ability by observing subsystem monitoring displays. Adjunct to station readiness confirmation, a visual inspection of the site grounding network was accomplished. A number 0000 jacketed cable was installed, tying the antenna structure, hydromechanical/power buildings and both DSSs (MSFN wings) to the sites' common ground counterpoise. All equipment was also grounded directly to this cable.

3. System Noise Temperature

A quantitative test (Fig. 4) measuring the system noise temperature of each receiver reference channel was conducted, using the standard Y-factor technique. This measurement technique follows the TWM with a receiver which has a precision attenuator in its IF section plus an output detector and a strip chart recorder. Two well-matched sources at temperatures T_N (nitrogen RF load) and T_0 (ambient RF load) are alternately connected to the TWM input. The measured quantity, or Y-factor, is the additional attenuation which must be introduced with the precision attenuator when the hotter source is connected, in order to obtain the same chart reading as when the colder source had been connected. This initial measurement determines the equivalent receiver noise temperature contribution T_R. The system noise temperature T_S is then computed by switching between the ambient RF load and the antenna.

Figure 4 illustrates the system noise temperature test configuration used. The resulting system temperatures for the respective sites are tabulated in Table 2.

4. Dual Transmitter/Combiner Test

Demonstration of the dual transmitter capability and an assessment of system degradation due to the transmitters when radiating into the feed were the primary objectives of this test. The 5K70SG 20-kW klystron power amplifiers used in the 20-kW transmitters were saturated across a 14-MHz, −1 dB bandpass, with a maximum of 700-MW drive power to the klystron. Specified bandwidths were readily obtained with the MSFN exciter buffer-amplifiers. Figure 5 illustrates the dual transmitter/combiner output test configuration and the test results are tabulated in Table 2.

5. Up-Link Data Test

A system demonstration of the interface compatibility and conformance to requirements of the up-data buffer, subcarrier oscillators, exciters, power amplifiers and verification receivers was obtained. As indicated in Table 2, frequency response, percent distortion and test pattern verification were within specifications.

6. Down-Link Data Test

An A and B type substitution test determined the interface compatibility between the signal data demodulator set (SDDS) test unit, exciter, test translator, TWM 1, and 2, receivers and demodulators for both PM and FM mode signals. The referenced test unit simulated spacecraft down-link signals which were modulated on PM and FM carriers, sent through the system and percent distortion measured. The PM test signals originated at the MSFN prime site and used the intersite microwave

[1]Schiffman, F., "DSIF/MSFN *Apollo* Backup System," JPL Functional Specification DOW-1198-FNC A.

Table 2. System test data—MSFN/DSS 11, 42, and 61

Static system parameters	Performance			Specification
	MSFN/DSS 11	MSFN/DSS 42	MSFN/DSS 61	
Mission system interface	D	D	D	Assume MSFN mission within minutes
System temperature, °K				P_s 120 dBmW, quiet sky, antenna at zenith, 140°K (+10, −20)
SCM TWM 1 Receiver				
2a1	205	105	142	
2a2	183	114	152	
2b1	83	67	117	
2b2	128	80	104	
SCM TWM 2 Receiver				
2a1	150	130	118	
2a2	166	—	132	
2b1	90	—	118	
2b2	116	—	94	
Dual transmitter/combiner transmitter 1 — 20-kW water load bandwidth, MHz				10-MHz 1-dB points, from 2100 to 2110 MHz
1 dB	17.5	16.7	14.0	
3 dB	—	19.7	15.9	
Transmitter 2 — 20-kW water load bandwidth, MHz				
1 dB	19.0	16.5	12.7	
3 dB	—	20.0	15.6	
Dual transmitter third-order products				Products 30 dB below either carrier
Upper frequency	36 dB below carrier	44 dB below carrier	36 dB below carrier	
Lower frequency	35 dB below carrier	52 dB below carrier	50 dB below carrier	
Up-link data test command channel frequency response				100 to 3000 Hz (+1 dB, −3 dB)
System 1	D	D	D	
System 2	D	D	D	
Command channel distortion, %				Less than 5%
System 1	D	D	D	
System 2	D	D	D	
70-kHz Up-data pattern verified				
System 1	D	D	D	
System 2	D	D	D	
Down-link data test				Less than 5%
PM telemetry 5.2-kHz tone distortion	D	D	D	
PM voice, telemetry carrier demodulation drop locks	D	D	D	
FM system distortion	D	D	D	
FM voice, telemetry carrier demodulator drop locks	D	D	D	
Tracking receiver cross-over slope				
SAA HA	—	80 mV/deg	—	70 mV/deg
Dec	—	74 mV/deg	—	70 mV/deg
SCM HA	154 mV/0.1 deg	258 mV/deg	198 mV/0.1 deg	200 mV/0.1 deg
Dec	190 mV/0.1 deg	214 mV/deg	210 mV/0.1 deg	200 mV/0.1 deg

D = demonstrated.
SAA = S-band acquisition aid.
SCM = S-band cassegrain main.

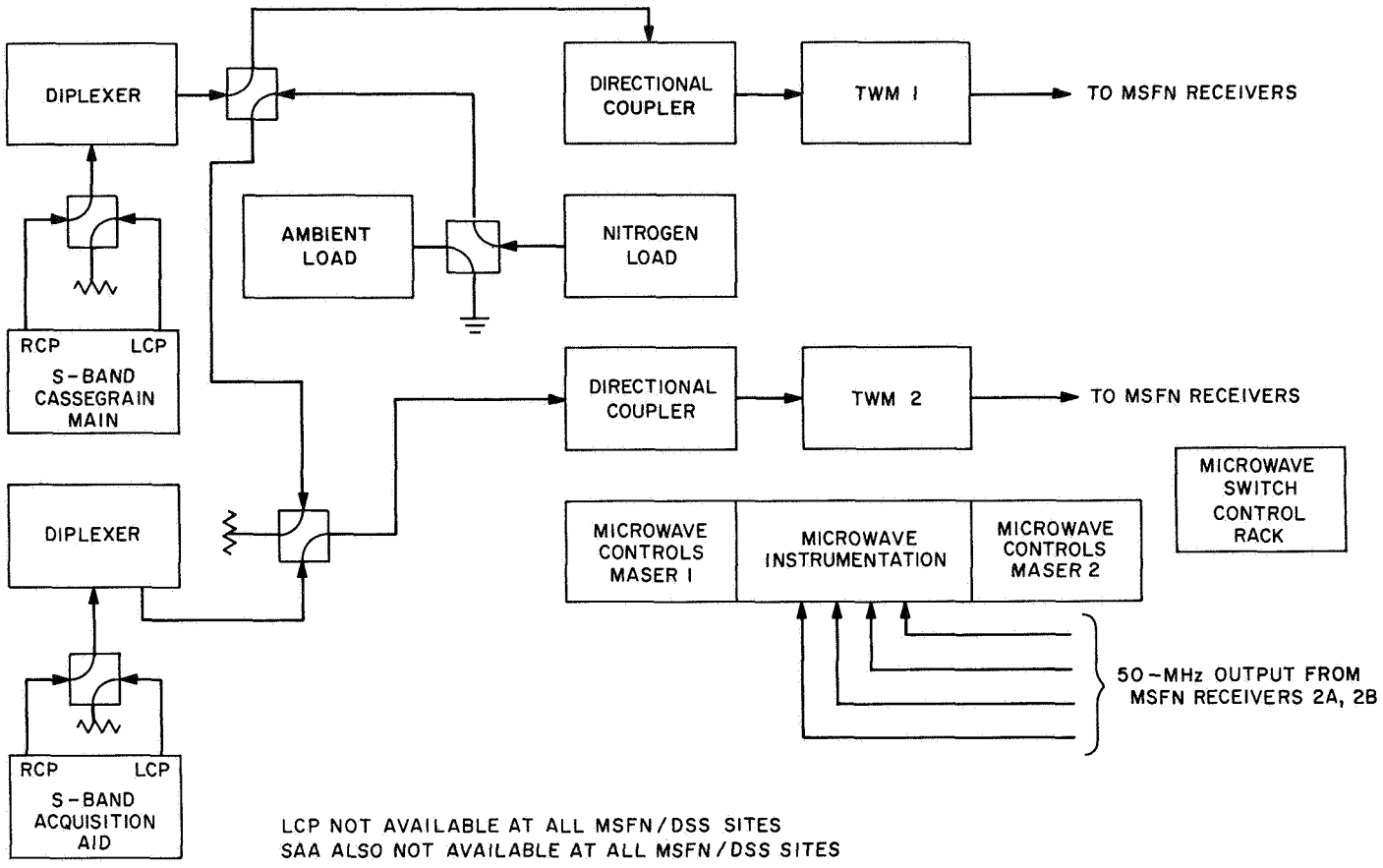

Fig. 4. System noise temperature configuration

link. DSS 61's (MSFN wing) FM test was incomplete during system tests because of equipment malfunction and station flight commitments. Closed loop FM system tests will be completed during subsequent GSFC scheduled aircraft tracks. Distortion measurements, in both the up-link and down-link data tests, were accomplished with the use of the HP 302-A wave analyzer obtaining fundamentals and harmonics of the test tone. In all distortion readings using this method, specifications were met (Table 2).

7. Static Tracking Error Analog

This test measures the tracking error voltage out of the tracking receiver as a function of target angular error, to determine crossover slopes. Table 2 tabulates the test results.

8. Position Accuracy-Star Tracks

The purpose of this test (Fig. 6) is to determine the accuracy to which the antenna can be positioned. The programmed star tracks indicate how accurately the antenna position programmer (APP) can position the antenna along a given path. This test indicates errors in optical axis and the true encoder axis. Also included are the mechanical errors. A prepared punched tape containing the ephemerides of 12 selected stars was furnished by Goddard Space Flight Center for input data to the antenna position programmer.

Essentially, there is one error equation for each antenna axis describing errors between the optical and encoder or mechanical axes. The first computer program processed antenna pointing angles and time and film coordinates of each star. Film data showed how far the optical axis was mispointed from the star at the time of recording. These data were used to correct the antenna pointing directions as measured by the encoders. Ephemeris data from the Nautical Almanac was used to predict the time coordinates of each star, after adjustment for optical refraction using site weather data. Errors between this true axis and the positioned optical axis were obtained by subtraction. These data were examined for functional

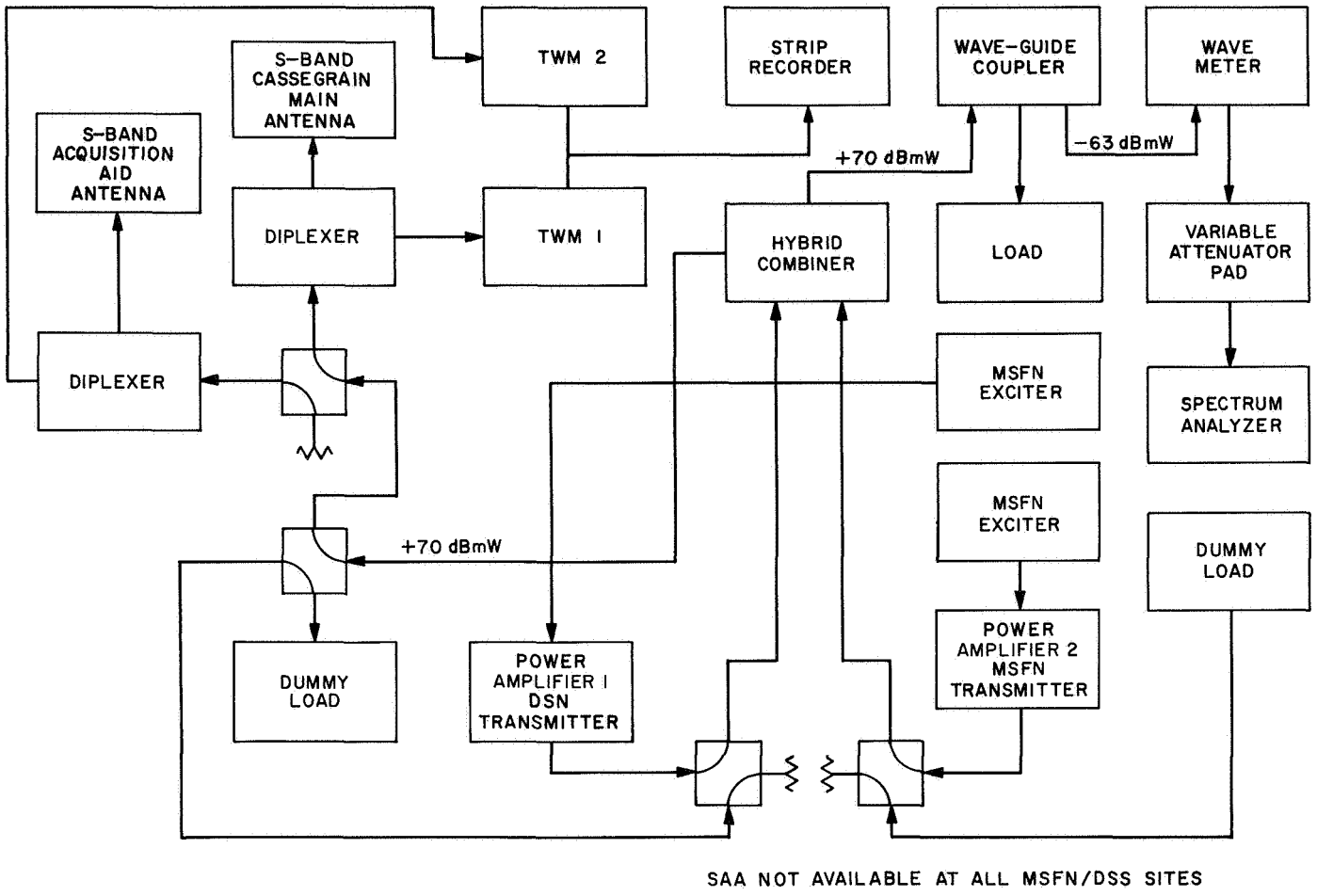

Fig. 5. Dual transmitter/combiner output configuration

relationships resulting in the following two optical-to-encoder star shot error equations:

$$\text{star shot error}_{HA} = S_1 + S_2 - S_3 \sin t \quad (1)$$

$$\text{star shot error}_{dec} = S_4 + S_5 \cdot \delta + S_6 \cdot t \quad (2)$$

where

S_1 = HA optical-to-encoder bias error

S_2 = HA optical-to-encoder linearly t (dec)

S_3 = HA optical-to-encoder error sinusoidal t (dec)

S_4 = dec optical-to-encoder bias error

S_5 = dec optical-to-encoder error linearly t (dec)

S_6 = dec optical-to-encoder error linearly dependent on HA, deg/deg

δ = dec encoder angle, deg

t = HA encoder angle, deg

To preclude the error model from becoming discontinuous at 0 deg dec and 0 deg HA, plus and minus dec and HA must be submitted into the error models (e.g., $t = 330$ deg would be substituted as $t = -30$ deg; $t = 315$ deg would be substituted as $t = -45$ deg).

A second star shot regression computer program solved for the data in Table 3, using a least squares estimate evaluation of the error model coefficients, the coefficients standard errors and the standard deviation of the residual (random) errors.

A simplified reduction of data resulted in a histogram of the frequency distribution of total errors shown in Figs. 7 and 8 for DSS 11 (MSFN wing), Figs. 9 and 10 for DSS 42, and Figs. 11 and 12 for DSS 61 (MSFN wing). Good statistical grouping of the errors is evident at the newer Madrid DSS antenna. Simple linear regression graphs with tick marks indicating standard deviation are

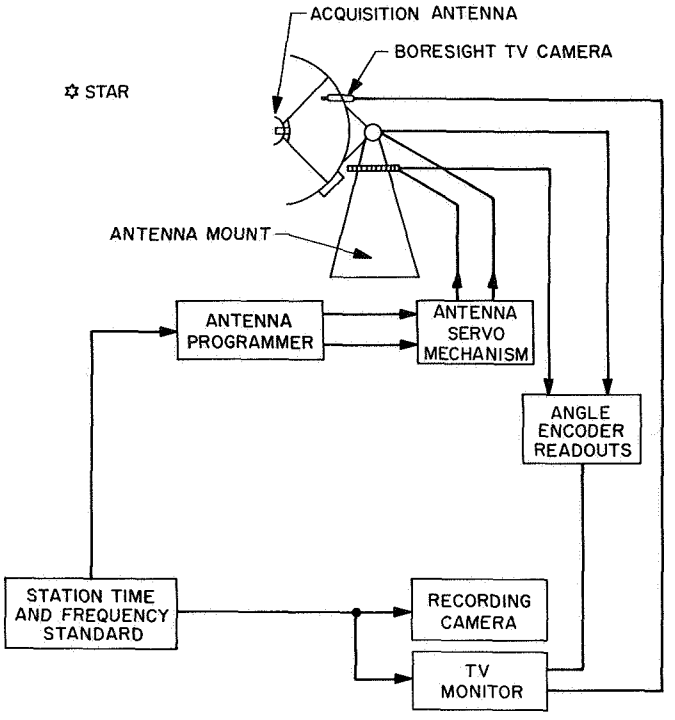

Fig. 6. Programmed star track block diagram

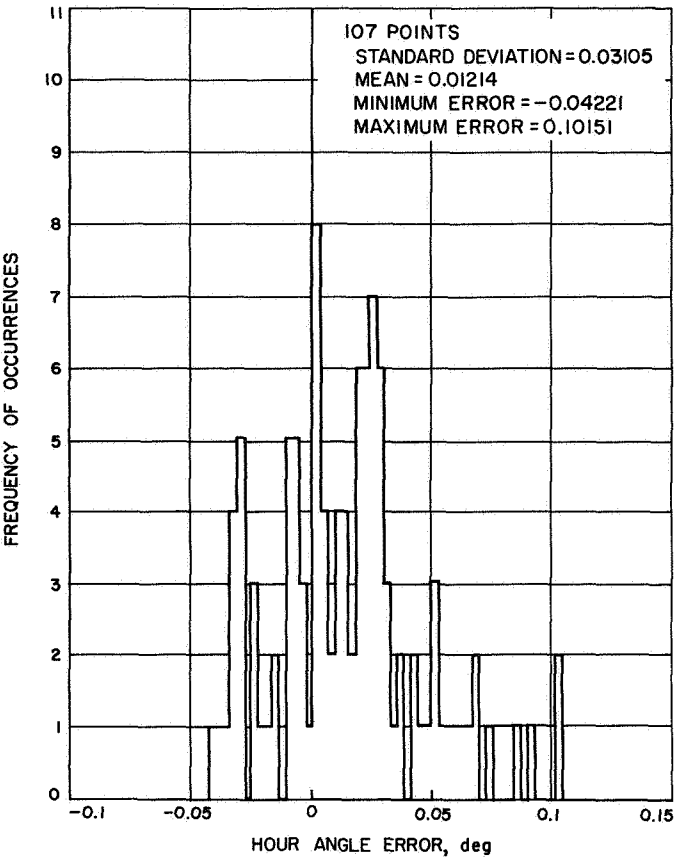

Fig. 7. Pioneer DSS optical star track data frequency diagram for HA error

Table 3. Star shot data

	Measurement	DSS 11	DSS 42	DSS 61
S_1	HA optical-to-encoder bias error, deg	−0.010 ±0.007	0.002 ±0.003	−0.012 ±0.002
S_2[a]	HA optical-to-encoder error linearly dependent on dec, deg/deg	±0.0011 ±0.0003	−0.0001 ±0.0001	0.00003 ±0.0002
S_3	HA optical-to-encoder error sinusoidal dependent on HA, deg	+0.040 ±0.010	0.016 ±0.005	0.022 ±0.005
S_4	Dec optical-to-encoder bias error, deg	+0.010 ±0.006	−0.002 ±0.003	0.106 ±0.002
S_5[a]	Dec optical-to-encoder error linearly dependent on dec, deg/deg	0.00036 ±0.00024	0.0009 ±0.0001	0.0007 ±0.0002
S_6[a]	Dec optical-to-encoder error linearly dependent on HA, deg/deg	— —	0.0002 ±0.0001	−0.0004 ±0.00008
HA	HA residual standard deviation	0.013	0.007	0.006
Dec	Dec residual standard deviation	0.051	0.019	0.019
δ	Dec encoder angle, deg	—	—	—
t	HA encoder angle, deg	—	—	—

[a]In order to prevent an error model which is discontinuous at 0-deg dec, plus and minus dec must be submitted into the error models (e.g., 330 deg would be substituted as −30 deg).

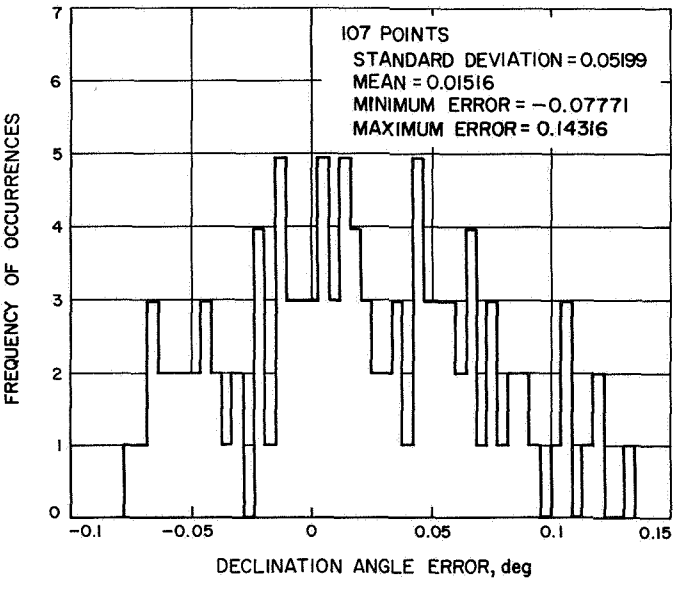

Fig. 8. Pioneer DSS optical star track data frequency diagram for dec angle error

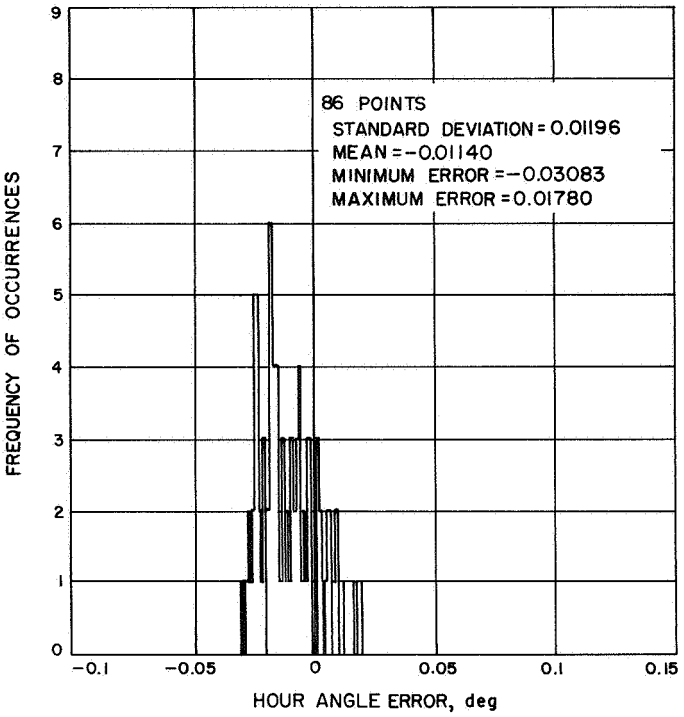

Fig. 9. Canberra DSS optical star shot data frequency diagram for HA error

shown in Figs. 13, 14, 15, 16, 17, and 18 for both axes at the subject sites. Again tighter error tolerances are shown on the Madrid DSS antenna. Allowable errors specified are position repeatability of no more than ±0.01 deg with position resolution of ±0.005 deg. Figure 6 illustrates the test configuration for the star track test.

9. Dynamic Aircraft Tracks

The ability of the tracking system to acquire and automatically track a moving target was established with this system exercise. In particular, after initial acquisition, two-way lock and ranging were demonstrated. Of paramount importance with these aircraft tests was the accumulation of film data for the determination of system tracking errors between the optical and RF axes.

Figure 19 illustrates the test configuration. A computer program processed antenna pointing angles and time and film coordinates of the aircraft light (night tracking). Parallax errors caused by the TV antenna camera offset from the center of the dish and by the displacement of the light from the antenna on the aircraft were corrected. The parallax corrected errors became total RF-to-optical tracking errors which include error contributions from paraboloid and quadripod sag and hyperboloid and feed

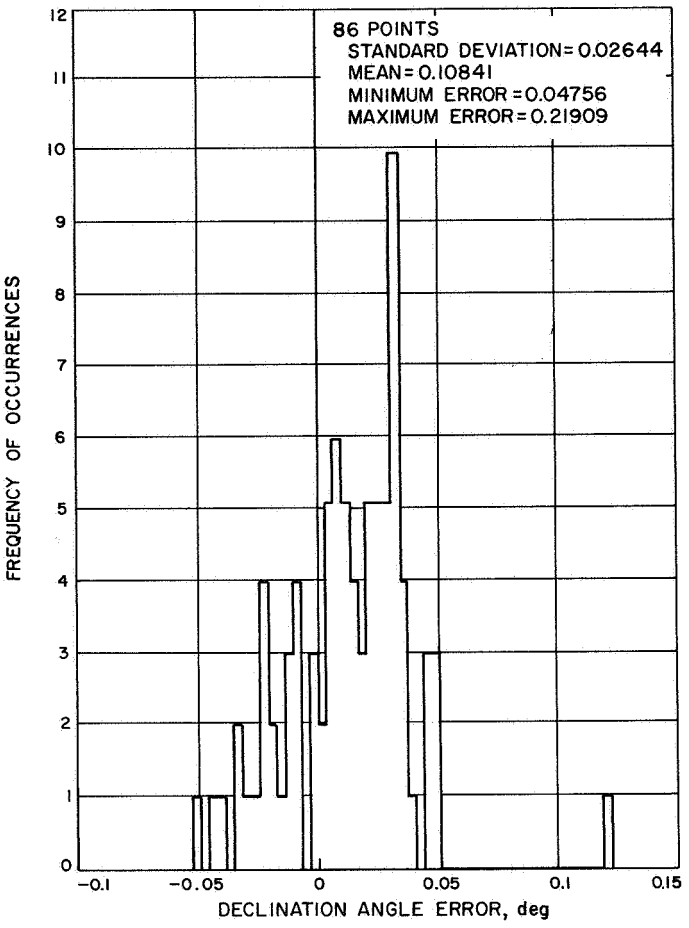

Fig. 10. Canberra DSS optical star shot data frequency diagram for dec angle error

rotation. The following two RF-to-optical aircraft track error equations were solved by another computer program obtaining least square estimates of the error model coefficients:

$$\frac{\text{aircraft track error}_{HA}}{\cos\delta} = \frac{A_1}{\cos\delta} + A_2\ddot{t} \qquad (3)$$

$$\text{aircraft track error}_{dec} = A_3 + A_4 \cdot \ddot{\delta} \qquad (4)$$

where

A_1 = RF-to-dec axis lack of orthogonality

A_2 = HA acceleration lag coefficient

A_3 = dec RF-to-optical bias error

A_4 = dec acceleration lag coefficient

$\ddot{\delta}$ = dec encoder angle, deg

$\ddot{t}$ = HA encoder angle, deg

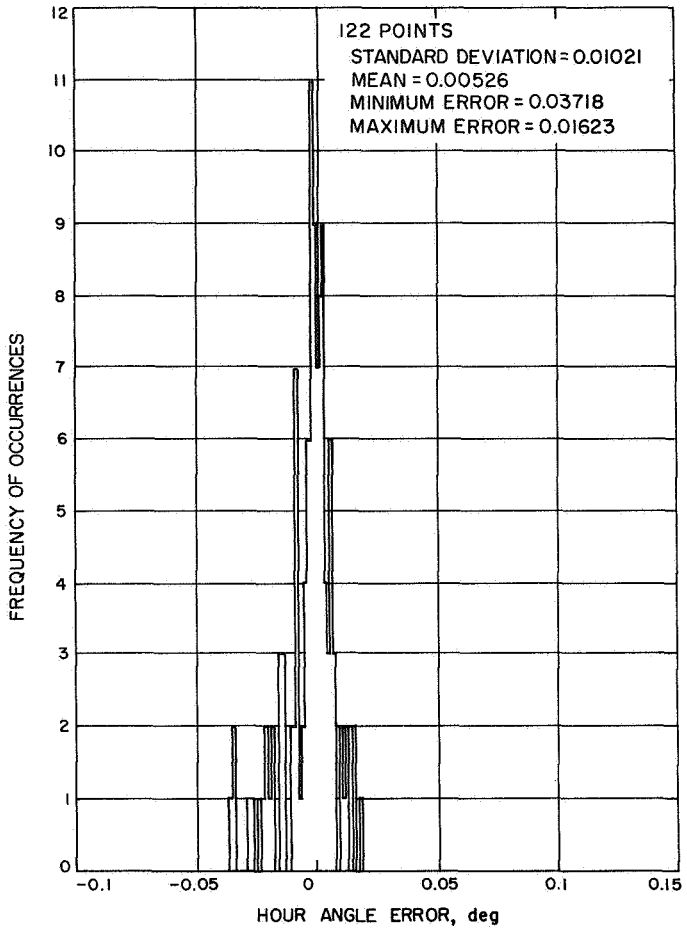

Fig. 11. Madrid DSS optical star track data frequency diagram for HA error

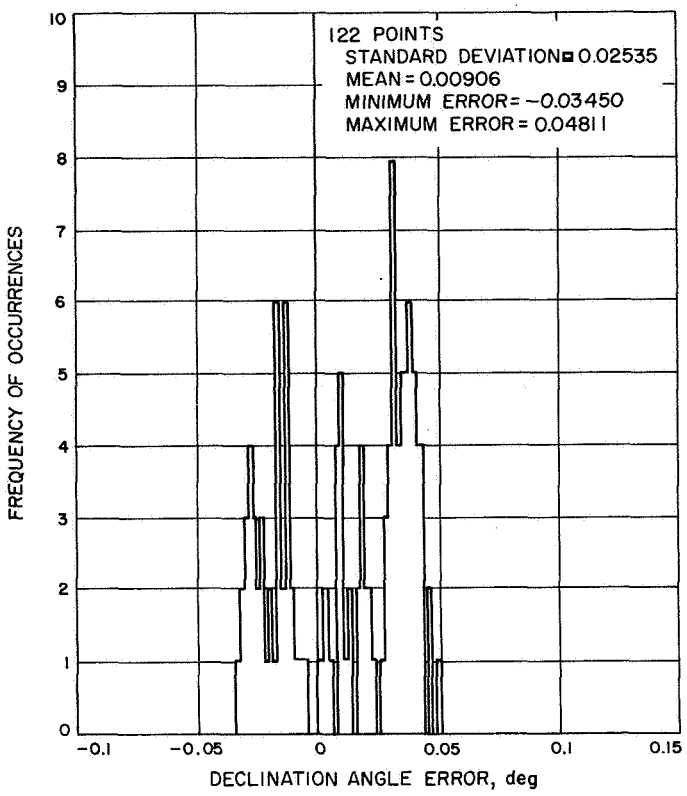

Fig. 12. Madrid DSS optical star track data frequency diagram for dec angle error

These equations are based on a type II servo system where the principal errors are bias errors and lag errors proportional to antenna acceleration. Antenna encoder accelerations which were computed as more than 0.01 deg/s/s were discarded.

Since the DSS 61 (MSFN wing) had no acquisition aid antenna, successful aircraft tracks were accomplished by using a modified optical acquisition aid (OAA) with a 3-deg field of view to acquire the aircraft. With the aid of the MSFN servo ball-tracker, the aircraft was then "walked" into the OTA 0.5-deg field of view where RF carrier lock was possible.

10. Data Analysis and Reduction

Two steps are necessary to develop expressions for the random and systematic errors in the measurement of RF axis position as determined by the digital shaft encoders. Figure 20 illustrates the procedure.

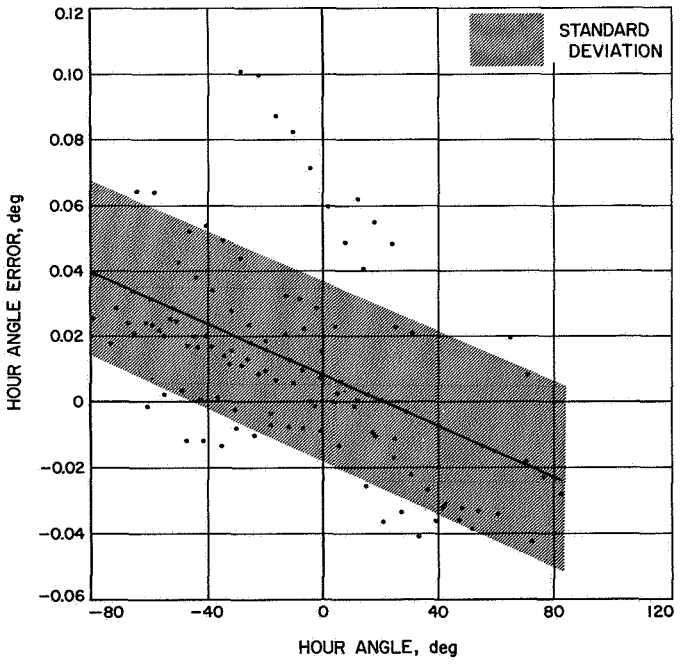

Fig. 13. Pioneer DSS optical star track data HA error versus HA

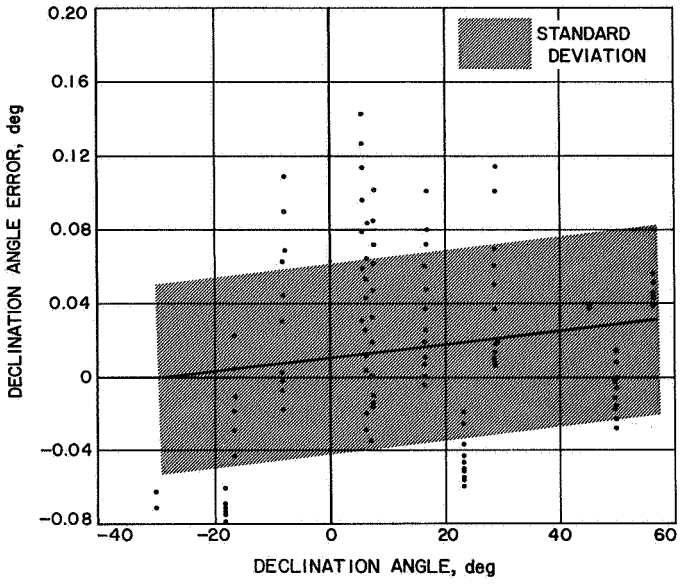

Fig. 14. Pioneer DSS optical star track data dec angle error versus dec angle

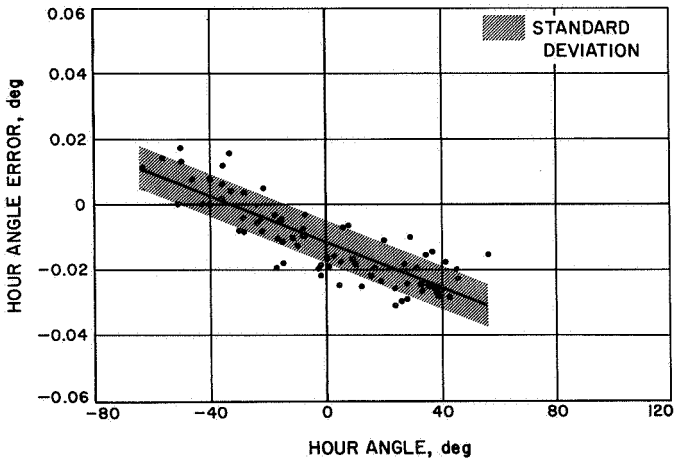

Fig. 15. Canberra DSS optical shot data HA error versus HA

The total instantaneous system tracking error per axis is represented by the angle α; it is determined by measurement of the error angles δ and β which are subsequently summed linearly to yield the total error. The β error contribution is measured by a series of optical star shots randomly covering the celestial hemisphere, while the α error contribution is determined from aircraft autotrack/optical tests. The raw data was processed statistically through a linear regression analysis to yield the best fit coefficients (in the least squares sense) of the system error model and the residual errors (random) after

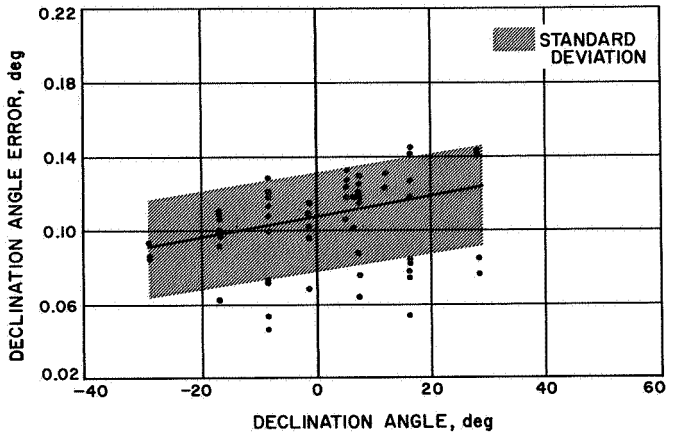

Fig. 16. Canberra DSS optical star shot data dec angle error versus dec angle

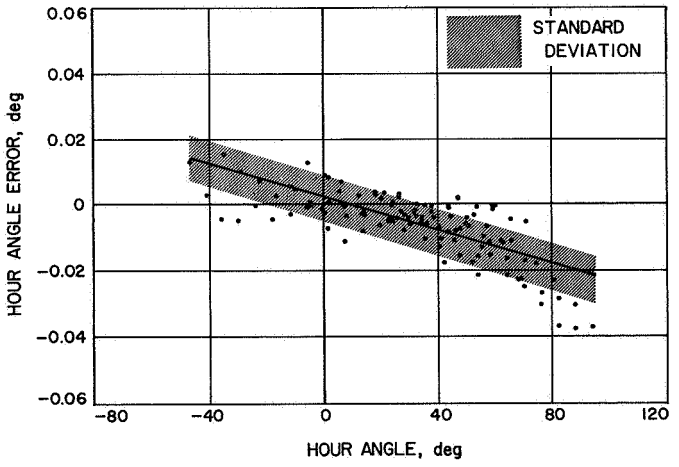

Fig. 17. Madrid DSS optical star track data HA error versus HA

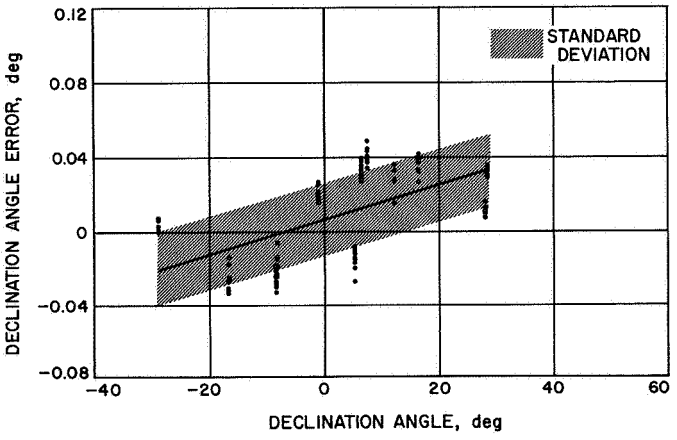

Fig. 18. Madrid DSS optical start track data dec angle error versus dec angle

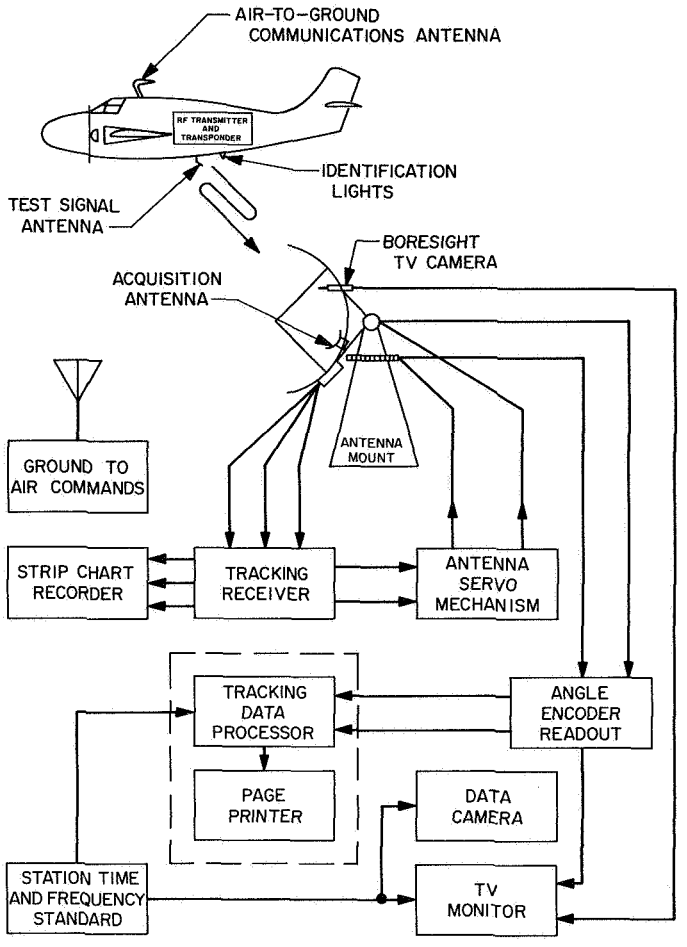

Fig. 19. Dynamic tracking test configuration

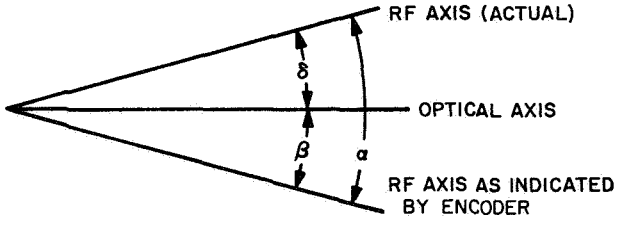

Fig. 20. Random and systematic error computation

best fitting the data in accordance with the equations of the error model.

When the system error equations were evaluated at any chosen value of HA and dec angles, velocities, and accelerations, the resulting pointing error estimates are the best least squares estimates of the systematic errors for the chosen conditions.

a. Star shot total errors. To produce star shot errors, the first computer program processed antenna pointing angles, time, and film coordinates of each star, HA, dec, T, F_{HA}, and F_{dec}, respectively. The 35-mm camera film data coordinates of the star showed how far the optical axis was mispointed from the star at the recorded time, these coordinates were used to correct the antenna pointing directions HA and dec as measured by the encoders. These adjusted coordinates state where the antenna recorded that the star was located. Ephemeris data from the Nautical Almanac was used to predict the true coordinates of each particular star. Predicted HA and dec coordinates were adjusted for optical refraction, using recording temperature and pressure. Errors in HA and dec angles between the optical axis (as positioned by the measured encoder axis) and the true axis (refraction adjusted) were obtained by subtracting true values from the measured values. Two optical-to-encoder star error equations were established by a second computer program which evaluated trends from two plots. The two plots consisted of antenna encoder angles and total error (dividing the opposite encoder angle into 20-deg intervals), as produced by the first computer program. Equations (1) and (2) were established from trends in these two plots.

The HA and dec errors and encoder angles for each star from the first program were entered into a second program (star shot regression) which obtained the least squares estimates of the error model coefficients in Eqs. (1) and (2). This program solved for the unknown coefficients S_1 to S_6, their standard errors, and the standard deviation of the residual (random) errors. The residual randomness with respect to encoder angles and dependent variable variance reduction indicates a successful solution for the predominant trends in the star shot error data.

b. Aircraft track total errors. To obtain aircraft track total errors, the first computer program processed antenna pointing angles, time, and film coordinates of the aircraft light, HA, dec, T, F_{HA}, and F_{dec}, respectively. F_{HA} and F_{dec} are corrected for two parallax effects in a third computer program. Parallax is caused by the TV camera offset from the center of the dish and by the displacement of the light from the antenna on the aircraft. The parallax corrected errors thus become total RF-to-optical tracking errors.

Aircraft data points were rejected (not processed in the regression program) which have antenna encoder accelerations computed as more than about 0.01 deg/s/s (which is approximately the maximum antenna acceleration during testing) difference from a 7-point moving

average value. This permitted automatic rejection of data reduction errors due to noisy accelerations which occur when one antenna axis is stationary, and key punch errors. Based on past antenna tracking error experience, there are two predominant factors which contribute to RF-to-optical aircraft track errors. These are bias errors and lag errors proportional to antenna acceleration for a type II servo system. Therefore, the following two RF-to-optical aircraft track error equations were solved from the aircraft track data (using a fourth computer program):

$$\frac{\text{aircraft track error}_{HA}}{\cos\delta} = \frac{A_1}{\cos\delta} + A_2\ddot{t} \tag{5}$$

$$\text{aircraft track error}_{dec} = A_3 + A_4 \cdot \ddot{\delta} \tag{6}$$

In order to prevent an error model which is discontinuous at 0 deg dec and 0 deg HA, *plus* and *minus* dec and HA must be submitted into the error models (e.g., $t = 330$ deg would be substituted as $t = -30$ deg; $t = 315$ deg would be substituted as $t = -45$ deg).

All the information listed in the third computer program was entered into another program (aircraft track regression) which obtained the least squares estimates of the error model coefficients in Eqs. (5) and (6). This program solved for the unknown coefficients, A_1 through A_4, their standard errors, and the standard deviation of the residual (random) errors, for each aircraft track run.

Table 4. RF-to-true-encoder error equation results (combined aircraft and star shot error equations)

Symbol	Parameter	DSS 42	DSS 61
A_1	RF-to-dec axis lack of orthogonality, deg	0.070 ±0.001	−0.006 ±0.0002
S_1	HA encoder bias, deg	−0.012 ±0.002	0.002 ±0.003
A_2	HA acceleration lag coefficient, deg/deg/s²	−0.228 ±0.001	−2.331 ±0.014
S_2[a]	HA optical-to-encoder error linearly dependent on dec, deg/deg	0.00003 ±0.0002	−0.0001 ±0.0001
S_4	Dec optical-to-encoder bias error, deg	0.106 ±0.002	−0.002 ±0.003
C_1	Dec RF-to-encoder bias, deg	−0.201 ±0.005	−0.002 ±0.019
A_4	Dec acceleration lag coefficient, deg/deg/s²	−1.287 ±0.030	−0.277 ±0.009
S_5[a]	Dec optical-to-encoder error linearly dependent on dec, deg/deg	0.0007 ±0.0002	0.0009 ±0.0001
S_6[a]	Dec optical-to-encoder error linearly dependent on HA, deg/deg	−0.0004 ±0.00008	0.0002 ±0.0001
α_t (C)	HA RF-to-encoder residual standard deviation	0.008	0.015
α_δ (C)	Dec RF-to-encoder residual standard deviation	0.021	0.023

[a] In order to prevent an error model which is discontinuous at 0 deg dec, plus and minus dec must be submitted into the error models (e.g., 330 deg would be substituted as −30 deg).

c. Combined star shot and aircraft error equations. The coefficient and variance results of the aircraft track regression equation solutions were processed through a weighted average and probable error program that weighted each coefficient inversely as its variance (index of precision). The coefficient averages and probable errors were computed according to Eqs. (7) and (8), and the results are listed in Table 4. All the variances were assigned equal weights in order to average them.

Letting b_{ij} signify the jth coefficient from the ith aircraft run, the weighted average of the jth coefficient B_j is:

$$B_j = \frac{\sum_{i=1}^{n} \frac{b_{ij}}{\sigma_{ij^2}}}{\sum_{i=1}^{n} \frac{1}{\sigma_{ij^2}}} \tag{7}$$

$$i = 1, 2, \cdots, n$$

$$j = 1, 2, \cdots, 4$$

n = number of aircraft track data groups

σ_{ij} = variance of the ith value of the jth coefficient

The probable error in the jth weighted coefficient average is

$$\text{pe} = 0.6745\left(\left[\frac{\sum (b_{ij} - B_j)^2}{\sigma_{ij^2}}\right] \Big/ \left[n(n-1)\frac{1}{\sigma_{ij^2}}\right]\right)^{1/2} \tag{8}$$

Table 4 lists the symbols, definitions, and values for the combined aircraft coefficients and standard deviations of Eqs. (7) and (8). Probable errors are listed for each coefficient.

Only DSS-42 and DSS-61 are shown in Table 4. Data from DSS-11 was not available at the time this article was prepared.

d. RF-to-encoder error equations. The system model RF-to-encoder error equations are stated in Eqs. (9) and (10) and the coefficient definitions and values are presented in Table 4. The error equation terms are also developed and combined later in the pertinent star shot, aircraft track, and combination sections, which is described later.

e. HA and dec RF-to-encoder error quotations. In order to obtain error equations in HA and dec, between RF and true encoder axes, Eqs. (1) and (3) and Eqs. (2) and (4) must be combined. The combined RF-to-true-encoder error equations in HA and dec, respectively, are:

$$\text{RF-to-true-encoder}_{\text{HA}} = (A_1/\cos\delta) - S_1 + A_2 \cdot \ddot{t} - S_2\,\delta + S_4 \sin t \tag{9}$$

$$\text{RF-to-true-encoder}_{\text{dec}} = C_1 + A_4\,\ddot{\delta} - S_5\,\delta - S_6\,t \tag{10}$$

where

$$C_1 = A_3 - S_4$$

The combined RF-to-true-encoder residual standard deviations in HA and dec, $\alpha_t\,(C)$ and $\alpha_\delta\,(C)$, are given by Eqs. (11) and (12):

$$\alpha_t\,(C) = \alpha_t^2\,(A/C) = \alpha_t^2\,(S/S) \tag{11}$$

$$\alpha_\delta\,(C) = \alpha_\delta^2\,(A/C) = \alpha_\delta^2\,(S/S) \tag{12}$$

where

$\alpha^2\,(A/C)$ is the aircraft track combined residual variance

$\alpha^2\,(S/S)$ is the star shot residual variance

The symbols, definitions, and values (including probable errors) for the coefficients and the standard deviations of Eqs. (9), (10), (11), and (12) are listed in Table 4.

The standard deviations, $\alpha_t\,(C)$ and $\dot{\alpha}_\delta\,(C)$, are upper limits on the RF-to-true-encoder random system errors. They are upper limits, due to removing only the predominant functional forms contained in the total errors. Any unremoved functional forms remain in the residuals, which may be viewed as an unremoved systematic error causing some small inflation of the random error.

11. Conclusion

The DSN/MSFN wing systems capability at Goldstone, California, Canberra, Australia, and Robledo, Spain has been successfully demonstrated. As a result, these stations are now prepared to support the *Apollo* Project during the cislunar trajectory consistent with specifications described in this article.

F. DSN Ground Communications Facility, *E. Yinger*

1. Purpose

The primary purpose of DSIF communications, working in conjunction with certain elements of the Ground Communications Facility (GCF), is to:

(1) Relay tracking data, in real-time, from each deep space station in the DSN to the SFOF Pasadena. At the same time, each DSS will record the data on teletype tape and page print as a real-time check of equipment in the data chain. Tapes and page print are also stored for a period of time for record purposes.

(2) Provide voice communications between each DSS and the SFOF to allow them to coordinate their activities during tracking and test simulation periods.

The secondary purpose of DSIF communications is to provide voice communications within each DSS.

2. GCF Circuits Linking the DSN

DSN/GCF is, in part, a specific configuration of a portion of a larger communications network, namely NASCOM. Circuits are provided by NASCOM to the DSN as if the DSN were a subscriber and NASCOM was a communications common carrier. Similarly, NASCOM leases their circuits from a world-wide system of common carriers such as:

(1) American Telephone and Telegraph Company (AT&T) in the United States.

(2) RCA Communications (RCAC) to Ascension Island.

(3) Australian Postmaster General (PMG) in Australia.

(4) Compania Telefonica Nacional Espana (CTNE) in Spain.

The maximum complement of circuits provided by NASCOM for a typical overseas DSS is two voice/data circuits (one voice, one data) plus four teletype circuits.

A functional assignment of circuits in this complement is typically as follows:

(1) Three teletype circuits inbound (DSS to SFOF) are used to transmit spacecraft telemetry and tracking data.

(2) The outbound (SFOF to DSS) sides of the above three teletype circuits are used to transmit commands and mission coordination information.

(3) One two-way teletype circuit (DSS/SFOF) is used for DSN systems maintenance, station control, and coordination (mission independent) and for project control and operations.

(4) An additional teletype orderwire is used between each DSS and the nearest NASCOM communications center for operational coordination between communications personnel—not necessarily extended to GSFC or the SFOF.

(5) The data circuit is used as an inbound (DSS to SFOF) high-speed data circuit transmitting spacecraft telemetry data.

(6) One project/DSN shared voice circuit (DSS/SFOF) is used for coordination and control of the spaceflight project-unique equipment and for operational and administrative DSIF station control, which may be shared with projects or missions, or with other DSS stations in the area.

See Figs. 21 and 22.

3. Description of Equipment

The ground communications equipment found within the DSIF is comprised of the following functional equipment groups: station communications control group (SCCG), high-speed data (HSD), teletype (TTY), tactical intercom (TIC), and microwave (intersite within a complex). The SCCG and HSD are elements of the GCF.

a. SCCG. The teletype portion of the SCCG consists of two racks of equipment. The equipment is used to terminate and condition GCF circuits of varying electrical parameters (depending on geographic location) for further distribution to teletypewriter equipment within the DSS. Distribution is accomplished using either a manually operated switch-button matrix or patch cords. Conversely, the SCCG also accepts the teletype output from the telemetry and command processor (TCP) comm buffer, tracking

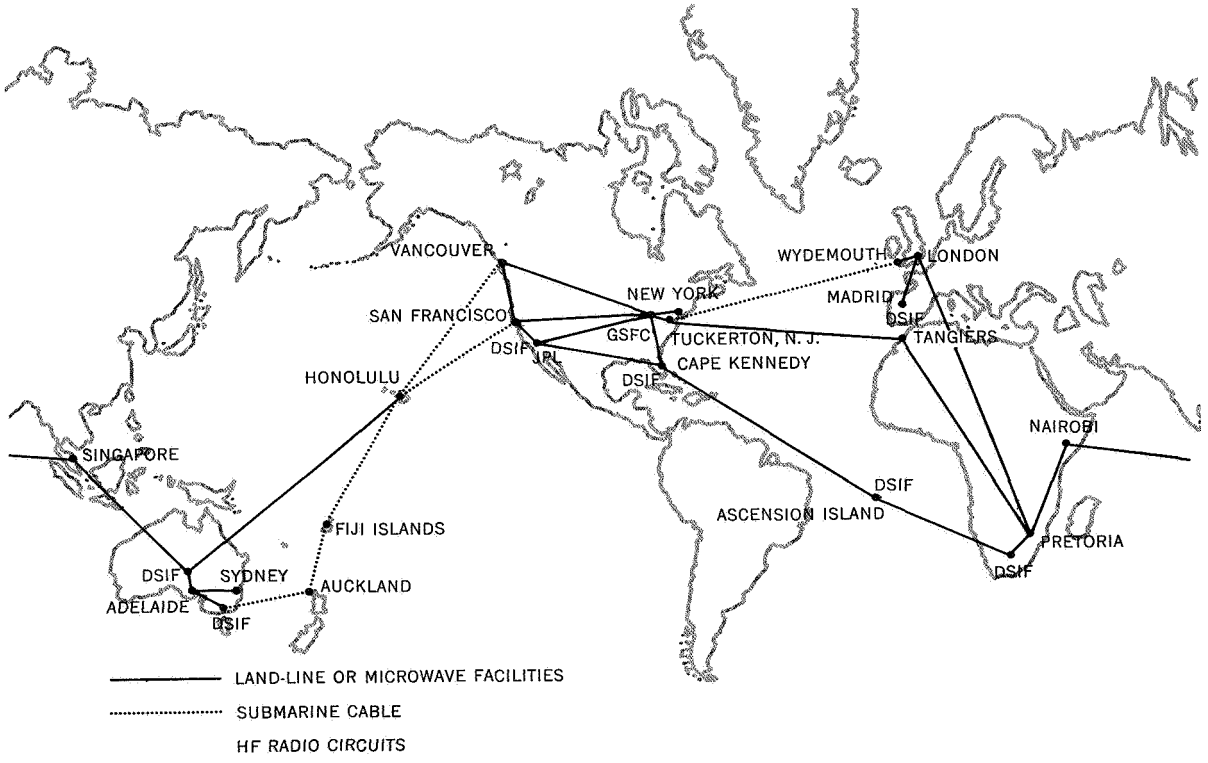

Fig. 21. DSN communications system

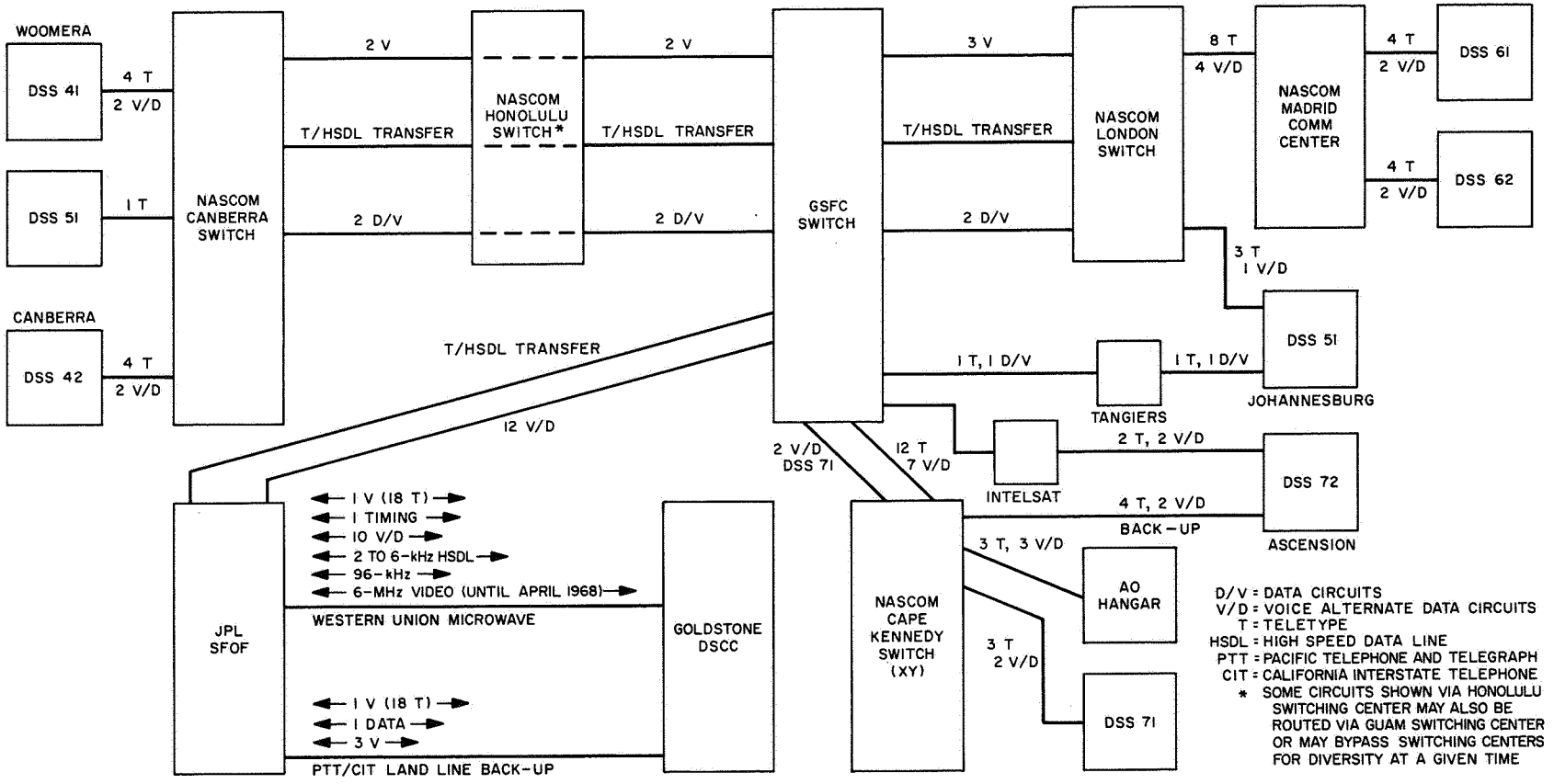

Fig. 22. NASCOM DSN/GCF circuits

data handling (TDH), teletype keyboard (KB) or transmitter distributor (TD). The SCCG then converts these outputs to the proper telemetry circuit parameters for transmission to SFOF via GCF circuits.

The voice portion of the SCCG consists of one rack of equipment used to condition as many as six voice circuits entering and leaving a DSS via the GCF circuits. A patchable system of bridges and amplifiers provides multiple outputs at required levels to the tactical intercom, mission monitor comm panels and the voice frequency side of the high-speed data sets.

The only SCCG equipment installed to date is the teletype bays at DSC 10 communications center. This equipment conditions and passes all teletype traffic between SFOF and the Goldstone DSCC. The SCCG equipment should be operational throughout the DSN by the third quarter of 1968.

b. High-speed data. The high-speed data equipment is presently contained in one rack and consists of:

(1) Data Set. A general-use phase-modulated transmitting and receiving data terminal designed for full duplex four-wire service. The data set transmitter receives dc polar pulses from the computer (via the comm buffer) and phase modulates them on an 1800-Hz carrier frequency at audio level. It is designed to operate at 600, 1200, and 2400 bits/s. Each rack contains two data sets for redundancy.

(2) Data Quality Monitor. Used for on-line testing of signal (dc) from comm buffer into data set.

(3) Dual Trace Scope. Used for on-line testing of the audio signal output of the data set.

(4) VTVM. General testing.

(5) Data Transmission Test Set. Provides a test signal to the data set.

(6) Patch and test jackfield.

The new high-speed data equipment will require two racks. The equipment in the present rack will be reinstalled in the new rack and the following new equipment will be added:

(1) Block Multiplexer (BMXR). Will accept four on-site computer outputs, assign them a priority, and provide time sharing of the data set and line.

(2) BMXR Switch and Test Panel. Permits on-line selection of redundant BMXR. It also provides limited dc test capability.

(3) Encoder. Generates and applies a 33-bit error-detection code to each block of HSD.

(4) Decoder. Detects HSD transmission errors.

c. Teletype. There are four types of teletype machines used by DSIF communications.

(1) Automatic Send and Receive (ASR). This machine has the following capabilities:

(a) Keyboard. Types messages.

(b) Page Printer. Provides typed page print.

(c) Reperforator. Punches a tape.

(d) Transmitter Distributor. Transmits message from punched tape.

(2) Receive-Only Page Printer (RO). Provides typed page print of message.

(3) Transmitter Distributor (TD). Transmits message from punched tape.

(4) Receive-Only Typing Reperforator (ROTR). Provides a punched tape with typed message on the tape.

d. Tactical intercom. The tactical intercom provides voice intercommunication facilities within the DSS. It is made up of the following equipment:

(1) Program and Test Bay. This bay houses dual amplifiers, distribution and access bridges, power supply, and a patch and test jackfield—all to support up to fifty intercom panels.

(2) Dual-Position, Five-Channel, Rack-Mounted Intercom Panels. These are used in any standard DSIF rack requiring an intercom panel.

(3) Single-Position, Five-Channel, Weatherproof Intercom Panel. These are used anywhere in the DSS where intercom is required and no DSIF racks are available. These would usually be found in the generator building, collimation tower, hydromechanical building, and on the antenna structure itself.

(4) Dual-Position, 12-Channel, Rack-Mounted Intercom Panel. Each DSS has one of these installed in the SMC.

(5) Mission Monitor Comm Panel. Each DSS will have two. Each panel is capable of terminating up to 10 four-wire nets, 2 speaker modules, and a paging access unit. This unit gives the operator the capability of monitoring or transmitting on up to ten circuits simultaneously.

e. Microwave. Two complexes within the DSN use microwave to relay telemetry data interstation. One is DSC 60 in Spain and is discussed in Section VI-H. The other is at DSC 10 in Goldstone, California.

DSC 10 to DSS 11. This link consists of six full duplex 100-mW channels. There are two racks of equipment at each terminal. This is a one-hop system using passive repeaters.

The frequency response is:

Channels 1 to 4	1 kHz to 4.5 MHz ±0.5 dB 4.5 to 6.5 MHz ±3.0 dB
Channels 5 to 6	1 kHz to 4.5 MHz ±0.5 dB 4.5 to 7 MHz ±3.0 dB

DSC 10 to DSS 13. This link is essentially the same as the link DSC 10 to DSS 11 with the following exceptions:

(1) The equipment at each terminal occupies four racks.

(2) Frequency response on all six channels is the same as that shown above for channels 1 to 4 of the DSC 10 to DSS 11 link.

DSC 10 to DSS 14. This link consists of 5 full duplex 1-W wideband channels and 12 voice frequency multiplex channels. The equipment at each terminal occupies four equipment racks.

The frequency response (wideband channels 1 to 5) is:

50 Hz to 5 kHz	+0.5, −1.5 dB
5 to 500 kHz	±0.2 dB
500 kHz to 2 MHz	±0.4 dB
2 to 4.5 MHz	±0.5 dB
4.5 to 8.5 MHz	±3.0 dB

G. Tidbinbilla Foundation Study for DSS 42,

A. A. Riewe

1. Introduction

A foundation study was conducted at DSS 42, Tidbinbilla, Australia to determine if adequate foundation support was available within the existing station property and to develop the necessary foundation configuration for a 210-ft-diam antenna instrument tower provided satisfactory support existed. A contract for the study was awarded to the Donald R. Warren Company of Los Angeles on May 9, 1967. Field work took place during the period May 22, 1967 to June 7, 1967. Laboratory testing, engineering analysis, and report preparation were completed October 20, 1967.

2. Scope of Study

Briefly, the investigation included: observation of the drilling of borings made at the locations shown on Fig. 23; sampling operations; laboratory testing of selected samples, and engineering analysis in order to formulate recommendations. The areas of study include the following:

(a) Minimum dimensions and depths of embedment of the pedestal and instrument tower foundation components.

(b) Expected dead load settlements of the foundation components.

(c) Rotational stability of both components of the foundation structure under given lateral (wind) load conditions.

(d) Excavation, backfilling and dewatering recommendations.

Rotational stability and dead load settlements were determined for two foundation configurations. One configuration was developed to give the minimum foundation system sizes compatible with the maximum allowable rotations and settlements assuming a static lateral load condition. The second configuration analyzed was that of the existing Goldstone 210-ft-diam antenna instrument tower foundation.

3. Regional Surface Characteristics, Geology and Seismicity

The site is located within the lower portion of a broad northwest draining valley on the east side of the distinctly cut Larry's Creek Channel. Portions of the creek bed were observed to contain standing water during the field investigating period, therefore, any permanent flow condition would have to be subsurface.

The site has an average surface elevation on the order of 2088 ft and is approximately 600 ft due south of the existing 85-ft antenna installation. Ground cover consists

Fig. 23. Tidbinbilla site plan

of domestic grasses maintained as part of the existing facilities landscaping.

A plan showing the general topographic expression of the area and the existing facilities is presented in Fig. 23.

The site is located within the tributary alluvial flats of Paddy's River and is underlain by bedrock of the Murrumbidgee Batholith (Ref. 1) which was defined as being a member of the Shannon Flat Granodiorites.

The batholith structure lies between two major fault systems which are the Murrumbidgee and Cotter faults. Most component bedrock members of the batholith structure are foliated to some extent and all of them are strongly jointed. A highly jointed rock structure was observed in the bedrock samples obtained from the test borings.

A previous study reported in JPL Technical Memorandum 33-115 indicates that the probability of strong-motion earthquake in southeastern Australia is approximately two orders of magnitude less than in the Goldstone DSCC area.

4. Subsurface Profile

In general, the site is underlain by foundation materials normally considered excellent. However, the extremely small allowable foundation deflections make it necessary to examine each site in detail. A general discussion of the foundation conditions revealed by the field explorations is presented in the following paragraphs.

Two seismic profiles (traverses A–C and B) were made at the site at the locations shown in Fig. 23. The profiles were interpreted by geophysicists of the Australian Bureau of Mineral Resources as showing a structure of five layers which are, namely, from the surface downward: soil ($V = 1000$ ft/s), alluvium ($V = 1700$ ft/s), dense alluvium or decomposed granite ($V = 3800$ to 4500 ft/s), highly weathered and jointed bedrock ($V = 6150$ to 7500 ft/s), and sound bedrock ($V = 11{,}400$ to 16,000 ft/s).

Five borings were made at the locations shown in Fig. 23 to depths ranging from 18 to 100 ft. Borings 1 and 1A were made using a lightweight, trailer-mounted, Model B Pendrill drilling rig. Due to insufficient water circulation and inadequate casing equipment, only a small portion of the information obtained from these borings is reliable. Borings 1B, 2 and 3 were accomplished satisfactorily using a heavy-duty truck mounted Mayhew 1000 drilling rig.

The general soil and rock profile consists of a thin surface layer of topsoil underlain by alluvium consisting of mixtures of clayey sand and gravel which was underlain at depths of between 15 and 18 ft by weathered granite bedrock which extended to the depths penetrated. The alluvium was firm to stiff, but porous in the upper 5 ft, becoming stiff to hard and dense with depth. The bedrock was observed to be very weathered in the upper 10± ft, becoming generally less weathered with depth merging into relatively fresh granite bedrock at depths on the order of 70 ft. Fresh rock was taken from boring 1A in the form of a continuous core between the depths of 92 to 100 ft.

Borings 1B, 2 and 3 were purged of drilling mud to depths in excess of 25 ft and left standing 48 h. The water levels in all borings rose to depths on the order of 12 ft below the surface. As known water wells in the area are at a depth of 100 ft or more, it is the opinion of the foundation consultant that the observed water levels represent a perched water condition. That is to say, there appears to be a 3- to 4-ft thick zone of soil on top of the relatively impermeable bedrock which is carrying subsurface low-velocity flow from the upper slopes of the valley.

5. Modulus of Elasticity Determination

The critical factor in the foundation system evaluation is the action of the foundation under repeated loading and unloading. This factor is analyzed by determining the governing modulus of elasticity in compression of the materials representing the foundation substructure. The modulus of elasticity determinations were made using conventional consolidation-pressure apparatus. Samples were tested in both *in situ* and saturated moisture content conditions. As the specimens were loaded with increasing pressure, they consolidated. This was due primarily to closure of joint and fracture surfaces and, to a minor degree, from expulsion of moisture. When the specimens were unloaded, an apparent increase in volume, or rebound, occurred. Upon repeated loading and unloading cycles, the stress-strain curves closely followed the rebound curves, producing a form of hysteresis loop. The slope of the loading portion of the loop determines the usable elasticity modulus or hysteresis modulus. Initial compression is not considered significant in determination of the long-term rotational stability of the foundation components.

An example consolidation-pressure curve is presented in Fig. 24. An example of the computation for the modulus of elasticity or hysteresis modulus is presented as follows:

Boring 1-B (Fig. 24) at 20-ft depth shows:

$$\delta_{corr} = \frac{\Delta P L_0}{AE} \qquad \text{or,} \qquad E = \frac{\Delta P L_0}{A \delta_{corr}}$$

where

E = modulus of elasticity (hysteresis), tons/ft²

$\frac{P}{A}$ = change in applied pressure, 4.55 tons/ft²

L_0 = original length of specimen, 0.9924 in.

corr = deformation of specimen corrected for machine deformation, 0.00095 in.

$$E = \frac{4.55 \times 0.9924}{0.00095} = 4750 \text{ tons/ft}^2 \text{ (or } 66{,}000 \text{ lb/ft}^2\text{)}$$

A total of ten samples were tested to determine the modulus of elasticity in compression.

6. Causes of Foundation Movement

a. Instrument tower silo footing settlement due to dead loads. The silo footing will initially settle due to pressure increases in the underlying weathered rock mass induced by its weight. Some additional settlement will occur due to pressure increases induced by the pedestal loads. In foundation materials typical of those found the dead

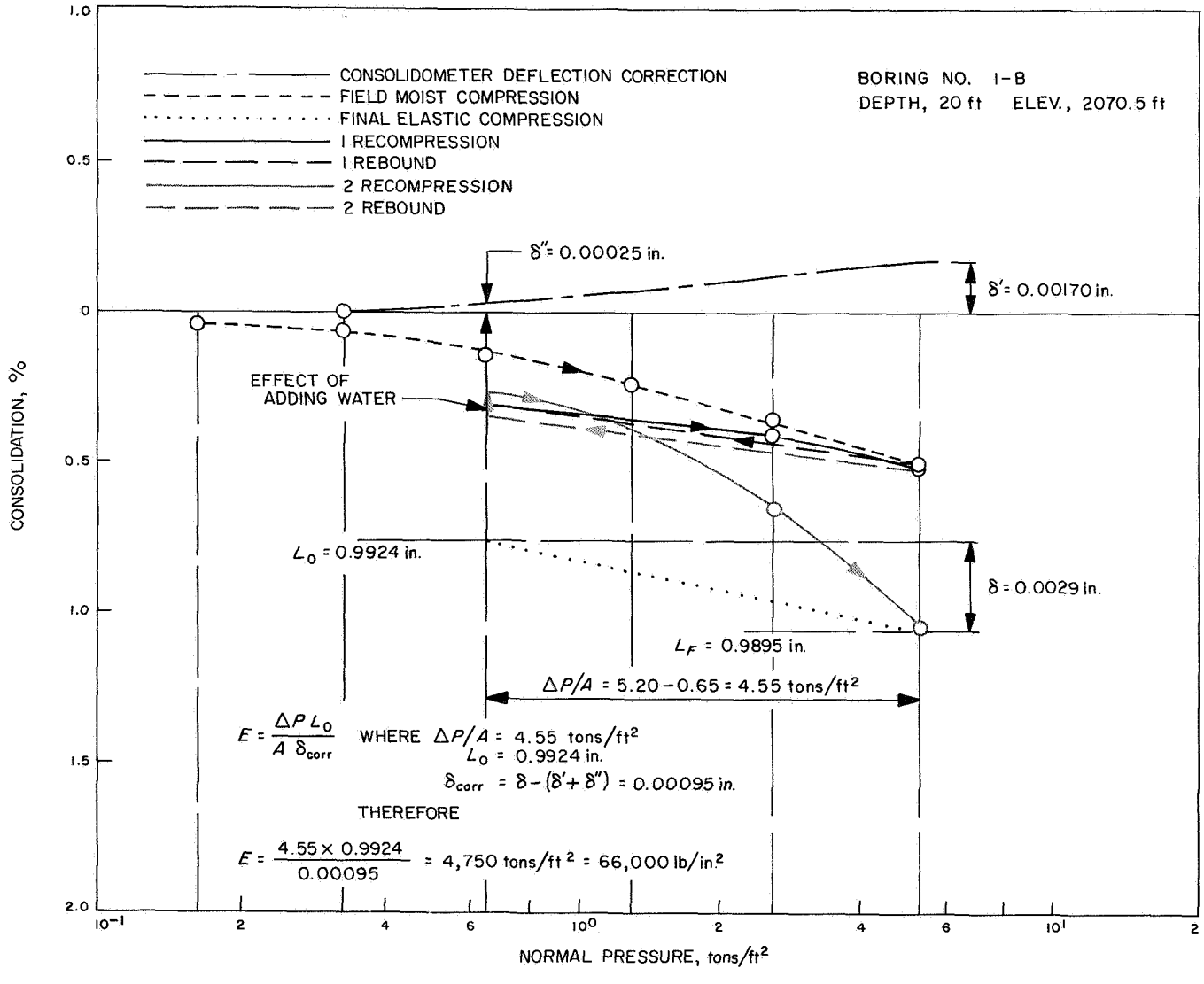

Fig. 24. Consolidation-pressure curve

load settlement should occur over a very short period of time after the dead load is applied and will, therefore, not present a problem in connection with operation of the antenna.

b. Pedestal footing settlement due to dead loads. The pedestal ring footing will experience similar over-all settlement due to dead loads imposed by the pedestal footings. This settlement is also expected to occur during the period of construction and initial live loading.

c. Instrument tower silo footing movement due to wind load on antenna. When a lateral load is applied to the antenna superstructure, pressures beneath one half of the pedestal footing will increase, while pressures beneath the remaining half will decrease correspondingly. For instance, if the wind direction is from left to right, as indicated in Figs. 25 and 26, the antenna structure will tend to overturn in a clockwise direction. Overturning is resisted by pressure increases beneath the right half of the pedestal footing accompanied by pressure decreases beneath the left half. The neutral axis passes through the centroid of the pedestal footing area and is perpendicular to the direction of the wind. Referring to Figs. 25 and 26 again, the neutral axis would pass through line C and would be perpendicular to the plane of the paper. The increased load on the right side of the footing would also influence pressures at other points below the plane of the bottom of the footing, such as points along lines R1, C, L1, and L2. The decreased load on the left side would likewise decrease vertical pressures in the foundation material below the plane of loading. The wind loading described would result in a net increase in pressure along vertical lines lying to the left of line C, such as lines L1 and L2. The resulting compression of foundation material on the right side, accompanied by rebound of material on

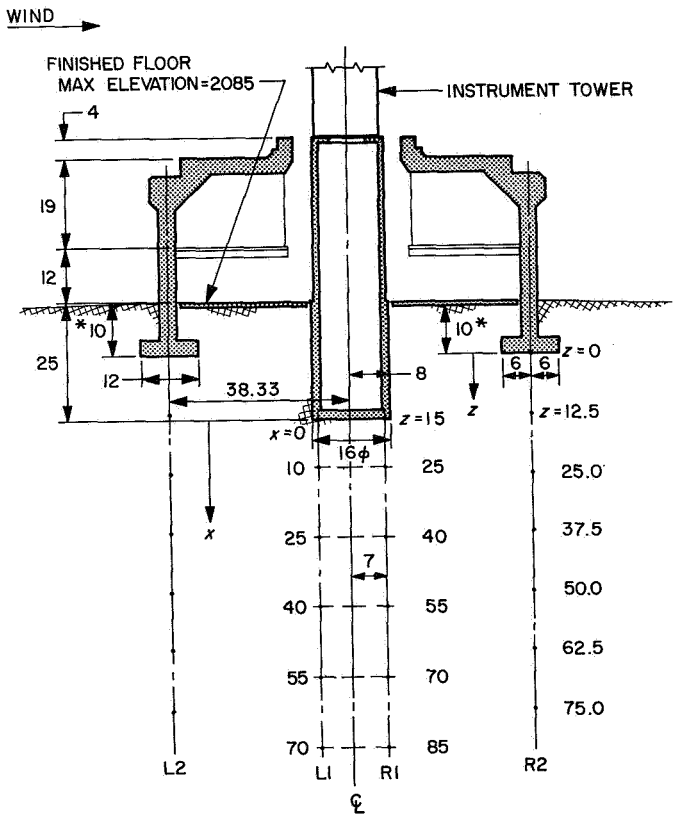

* 10-ft EMBEDMENT DEPTH IS A MINIMUM
DEPTH TO ACHIEVE 2-ft EMBEDMENT IN WEATHERED BEDROCK WILL RANGE FROM 10 TO 15 ft DEPENDING ON SITE GRADING

ALL DIMENSIONS IN FEET
SCALE: 1 in. = 20 ft

Fig. 25. Cross section of footing, alternate arrangement

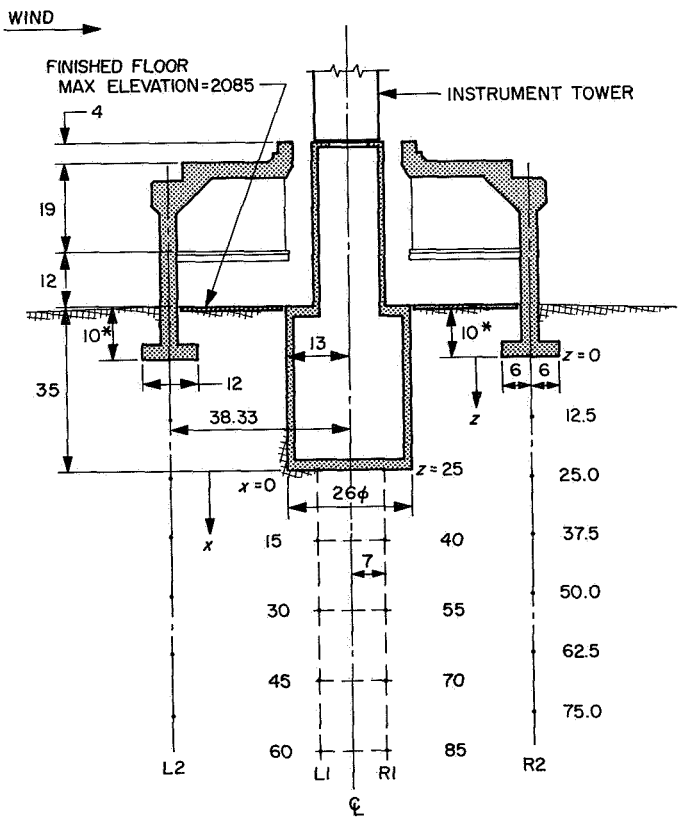

* 10-ft EMBEDMENT DEPTH IS A MINIMUM
DEPTH TO ACHIEVE 2-ft EMBEDMENT IN WEATHERED BEDROCK WILL RANGE FROM 10 TO 15 ft DEPENDING ON SITE GRADING

ALL DIMENSIONS IN FEET
SCALE: 1 in. = 20 ft

Fig. 26. Cross section of footing, Mars DSS arrangement

the left side, would tend to rotate the tower footing slightly in a clockwise direction, but would not tend to cause any net permanent vertical displacement, providing the foundation material exhibits essentially elastic behavior.

d. Pedestal footing movement due to wind load on antenna. Due to the phenomena described in (c) above, the pedestal footing would also tend to rotate about a horizontal axis but should experience no permanent vertical displacement for the same reasons as described above.

e. Tower and pedestal footing movements due to microseismic activity. Lateral loading of the foundation structures imposed by microseismic activity will have effects on foundation pressures similar to those described in (c) above. The magnitudes of pressure changes imposed by microseismic forces are estimated to be many times smaller than those imposed by a 45-mph wind acting on the antenna. However, the time variation of these forces may be such that resonating oscillatory motion of the foundation could occur.

Little is known regarding microseismic activity and its effect on structures. Amplitude values lying between 10^{-3} and 10^{-4} cm are normal, with periods ranging from 4 to 6 s/cycle. Rotation of the instrument tower due to these accelerations would be negligible unless resonance developed. The amplitude of microseisms may be amplified to ten times the original value in extensive alluvial deposits of a relatively compressible nature. The foundation materials at the subject site, however, more nearly exhibit the qualities of rock rather than of soil, and very little amplification is expected.

f. Analysis of foundation movements. Foundation movements are assumed to result primarily from vertical pressure changes on loaded surfaces. Vertical pressure changes were calculated using the Westergaard formulas for determining vertical stresses caused by surface loads in elastic materials. A discussion of the development and use of the formulas can be found in Ref. 2.

Table 5 presents a summary of the results of the stability analysis.

Table 5. Results of stability analysis

Stability condition	Allowable values	Values for Mars configuration foundation	Values for modified configuration foundation
Dead load settlement instrument tower silo footing	0.25 in.	0.10 in.	0.18 in.
Dead load settlement antenna pedestal ring footing	0.50 in.	0.12 in.	0.12 in.
Wind load rotation horizontal axis instrument tower silo footing	2.0 s of arc	0.7 s of arc	1.0 s of arc
Wind load rotation horizontal axis antenna pedestal ring footing	5.0 s of arc	5.0 s of arc	5.0 s of arc

7. Excavation

The surface alluvial soil can be readily excavated using relatively light-duty earth-moving equipment. Based on the results of triaxial shear tests it is recommended that permanent slopes excavated into either the surface alluvial soils or very weathered (decomposed) granite be cut at a slope of 1½ horizontal to 1 vertical.

Excavation for the pedestal footing will range from 10 to 15 ft below the finished site grade and can most likely be accomplished with a heavy-duty telescoping shovel type backhoe or lighter duty track-mounted equipment.

Based on stability considerations, it is recommended that the silo footing excavation be made, without the use of an access ramp. Use of an access ramp would result in an undesirable discontinuity in the lateral foundation structure.

The bedrock below a depth of 30 ft may be difficult to excavate by conventional means and line drilling; prying and wedging may be required. In no case should explosives be used to aid in the excavation operation for the instrument tower footing.

Temporary vertical cuts made in both the surface clay type alluvial soils and granite bedrock material should stand well without the necessity of shoring, provided the zone of excavation is properly dewatered. Should isolated zones of granular soils possessing insufficient cohesive characteristics to assure stability be exposed in the sidewalls of excavations, they should be stabilized by shoring or other means to prevent gross failure in the adjacent areas of the cut. Large areas of unstable materials are not expected to be exposed in the sidewalls of the excavations based on the materials encountered in the borings.

8. Dewatering

As stated previously in this report, a groundwater condition was encountered in borings 1B, 2 and 3 which were

bailed out to depths on the order of 25 ft and then observed for a 48-h period. In each boring the water level rose to a depth of 12± ft below existing grade. It is not believed that the elevation to which the water rose constitutes a true groundwater table elevation considering the known depths of water wells in the immediate area. It is more likely that a water seepage condition exists in a 2- to 3-ft thick zone of the alluvium which coverlies the relatively impermeable granite bedrock.

The construction site can most likely be dewatered by construction of a seepage cut-off diversion trench drain in the area above and to the east of the construction site. The trench should be excavated 3 or 4 ft into the bedrock below the seepage zone to provide reservoir capacity. The seepage flow can be pumped from the trench and disposed of in Larry's Creek.

H. High Performance Microwave Link Between DSS 61 and DSS 62, *B. Bridges*

1. Requirement

The requirement was for a system that would increase transmission capabilities to satisfactorily fulfill the requirements of the multiple mission support area (MMSA) and other facilities. Prior to installation of the microwave link the only connection between stations was by cable. With the microwave system there will be an alternate route capability.

2. Performance

This system, developed by Collins Radio Co., is fully transistorized except for the transmitter klystron. It operates between 7.125 and 8.4 kMHz, and consists of 2 full duplex RF channels, 12 channels of duplex multiplex and 4 channels of teletype VFTG (voice frequency telegraph gear). It has the following performance characteristics:

Bandwidth	dc to 8.5 MHz
Radio baseband impedance	75 Ω, unbalanced
Transmitter	
Modulation	FM
Power output at waveguide flange	1 W, +30 dBmW, 4 to 8 GHz
Receiver	IF bandwidth, 15 or 25 MHz at −3 dB points
IF	70 MHz
Noise figure (including branching losses)	12 dBmW max, 4 to 8 GHz
Preselector	8-section cavity, 4 to 8 GHz

3. Implementation

An interim 100-mW system was installed and operational on June 2, 1967. The prime 1-W system is presently on site and will be installed and operational not later than November 11, 1967.

References

1. Snelling, N. J., "The Geology and Petrology of the Murrumbidgee Batholith," *Quart. J. Geolog. Soc. London*, No. 462, November 1959.
2. Taylor, D. W., *Fundamentals of Soil Mechanics*, Chap. 11, John Wiley & Sons, Inc., New York, N. Y., 1948.